

Retrofitting Metal-Organic Frameworks

TCNQ@Cu₃BTC₂ as a Case Study for Functional Material Design

Christian Schneider

Vollständiger Abdruck der von der Fakultät für Chemie der Technischen Universität München zur Erlangung des akademischen Grades eines

Doktors der Naturwissenschaften (Dr. rer. nat.)

genehmigten Dissertation.

Vorsitzender: Prof. Dr. Karsten Reuter
Prüfer der Dissertation: 1. Prof. Dr. Roland A. Fischer
2. Priv.-Doz. Dr. Mark D. Allendorf
3. Prof. Dr. Thomas Weitz

Die Dissertation wurde am 07.08.2019 bei der Technischen Universität München eingereicht und durch die Fakultät für Chemie am 10.09.2019 angenommen.

Acknowledgement

Firstly, I would like to thank my advisor, Prof. Dr. Roland A. Fischer, for his support, trust and wisdom. He allowed me to pursue my research interests without restriction, and gave me guidance when needed. From the first lecture in coordination chemistry to the final stage of my PhD, he played a key role in my academic career and has helped me to become the scientist I am today.

Further, I would like to acknowledge Dr. Mark D. Allendorf for being my second advisor, and for hosting me in his group during my research stays in California. The welcoming and inspiring atmosphere in his group has made the visits a highlight of my PhD studies. Mark's mentoring and encouragement, particularly during the first half of my PhD, have helped me to stay focused and motivated which I am very grateful for.

Next, I would like to thank Dr. Gregor Kieslich for his excellent guidance, his enthusiasm and the numerous scientific discussions. He has helped me to ask the right questions, and has been very influential for the work in this thesis. Beyond that I thank Gregor for his contagious passion for science and the great working atmosphere during our joint research projects.

I gratefully acknowledge the many collaborators who enabled me to perform important measurements for my research. Particularly, I want to thank Drs. A. Alec Talin and Vitalie Stavila (Sandia National Laboratories) for help with thin film synthesis and conductivity measurements, Dr. Raimund Koerver (Gießen University) for help with electrochemical characterization, and Dr. Valentina Crocellà (Turin University) for help with infrared spectroscopy measurements.

In addition to my direct advisors and collaborators, there are a number of people who were very influential for my thesis and have made the past 3.5 years a memorable period of my life. I would like to acknowledge...

... Dr. Alexander Pöthig for various discussions about science, politics and life. I thank him for his advice to my research, his great humor, and friendship.

... the numerous friends and colleagues I worked with in the Fischer lab. Particularly, I want to thank Margit Aust, Dr. Konstantin Epp, Patricia Heiß, David Mayer, Anna Lisa Semrau, Miguel Rivera Torrente, Dardan Ukaj, and Pia Vervoorts as well as the former group members Drs. Philipp Altmann, Andreas Schneemann, and Suttipong Wannapaiboon. I will remember the fantastic atmosphere in the lab, numerous parties and great conference visits with you.

... all the lab members from the Kühn group, but specifically Elisabeth Bauer and Benjamin Hofmann, for fun parties and unforgettable group retreats to the Austrian Alps.

... all the Bachelor and Master students I had the chance to work with and to whom I could pass on my knowledge in chemistry. Particularly, I would like to thank Margit Aust, David Bodesheim, and Dardan Ukaj for their efforts in the research projects and the great time together.

... the academic and technical staff of the AMC group and the CRC for a stimulating working atmosphere and the support in everyday laboratory work. Special thanks goes to Martin Schellerer for his constant willingness to help with the smaller and bigger issues and the battle against bureaucracy.

... my (former) roommates Armin, Katharina, Lara, and Leon, my friends from the Studienstiftung, particularly Lea and Lukas, my friends in the U.S., particularly Amanda and Jonathan, my friends from university, particularly Christoph, Katharina, and Raimund, as well as my friends from home, particularly Daniel, Fabian, Fabio, Florian, Hendrik, and Simon. Thank you for your great friendship and for always being there despite the long distance.

At this point I would like to acknowledge my scholarship from the German National Academic Foundation (Studienstiftung), particularly for the ideational support including seminars, workshops, language courses and a valuable network, as well as my scholarship from the German Chemical Industry Association (FCI), and financial support from the German Academic Exchange Service (DAAD).

Finally, without the support and love of my family I would not be in the position I am today and for that I want to acknowledge and thank, from the bottom of my heart, my brother Martin and my parents Heinz and Gisela Schneider.

Abstract

Metal-organic frameworks (MOFs) are one of the most exciting recent developments in materials chemistry. Their modular building block principle allows the assembly of metal nodes and organic linkers to form open framework structures with different topologies and properties. Over the past two decades tens of thousands of MOFs have been synthesized and proposed for a number of applications ranging from gas storage and separation to microelectronics and sensing. A more recent advance of the field is the post-synthetic installation of cross linkers (CLs) between metal nodes with open metal sites (OMSs) as a means to manipulate the properties of the framework. The method established as *retrofitting* has proven to be particularly useful in improving mechanical robustness and gas sorption properties, but the concept can be translated into other areas. For instance, 7,7,8,8-tetracyanoquinodimethane (TCNQ) can be infiltrated into the pores of the MOF Cu_3BTC_2 (HKUST-1, BTC = 1,3,5-benzenetricarboxylate) and bridge the OMSs of the framework, which was observed to come with a significant increase in the electrical conductivity of the material. Subsequently, several research groups conducted computational and experimental studies to elucidate the conduction mechanism in $\text{TCNQ}@Cu_3\text{BTC}_2$ based on an ideal structural model of TCNQ-bridged metal nodes. However, for a detailed understanding of the macroscopic properties, a profound description of the microscopic structure is essential. Influences of synthesis conditions, structural defects, and the degree of order and disorder (*i.e.* heterogeneity) of the TCNQ molecules must be considered to obtain a clearer picture of the complex system.

The work presented in this thesis is divided into two parts. First, an in-depth study on $\text{TCNQ}@Cu_3\text{BTC}_2$ is presented, which aims at a better understanding of the structure-property relationships in the system. Second, retrofitting as a post-synthetic modification method is revisited and guidelines for a systematic expansion of the concept are established. In a first study, the reactivity of Cu_3BTC_2 with methanol solutions of TCNQ was investigated which revealed a complete transformation of the MOF to the dense coordination polymer $\text{Cu}(\text{TCNQ})$ caused by the non-inert solvent. Consequently, a new solvent-free synthesis method based on gas-phase loading was developed to exclude external influences of traces of water and (non-inert) solvent, which allowed an unperturbed study of the host-guest system with precise control of the TCNQ loading amount. For the first time, crystallographic evidence was presented confirming the ditopic binding of TCNQ to two neighboring metal nodes. The room temperature electrical conductivity was found to increase exponentially with the TCNQ loading up to a value of $\sigma = 1.5 \cdot 10^{-4} \text{ S cm}^{-1}$, while the residual specific surface area remained at a high level with $574 \text{ m}^2 \text{ g}^{-1}$. A small byproduct formed at the surface of the crystallites in very low quantities which was identified as $\text{Cu}(\text{TCNQ})$. This finding triggered a detailed investigation into the influence of framework Cu(I) defects that were hypothesized to be the reducing agent for TCNQ. Indeed, it was found that Cu(I)-Cu(II) metal nodes, which inevitably form during the thermal activation of Cu_3BTC_2 , correlate quantitatively with the amount of TCNQ radical anions present in the pores of the infiltrated samples. These results have implications for the understanding of the TCNQ-induced electrical

conductivity in the material. While the preferential ordering of TCNQ along the paddlewheel units confirms previous computational modeling, the complex defect chemistry described in this study represents an important aspect that has to be taken into account when modelling the charge transport in the material. In the second part of this thesis project, the mechanical properties of Cu_3BTC_2 were investigated as a function of retrofitting. It was found that the negative thermal expansion (NTE) of the material can be systematically tuned by installation of TCNQ. The increased connectivity through retrofitting is associated with a stiffening of the framework leading to decreased NTE. Finally, a heuristic computational framework was developed to evaluate the fit of a CL in a MOF depending on the geometry of the CL, the relative location of neighboring metal nodes and a model interaction potential between the two components. The program named *RetroFit* was used to identify further potential $\text{CL}@\text{Cu}_3\text{BTC}_2$ materials of which three were successfully synthesized in the lab. Even though the three materials show the same structural features as $\text{TCNQ}@\text{Cu}_3\text{BTC}_2$, they did not show emergent electrical conductivity. The algorithm was then applied to other Cu-based MOFs and can guide the synthesis of new retrofitted $\text{CL}@\text{MOF}$ systems with tailored materials properties in the future.

Zusammenfassung

Metallorganische Gerüstverbindungen (MOFs) sind eine der spannendsten aktuellen Entwicklungen in der Materialchemie. Das modulare Baukastenprinzip ermöglicht es, aus Metallknoten und organischen Linkern poröse Gerüststrukturen mit unterschiedlichen Topologien und Eigenschaften herzustellen. In den letzten zwei Jahrzehnten wurden Zehntausende MOF Strukturen synthetisiert und für verschiedene Anwendungen untersucht, die von der Gasspeicherung und -trennung bis hin zur Mikroelektronik und Sensorik reichen. Ein aktueller Fortschritt ist der post-synthetische Einbau von Cross Linkern (CLs) zwischen unterkoordinierten Metallknoten wodurch die Materialeigenschaften modifiziert werden können. Die als *Retrofitting* etablierte Methode hat sich als besonders nützlich erwiesen, um die mechanische Stabilität und Gasadsorption des Materials zu verbessern, aber das Konzept lässt sich auch auf andere Bereiche übertragen. So kann beispielsweise 7,7,8,8-Tetracyanoquinodimethan (TCNQ) in die Poren des MOFs Cu_3BTC_2 (HKUST-1, BTC = 1,3,5-Benzoltricarboxylat) eingebracht werden und offene Metallstellen (OMSs) des Gerüsts überbrücken, woraufhin eine deutliche Steigerung der elektrischen Leitfähigkeit des Materials beobachtet wurde. Nachfolgend führten mehrere Forschergruppen theoretische und experimentelle Studien durch, um den Leitungsmechanismus in $\text{TCNQ}@Cu_3\text{BTC}_2$ aufzuklären. Dabei sind sie von einem idealisierten Strukturmodell ausgegangen, in dem TCNQ systematisch Metallknoten miteinander verbindet. Für eine detaillierte Beschreibung der makroskopischen Eigenschaften ist jedoch ein tiefes Verständnis der mikroskopischen Struktur erforderlich. Notwendigerweise müssen dabei auch Einflüsse durch Synthesebedingungen, strukturelle Defekte sowie der Grad der Ordnung bzw. Unordnung der TCNQ-Moleküle (heterogene Verteilung) berücksichtigt werden.

Die in dieser Doktorarbeit präsentierten Ergebnisse lassen sich in zwei Teile gliedern. Zunächst zielt eine vertiefte Studie zu $\text{TCNQ}@Cu_3\text{BTC}_2$ auf ein besseres Verständnis der Struktur-Eigenschaftsbeziehungen in dem System ab. Danach wird Retrofitting als post-synthetische Modifikationsmethode diskutiert und etabliert und schließlich werden Empfehlungen für eine systematische Erweiterung des Konzepts gegeben. In einer ersten Studie wurde die Reaktivität von Cu_3BTC_2 mit TCNQ in Methanol untersucht. Es wurde festgestellt, dass der MOF sich bedingt durch das nicht-inerte Lösemittel vollständige in das Koordinationspolymer $\text{Cu}(\text{TCNQ})$ umsetzt. Daraufhin wurde eine neue lösungsmittelfreie Infiltrationsmethode über die Gasphase entwickelt, welche Kontrolle über die TCNQ-Menge ermöglicht und äußere Einflüsse wie Spuren von Wasser und (nicht-inertem) Lösungsmittel auszuschließt, wodurch eine präzise Untersuchung des Systems ermöglicht wird. Zum ersten Mal wurden kristallographische Hinweise gefunden, welche die ditopische Bindung von TCNQ an zwei benachbarte Metallknoten bestätigen. Es wurde festgestellt, dass die elektrische Leitfähigkeit bei Raumtemperatur mit der TCNQ-Beladung exponentiell bis zu einem Wert von $\sigma = 1,5 \cdot 10^{-4} \text{ S cm}^{-1}$ ansteigt, während die verbleibende spezifische Oberfläche mit $574 \text{ m}^2 \text{ g}^{-1}$ auf einem hohen Niveau bleibt. Darüber hinaus wurde entdeckt, dass sich in geringer Menge eine Nebenphase an der Oberfläche der MOF-Kristallite bildet, welche als $\text{Cu}(\text{TCNQ})$ identifiziert wurde. Dieser Befund führte zu einer

detaillierten Studie der intrinsischen Cu(I)-Defekte im MOF, da diese im Verdacht standen als Reduktionsmittel für TCNQ zu dienen. Darin wurde festgestellt, dass tatsächlich die Menge an Cu(I)-Cu(II)-Metallknoten, die sich unausweichlich bei der thermischen Aktivierung von Cu_3BTC_2 bilden, quantitativ mit der TCNQ-Radikalanionenkonzentration in den beladenen Proben korreliert. Diese Ergebnisse haben tiefgreifende Auswirkungen auf das Verständnis der TCNQ-induzierten elektrischen Leitfähigkeit im Material. Obwohl die postulierte Anordnung von TCNQ Molekülen entlang der Cu Koordinationsstellen bestätigt werden konnte, stellt die in dieser Arbeit beschriebene komplexe Defektchemie einen wichtigen Aspekt dar, und muss bei der Modellierung der Leitfähigkeit des Materials berücksichtigt werden. Im zweiten Teil dieser Arbeit wurden die mechanischen Eigenschaften von Cu_3BTC_2 in Abhängigkeit von Retrofitting untersucht. Es wurde festgestellt, dass die negative thermische Ausdehnung (NTE) des Materials durch die Installation von TCNQ systematisch manipuliert werden kann. Die erhöhte Konnektivität durch Retrofitting geht mit einer Versteifung der Gerüstverbindung einher, die zu verringerter NTE führt. Schließlich wurde ein heuristisches Berechnungsmodell entwickelt, das auf Basis der Geometrie des CLs, der relativen Lage der Metallknoten im MOF und eines Interaktionspotentials zwischen CL und MOF bewertet, wie gut der CL in den MOF eingebaut werden kann. Mit dem Programm namens *RetroFit* wurden weitere potenzielle $\text{CL}@\text{Cu}_3\text{BTC}_2$ Materialien identifiziert, von denen drei im Labor erfolgreich synthetisiert wurden. Obwohl die drei Verbindungen die gleichen strukturellen Eigenschaften wie $\text{TCNQ}@\text{Cu}_3\text{BTC}_2$ aufweisen, zeigten sie keine elektrische Leitfähigkeit. Der Algorithmus wurde anschließend auf andere Cu-basierte MOFs angewendet und soll in der Zukunft helfen die Synthese neuer $\text{CL}@\text{MOF}$ -Systeme mit maßgeschneiderten Materialeigenschaften zu steuern.

List of Abbreviations

0D	zero dimensional
1D	one dimensional
2D	two dimensional
3D	three dimensional
Ac	acetate
AES	Auger electron spectroscopy
AFM	atomic force microscopy
BDC	DMF
BET	Brunauer–Emmett–Teller
BPDC	biphenyl-4,4'-dicarboxylate
BTB	1,3,5-benzenetribenzoate
BTC	1,3,5-benzenetricarboxylate
CL	cross linker
COF	covalent organic frameworks
DBA	donor bridge acceptor
DCM	dichloromethane
DCNQI	N,N'-dicyanoquinonediimide
DDQ	2,3-dichloro-5,6-dicyano- <i>p</i> -benzoquinone
EPR	electron paramagnetic resonance
EtOH	ethanol
GIXRD	grazing incidence X-ray diffraction
H ₂ BDT	5,5'-(1,4-phenylene)bis(1H-tetrazole)
H ₂ TPyP	5,10,15,20-tetra-4-pyridyl-21 <i>H</i> ,23 <i>H</i> -porphine
H ₄ TBAPy	1,3,6,8-tetrakis(<i>p</i> -benzoic acid)pyrene
HKUST	Hong Kong University of Science and Technology
HOMO	highest occupied molecular orbital
IR	infrared
IRMOF	isorecticular metal-organic framework
ITO	indium thin oxide
IUPAC	International Union of Pure and Applied Chemistry
JACS	The Journal of the American Chemical Society
LIFM	Lehn Institute of Functional Materials
LUMO	lowest unoccupied molecular orbital
MeOH	methanol

MOF	metal-organic framework
NMR	nuclear magnetic resonance
NTE	negative thermal expansion
OH-TPCB	4,4'-dihydroxybiphenyl-3,3',5,5-tetra(phenyl-4-carboxylate)
OMe-TPCB	4,4'-dimethoxy-biphenyl-3,3',5,5-tetra(phenyl-4-carboxylate)
OMS	open metal site
PCN	porous coordination network
PXRD	powder X-ray diffraction
RUM	rigid unit mode
SBU	secondary building unit
SCE	saturated calomel electrode
SEM	scanning electron microscopy
SSA	specific surface area
TCNB	tetracyanobenzene
TCNE	tetracyanoethylene
TCNP	tetracyanopyrazine
TCNQ	7,7,8,8-tetracyanoquinodimethane
TCNX	the group of TCNQ, TCNE, TCNB and TCNP
TPDC	terphenyl-4,4''-dicarboxylate
TPP	5,15-bis-(3,4,5-trimethoxyphenyl)-10,20-bis-(4-carboxyphenyl)
TTF	tetrathiafulvalene
UiO	University of Oslo

Table of contents

Acknowledgement.....	i
Abstract.....	iii
Zusammenfassung	v
List of Abbreviations.....	vii
1 Introduction.....	1
1.1 Towards Functional Materials	1
1.2 Metal-Organic Frameworks.....	3
1.2.1 Emergence of Metal-Organic Frameworks.....	3
1.2.2 Reticular Chemistry	7
1.2.3 Defects in Metal-Organic Frameworks	9
1.2.4 Properties and Applications.....	10
1.2.5 Post-Synthetic Modification	12
1.3 Retrofitting Metal-Organic Frameworks	14
1.4 TCNQ@Cu ₃ BTC ₂ as a Model System for Retrofitting.....	18
1.4.1 Cu ₃ BTC ₂	18
1.4.2 TCNQ	22
1.4.3 TCNQ@Cu ₃ BTC ₂	24
2 Objective	28
3 Results and Discussion	29
3.1 Study I: Surface Morphology and Electrical Properties of Cu ₃ BTC ₂ Thin Films Before and After Reaction with TCNQ	30
3.2 Study II: High Electrical Conductivity and High Porosity in a Guest@MOF Material: Evidence of TCNQ Ordering within Cu ₃ BTC ₂ Micropores.....	42
3.3 Study III: Scrutinizing the Pore Chemistry and the Importance of Cu(I) Defects in TCNQ-Loaded Cu ₃ BTC ₂ by a Multitechnique Spectroscopic Approach	51
3.4 Study IV: Tuning the Negative Thermal Expansion Behavior of the Metal-Organic Framework Cu ₃ BTC ₂ by Retrofitting.....	64
3.5 Study V: Retrofitting Metal-Organic Frameworks.....	71
4 Conclusion and Outlook	82
4.1 TCNQ@Cu ₃ BTC ₂	82
4.2 Retrofitting.....	86
5 Bibliography.....	88
6 Supporting Information	100
6.1 Supporting Information Study I	100
6.2 Supporting Information Study II	105
6.3 Supporting Information Study III	123
6.4 Supporting Information Study IV	143
6.5 Supporting Information Study V	163
7 Appendix	196
7.1 Complete List of Publications.....	196
7.1.1 Publications on which this Thesis is Based.....	196
7.1.2 Other Publications	198
7.2 Reprint Permissions.....	199

1 Introduction

1.1 Towards Functional Materials

The systematic design of functional materials with tailor-made properties is the main goal of materials chemistry. The development of such materials it is essential in order to meet the technological, socio-economic and environmental challenges of society. Thereby, each application comes with its own ensemble of specifications that the material must meet in order to find its way onto the market. For example, the efficient capture of CO₂ from exhaust gases is important for sustainable energy production and the requirements for a potential material would be a high capacity and selectivity for the uptake of CO₂, a facile regeneration of the material (desorption of CO₂) and chemical robustness against other components of the exhaust gas. Another application that requires the use of functional materials is sensing. Thereby, the active component of a sensor must selectively recognize a specific compound and show a measureable response when the analyte is present. Typical sensor materials are metal oxides such as SnO₂ or ZnO which are used in chemiresistive sensing of gases like CO or O₂.¹ For the selective detection of more complex analytes, a sensor material could be developed that can recognize the molecule size or specific functional groups, clearly exceeding the technical feasibility of common sensor materials.² Such sensor materials will necessarily consist of more sophisticated structures and may resemble the recognition abilities of bio molecules. Potential read out of such a sensor would be a change in its electrical, optical or magnetic properties.

Searching for a suitable material for a specific application, a lot of research focuses on existing materials and their modification, as the bottom up design of new structures can be very challenging and the inverse “material retro synthesis” is largely absent. The question arises: *How can we design new materials with desired properties?* When thinking of design principles, materials can be distinguished by the interaction between their components. For instance, purely inorganic compounds such as chalcogenides and halides are formed by ionic interactions, while organic materials such as polymers are held together by covalent bonds. Single polymer chains as well as other supramolecular structures (e.g. bio molecules) are held together by weak non-covalent interactions such as dispersion interactions or hydrogen bonding. Finally, coordination compounds are composed of a central metal ion and a sphere of coordinating ligands. For the rational design of structural motifs, the exploitation of coordination bonds seems intriguing as the directionality of coordination compounds is well defined and understood. In addition, the virtually infinite number of combinations of metal ions and ligands with distinct geometries allows for a high synthetic versatility. The use of bi- or polydentate ligands translates the molecular coordination compound into three dimensional space allowing for the assembly of supramolecular structures.³ Thereby, the choice of metal and ligand determines whether a discrete supramolecular structure such as a polygon or a cage, or an extended two- or three dimensional coordination network is formed.⁴ Importantly, the control over the spatial arrangement of the different components as well as the

opportunities to tune the physicochemical properties make coordination networks interesting candidates for the design of new materials. In fact, coordination networks are heavily researched for a wide range of potential applications ranging from energy storage and electrocatalysis to electronic devices and chemical sensing.⁵⁻⁶ Looking at the two applications discussed above, one prerequisite for a suitable material is a considerable porosity to either store CO₂ or to detect an analyte molecule, for example by size (molecular sieving).⁷ While most coordination networks exhibit no or only limited accessible pore space, metal-organic frameworks (MOFs), a sub-class of coordination networks, are characterized by high crystallinity and permanent porosity and thus vastly interesting in the context of gas storage and sensing.^{6, 8-9} Beyond industrial applications, the high level of control over the spatial arrangement of molecular entities in coordination networks and MOFs provides researcher with an excellent platform to identify and establish fundamental structure-property relations, thereby increasing our understanding of materials chemistry.

1.2 Metal-Organic Frameworks

1.2.1 Emergence of Metal-Organic Frameworks

Metal-organic frameworks (MOFs) as they are known and studied today are the product of a long development that dates back to the late 19th century.¹⁰ At that time the chemist and later Nobel Prize winner A. Werner set the groundwork for what is today known as classical coordination chemistry. He studied hexamminecobalt(III) chloride and related compounds, which are today described as Werner complexes (Figure 1).¹¹⁻¹³

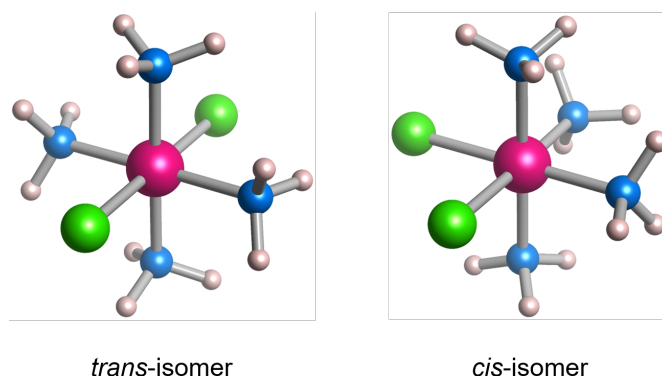


Figure 1. Representation of the two possible isomers of the octahedral complex $[\text{Co}(\text{NH}_3)_4\text{Cl}_2]$. In the *trans*-isomer, the chloride ligands are on opposite sites while the ammine ligands are in one plane. In contrast, the chloride ligands in the *cis*-isomer are located on neighboring positions. Co, Cl, N, and H atoms are depicted in magenta, green, blue and off-white, respectively.

Werner's research inspired other researchers like K. A. Hofmann (1870 - 1940) to translate coordination chemistry of isolated metal complexes (zero-dimensional, 0D) into higher dimensions which resulted in the advent of coordination compounds with extended structures in one, two or three dimensions (1D, 2D, or 3D). One of the early examples is the so-called Hofmann clathrate $[\text{Ni}(\text{CN})_2(\text{NH}_3)](\text{C}_6\text{H}_6)$ in which Ni(II) ions are interconnected by cyanide to form a 2D structure (Figure 2).¹⁴ Therein, Ni ions that are coordinated by carbon atoms exhibit a square planar coordination environment, while those coordinated via the N-side of cyanide bind two additional ammonia ligands resulting in an octahedral ligand sphere. Benzene molecules reside in between the layers. The elucidation of the structure was only possible in 1952 – 55 years after its discovery by Hofmann – by the advent of X-ray crystallography.¹⁵ Following on from Hofmann's work, chemists substituted the monodentate ammonia ligands by di- or polydentate alkyl amines to form 3D structures.¹⁶⁻¹⁸ Interestingly, the Pigment *Prussian blue*, which had been known since the beginning of the 18th century, has the structure $\text{Fe}_4[\text{Fe}(\text{CN})_6]_3$ and represents a 3D extended coordination complex.¹⁹ During the second half of the 20th century a large number of structures was published that today are categorized as coordination polymers or coordination networks.³

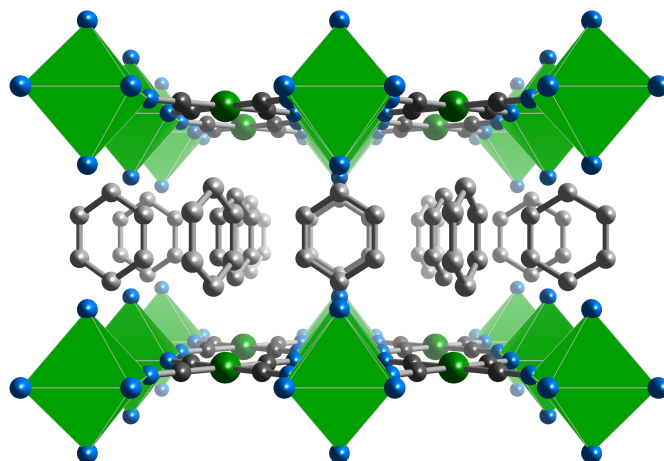


Figure 2. Crystal structure of the Hofmann clathrate $[\text{Ni}(\text{CN})_2(\text{NH}_3)](\text{C}_6\text{H}_6)$, viewed along the a axis. Hexa-coordinated Ni ions, depicted as green octahedra, are connected via bidentate cyanide ligands with Ni ions in a square planar coordination geometry to form a 2D coordination polymer. Within the layered structure, benzene molecules are intercalated. Color code: Ni, green; N, blue; C, grey. H atoms are omitted for clarity.

Most of these compounds were constructed from di- or polydentate organic ligands with amine or nitrile groups that bind to the metal center. Although different structures and topologies could be realized, the stability of these structures were dependent on the presence of solvent molecules within the scaffold to prevent their collapse. It was until 1995 when O. M. Yaghi coined the term *metal-organic framework* to describe coordination networks that exhibit stability even after removal of solvents and retain permanent porosity after adsorption and desorption of guest molecules.²⁰⁻²¹ Four years later, he published the structure of the iconic MOF $[\text{Zn}_4\text{O}(\text{BDC})_3](\text{DMF})_x$ (BDC = benzene-1,4-dicarboxylate, DMF = N,N'-dimethylformamide), better known by its trivial name *MOF-5*, in which the ditopic linker interconnects tetrahedral Zn_4O clusters to form a cubic structure (see Figure 3).²² In contrast to previous coordination networks, the use of carboxylate-ligands affords a more stable coordination bond between the linker and the metal node. Later, S. Kitagawa distinguished labile (collapsing) and rigid (stable) coordination networks as 1st and 2nd generation of MOFs and introduced a 3rd generation describing MOFs that exhibit structural flexibility (responsivity) to undergo a phase transition upon removal of solvents.²³

Considering the vast amount of materials known today, there was a strong need for terminology guidelines. According to the recommendations of the International Union of Pure and Applied Chemistry (IUPAC) from 2013 a MOF is defined as “a coordination network with organic ligands containing potential voids”.²⁴ A coordination network, in turn, is a 1D coordination polymer that extends in two or three dimensions through cross links of individual coordination polymer chains, or is a coordination compound that extends in two or three dimensions through coordination bonds.²⁴⁻²⁵ Following this relatively broad definition, MOFs characterize as crystalline organic-inorganic materials with an at least 2D structure and the potential existence of guest-accessible pore space. Strictly speaking, the word “organic ligands” can be controversial in this context, as arguments can be found that classify ligands such as oxalate, cyanides and tetracyanoethylene (TCNE) as either organic or inorganic compounds,²⁵ and

consequently, coordination networks constructed from such linkers would qualify as MOFs or not.

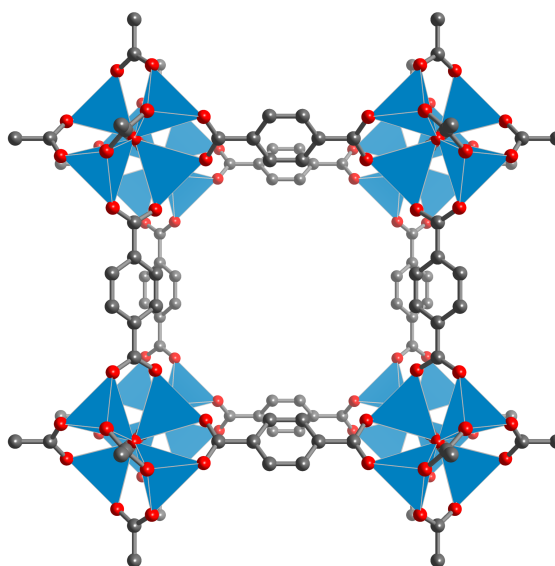


Figure 3. Crystal structure of MOF-5 viewed along the a axis. Hexa-coordinating metal nodes consisting of Zn_4O tetrahedra are interconnected by linear BDC linkers to form a cubic network. The coordination sphere around the Zn atoms is represented by blue tetrahedra and the O and C atoms are depicted in red and grey. H atoms are omitted for clarity.

In general, MOFs are assembled from metal ions or clusters that are interconnected by polydentate organic ligands to form supramolecular 2D or 3D frameworks (Figure 4).^{6, 8-9} Staying within the semantic field of networks, the ligands are often referred to as linkers while the metal clusters are called nodes. The topology and geometry of the linker together with the coordination geometry of the metal node define the topology of the MOF.²⁶⁻²⁸ Typically, the metal node, also referred to as secondary building unit (SBU), consists of first row transition metal ions such as Zn^{2+} , Cu^{2+} or Ni^{2+} but also MOFs with second and third row transition metals (particularly Zr^{4+}) or lanthanides are known.²⁹⁻³⁰ Common linker molecules are carboxylates or N-heterocycles, such as imidazolates.²⁸

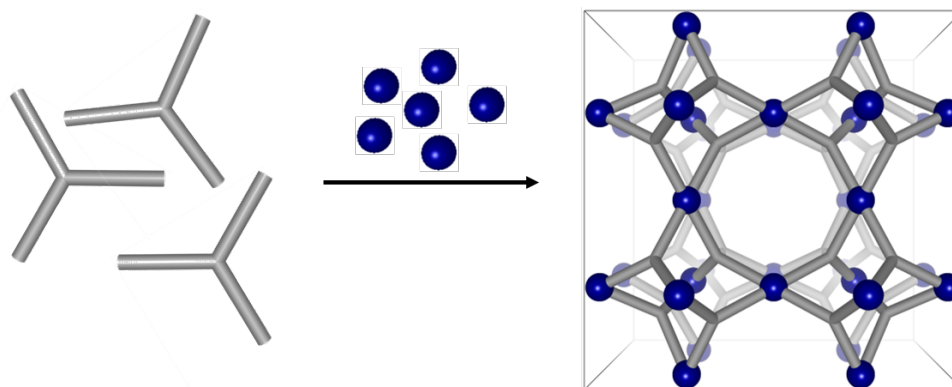


Figure 4. Illustration of the assembly of a metal-organic framework. Here, a tritopic linker (grey) is combined with a tetratopic metal node (blue) to form a highly symmetric, cubic coordination network exhibiting void space.

An important aspect in the formation of MOFs is the coordination bond equilibrium. Unlike in classical coordination polymers which are held together by relatively weak donor/acceptor bonds between the metal centers and neutral amine- or nitrile- based ligands, anionic carboxylate ligands form relatively strong ionic coordination bonds. In combination with substitution-labile 3d metal ions this leads, in general, to fast coordination bond formations and reaction kinetics. Compared to above-mentioned coordination polymers which are relatively easy to crystallize, the thermodynamics and fast kinetics of the MOF formation must be taken into account when designing the experiment. To allow for a steady crystallization and error correction of wrongly attached building blocks, a competitive reaction equilibrium needs to be established by the choice of the reaction conditions. Typically, MOF syntheses are done at elevated temperatures for example under solvothermal conditions. Moreover, solvents and additives can stir the reaction kinetics; for example addition or *in-situ* formation of a base results in the liberation of the linker by deprotonation of the carboxylic acid.^{22, 31} Moreover, by employing a modulator such as a monotopic carboxylic acid, the crystallization can be slowed down due to the competitive reaction equilibrium between linker, modulator and metal ion.³² This way, highly crystalline MOF structures can be synthesized. On the contrary, imperfect assembly of the molecular building blocks, *i.e.* the formation of structural defects, is an interesting means to manipulate the material's properties and has spawned a new area of defect-engineered MOFS (chapter 1.2.3).

Concept Box 1: MOFs, the Hybrid Siblings of Inorganic Zeolites

The closest relatives of MOFs in the world of inorganic materials are zeolites. The crystalline microporous aluminosilicates are composed of vertex-sharing SiO_4 and AlO_4 tetrahedra and have the general formula $[\text{Si}_{1-n}\text{Al}_n\text{O}_2]^{n-}$.³³ The negative charge of the framework is compensated by cations of group I or II elements (Na, K, Mg, Ca) residing in the microporous cavities. Around 200 zeolites with different Si/Al ratios and distinct topologies are known today, of which around 40 occur naturally.³⁴ Compared to MOFs, the parameter space for the synthesis of zeolites is limited as only the Si/Al ratio and the reaction conditions determine the structure and properties. Commercialized since the mid-20th century,³⁵ zeolites have become an integral part of heterogeneous catalytic processes in the chemical industry and are further used as molecular sieves or in water purification.³⁶ MOF chemists tried to mimic zeolites by replacing the O atom by imidazole ligands and introduced a new sub-class of MOFs termed zeolitic imidazolate frameworks (ZIFs).³⁷ Even though ZIFs are topologically isomorphic with zeolites, the purely inorganic version outperforms ZIFs and MOFs in many applications owing to their higher mechanical and chemical stability, particularly in heterogeneous catalysis.³⁸⁻⁴⁰

1.2.2 Reticular Chemistry

The formation of extended open framework structures by systematically linking discrete molecular building blocks via strong bonds is described by reticular chemistry.¹⁰ Thereby, the term *reticular* is derived from the Latin word *reticulum* and translates to *having the form of a net, or netlike*.¹⁰ Indeed, reticular chemistry is at the heart of MOF chemistry, in which organic and inorganic building blocks with defined sizes and geometries are combined to form a crystalline network structure. In a way, this idea resembles a molecular version of *Lego*[®] or *Tinkertoy*[®]. This distinguishes MOFs from other inorganic materials such as zeolites (see Concept Box 1), which are restricted in their composition space and synthetic versatility. Looking at the molecular building blocks as linkers and connectors rather than as organic molecules or metal clusters, it is possible to describe the MOF structure as a network. In fact, the idea to simplify the geometric principles of crystal structures in terms of network topologies was introduced by A. F. Wells in 1954.⁴² Thereafter, structures have been assigned three-letter codes to distinguish different nets, e.g. **dia** for the topology of the carbon allotrope diamond. To deduce the sometimes-complicated topologies of MOFs, the structure can be expressed by the connectivity of their building blocks. A MOF made from m -connecting linkers and n -connecting SBUs possesses an underlying net that is (m,n) -coordinated and possible nets can be compared with a topology database.⁴³ For example, MOF-5 (see Figure 3 and Figure 5) is constructed from a linear linker and a six-connecting SBU (using the C atoms of the carboxylates as points of extension) resulting in a $(2,6)$ -coordinated net which has the symbol **pcu**. Fascinatingly, the topology is retained when the BDC linker of MOF-5 is replaced by a linear linker with different length or additional functionality.³¹ The concept called isorecticular expansion is illustrated in Figure 5. Increasing the linker size from BDC (IRMOF-1) via biphenyl-4,4'-dicarboxylate (BPDC, IRMOF-10) to terphenyl-4,4''-dicarboxylate (TPDC, IRMOF-16) while maintaining the Zn_4O SBU gives isorecticular MOFs (IRMOFs) with different pore sizes.³¹ It has to be noted, that the torsion of the TPDC linker allows two configurations of the tetrahedral Zn_4O SBU at the octahedral vertex, allowing for isorecticular isomerism which constitutes a certain form of polymorphism.⁴⁴

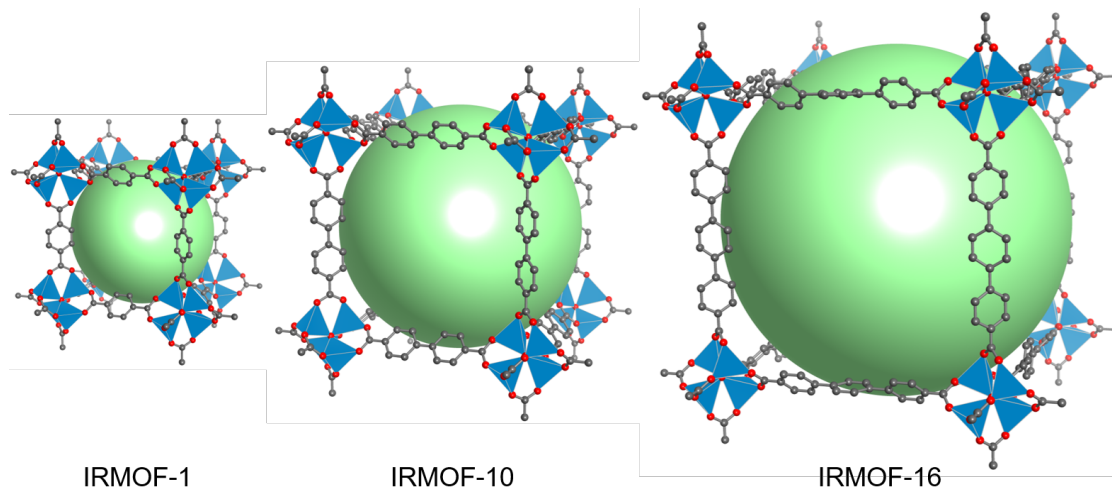


Figure 5. Crystal structure of IRMOF-1 (MOF-5), IRMOF-10 and IRMOF-16 viewed along the a axis. The systematic expansion of the linker results in increasingly larger pore sizes as illustrated by the green spheres inside the cavities of the MOFs.

1.2.3 Defects in Metal-Organic Frameworks

Despite its high crystallinity, the occurrence of defects within the crystal lattice of a MOF is not unusual. In fact, the study of intrinsic defects or the deliberate introduction thereof has always been at the heart of materials and crystal chemistry with doped silicon, which has spawned the entire semiconductor industry, being the most prominent example.⁴⁵⁻⁴⁶ Therefore, it appears like a natural development that an entire field of defect-engineered MOFs has emerged over the recent years, exploiting defects as a means to modulate materials properties.⁴⁷⁻⁴⁹ In general, a defect is defined as a feature that locally breaks the periodicity of the static crystal lattice.⁴⁹ Besides the external crystal surface which breaks periodicity and thus always represents a (2D) defective state, (i) missing linker defects, (ii) missing node defects, (iii) modified linker defects, and (iv) modified node defects are the most common types of point defects (1D) in MOFs.

Two particular MOF systems were shown to be particularly interesting in the context of defect engineering of MOFs, namely Cu_3BTC_2 (HKUST-1, BTC = 1,3,5-benzenetricarboxylate) and $\text{Zr}_6\text{O}_4(\text{OH})_4(\text{BDC})_6$ (UiO-66).⁴⁷⁻⁵² The defect chemistry in Cu_3BTC_2 will be of high importance for the discussion of the results obtained in this dissertation and is separately discussed in chapter 1.4.1. Briefly, Cu_3BTC_2 is prone to form intrinsic defects during the MOF synthesis or thermal activation of the material.⁵³⁻⁵⁴ Moreover, the defect concentration in Cu_3BTC_2 can be manipulated by the use of defective linkers, e.g. isophthalate instead of BTC, thereby creating modified node defects.^{48, 51} Similarly, UiO-66 is known for its complex defect chemistry as a result of the coordination bond equilibrium between the Zr-nodes and the carboxylate-linkers. The addition of a modulator to the reaction solution allows the manipulation of the connectivity of the Zr-node.^{52, 55} Interestingly, these defects do not occur randomly but form correlated arrays that reduce the total energy of the lattice.⁵⁰

The generation of structural defects in a MOF can have a considerable effect on its physicochemical properties. For example, a complex correlation was found between the bulk modulus and the coordination number of the Zr-node in UiO-66, *i.e.* the number of missing linker defects.⁵⁶ Similarly, the defect concentration was shown to have a significant effect on the thermal expansion behavior of UiO-66(Hf).⁵⁷ In terms of applications, defect-engineered MOFs have shown to be of particular interest in the context of heterogeneous catalysis as defective sites such as OMSs represent additional active centers for the catalytic reaction.^{55, 58-61} In general, defect-engineering has emerged as a recent research direction within MOF chemistry and was shown to be an effective tool to manipulate materials properties.^{49, 62}

1.2.4 Properties and Applications

Unlike any other material, MOFs combine facets from crystalline inorganic materials with the synthetic versatility of organic compounds. The variety of possible metal nodes and the creative design of organic linkers gives access to a virtually infinite number of possible MOF structures.^{6,27} As a result, MOFs can be systematically designed to target specific properties and represent the perfect platform to establish and study structure-property relationships. In general, the key characteristics of a MOF are a high crystallinity and a permanent porosity which is maintained upon removal of solvents. In fact, MOFs hold the record for the highest Brunauer–Emmett–Teller (BET)⁶³ specific surface area (SSA) of $\sim 7800 \text{ m}^2 \text{ g}^{-1}$ for $\text{Zn}_4\text{O}(\text{BBC})_{4/3}(\text{BCPDB})$ (DUT-60, $\text{H}_3\text{BBC} = 1,3,5\text{-tris}(4'\text{-carboxy}[1,1'\text{-biphenyl}] \text{-4-yl})\text{benzene}$, $\text{H}_2\text{BCPDB} = 1,4\text{-bis-}p\text{-carboxyphenylbuta-1,3-diene}$), which is more than twice as high as for common porous materials such as mesoporous carbon, silica, or zeolites.⁶⁴⁻⁶⁵ The guest accessible pore space in combination with the synthetic versatility enables materials scientists to tune the pore chemistry of the material in a way that is not possible with conventional porous materials. Consequently, MOFs have been proposed for a number of industry-relevant applications, such as gas storage, gas separation, or heterogeneous catalysis.⁶⁶⁻⁶⁹ Even though MOFs outperform conventional materials in some cases, for example as cathode materials in the electro-chemical oxygen evolution reaction,⁷⁰⁻⁷³ the associated investment costs for the application of MOFs on an industrial scale are still too high. The same was true when BASF invested in research into MOFs as a potential storage material for natural gas, used in tanks of gas-powered cars, but the falling oil price had made the implementation unprofitable.⁷⁴⁻⁷⁵ Both aforementioned examples show that MOFs have practical applications *per sé*, but are currently not economically competitive in large industrial applications due to their high costs and scale-up problems. Consequently, some start-up companies focus on niche markets in which the advantages of MOFs outweigh the relatively high investment. For instance, a team around O. Farha from Northwestern University founded the company *NuMat Technologies* and produce MOF-filled gas cylinders for the storage of toxic gases at low pressures in the semiconductor industry.⁷⁶ Another exciting example with high socio-economic relevance is the use of MOFs for non-toxic water recovery in arid climates.⁷⁷⁻⁷⁸ The application of MOFs in the future will largely depend on the upscaling of MOF syntheses and the associated cost reduction. Alternatively, the unique properties of MOFs can be exploited to address new applications, for example in sensing of specific molecules that can be recognized by the tailored pore environment. A potential read out of such a sensor material could be the change in its resistance which would constitute a chemiresistor. This requires the ability to conduct charges through the lattice which is rather uncommon in MOFs. Strategies how to evoke electrical conductivity in these highly porous materials are discussed in Concept Box 2.

Concept Box 2: Electrical Conductivity in Metal-Organic Frameworks

Electrical conductivity in MOFs has been one of the emerging topics in MOF research over the past few years.⁷⁹⁻⁸¹ The great interest in this area results from the enormous potential offered by electrically conductive, highly porous crystalline solids for application in microelectronics,⁸²⁻⁸⁵ chemiresistive sensing,⁸⁶⁻⁸⁹ energy storage,⁹⁰⁻⁹¹ and electrocatalysis.⁹²⁻⁹⁴ However, only a small fraction of the tens of thousands of MOFs known today exhibit considerable electrical conductivity. This is largely due to the inherent nature of MOFs, which typically consist of hard metal ions and linkers with hard donor atoms that form ionic bonds resulting in a poor orbital overlap and low charge mobility.⁸⁰ In general, the electrical conductivity of a material is directly proportional to its charge mobility and charge carrier density. Recent literature describes a number of strategies to improve these two parameters in MOFs.^{80, 83, 95} For instance, the design of linkers with softer donor atoms (*e.g.* S instead of O) showed increased charge mobility and ultimately higher electrical conductivity.⁹⁶⁻⁹⁸ To increase the charge carrier density in MOFs metals with unpaired *d*-electrons (*e.g.* high-spin Fe²⁺)⁹⁹ or redox-active building blocks as part of the framework (*i.e.* redox active ligands or metal nodes), or as non-innocent guest molecules have been employed.^{81, 100-102} The most successful approach so far to impart electrical conductivity with MOFs is the creation of expanded conjugated π -systems (high charge mobility) giving rise to a family of 2D MOFs with record conductivities of up to $10^2 - 10^3 \text{ S cm}^{-1}$.^{79, 86, 103-105} In comparison, the current benchmark for a 3D MOF is Fe₂(BDT)₃ (H₂BDT = 5,5'-(1,4-phenylene)bis(1H-tetrazole)) with a room temperature conductivity in the order of 1 S cm^{-1} .⁸¹

1.2.5 Post-Synthetic Modification

As discussed in the previous chapter, MOFs allow the targeted design of the pore chemistry and the associated properties by the choice of the organic and inorganic building blocks. However, sometimes it is not possible to introduce a desired functionality, for example a distinct functional group on the linker, during a *de novo* MOF synthesis. There may be several reasons for this, including the stability of the functional group under the conditions of the MOF synthesis or an interference of the functional group with the crystallization process. For example, the use of an amine-functionalized linker may not work under the same synthesis conditions as the unfunctionalized linker since the amino group is a Lewis base and can compete for coordination sites at the metal node. A workaround, in this case, could be the use of a protection group during the MOF synthesis which is removed post-synthetically.¹⁰⁶ Consequently, some materials cannot be obtained by simple one-pot reactions but require the synthesis of a precursor MOF that is converted to the desired MOF structure via post-synthetic modification (PSM). PSM methods are conceptually summarized in Figure 6.¹⁰⁷⁻¹⁰⁹

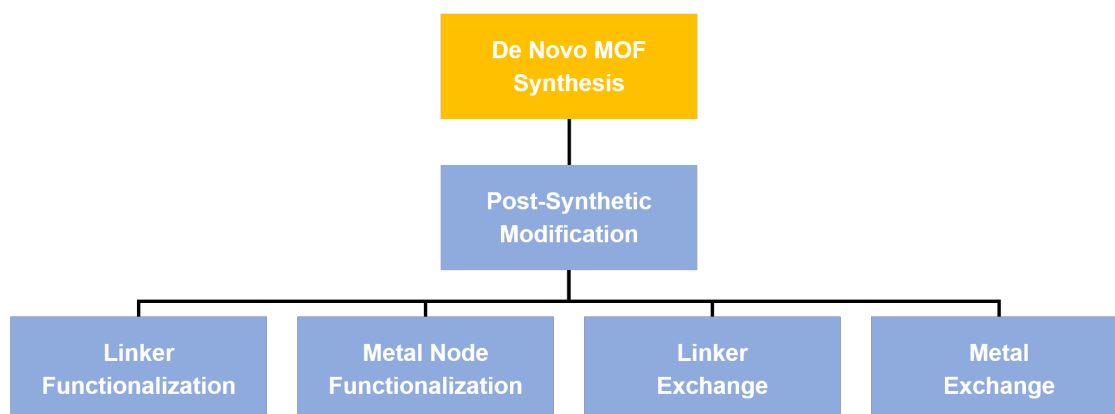


Figure 6. A tentative hierarchy of the synthetic tool box of MOF chemistry. As-synthesized MOFs (yellow) can be altered via post-synthetic modification (light blue).

The most common PSM method is linker functionalization, in which a functional group that is accessible through the open pore structure of the MOF is transformed by reaction with a compound in solution. Examples include reactions of amine groups with acid anhydrides or aldehydes to give amides or imines, reactions of azides with alkynes to triazoles, or the coordination of metal complexes to donor groups such as 2,2'-bipyridines or N-heterocyclic carbenes.¹⁰⁷⁻¹⁰⁹ Of particular interest is the coordination of metal complexes, which show good catalytic performance in solution, to an additional binding site at the linker. This way a homogeneous catalysts can be immobilized at MOFs with high surface areas and work as a heterogeneous catalyst allowing for a considerably easier workup of the catalytic reaction.¹¹⁰ Another example that nicely demonstrates the impact on PSM on the structural properties of MOFs was presented by S. Cohen and co-workers who rendered a formally rigid MOF flexible by introduction of side chains at the linker molecules.¹¹¹ Besides linker functionalization, also the metal nodes can be modified which requires the presence of labile monodentate ligands (solvents, acetate, or water) or accessible coordination sites, so-called open metal sites (OMSs). For instance,

it was demonstrated that the coordination of L-proline derivatives to the OMSs of $\text{Cr}_3(\text{F})\text{O}(\text{BDC})_3$, known as MIL-101(Cr), influenced the enantioselectivity of a catalytic test reaction.¹¹² In addition, the reversibility of the coordination bond in MOFs becomes evident when complete building units were replaced.¹¹³⁻¹¹⁴ For the substitution of linkers, this method is referred to as *linker replacement*, *post-synthetic linker exchange* or *solvent assisted linker exchange (SALE)* and allows the pore size of a MOF to be engineered by replacing the original linker with a shorter or longer version.¹¹⁵⁻¹¹⁶ SALE in particular has become the accepted terminology as it highlights the role of the solvent molecule during the dissociation of one linker and its replacement by another.¹¹⁴ The abovementioned examples and the large number of post-synthetic reactions in the literature,¹⁰⁷⁻¹⁰⁹ highlight the potential of PSM methods to systematically manipulate the structure and pore chemistry of MOFs.

1.3 Retrofitting Metal-Organic Frameworks

Retrofitting is a PSM method that was introduced as a categorization by O. M. Yaghi and co-workers in 2017 and describes the post-synthetic installation of additional linkers into a MOF with undercoordinated metal nodes (*i.e.* nodes that are not fully coordinated by linkers and OMS are occupied by labile monotopic ligands).¹¹⁷ In general, retrofitting is applicable to all MOFs with available coordination sites at the metal nodes, so-called open metal sites (OMSs), or labile monotopic ligands that bind to the metal node. During the retrofitting experiment, the MOF is exposed to the additional linker, referred to as cross linker (CL), which diffuses into the MOF and coordinates to the available OMSs or replaces the labile monotopic ligands. A schematic illustration of retrofitting is presented in Figure 7.

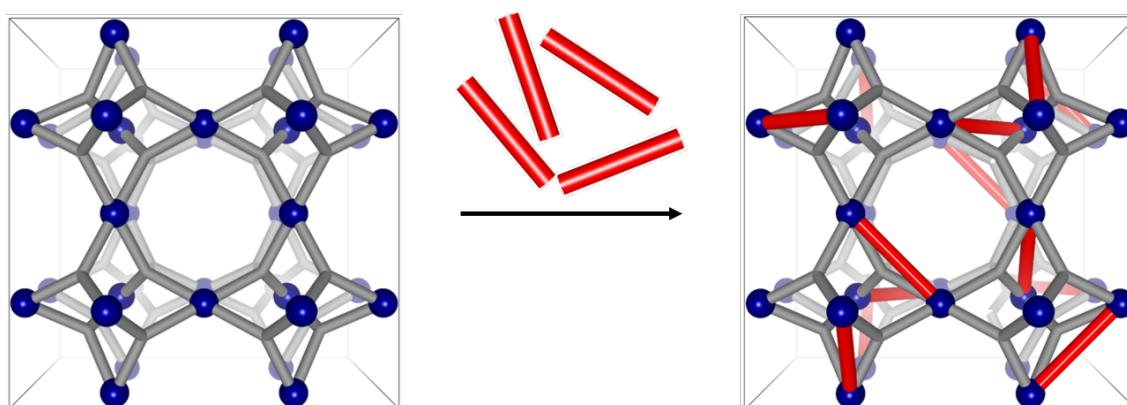


Figure 7. Illustration of the concept of retrofitting. Available connection sites (blue) in an open framework structure are bridged by the introduction of cross linkers (red). Notably, in this illustration the high cubic symmetry of the pristine MOF (left) is reduced after installation of the CLs (right).

The incorporation of a CL increases the connectivity of the parent framework which was demonstrated to have an effect on the physicochemical properties of the material. For instance, retrofitting of the mechanically labile MOF $[\text{Al}_8(\mu\text{-OH})_8(\text{HCOO})_4(\text{BTB})_4]$ (MOF-520, BTB = 1,3,5-benzenetribenzoate) (stable up to 2.8 GPa) with the linear, ditopic CL 4,4'-biphenyldicarboxylate (BPDC) renders the material robust towards hydrostatic pressures of up to 5.5 GPa.¹¹⁷ It is important to note, that O. M. Yaghi and co-workers did coin the term *molecular retrofitting*, though, they were not the first to post-synthetically introduce new linkers into an undercoordinated MOF. In 2015, H. C. Zhou and co-workers published a study on the sequential installation of two dicarboxylate-CLs in the MOF $[\text{Zr}_6(\mu_3\text{-O})_4(\mu_3\text{-OH})_4(\text{OH})_4(\text{H}_2\text{O})_4((\text{CH}_3)_2\text{-BPDC})_4]$ (PCN-700) to increase the connectivity between the Zr nodes of the framework.¹¹⁸ One year later, they expanded the concept and installed 12 different CLs in PCN-700 and demonstrated increased sorption performance for N_2 and H_2 in some of the new retrofitted MOFs. In a proof of principle experiment, they also showed that retrofitting can introduce size selectivity for a catalytic test reaction depending on the substitution pattern on the CLs.¹¹⁹ Around the same time, C.-Y. Su and co-workers published a study in which they installed four dicarboxylate-CLs between the Zr nodes of the flexible MOF $[\text{Zr}_6(\mu_3\text{-O})_8(\text{H}_2\text{O})_8((\text{CF}_3)_2\text{-$

BPDC)₄] (LIFM-28). Depending on the CL length they were able to stop the breathing mode at different stages between the narrow-pore and large-pore forms of the framework, and studied the adsorption and selectivity of N₂ and CO₂ for the retrofitted MOFs.¹²⁰ Only 10 month after the work on PCN-700 by H. C. Zhou *et al.* had been published in *The Journal of the American Chemical Society (JACS)*,¹¹⁹ a very similar study by C.-Y. Su *et al.* was published in *JACS* also exploring the adsorption and catalytic properties of the closely related MOF LIFM-28 after retrofitting with the same class of dicarboxylate-CLs.¹²¹ In a very recent study, Zhou and co-workers studied the reaction kinetics of linker installation in two other Zr-based MOFs, namely [Zr₆(μ₃-O)₄(μ₃-OH)₄(OH)₄(H₂O)₄(L)₄] with L = 4,4'-dihydroxybiphenyl-3,3',5,5-tetra(phenyl-4-carboxylate) (OH-TPCB, PCN-606-OH) or 4,4'-dimethoxy-biphenyl-3,3',5,5-tetra(phenyl-4-carboxylate) (OMe-TPCB, PCN-606-OMe).¹²²

H. C. Zhou *et al.* refer to the post-synthetic introduction of an additional ligand into a MOF as *sequential linker installation*,¹¹⁸⁻¹¹⁹ while C.-Y. Su *et al.* named their strategy *post-synthetic variable-spacer installation*.¹²⁰ Both expressions accurately describe the work performed by the two groups, but at the same time, appear wordy and too specific for a general classification. In 2016, M. D. Allendorf and R. A. Fischer proposed that (coordinating) guests can be a design element for MOFs, which they coined *Guest@MOF concept*.¹²³ However, this terminology does not necessarily requires the binding of the Guest to at least two OMS of the MOF. In contrast, *retrofitting* applies to all cases in which the connectivity of a MOF is post-synthetically increased, inherently implies a PSM method and has also been established as a concept in other research areas, e.g. construction and mechanical engineering (see Concept Box 3).¹²⁴⁻¹²⁵ Moreover, examples from the world of covalent organic frameworks, where functional groups are linked or 2D sheets are interconnected by coordinating metal complexes,¹²⁶⁻¹²⁷ fall under the umbrella of “retrofitting” but would not be well described by other expressions proposed before. Therefore, *retrofitting* appears to be the more general and intuitive categorization and is used throughout this thesis and is encouraged as terminology in the future.

From a structural chemistry standpoint, the introduction of a CL molecule into the lattice of a pristine MOF generates a defect. Following this train of thought, retrofitting is exciting as it adds a new category to the field of defect-engineered MOFs alongside

Concept Box 3: The Origin of Retrofitting

Retrofitting is a concept that was introduced well before MOFs were discovered and originally describes the addition of new components to an existing system, e.g. in construction to reinforce the structural stability of historical buildings or buildings in seismic zones.^{124-125, 128-129} Due to the strong analogy, O. M. Yaghi adopted this concept as *molecular retrofitting* into the world of solid-state chemistry and MOFs.¹¹⁷ Besides structural reinforcement, retrofitting is a general term that is used when upgrading an existing system with new components. Examples range from thermal insulation in buildings (energy retrofitting),¹³⁰⁻¹³² and renewal of equipment in industrial plants,¹³³⁻¹³⁵ to the world of computer science and programming.¹³⁶⁻¹³⁷

properties. If all available coordination sites were connected, *i.e.* translational periodic CL incorporation was achieved, the “defect” would be fully incorporated into the structure and retrofitting would leave the territory of a defective state. However, most of the literature examples reviewed above represent a defective state, with reported bulk occupancies of 70%,¹¹⁷ or 56%,¹²² or with bulk characterization (*e.g.* nuclear magnetic resonance (NMR) spectroscopy, or powder X-ray diffraction (PXRD)) revealing a slight deviation from the predicted stoichiometry.¹¹⁸⁻¹²¹ Achieving quantitative occupation will be challenging (analogously to the defect-free formation of MOFs in general), as it largely depends on the diffusion kinetics and the reversibility of the binding between metal node and CL. In other words, large CLs that strongly interact with the MOF successively block diffusion pathways through the pores as the retrofitting experiment progresses. This is the case in the aforementioned examples, in which carboxylate-based MOFs are constructed from metal nodes with *hard* Al³⁺ or Zr⁴⁺ ions, and CLs containing *hard* carboxylate groups are used. The resulting strong coordination bonds (see Pearson’s *hard and soft acids and bases* concept¹³⁸) are beneficial for the stability of the parent MOF and the respective CL@MOF system under the condition of the retrofitting experiment. However, for retrofitting of carboxylate-based MOFs with *softer* metal ions such as Zn²⁺ or Cu²⁺, the use of carboxylate-CLs can result in post-synthetic linker exchange as a competing reaction.¹¹⁴ Therefore, the consequent strategy to fully retrofitted MOFs must involve orthogonal coordination bond chemistry between linkers of the parent MOF and CLs in the retrofitting experiment. Specifically, CLs should exhibit a lower binding energy with the metal node compared to the linker and thus provide better diffusion kinetics and prevent linker exchange. For instance, the MOF Cu₃BTC₂ features OMSs at the dimeric Cu nodes that are available for coordination of a CL (see chapter 1.4.1). In 2014, two years before the concept of *retrofitting* or *linker installation* was introduced, Allendorf and co-worker infiltrated the nitrile-CL TCNQ (7,7,8,8-tetracyanoquinodimethane) into the pores of Cu₃BTC₂, which was reported to come with an increase in the electrical conductivity of the material. Even though, crystallographic evidence of the coordination could not be provided and the occupancy estimated by elemental analysis was only 1 TCNQ molecule per 6 Cu atoms (0.5 TCNQ molecules per Cu₃BTC₂), essentially TCNQ@Cu₃BTC₂ represents the first example of a retrofitted MOF,¹⁰¹ and the potential of post-synthetically tuning materials properties by infiltration of guests was introduced as *Guest@MOF concept*.¹²³ TCNQ@Cu₃BTC₂ is reviewed in detail in chapter 1.4.3.

In summary, retrofitting of MOFs has only recently emerged as a PSM strategy with a still limited number of structures that have been published in the literature so far.^{101, 117-122} Most of the retrofitted systems involve the use of linear dicarboxylate molecules and Zr (or Al) based MOFs, whereas the example of TCNQ@Cu₃BTC₂ suggests the general applicability of retrofitting and underlines its potential for the modulation of materials properties. Noteworthy, retrofitting as a general concept is not only limited to MOFs. While non-porous and purely inorganic materials will not allow the incorporation of a bridging cross linker (the closest analogy would be classical doping or solid solutions), other coordination polymers or purely organic materials will certainly provide the opportunity for retrofitting. For instance, in some covalent organic frameworks (COFs) functional groups can be used to interconnect the 2D sheets or to increase the

connectivity along the 2D sheets post-synthetically which in a broader sense classifies as retrofitting.¹²⁶⁻¹²⁷

1.4 TCNQ@Cu₃BTC₂ as a Model System for Retrofitting

1.4.1 Cu₃BTC₂

Cu₃BTC₂, also known as HKUST-1 (HKUST = Hong Kong University of Science and Technology), is a prototypical MOF synthesized for the first time by Ian D. Williams and co-workers in 1999.¹³⁹ In Cu₃BTC₂, the carboxylate groups of the BTC linkers coordinate in a bidentate fashion to dimeric Cu(II) nodes, which in turn are surrounded by four carboxylates in a square planar coordination geometry. Thereby, the four positive charges of the two Cu(II) ions are compensated by four negative charges of the carboxylates. This structural motif is known as a Cu paddlewheel, and is also known from molecular (0D) complexes such as Cu(Ac)₂ (Ac = acetate)¹⁴⁰. Every Cu(II) ion exhibits one OMS in the axial position of the paddlewheel, which is available for coordination of a guest molecule. These sites are typically coordinated by water leading to a chemical formula of [Cu₃(BTC)₂(H₂O)₃]_n or [Cu₃(C₉H₃O₆)₂(H₂O)₃]_n. Chemisorbed H₂O can be removed by thermal treatment in vacuum. Cu₃BTC₂ crystallizes in the face-centered cubic space group *Fm*-3*m* and contains 48 Cu atoms and 32 BTC molecules per unit cell, which enclose eight small pores of 1.0 nm and eight large pores of 1.6 nm in diameter. Cu paddlewheel units are located at the interface between four large pores. Therefore, the large pores can be distinguished based on their chemical environment; while 50% of the large pores feature 12 OMS that point to the center of the pore and allow chemisorption of guest molecules (pore A), in the other half of the pores the Cu paddlewheels are arranged tangentially to the pore and their OMS are therefore not available for coordination of molecules in that pore (pore B). The crystal structure of Cu₃BTC₂ is shown in Figure 8 and further important parameters of Cu₃BTC₂.

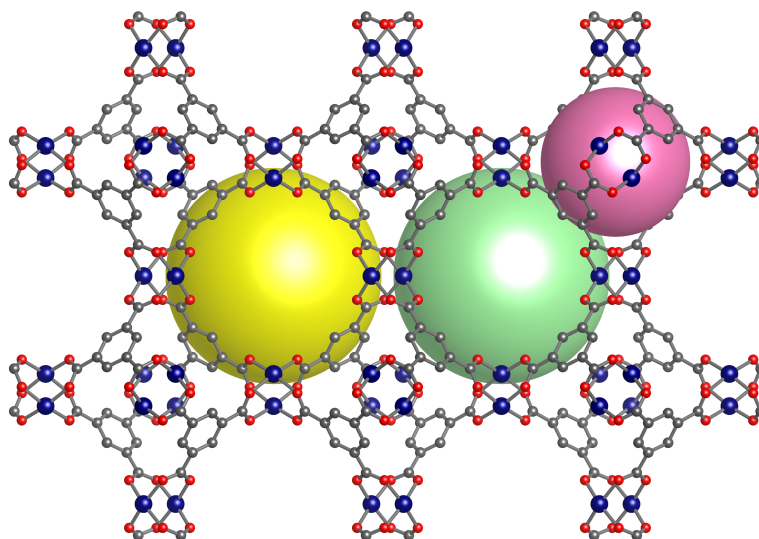


Figure 8. Crystal structure of Cu₃BTC₂ viewed along the *a* axis. Cu, O, and C atoms are depicted in blue, red, and grey, respectively. The two different large pores are illustrated as green (pore A) and yellow (pore B) spheres. The small pore is shown in magenta. H atoms are omitted for clarity.

Some of the most relevant physicochemical properties of Cu_3BTC_2 are summarized in Table 1. Key characteristics of the material are a high specific surface area of up to $2000 \text{ m}^2 \text{ g}^{-1}$ (depending on the synthesis conditions)¹⁴¹, and relatively high thermal stability of up to around $300 \text{ }^\circ\text{C}$. Interestingly, upon heating the structure of Cu_3BTC_2 shrinks. The phenomenon is known as negative thermal expansion and explained in Concept Box 4.

Table 1. Important physicochemical quantities of activated Cu_3BTC_2 .

Parameter	Symbol	Value	Method	Ref.
lattice parameter [§]	a	26.25 \AA	synchrotron powder X-ray diffraction	142
crystallographic volume [§]	V	18096.60 \AA^3	synchrotron powder X-ray diffraction	142
crystallographic density [§]	ρ	0.535 g cm^{-3}	synchrotron powder X-ray diffraction	142
specific surface area [§]	SSA	$1874 \text{ m}^2 \text{ g}^{-1}$	N_2 adsorption isotherm	142
thermal decomposition	T_{decomp}	$330 \text{ }^\circ\text{C}$	thermogravimetric analysis	143
electrical conductivity [§]	σ	$<10^{-12} \text{ S cm}^{-1}$	2-point probe I/V measurement on powder pellets	143

[§] at 300 K

[§] surface area calculation according to BET theory⁶³

Concept Box 4: Negative Thermal Expansion

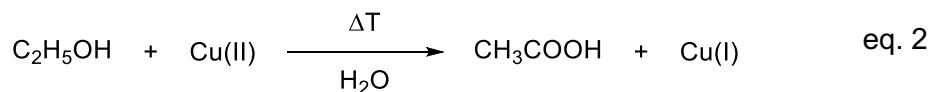
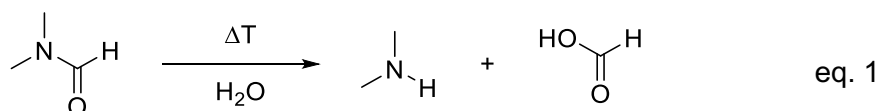
Cu_3BTC_2 as well as a number of other MOFs show an interesting, yet counterintuitive, phenomenon. While most materials expand with increasing temperature, they shrink upon heating.¹⁴⁴⁻¹⁴⁵ This effect is called negative thermal expansion (NTE),¹⁴⁶⁻¹⁴⁸ and has been intensively studied in metal oxides,¹⁴⁹⁻¹⁵⁰ metal cyanides,¹⁵¹⁻¹⁵² and zeolites.¹⁵³⁻¹⁵⁴ Besides electronic or magnetic coupling phenomena, the most prevalent cause of NTE are low energy phonons, *i.e.* collective lattice motions that result in an on average shortened distance between the building blocks of the material.¹⁴⁶⁻¹⁴⁷ An elegant and intuitive concept that describes how lattice dynamics and NTE in a material are linked on a microscopic level are rigid unit modes (RUMs).¹⁴⁷ It is intriguing that the building block principle of MOFs naturally reflects the RUM concept and in combination with the void pore space results in low excitation energies for correlated lattice modes.¹⁵⁵ On a molecular level, these lattice modes include for example transversal replacement of the linker molecules and torsions of the metal nodes.¹⁵⁶⁻¹⁵⁹ Typical volumetric thermal expansion coefficients α_V in MOFs are in the order of $10^{-5} - 10^{-4} \text{ K}^{-1}$,^{57, 145, 148, 157} exceeding those of common NTE materials such as ZrW_2O_8 ($\alpha_V = -1.03 \cdot 10^{-5} \text{ K}^{-1}$).¹⁴⁹

Cu_3BTC_2 can be obtained by a number of well-established synthesis methods. For instance, a typical solvothermal synthesis protocol that was used during this thesis involves the dissolution of $\text{Cu}(\text{NO}_3)_2 \cdot 2.5\text{H}_2\text{O}$ and H_3BTC in a 1:1:1 (v/v/v) mixture of DMF, ethanol (EtOH) and H_2O which is then heated to 85 °C for 20 h in a screw-capped jar.¹⁶⁰ The teal crystalline product is collected by filtration and washed with DMF. The powder is activated, *i.e.* desolvated, by repeated washing with EtOH and dichloromethane (DCM) for several days and subsequent heating to 180 °C under dynamic vacuum. Upon activation, Cu_3BTC_2 undergoes a change in color from teal to dark purple. The color change is fully reversible. For example, upon exposure to the atmosphere, *i.e.* moisture, H_2O re-adsorbs and the material changes its color back to teal. It has to be noted, that the structural defects in the structure have a strong contribution to the observed color of the material.¹⁶¹

Besides its synthesis as a crystalline powder, the deposition of Cu_3BTC_2 as thin films has been extensively investigated.¹⁶²⁻¹⁶⁵ In this context numerous deposition methods were employed such as solvothermal growth, dip coating, spin coating, layer-by-layer growth, spray coating, ink jet printing, to name just a few, as well as the deposition on various substrates was tested such as Au, SiO_2 , quartz, and polymers.¹⁶⁶⁻¹⁶⁷ The deposition on substrates is particularly important for the integration of MOFs into devices for microelectronics and sensing applications.^{83-84, 168-169} In this thesis, Cu_3BTC_2 was deposited on SiO_2 and indium tin oxide (ITO) substrates following the layer-by-layer method, involving subsequent immersion of the substrate in ethanolic solutions of $\text{Cu}(\text{Ac})_2$ and BTC followed by rinsing steps with fresh EtOH. Repetition of this sequence yields a uniform film of defined thickness; *e.g.* 50 cycles correspond to a film thickness of ~100 nm. It should be noted that despite its high crystallinity, Cu_3BTC_2 (bulk and thin film) is never completely free from defects. For example, Wöll and co-workers showed that the blue hue of common Cu_3BTC_2 thin films stems from defective paddlewheel units, in which one BTC is replaced by Ac from the precursor, whereas films with low defect concentrations appear transparent.^{47, 161, 170} A number of strategies to improve the film quality (crystallinity, defects, roughness) have been presented.¹⁷⁰⁻¹⁷³

Cu_3BTC_2 is one of the most studied MOF systems, with most of the research focusing on gas sorption, heterogeneous catalysis and device integration.^{68-69, 83, 162, 174-176} Due to its facile synthesis and commercial availability (*e.g.* BASF sells Cu_3BTC_2 under the tradename Basolite® C300), Cu_3BTC_2 is often used as a reference system to compare the properties of new MOFs. The importance of Cu_3BTC_2 and resulting potential applications was nicely summarized by Hendon and Walsh.¹⁷⁷ For many applications, the OMSs of Cu_3BTC_2 are of particular interest as they can act as adsorption sites for gas molecules or catalytic centers in heterogeneous catalysis.^{69, 178} Much like OMSs, modified metal nodes, for example created through missing linker defects, can act as catalytically active centers in MOFs.^{49, 60, 62} In Cu_3BTC_2 such defective sites are characterized by mixed-valence Cu(I)-Cu(II) paddlewheels as compensation for the missing negative charge of the linker and can occur intrinsically or as the result of the reduction of Cu(II) to Cu(I) through thermal treatment or high energy radiation of spectroscopic methods.⁵³⁻⁵⁴ Moreover, intrinsic Cu(I) defects can potentially form under the conditions of the solvothermal synthesis by reaction between the Cu(II) precursor and the non-inert solvents. For example, DMF decomposes in the presence of H_2O to

dimethylamine and formic acid (see eq. 1). The latter could act as reducing agent for Cu(II). Similarly, ethanol can promote the formation of Cu(I) whilst being oxidized to acetic acid (see eq. 2).



A more recent advance in the research on Cu_3BTC_2 , was the use of the available OMSs as anchoring points for di- or polytopic guest molecules that can bridge two neighboring Cu paddlewheel nodes. $\text{TCNQ@Cu}_3\text{BTC}_2$ was the first host-guest material of this kind and was introduced by Allendorf and co-workers in 2014 (see 1.4.3).¹⁰¹ In fact, this example of bridging undercoordinated metal nodes by introducing guest molecules was at the same time the first example of retrofitting in the context of MOFs. Before going into further details about $\text{TCNQ@Cu}_3\text{BTC}_2$, the next sub-chapter will introduce TCNQ as an important molecule for organic electronics and coordination polymers.

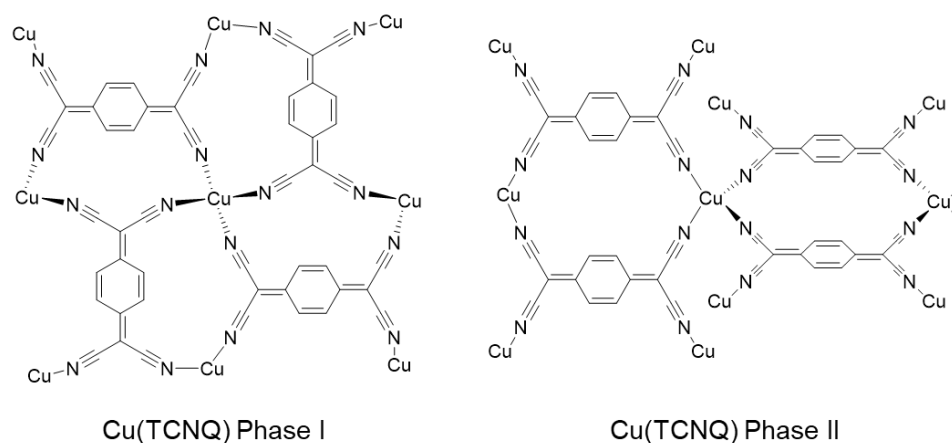


Figure 10. Schematic structure of Cu(TCNQ) Phase I (left) and Phase II (right) as proposed by Dunbar and co-workers.¹⁹¹ In Phase I the TCNQ⁻ molecules form planar stacks, whereas in Phase II they are arranged perpendicular to each other.

Further electron-accepting molecules have been reported over the past decades that are structurally closely related to TCNQ. For example, the electronic properties of TCNQ can be tuned by variation of the substitution pattern of the quinone ring.¹⁹³ One prominent example is F₄-TCNQ, in which all H atoms are substituted by F atoms, resulting in an even higher electron-withdrawing character.¹⁹⁴ Tetracyanoethylene (TCNE), tetracyanobenzene (TCNB) and tetracyanopyrazine (TCNP) are closely related to TCNQ and sometimes studied together using the general expression TCNX to describe the entire family of molecules.^{181, 195} Further important Wurster-type compounds whose charge transfer salts attracted significant attention from the micro-electronics community include N,N'-dicyanoquinonediimide (DCNQI) and its derivatives,¹⁹⁶⁻¹⁹⁷ as well as a number of quinone derivatives¹⁹⁸ such as 2,3-dichloro-5,6-dicyano-*p*-benzoquinone (DDQ).¹⁹⁹

1.4.3 TCNQ@Cu₃BTC₂

Aiming at the integration of electrical conductivity with MOFs, M. D. Allendorf and co-workers followed a new approach. Instead of synthesizing a conductive coordination polymer that is porous, they tried to render an electrically insulating MOF conductive through loading with redox-active guest molecules. Published in 2014 in *Science*, TCNQ-loaded Cu₃BTC₂ was the MOF with the highest reported electrical conductivity of up to $7 \cdot 10^{-2} \text{ S cm}^{-1}$ (thin film, 2-point probe measurement) and remained some porosity ($214 \text{ m}^2 \text{ g}^{-1}$).¹⁰¹ Moreover, the conductivity was shown to be tunable depending on the amount of TCNQ infiltrated into the porous host-material, which is also one aspect of this thesis (see chapter 3.2). The synthesis of TCNQ@Cu₃BTC₂ is relatively straightforward; pristine, activated Cu₃BTC₂ (powder or thin film) is immersed in a TCNQ solution in DCM at room temperature to allow TCNQ to diffuse into the pores of the MOF. The integrity of the Cu₃BTC₂ framework after TCNQ-loading was verified by X-ray diffraction and successful loading is confirmed by elemental analysis (for powders) and vibrational spectroscopy. Particularly the nitrile stretching vibration of TCNQ is sensitive to charge transfer,²⁰⁰ which served as an indication for the coordination of TCNQ to Cu₃BTC₂ accompanied by a (partial) electron transfer from the MOF to TCNQ. Even though crystallographic evidence was missing at that time, Talin *et al.* proposed the coordination of two geminal nitrile groups of TCNQ to two neighboring OMS in the large pores of Cu₃BTC₂ and supported this by DFT calculations.¹⁰¹ An illustration of this arrangement is shown in Figure 11.

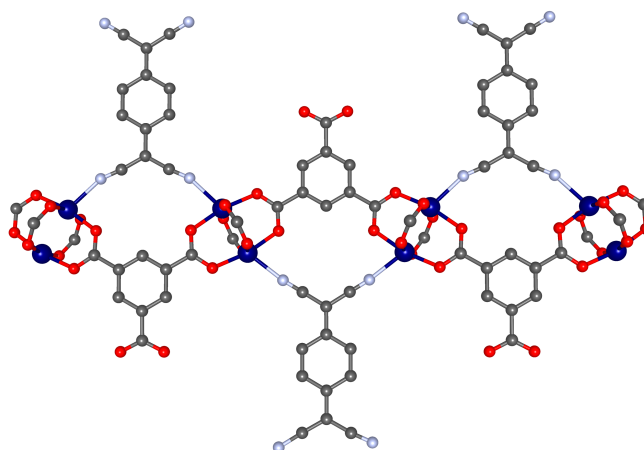


Figure 11. Proposed arrangement of TCNQ within the (111) lattice of Cu₃BTC₂. Cu, O, N and C atoms are depicted in blue, red, light blue and grey, respectively. H atoms are omitted for clarity. For better visualization, the structural details and the restrictions caused by the cubic symmetry and the exact pore structure are not applied.

Following their initial work, Allendorf and co-workers as well as other research groups focused their efforts to elucidate the conductivity mechanism in TCNQ@Cu₃BTC₂ in several experimental and computational studies.²⁰¹⁻²⁰⁵ Given the large number of publications referencing this material (>200 citations for the initial publication), only the most significant contributions are discussed in the following. A computational study by Wöll and co-workers suggests a superexchange charge transport mechanism with

electrons being the majority charge carrier.²⁰³ However, thermoelectric studies show a relatively high positive Seebeck coefficient of $375 \mu\text{V K}^{-1}$ at 298 K,²⁰² and $422.32 \mu\text{V K}^{-1}$ at 350 K,²⁰⁴ indicating that holes are the majority charge carrier and the material is a *p*-type semiconductor. Interestingly, Redel and co-workers claimed that the conductivity shows a high anisotropy in oriented thin films; *i.e.* no horizontal charge transport is observed for Cu_3BTC_2 thin films grown along the (001) direction, whereas the reported conductivity could be confirmed when measured perpendicular to the substrate and for polycrystalline films.²⁰⁴ Given the experimental and computational evidence described above, the general opinion discussed in the literature regarding the conductivity mechanism in $\text{TCNQ}@\text{Cu}_3\text{BTC}_2$ is a *through bond transport* of charge carriers through one dimensional paths of TCNQ-bridged Cu paddlewheels.^{80, 101, 177} Theoretical modelling of the energy levels of Cu_3BTC_2 and TCNQ shows that the LUMO (lowest unoccupied molecular orbital) of TCNQ falls within the gap between the HOMO (highest occupied molecular orbital) and LUMO of Cu_3BTC_2 .²⁰¹ The Cu(II) ions in a classical Cu paddlewheel, for example in $\text{Cu}(\text{Ac})_2$, are antiferromagnetically coupled, which Pöppel and co-workers have also confirmed in Cu_3BTC_2 by EPR spectroscopy.²⁰⁶ Together with magnetic susceptibility data²⁰⁷ the splitting between the singlet ground state and the triplet excited state was determined to be 340 cm^{-1} (0.042 eV) suggesting a thermal activation of the triplet state at room temperature. Therefore, M. D. Allendorf *et al.* proposed a donor bridge acceptor (DBA) mechanism between neighboring paddlewheels based on a superexchange model given the good orbital overlap between the Cu (d_{z^2}) orbital in the axial position of the paddlewheel and the free electron pair of the nitrile group in TCNQ, which was predicted by computational methods.²⁰¹ Interestingly, the electronic coupling is significantly decreased when replacing TCNQ with its fully fluorinated ($\text{F}_4\text{-TCNQ}$) or hydrogenated ($\text{H}_4\text{-TCNQ}$) analogues, which results in a considerably lower electrical conductivity of the host-guest material.^{101, 201} While the DBA mechanism explains local charge transport between neighboring paddlewheels, long-range ordering is necessary for charge transport on a macroscopic scale. A. A. Talin *et al.* rationalize this by classical percolation theory²⁰⁸ as the conductivity increases depending on the time the Cu_3BTC_2 is immersed in the TCNQ solution, which correlates with the loading amount and thus the number of available conduction pathways within the MOF.^{101, 201} However, no evidence for a long range order of TCNQ molecules in the lattice of Cu_3BTC_2 is presented and potential arrays could only constitute 1D coordination polymers of alternating TCNQ-Cu paddlewheel units. At this point, it should be noted that the literature cited above discusses the conductivity in $\text{TCNQ}@\text{Cu}_3\text{BTC}_2$ based on bulk, *i.e.* single crystalline material. However, grain boundaries and local defects in the crystal structure may contribute to the observed phenomena as well. For example, S. Tominaka and A. Cheetham critically discuss the contributions of intrinsic (through the lattice or micropores) and extrinsic (along interparticle phases) conductivity of protons in MOFs.²⁰⁹ In a way, this might be relevant also for $\text{TCNQ}@\text{Cu}_3\text{BTC}_2$. Moreover, the charge carriers may predominantly move through the unit cells close to the crystal surface if diffusion limitations during the liquid phase impregnation with TCNQ play a role. The importance of the setup of the electrical conductivity measurement was nicely highlighted by L. Sun *et al.* who observed differences in the conductivity of a material of several orders of magnitude depending on the specimen type, *i.e.* single crystals, thin films or pressed powder pellets, and the conditions used (contacts, pressure, etc.).²¹⁰ Own attempts to

measure the conductivity of a TCNQ@Cu₃BTC₂ single crystals together with A. M. Ullman and M. D. Allendorf at the Sandia National laboratories remained unsuccessful (unpublished results, not included in this thesis), which is likely due to diffusion limitations of TCNQ into large crystals of Cu₃BTC₂.

The results presented in the author's Master thesis entitled "*Thin Film Synthesis and Guest Molecule Interactions in Copper Paddlewheel Metal-Organic Frameworks*"²¹¹ showed that the water content of the TCNQ solution and the choice of solvent, *i.e.* DCM or methanol (MeOH), has a significant effect on the nature and electronic properties of the resulting material. In the case of MeOH as the solvent an unprecedented phase transformation was observed, which could not be explained at that time. Later, further investigations showed that Cu₃BTC₂ was fully transformed to Cu(TCNQ); see Chapter 3.1.

D'Alessandro and co-workers chose a different approach to synthesize TCNQ@Cu₃BTC₂. Instead of introducing TCNQ via solution impregnation, they mixed Cu₃BTC₂ with an excess of TCNQ and heated the powder mixture in a sealed glass pipette. Varying the reaction temperature and time they were able to control the amount of incorporated TCNQ, while unreacted TCNQ was rinsed away with solvent. Compared to solution impregnation, higher TCNQ loading quantities were achieved by this process.²⁰⁵ Although a number of unknown variables (moisture, solvent) were excluded during the reaction, the advantage of the solvent-free vapor phase loading was compromised by washing the material with solvent and handling it under atmospheric conditions. While spectroscopic results may be perturbed by adsorbed moisture and solvent and thus are less conclusive, an important contribution by D. d'Alessandro *et al.* is the proof of the generality of the guest loading concept for the system guest@Cu₃BTC₂. Besides TCNQ, they infiltrated the smaller molecule TCNE into the pores of Cu₃BTC₂ and could achieve even higher loadings (up to 1.75 equivalents per chemical formula Cu₃BTC₂) compared to TCNQ (1 equivalent per chemical formula Cu₃BTC₂).²⁰⁵

The work by A. A. Talin, M. D. Allendorf *et al.* has inspired other groups to look for emergent properties in MOFs loaded with non-innocent guest molecules. Shortly after the initial publication, D. S. Sholl and co-workers conducted an elaborate DFT screening of Cu paddlewheel-based MOFs with OMS available for binding TCNQ to identify further systems that could be rendered electrically conductive.²¹² A year later, in 2016, K. P. Loh and co-workers infiltrated the two dimensional porphyrin-based MOF [Cu(TPyP)Cu₂(Ac)₄] (H₂TPyP = 5,10,15,20-tetra-4-pyridyl-21*H*,23*H*-porphine) with TCNQ and observed a conductivity increase from $\sim 10^{-7}$ S cm⁻¹ to $1 \cdot 10^{-4}$ S cm⁻¹ at room temperature.²¹³ Another electron acceptor that has been used to render insulating frameworks electrically conductive is C₆₀ fullerene. Loading C₆₀ into the pores of the insulating MOF NU-901, which is constructed from Zr₆-nodes and TBAPy (H₄TBAPy = 1,3,6,8-tetrakis(*p*-benzoic acid)pyrene) linkers, results in a conductivity of 10^{-3} S cm⁻¹.²¹⁴ Just recently, C. Wöll and co-workers used C₆₀ as an additional step during the layer by layer growth of Zn(TPP) (TPP = 5,15-bis-(3,4,5-trimethoxyphenyl)-10,20-bis-(4-carboxyphenyl) porphyrinato zinc(II)) thin films and thereby filled the pores of the MOF successively with the fullerene guest. While the conductivity of Zn(TPP) is insignificant ($1.5 \cdot 10^{-13}$ S cm⁻¹), C₆₀@Zn(TPP) shows a conductivity of $1.5 \cdot 10^{-11}$ S cm⁻¹, which

increases even further upon light irradiation ($\lambda = 435 \text{ nm}$) to $1.3 \cdot 10^{-7} \text{ S cm}^{-1}$.²¹⁵ These examples show, that MOFs can show guest-induced emergent properties with TCNQ@Cu₃BTC₂ being the prototypical example. In the future, the enormous toolset of organic chemistry combined with the large variety of inorganic building blocks bears great potential for materials scientists to develop new MOF materials relevant in (opto-)electronics, sensing and energy storage applications.

2 Objective

At the beginning of this thesis project, a number of studies elucidating the electrical conductivity in $\text{TCNQ}@Cu_3\text{BTC}_2$ both experimentally and computationally had been published in the literature (see chapter 1.4.3). While critically studying this literature, including the Master thesis of this PhD candidate²¹¹, a number of questions arose that became the nucleus of this doctoral study.

“How do water and the choice of solvents influence the adsorption of TCNQ and ultimately the obtained materials properties?”

“Can the location and the arrangement of TCNQ within the framework be determined experimentally and prove the coordination of TCNQ as suggested by computational modeling?”

“Is $\text{TCNQ}@Cu_3\text{BTC}_2$ unique, or can other (electrically conductive) $\text{Guest}@MOF$ materials be synthesized using related guest molecules and Cu paddlewheel MOFs?”

Consequently, the goals of this thesis project were defined along two dimensions. First, a better understanding of $\text{TCNQ}@Cu_3\text{BTC}_2$ system should be achieved by careful characterization of the microscopic structure of the material. Second, the concept of installing (redox-active) guest molecules between the OMSs of a MOF should be expanded to other MOF and guest molecule combinations.

For a systematic study of $\text{TCNQ}@Cu_3\text{BTC}_2$, it had to be acknowledged that the material has a highly complex nature, particularly due to its defect chemistry. As a hybrid material, a MOF contains organic linkers and metal nodes that create a spatially inhomogeneous pore environment. In addition, the metal nodes can expose OMSs and the formation of defects (e.g. by decarboxylation of the linker during thermal activation) is inevitable. The infiltration of TCNQ as a redox-active guest molecule adds further complexity to the system. Therefore, a profound understanding of the host-guest system required the detailed study of the arrangement of TCNQ within the pores, the defect chemistry of the MOF, the redox-chemistry between MOF and guest molecule, and the influence of the synthesis conditions on the chemistry of the material. A key step to reduce the complexity of the system was comparison of the standard solution impregnation with a synthesis method that excludes as much external factors as possible, e.g. solvents and moisture. Therefore, the development of a solvent-free synthesis of $\text{TCNQ}@Cu_3\text{BTC}_2$ under inert conditions was the core element of this study.

The expansion of the host-guest concept was clearly encouraged by the work on retrofitted MOFs published in 2016 and 2017 (see chapter 1.3). Here, it was particularly important to find a systematic approach to design new $\text{CL}@MOF$ materials instead of relying on serendipity in the lab. Consequently, the development of an approach that takes the spatial arrangement of the MOF's OMSs and the geometry of potential CLs into account, was the only viable strategy to achieve this goal.

3 Results and Discussion

The two overarching research questions, which are a better understanding of TCNQ@Cu₃BTC₂ and an expansion of the concept to other CL@MOF materials, served as a compass for PhD project. The research conducted was divided into five subprojects, the results of which are presented in this chapter as Studies I – V.

In Study I the morphological and chemical changes of Cu₃BTC₂ thin films upon infiltration with TCNQ in MeOH were studied and it was found that a quantitative transformation to Cu(TCNQ) takes place. Thus, with the goal of minimizing the parameter space during the infiltration reaction and in order to study the pure host-guest material, a new infiltration procedure via the vapor phase was established in Study II. Importantly, this way it was possible for the first time to proof the ditopic, bridging binding mode of TCNQ to two neighboring Cu paddlewheels. Going beyond standard characterization techniques, in Study III TCNQ@Cu₃BTC₂ was then subjected to in-depth characterization with CO probe infrared (IR) spectroscopy and electron paramagnetic resonance (EPR) spectroscopy revealing the importance of defects and charge transfer processes (redox reactions) during the synthesis of this material. In summary, Study I - III aimed at a profound understanding of the structure-property relationships in TCNQ@Cu₃BTC₂ with focus on its performance as an electrically conductive material. Subsequently, the scope of the work was conceptually expanded. From a more general perspective, TCNQ@Cu₃BTC₂ represents an example of a retrofitted MOF (see chapter 1.3) in which TCNQ acts as a CL between the OMS in Cu₃BTC₂. Only a handful of publications exist in the area of retrofitted MOFs. Thus using TCNQ@Cu₃BTC₂ as a model system to study the effect of retrofitting on the mechanical properties of MOFs was the consequent path forward. In Study IV it is shown how the lattice dynamics of Cu₃BTC₂ can be manipulated by retrofitting which translates in a reduced negative thermal expansion behavior on a macroscopic level. Ultimately, all the aforementioned findings are condensed in Study V, which paves the way for the development of further retrofitted MOFs by providing a heuristic computational tool to evaluate the fit of potential CLs in MOFs with OMSs.

3.1 Study I: Surface Morphology and Electrical Properties of Cu₃BTC₂ Thin Films Before and After Reaction with TCNQ

The infiltration of TCNQ into the pores of Cu₃BTC₂ thin films causes considerable changes in the electronic properties of the material.¹⁰¹ Besides the significant increase in the electrical conductivity, evidence was found that the choice of solvent and the water content in the infiltration solution has an impact not only on the performance of the device, but also on its crystal structure and morphology.²¹¹ This change was observed for the first time when the non-inert solvent MeOH was used. To shed light on the transformation, Cu₃BTC₂ thin film samples with different thicknesses were studied before and after infiltration with TCNQ using atomic force microscopy (AFM), grazing incidence X-ray diffraction (GIXRD), Auger electron microscopy (AES), and electrical conductivity measurements. This study yielded two important results; (i) pristine Cu₃BTC₂ shows an interesting bimodal crystallite size distribution on ITO substrates due to accelerated nucleation along the facets of two intergrown crystallites, and (ii) upon immersion of the films in a MeOH solution of TCNQ, Cu₃BTC₂ transforms to Cu(TCNQ) facilitated by the non-inert solvent. To test if the transformation was limited to thin films (crystallite size ~100 nm), the experiments were also conducted with bulk samples of Cu₃BTC₂ (crystallite size ~10 μm), which revealed a partial transformation of the MOF crystallites to Cu(TCNQ). The results suggest the use of inert solvents or fundamentally different synthesis routes to fabricate TCNQ@Cu₃BTC₂. In addition the quantitative conversion presents an alternative method to coat various substrates under very mild conditions with the *n*-type semiconductor material Cu(TCNQ) as thin films.

The paper was written by the two shared first authors and edited by the six co-authors, who contributed critically to the discussion of the results. The strategy and experiments presented in this study were developed by the author of this thesis in collaboration with K. Thürmer, V. Stavila, and A. A. Talin. The author of this thesis synthesized the MOF powder and thin film samples, performed GIXRD and PXRD, scanning electron microscopy (SEM), and electrical conductivity measurements. K. Thürmer performed scanning tunneling microscopy and AES, as well as AFM together with R. W. Friddle. V. Stavila supported the thin film synthesis and XRD experiments. The experiments were conducted under the supervision of M. D. Allendorf as the second supervisor of this thesis.

Reprinted with permission from *ACS Applied Materials & Interfaces*. Copyright (2018) American Chemical Society.

K. Thürmer[‡], C. Schneider[‡], V. Stavila, R. W. Friddle, F. Léonard, R. A. Fischer, M. D. Allendorf, A. A. Talin, Surface Morphology and Electrical Properties of Cu₃BTC₂ Thin Films Before and After Reaction with TCNQ. *ACS Appl. Mater. & Interf.*, **2018**, *10*, 39400-39410.

[‡] These authors contributed equally.

Surface Morphology and Electrical Properties of Cu_3BTC_2 Thin Films Before and After Reaction with TCNQ

Konrad Thürmer,^{*,†,§} Christian Schneider,^{‡,§} Vitalie Stavila,^{†,§} Raymond W. Friddle,[†] François Léonard,^{†,§} Roland A. Fischer,^{‡,§} Mark D. Allendorf,^{*,†,§} and A. Alec Talin^{†,§}

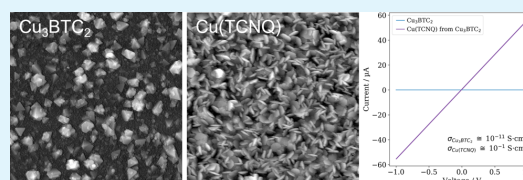
[†]Sandia National Laboratories, Livermore, California 94551, United States

[‡]Department of Chemistry, Technical University Munich, Lichtenbergstrasse 4, 85748 Garching, Germany

Supporting Information

ABSTRACT: HKUST-1 or Cu_3BTC_2 (BTC = 1,3,5-benzenetricarboxylate) is a prototypical metal–organic framework (MOF) that holds a privileged position among MOFs for device applications, as it can be deposited as thin films on various substrates and surfaces. Recently, new potential applications in electronics have emerged for this material when HKUST-1 was demonstrated to become electrically conductive upon infiltration with 7,7,8,8-tetracyanoquinodimethane (TCNQ). However, the factors that control the morphology and reactivity of the thin films are unknown. Here, we present a study of the thin-film growth process on indium tin oxide and amorphous Si prior to infiltration. From the unusual bimodal, non-log-normal distribution of crystal domain sizes, we conclude that the nucleation of new layers of Cu_3BTC_2 is greatly enhanced by surface defects and thus difficult to control. We then show that these films can react with methanolic TCNQ solutions to form dense films of the coordination polymer $\text{Cu}(\text{TCNQ})$. This chemical conversion is accompanied by dramatic changes in surface morphology, from a surface dominated by truncated octahedra to randomly oriented thin platelets. The change in morphology suggests that the chemical reaction occurs in the liquid phase and is independent of the starting surface morphology. The chemical transformation is accompanied by 10 orders of magnitude change in electrical conductivity, from $<10^{-11}$ S/cm for the parent Cu_3BTC_2 material to 10^{-1} S/cm for the resulting $\text{Cu}(\text{TCNQ})$ film. The conversion of Cu_3BTC_2 films, which can be grown and patterned on a variety of (nonplanar) substrates, to $\text{Cu}(\text{TCNQ})$ opens the door for the facile fabrication of more complex electronic devices.

KEYWORDS: MOFs, coordination polymers, thin-film growth, surface morphology, 2D nucleation, bimodal growth, electrical conductivity



INTRODUCTION

Metal–organic frameworks (MOFs) are being developed for a wide range of applications.¹ In addition to gas storage,² separations,³ and catalysis,⁴ much recent research is focused on the use of MOFs as active materials in chemical sensors and electronic devices.⁵ A crucial step is their integration with other materials; for this purpose, controlled deposition of the MOF as a thin film is essential. The step-by-step method developed by Wöll, Fischer, and co-workers, which we here define as a film growth process in which the substrate is sequentially exposed to the reagents used for the MOF film growth (i.e., the metal ion alternating with the organic linker molecule, both in solution), delivers smooth films with high control of the film thickness by adjusting the number of deposition cycles.⁶ MOF film growth by this method has been intensively studied, with Cu_3BTC_2 (also known as HKUST-1, BTC = 1,3,5-benzenetricarboxylate) serving as the model system.^{7,8} For many substrates, thin films of Cu_3BTC_2 consist of disordered arrays of octahedra,⁹ with the roughness dependent on the identity of the substrate.⁷

The growth of Cu_3BTC_2 films is of particular interest because, in addition to its relatively high surface area, solvent molecules weakly bound to the copper ions in the framework can be easily removed, generating reactive centers (“open metal sites”, OMS) that can chemisorb a variety of molecules. OMS provide an additional design element that can be exploited to modify the electronic and photonic properties of the material by introducing “noninnocent” guest molecules.¹⁰ We have recently shown that the infiltration of Cu_3BTC_2 thin films with the redox-active guest molecule 7,7,8,8-tetracyanoquinodimethane (TCNQ) transforms the insulating film into a semiconductor.^{11,12} This has high relevance for the aforementioned integration with electronic devices and has consequently attracted much attention by other groups.^{13–15} A number of infiltration protocols using various concentrations, infiltration times, and with or without solvent can be found in the literature.^{11,12,14–16} Although the method initially

Received: September 5, 2018

Accepted: October 24, 2018

Published: October 24, 2018

reported used the inert aprotic solvent dichloromethane (DCM),¹¹ more recent approaches employed alcoholic solutions of methanol (MeOH) and ethanol (EtOH).^{12,14} The effect of these differing infiltration conditions on the properties and morphologies of the film has not been considered. In general, however, we expect that microstructure will play a significant role in the charge-transport properties of MOF films. Indeed, a recent theoretical work suggests that polycrystallinity in some MOFs can change their charge-transport behavior from metallic to semiconducting,¹⁷ motivating us to consider the mechanisms of both film growth and guest molecule infiltration in a greater detail.

Herein, we report a chemical reaction observed during Cu₃BTC₂ infiltration using MeOH that leads to its complete reductive transformation to Cu(TCNQ) in *thin-film* samples. Previously, we reported that a Cu(TCNQ) byproduct phase forms after prolonged infiltration of Cu₃BTC₂ powder with TCNQ vapor in a solid-state-inspired synthesis.¹⁶ Interestingly, in this case, the reaction appears to be limited to the surface of the MOF crystallites, but does not completely transform the powder to Cu(TCNQ). These observations encouraged us to perform a more detailed study of the transformation of Cu₃BTC₂ thin films as a function of thickness, i.e., the number of deposition cycles, using atomic force microscopy (AFM), Auger electron spectroscopy (AES), and grazing incident X-ray diffraction (GIXRD). A basic question is whether the morphology of the grown films, i.e., the nature of the exposed surface, determines how this reaction proceeds. The Cu₃BTC₂ thin films deposited on polycrystalline indium tin oxide (ITO) substrates are extremely inhomogeneous, developing two distinct crystallite populations, i.e., small crystals with basic shapes and larger twinned crystals exhibiting dramatically accelerated growth. As discussed below, we interpret this bimodal crystal-size distribution as being caused by ideal crystallites coexisting with defect-containing ones.¹⁸ Upon infiltration, Cu₃BTC₂ films of all film thicknesses we considered reacted with TCNQ. For the thickest film used in this work (20 cycles, 54 nm average film thickness), AFM and AES revealed a full conversion to a dense Cu(TCNQ) film with a platelet morphology, with the GIXRD pattern matching that of Cu(TCNQ) phase I, as reported by Heintz et al.¹⁹ Since this reaction completely changed the morphology of the film, we suggest that the transformation involves mass transport in the solvent and does not depend on the precise crystallite morphology of the initial film.

Although the results we report are of fundamental interest for the development of MOF films with controlled electrical properties (in particular, the large MOF subcategory with the so-called “paddlewheel” secondary building unit²⁰), there are also implications from an application standpoint. Cu(TCNQ) is a well-known semiconducting coordination polymer that has attracted tremendous interest since the discovery of its electrical switching properties in 1979.²¹ However, its utility for electronic devices is hindered by complicated film growth methods, in which metallic Cu substrates are exposed to solutions of TCNQ in acetonitrile or are converted to Cu(TCNQ) under harsh conditions by gaseous or molten TCNQ.^{19,22} Deposition on oxides is possible, but sophisticated vacuum vapor co-deposition techniques are required,²³ as conventional spin-coating approaches are only successful with TCNQ derivatives due to the poor solubility of Cu(TCNQ) in common organic solvents.²⁴ Consequently, our discovery that Cu₃BTC₂ films, which can be grown and patterned by various

methods on virtually any type of substrate,^{5,25} can serve as a precursor to Cu(TCNQ) film formation opens the door to facile integration of this material to create complex electronic devices.

EXPERIMENTAL SECTION

Cu₃BTC₂ was deposited onto polycrystalline indium tin oxide (ITO) substrates (rms surface roughness: ≈ 1 nm, vendor: Thin Film Devices, Inc.) using the well-established step-by-step method. ITO is chosen because of its wide use as a substrate for the integration of MOFs with photovoltaic and other optoelectronic devices due to its electrical conductivity, optical transparency, and ease of deposition.^{26,27} Prior to deposition, the substrates were rinsed with ethanol and dried with dry N₂ before they were treated with an oxygen plasma (Micro RIE, Series 800 Plasma System) for 10 min to clean the substrate from residual organic molecules and to activate the surface.⁷ The substrate was alternately immersed in ethanol solutions of Cu(Ac)₂·H₂O (Ac = acetate, 1.0 mmol/L) and H₃BTC (0.1 mmol/L) for 7.5 and 15 min, respectively, followed by rinsing with ethanol after each immersion step. The temperature was kept constant at 50 °C. Several films with different numbers of deposition cycles, i.e., 0.5 (only immersed in the Cu(Ac)₂ solution), 2, 7, and 20, were fabricated to investigate the nucleation and growth of the crystalline Cu₃BTC₂ film.

Before infiltration with TCNQ, the thin-film samples were desolvated at 100 °C and 10⁻⁶ mbar for 1 h. They were then immersed in a saturated solution of TCNQ in reagent-grade methanol for 12 h. Afterward, the substrates were rinsed with fresh methanol prior to subsequent characterization.

The film morphology was examined *ex situ* with atomic force microscopy (AFM) (Bruker Dimension 3100, Nanoscope V controller), using back-side Al-coated cantilevers with a resonance frequency of 150 kHz and a force constant of 5 N/m. Typically, 1280 × 1280 pixel images were acquired using the tapping mode. The chemical composition of the surface was determined with Auger electron spectroscopy (AES) in an ultrahigh vacuum chamber using an Omicron CMA 100 operated at an electron primary energy of 2000 eV. To reduce electron-beam damage, a low emission current of 0.5 μ A was used, which previously had been verified to not produce measurable C deposition on Pt substrates under identical conditions. Since some residual e-beam damage is still likely to occur, in particular on the nonconductive Cu₃BTC₂ film samples, we performed the Auger spectroscopy always after completing the (nondestructive) AFM experiments.

Grazing incidence X-ray diffraction (GIXRD) data were recorded for 2θ angles between 5 and 30° on a PANalytical Empyrean system equipped with a position-controlled flat sample stage for thin-film measurements. X-ray radiation was generated using a Cu X-ray tube that was operated at 44 kV and 40 mA and directed onto the sample through a parallel beam X-ray mirror with a 1/16° antiscatter slit and a 0.02 radian Soller slit. Receiving optics include a parallel plate collimator and a PIXcel3D detector in receiving slit mode. Powder patterns were recorded on the same instrument in capillary mode using a fixed divergence slit (1/8°) and an antiscatter slit (1/16°) as an incident beam optic.

For electrical transport measurements, films were grown on Si substrates with a 100 nm thermal SiO₂ layer (Si/SiO₂), which was patterned with Au electrodes (500 μ m × 200 μ m). Current–voltage (*IV*) curves were recorded by contacting the Au electrodes with microprobes and sweeping the voltage between –1 and 1 V. The current was measured using a DL 1211 current preamplifier connected to a computer. The specific conductivity σ was calculated via

$$\sigma = \frac{I}{V} \cdot \frac{l}{w \cdot t} \quad (1)$$

with I , V , l , w , and t being the measured current, applied voltage, distance between the electrodes, width of the electrodes, and film thickness, respectively.

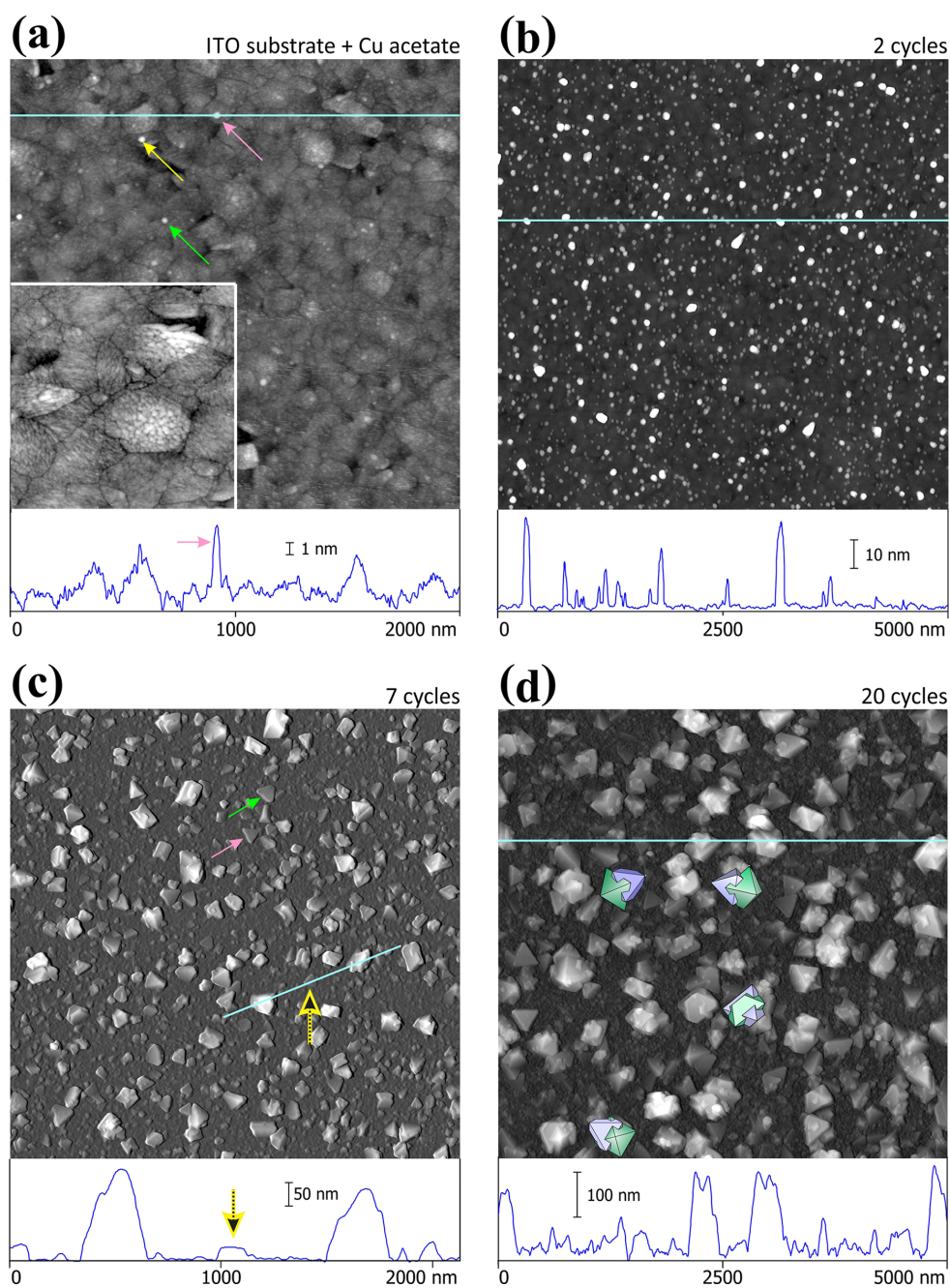


Figure 1. Surface topography of Cu_3BTC_2 films grown on an ITO substrate. This image sequence shows how Cu_3BTC_2 films evolve as a function of the deposited amount of material. The number of deposition cycles is (a) 0.5, (b) 2, and (c) 7, and (d) 20. A height profile along the light blue line is shown below each frame. All images were acquired with AFM except the inset in (a), which is a 500 nm \times 500 nm scanning tunneling microscopy image of the bare ITO substrate. The arrows in (c) point to the largest monocrystallites, which are much flatter than crystallites that have a complex compound shape. The blue-green schematics inserted next to some of the larger particulates in (d) illustrate their compound nature resulting from the merger of two or more octahedral crystallites.

Scanning electron microscopy (SEM) images were recorded on an FEI XL30s SEM equipped with a thermally assisted Schottky field emission gun operated at an acceleration voltage of 5 kV and an effective working distance of 3–4 mm. For a higher image quality and to avoid charging effects, samples were coated with a 3 nm layer of AuPd. The substrates were then mounted onto the sample holder using copper tape.

RESULTS AND DISCUSSION

Conversion of $\text{Cu}_3(\text{BTC})_2$ Films of Various Thicknesses to $\text{Cu}(\text{TCNQ})$. Thin films of the following thicknesses, as given by the number of growth cycles, were used: 0.5 (i.e., only immersion in $\text{Cu}(\text{Ac})_2$), 2, 7, and 20 cycles (alternate immersion in solutions of $\text{Cu}(\text{Ac})_2$ and H_3BTC) were grown on ITO substrates via step-by-step deposition from EtOH solutions of $\text{Cu}(\text{Ac})_2$ and H_3BTC . A second set of films was fabricated and immersed in a methanol solution of TCNQ overnight. For both sets of film samples, AFM was used to investigate the surface morphology, whereas the chemical surface composition was assessed with AES.

The AFM image sequence in Figure 1 summarizes how the surface morphology of Cu_3BTC_2 evolves with increasing film thickness, with the corresponding AES spectra shown in Figure 2. After 0.5 cycles, a few ~ 5 nm-sized particles of $\text{Cu}(\text{Ac})_2$ are

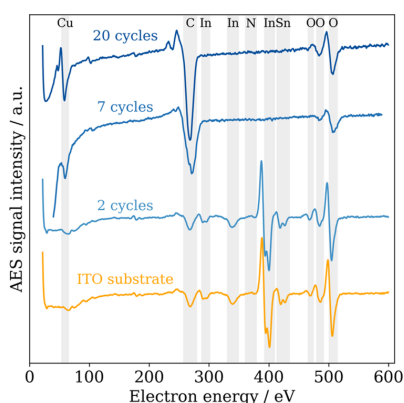


Figure 2. AES spectra of the ITO substrate and Cu_3BTC_2 films of various thicknesses deposited on ITO. The gray boxes indicate the electron energies expected for the respective elements.

visible, covering approximately 0.1% of the substrate; these serve as nuclei for the MOF growth. After two deposition cycles, the surface is decorated by many individual and well-separated 3D clusters, which are typically 10–40 nm tall and 40–120 nm wide and cover 3–5% of the surface. The strong signature of In and Sn in the AES spectrum indicates that most of the surface, i.e., the large regions between the 3D particles, is still the exposed ITO substrate. This is different for the films with 7 and 20 deposition cycles, where the substrate contributions are absent in the AES spectra. The AFM data of the 7- and 20-cycle films show that the entire substrate surface is covered and reveal a very wide crystallite size distribution. Very often, particle size distributions can be described as log-normal. However, in Figure 3, it is clear that a large-particle tail cannot be so described. Indeed, as shown in Figure 3, the distribution can be fit as a sum of two log-normal distributions, i.e., the distribution is bimodal. For the

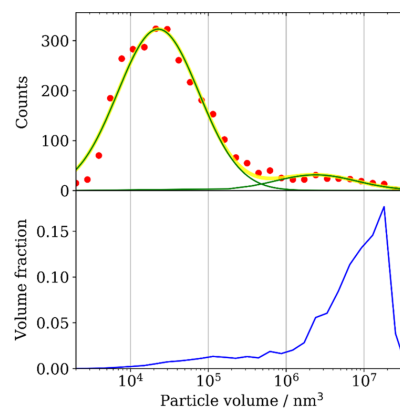


Figure 3. Histograms of the size distribution of crystallites of the 20-cycle Cu_3BTC_2 film grown on ITO, based on the data depicted in Figure 1d. Top: Histogram evaluating the particle numbers. The curve can be approximated by the sum (thick yellow line) of two log-normal distributions (thin green lines). Bottom: Histogram showing how the volume of film material is distributed. Its maximum is shifted to almost 3 orders of magnitude higher particle volumes with respect to the maximum of the histogram evaluating particle numbers.

20-cycle film, the majority of the crystallites are 10–20 nm tall and 20–50 nm wide, but in terms of volume, most of the film material is concentrated in just a few very large crystallites that are 100–200 nm tall and 200–400 nm wide. The histograms in Figure 3 capture this observation quantitatively: indeed, the peak of the distribution of crystallite numbers and the peak of the volume distribution are located almost 3 orders of magnitude apart, as measured by crystallite volume. In a separate section below, we discuss a proposed scenario leading to this striking size distribution.

AFM images acquired directly after immersing 0.5-, 2-, and 20-cycle films in TCNQ are depicted in Figure 4; the corresponding AES spectra are shown in Figure 5. Comparing image pairs from samples with an equal number of deposition cycles, one image taken from the pure Cu_3BTC_2 data (Figure 1), the other from the data set of TCNQ-treated films (Figure 4), reveals that, for all examined film thicknesses, the immersion in TCNQ completely alters the film morphology. For the 0.5-cycle sample from the first data set, we observe that all of the deposited material, i.e., $\text{Cu}(\text{Ac})_2$, has condensed to small islands, whereas the film material of the TCNQ-treated film has spread over the ITO substrate, exhibiting a web- or sponge-like morphology featuring ~ 10 nm-deep and 100–500 nm-wide depressions and a few 10–30 nm-tall and ca. 20–100 nm-wide clusters. The lack of intensity in the In or Sn region of the corresponding AES spectrum is evidence that no bare ITO substrate remains exposed. Instead, a peak corresponding to nitrogen is present, consistent with the deposition of TCNQ. By contrast, the 2-cycle film after immersion in TCNQ is dominated by a much larger number of small clusters, typically 20–50 nm tall and 30–150 nm wide.

With increasing film thickness, the morphology changes completely. The 20-cycle sample exhibits a very striking morphology after immersion in the TCNQ solution featuring randomly oriented thin platelets of 200–300 nm diameter. Their rather uniform size is in stark contrast to the extremely wide crystal-size distribution of the initial 20-cycle film before

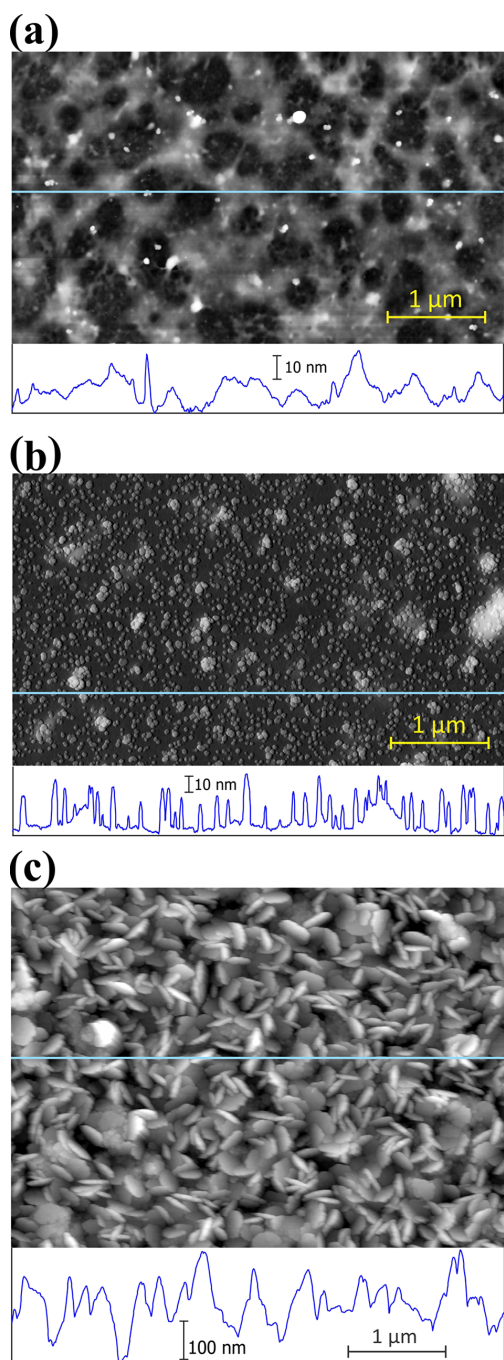


Figure 4. Surface topography of the Cu_3BTC_2 films of various thicknesses deposited on ITO after immersion in a solution of TCNQ in MeOH. The number of deposition cycles is (a) 0.5, (b) 2, and (c) 20. A height profile along the light blue line is shown below each frame.

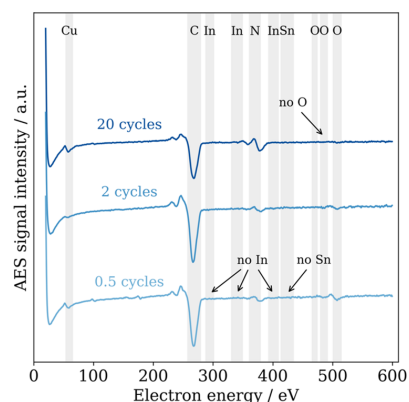


Figure 5. AES spectra of the Cu_3BTC_2 films of various thicknesses deposited on ITO after immersion in a solution of TCNQ in MeOH. The gray boxes indicate the electron energies expected for the respective elements.

immersion. Thus, apparently, the transformation upon immersion in TCNQ erases all memory of the initial film morphology, at least for film thicknesses up to and including 20 cycles. The absence of dendritic features and the near uniformity of crystal shape and size independent of their (random) orientation are strong indications that diffusion through the solution is not the rate-limiting step. Presumably, the platelet shape is either determined by how fast material is incorporated at the different crystal facets (growth shape due to attachment-limited kinetics) or these platelets represent the near-equilibrium shape, maintained by an approximate balance between deposition and dissolution. The platelet morphology we observe is reminiscent of the one reported for $\text{Cu}(\text{TCNQ})$ phase II by Heintz et al.¹⁹

The corresponding AES spectrum of the 20-cycle film contains only Cu, C, and N peaks. While the half-cycle and 2-cycle films still had small contributions from O, the 20-cycle film shows no hint of any remaining oxygen, implying that at least near the surface, the Cu_3BTC_2 film has completely transformed to $\text{Cu}(\text{TCNQ})$. To examine the chemical composition and crystal structure of the films beyond the near-surface regions, we performed GIXRD measurements on the 20-cycle films before and after immersion in the TCNQ solution (Figure 6). The diffraction pattern before immersion clearly matches the Cu_3BTC_2 reference structure. The film after immersion, on the other hand, reproduces the diffraction pattern of $\text{Cu}(\text{TCNQ})$ Phase I, whereas no reflections of the initial Cu_3BTC_2 structure can be seen. This confronts us with the apparent contradiction that the same sample that reproduces Heintz et al.'s¹⁹ GIXRD pattern of $\text{Cu}(\text{TCNQ})$ Phase I also exhibits a platelet morphology, which these authors had assigned to Phase II. However, the large variety of morphologies reported for $\text{Cu}(\text{TCNQ})$ films, including needles,^{19,28,29} thick rods,^{19,28} and cones,³⁰ highlights the sensitivity of the film morphology on the precise growth conditions, rendering our observation of platelets for $\text{Cu}(\text{TCNQ})$ Phase I less of a surprise. In addition, there is ample evidence that the two phases of $\text{Cu}(\text{TCNQ})$ are energetically close and thus can be easily interconverted.³¹

Partial Conversion of $\text{Cu}_3(\text{BTC})_2$ Powder to $\text{Cu}(\text{TCNQ})$. Due to the porous microstructure of the Cu_3BTC_2 film

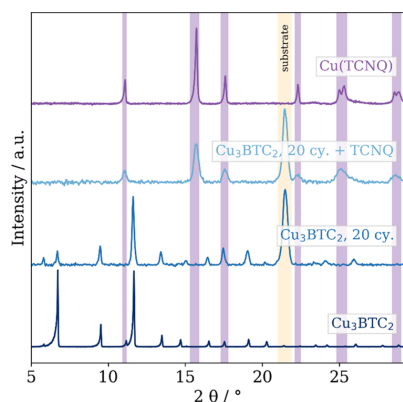


Figure 6. GIXRD patterns of the 20-cycle film of Cu_3BTC_2 before and after immersion in a solution of TCNQ in MeOH and reference powder X-ray diffraction (PXRD) patterns of Cu_3BTC_2 and $\text{Cu}(\text{TCNQ})$. The reflection at 21.46° stems from the substrate. The vertical boxes indicate the peak positions of $\text{Cu}(\text{TCNQ})$ (purple) and the substrate (yellow).

samples used in this study, we assume that the solution can easily penetrate the film to react with the individual particles. If the conversion proceeds by advancing reaction fronts from the surfaces of the particles toward their centers, we expect that the degree of conversion is mostly determined by the particle size. The 20-cycle film, which is converted fully, has most of its material concentrated in particles with a typical particle diameter of ~ 300 nm. To test whether the conversion becomes incomplete at larger particle sizes, we subjected activated Cu_3BTC_2 powder with a grain size of $10\text{--}30\ \mu\text{m}$ to infiltration with TCNQ in MeOH for prolonged times. We find similar transformations as described above for Cu_3BTC_2 films: Figure 7 shows the diffraction patterns of powders that were infiltrated at room temperature for 3 and 7 days. As indicated, a second phase, which matches the reflections of the $\text{Cu}(\text{TCNQ})$ reference, forms and becomes more pronounced with longer infiltration times. However, in contrast to the thin-

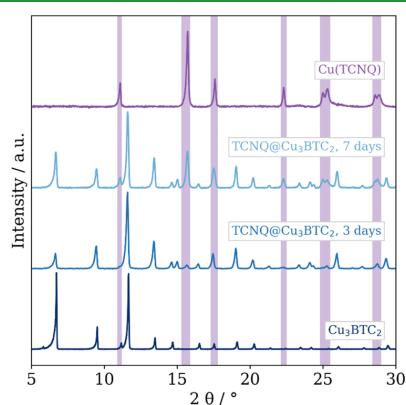


Figure 7. PXRD patterns of Cu_3BTC_2 powder after immersion in a solution of TCNQ in MeOH for 3 and 7 days and reference PXRD patterns of Cu_3BTC_2 and $\text{Cu}(\text{TCNQ})$. The purple boxes indicate the peak positions of the $\text{Cu}(\text{TCNQ})$ reference sample.

film samples, Cu_3BTC_2 powder could not be completely transformed to $\text{Cu}(\text{TCNQ})$ even after stirring in a saturated TCNQ solution in MeOH for 7 days. This observation implies that the conversion from $\text{Cu}_3(\text{BTC})_2$ powder to $\text{Cu}(\text{TCNQ})$ proceeds via advancing reaction fronts from the surface toward the centers of the individual particles. Evidently, the reaction front does not move fast enough to reach the center of $10\text{--}30\ \mu\text{m}$ large particles within a week. Most likely, the reaction is slowed down by a growing shell of nonporous $\text{Cu}(\text{TCNQ})$ through which the reagents must diffuse to reach the not-yet-converted particle core. We note that the color of the infiltration solution turned from yellow to green after 24 h and to brown-orange after 7 days, indicating the formation of TCNQ radicals in the MeOH solution.³²

Electrical Conductivity Change upon Chemical Conversion. To measure the change of electrical conductivity upon TCNQ-induced conversion, a 50-cycle Cu_3BTC_2 film was grown on a silicon wafer covered with 100 nm of SiO_2 and patterned Au electrodes and then infiltrated with TCNQ in MeOH. The crystal structure and the morphology before and after infiltration were examined by GIXRD (Figure S1) and SEM (Figures S2 and S3) and show similar diffraction patterns and morphologies as the films grown on ITO. Current–voltage (IV) curves of the Cu_3BTC_2 and the resulting $\text{Cu}(\text{TCNQ})$ films were recorded under ambient conditions (Figure 8), and

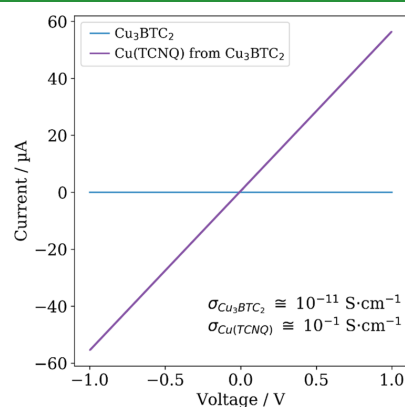
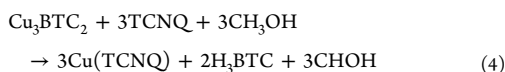
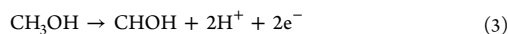
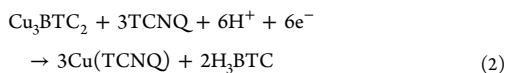


Figure 8. IV curves of a 50-cycle Cu_3BTC_2 film on Si/SiO_2 before (blue) and after (purple) immersion in a MeOH solution of TCNQ. Electrical measurements were made between $500\ \mu\text{m}$ wide Au pads that were $50\ \mu\text{m}$ apart from each other. For calculations of the conductivity, an average film thickness of 100 nm was assumed.

the specific conductivities were calculated. Although the pristine Cu_3BTC_2 shows very poor electrical conductivity as expected ($<10^{-11}$ S/cm), possibly due to residual reactant and/or solvent, a conductivity on the order of 10^{-1} S/cm was measured for the $\text{Cu}(\text{TCNQ})$ film. The electrical conductivity thus increased by 10 orders of magnitude through immersion in the TCNQ solution in MeOH and matches well with the reported literature value of 0.25 S/cm for $\text{Cu}(\text{TCNQ})$.¹⁹

Chemical Processes during the Conversion of $\text{Cu}_3(\text{BTC})_2$ to $\text{Cu}(\text{TCNQ})$. Clear evidence is presented for a chemical reaction of Cu_3BTC_2 (powder and thin films of different thicknesses) with MeOH solutions of TCNQ to form $\text{Cu}(\text{TCNQ})$. For the reaction to occur, both the $\text{Cu}(\text{II})$ species and TCNQ must be reduced to $\text{Cu}(\text{I})$ and TCNQ^- ,

respectively. Electrons for this reaction are most likely provided by MeOH that can be oxidized to formaldehyde or formic acid, as described by eqs 2–4



To assess whether this reaction scheme is energetically favorable, we estimated the enthalpy of reaction 4 using available thermodynamic data. A heat of formation at 298 K was reported for Cu_3BTC_2 ,³³ and heats of formation for TCNQ (solid),³⁴ CH_3OH (liquid),³⁵ H_3BTC (solid),³⁶ and CHOH (gas)³⁷ are also available. We were unable to locate data for $\text{Cu}(\text{TCNQ})$, so instead used the value reported for $\text{Ag}(\text{TCNQ})$.³⁸ On this basis, we obtained a value for (ΔH_f°) (298 K), reaction 4) of -3840 kJ/mol. The primary significance of this number is that it is very negative, suggesting that the reaction should be spontaneous. Its absolute value, which appears unreasonably large, is primarily due to the very large positive heat of formation for solid TCNQ (666.1 kJ/mol). Although heats of condensation can drive reaction enthalpies to be more negative than the corresponding gas-phase reaction, it is noteworthy that for reaction 4, replacing the condensed-phase heats of formation with gas-phase values, where available, only makes the computed reaction enthalpy more negative. On the basis of this (admittedly somewhat crude) estimate, we conclude that the reaction as written is plausible from a thermodynamic point of view.

The color change of the MeOH solution of TCNQ is an indication that some TCNQ^- radicals form.³² This change is also observed in nominally dry, aprotic, and inert solvents (DCM, chloroform, and acetonitrile), but to a lesser extent, suggesting that atmospheric water vapor or trace moisture in the solvent may be involved in the reaction. This explains why the formation of $\text{Cu}(\text{TCNQ})$ was not reported previously¹¹ when dichloromethane was used as the solvent for TCNQ, or in an earlier investigation in which anhydrous methanol was used.¹² The reaction is further enhanced because the formation of most carboxylate MOFs is reversible in solution,³⁹ which provides free Cu species for the formation of $\text{Cu}(\text{TCNQ})$. We have evidence that this transformation is not limited to Cu_3BTC_2 films, but also occurs in other Cu-paddlewheel MOF systems. For example, GIXRD data of a PCN-14 film (see the Supporting Information) show signatures of the $\text{Cu}(\text{TCNQ})$ phase I after infiltration with TCNQ in reagent-grade MeOH.

Enhanced Growth of Compound Cu_3BTC_2 Crystallites. A notable finding of this study is the striking bimodal size distribution of Cu_3BTC_2 crystallites in the pristine Cu_3BTC_2 films grown onto ITO substrates. As suggested in our initial discussion of Figures 1c,d, and 3, after 7 or more deposition cycles, most of the film volume is in large crystals, with the remaining film volume distributed over many much smaller crystals.

What is the reason for the emergence of this bimodal crystal-size distribution? The fact that 7- and 20-cycle films, which differ significantly in their surface fractions composed of large crystallites, have almost indistinguishable AES spectra (Figure

2) suggests that both crystallite populations are chemically identical. The crystallite shapes, however, are distinctly different. While most small crystals show the expected facets of a single crystal, all of the big crystals have complicated faceting. Even the largest crystallites that possess a monocrystalline shape (three examples are marked with arrows in Figure 1c) are much flatter and therefore have a much smaller volume than the intricately shaped members of the large-crystal population. The complex faceting of the large crystallites follows a common theme illustrated in the schematic green-and-blue drawings next to the example crystallites in Figure 1d. Each of the large crystals is composed of two (and sometimes three or even more) individual octahedral crystals that are rotated with respect to each other and have merged to a single particle, which we henceforth call a “compound crystal”. (We avoid the term “crystal twin” because of its implications for the mutual orientation of the two crystals.) Some deviations from this prototype occur due to truncated crystal corners or additional crystallites merging to the compound crystal. In the 7-cycle films, the large crystals are on average about 2 crystal diameters apart. At this density, it is implausible that the observed compound crystals are the result of a merger of two crystals that adventitiously formed next to each other and grew large independently from each other. Rather, the pairwise occurrence of the larger crystallites indicates that the two crystallites must have merged at an early stage, when they were still small, presumably giving this crystal pair a significant growth advantage over its monocrystalline neighbors.

Figure 9 illustrates a proposed scenario for the observed accelerated growth of compound crystals. Consistent with previous AFM observations by other groups,^{40–43} we assume the Cu_3BTC_2 crystallites to be substrate-truncated octahedra bound by {111} facets onto which the material is deposited layer by layer. In the absence of step-producing surface defects such as dislocations, these new two-dimensional (2D) layers must be nucleated (Figure 9a). The formation of a 2D nucleus is hindered by a free-energy barrier due to the energy cost of creating the surface steps bounding the nucleus.^{44–46} If driving forces are weak, this free-energy barrier can be insurmountable^{18,44–49} or will at least slow down the layer-by-layer growth on top of the crystal facets. That these rules apply for the layer-by-layer growth of Cu_3BTC_2 is supported by the observation of Shōaë et al.^{41,42} and John et al.⁴⁰ that, at low supersaturation, new 2D layers always emerged from defect sites on the crystal surface.

In contrast, for a compound crystal, new 2D layers can emerge from the domain boundary between the two crystallites without having to nucleate an isolated 2D layer. This scenario would facilitate the layer-by-layer deposition on the top facets and thus accelerate the growth of the compound crystals, provided that no significant free-energy barrier is associated with the emergence of new 2D layers from the domain boundary. As illustrated in Figure 9c,d, an elongated nucleus of a new 2D layer (red edge line) is emerging from the domain boundary. Figure 9d shows a cross section through the 2D nucleus along the black dash-and-dot line in Figure 9c. The formation energy of this nucleus $E_{\text{nuc}2\text{D}}$ can be approximated by the sum of the energy cost to form the bounding surface step (red edge) E_{step} , the formation energy E_{if} of the interface (green dotted line) between the new layer (pink) and the crystal (green) from which the layer emerges, and the energy $-E_{\text{surf}}$ gained by eliminating a portion of the surface of the

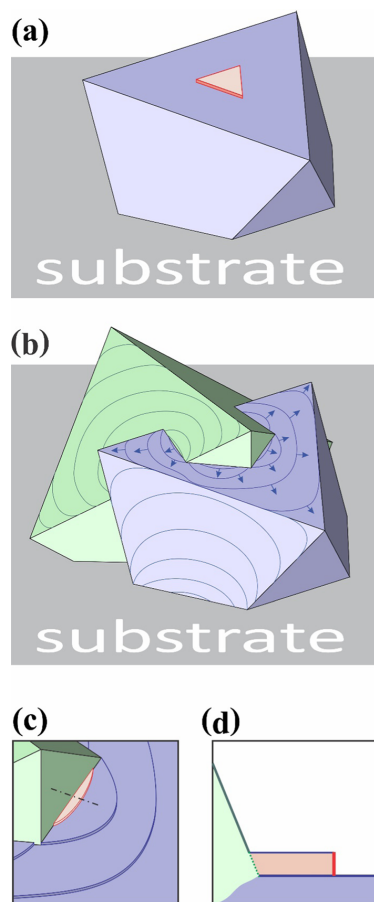


Figure 9. Accelerated growth of compound crystals. The schematic in (a) illustrates the growth of a monocrystal via nucleation of new 2D layers. This type of growth is slowed down by an activation barrier due to the energy cost of creating the surface steps bounding the 2D nucleus. (b) Schematic of the accelerated growth of compound crystals, where new 2D layers emerge from the domain boundary between the two crystallites. (c) Close-up of an elongated nucleus of a 2D layer. A cross section along the black dash-dotted line is shown in (d). The energy cost of creating the surface step (red) is assumed to be offset by the energy gain due to the elimination of a portion of the crystal surface (green dotted line) of the green crystallite.

facet (green) to the left of the domain boundary, i.e., $E_{\text{nuc2D}} \approx E_{\text{step}} + E_{\text{if}} - E_{\text{surf}}$. It seems plausible that the energy gain E_{surf} can roughly compensate the energy cost E_{step} because the nucleus is expected to create a similar number of new broken bonds at the surface step (on its right side) as it eliminates broken bonds of the facet by “covering them up” (left side of the nucleus). Thus, our observations of a bimodal size distribution with larger compound crystals suggest that the interface energy E_{if} is low.

Based on this mechanism, we expect an enhanced 2D nucleation on the side facets, where 2D layers can emerge from the boundary between the bottom of the facet and the substrate. This process would facilitate the lateral growth of both compound crystals and monocrystals, consistent with the

occurrence of flat triangular monocrystallites with a rather large footprint (examples are marked by arrows in Figure 1c). Such enhanced 2D nucleation on the side facets in contact with the substrate versus nucleation on the top facets parallel to the substrate could possibly explain Summerfield et al.’s⁵⁰ observation which supported that Cu_3BTC_2 crystallites of square-pyramidal shape grow faster in height than crystallites with a triangular top facet.

The film–substrate interaction should also affect whether two size groups of crystallites can be expected to grow simultaneously. In our experiments, Cu_3BTC_2 crystallites condense onto the polycrystalline ITO substrate with an intermediate nucleation density. Assuming that the orientation of the substrate grains imposes the orientation of the film crystallites growing on them, the few crystallites that nucleate near a substrate grain boundary have a higher chance to merge with a differently oriented crystallite grown on a neighboring substrate grain and subsequently can evolve into a large compound crystal. The majority of the crystallites, on the other hand, are surrounded by other crystallites that nucleated on the same substrate grain and thus are more likely to share their crystal orientation with their neighbors, preventing their evolution into fast-growing compound crystals.

On amorphous substrates, in contrast, crystallites grow with random orientations and thus are expected to equally benefit from enhanced growth, putting them all to the same size group. Indeed, we find a much narrower size distribution on amorphous $\text{SiO}_2/\text{Si}(001)$ than on polycrystalline ITO, as the comparison of 4-cycle films shown in Figure 10 reveals: For $\text{Cu}_3\text{BTC}_2/\text{ITO}$, the peak of the crystal-size distribution evaluating crystal numbers and the peak of the volume fraction histogram are separated by almost 3 orders of magnitude, whereas for Cu_3BTC_2 on amorphous $\text{SiO}_2/\text{Si}(001)$, those peaks are only a factor of 4 apart.

At this point, it is unknown to what extent material transport between crystallites occurs in our experiments. Nevertheless, the scenario we propose in the previous paragraphs has similarities with the theoretical model developed by Rohrer et al.,¹⁸ which quantifies capillary-driven coarsening of films composed of perfect faceted crystals as well as crystals that contain step-producing defects. Their prediction of bimodal size distributions similar to those reported here lends credence to our claim that nucleation-free material addition is responsible for the enhanced growth of compound crystals.

CONCLUSIONS

We demonstrated the solution-based conversion of Cu_3BTC_2 films to electrically conducting $\text{Cu}(\text{TCNQ})$ by growing Cu_3BTC_2 of different thicknesses on ITO substrates and immersing them in a TCNQ solution in MeOH. Enhanced Cu_3BTC_2 crystal growth was observed when two small crystallites of different orientations merge to form a compound crystal. We hypothesize that: (a) this growth-acceleration mechanism requires a film material that is structurally flexible enough to allow the formation of low-energy grain boundaries and (b) it is more likely to occur on polycrystalline substrates. When exposed to TCNQ, the Cu_3BTC_2 films slowly undergo a chemical transformation into $\text{Cu}(\text{TCNQ})$. That the morphology of the film changes dramatically during this transformation implies that long-ranged transport of molecules plays a key role. This transport seems most likely to occur through the solvent, again pointing out the importance of the solvent rather than, say, the thin-film quality in controlling the reaction.

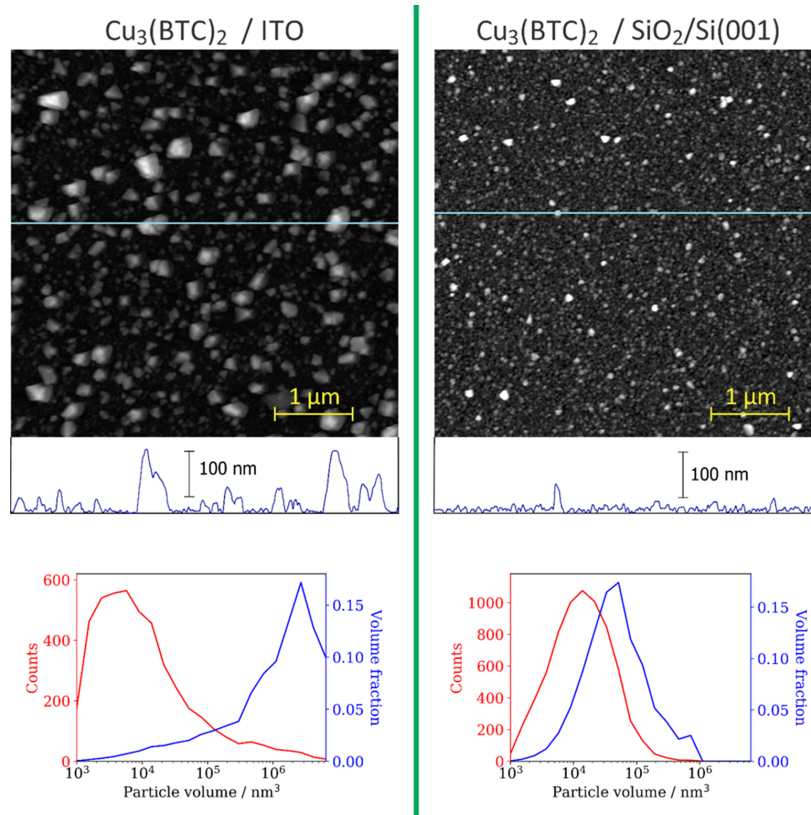


Figure 10. AFM images of 4-cycle Cu_3BTC_2 films grown on polycrystalline ITO and on amorphous $\text{SiO}_2/\text{Si}(001)$. At the bottom, histograms of the corresponding size distribution of crystallites are shown. The red plots show the distributions of particle numbers, whereas the blue curves depict how the volume of the film material is distributed. For $\text{Cu}_3\text{BTC}_2/\text{ITO}$, these two curves peak at particle volumes about 3 orders of magnitude apart. For $\text{Cu}_3\text{BTC}_2/\text{SiO}_2/\text{Si}(001)$, the peaks are merely offset by a factor of 4.

Since the transformation into $\text{Cu}(\text{TCNQ})$ was not observed in aprotic, redox-inert solvents, MeOH was identified as the initiator of the reaction and other protic, noninert solvents are likely to behave in a similar fashion. However, comparison of our results with prior literature reports^{12,14,15} suggests that water also plays a role, a variable that is difficult to control when methanol or ethanol is the solvent. In our prior publication, in which we used anhydrous MeOH,¹² GIXRD provided no indication of the presence of $\text{Cu}(\text{TCNQ})$, which is easily distinguished from Cu_3BTC_2 because of its much smaller unit cell. Moreover, $\text{Cu}(\text{TCNQ})$ is an n-type material, whereas our Seebeck coefficient measurements show that TCNQ-infiltrated Cu_3BTC_2 is p-type, indicating that, even if a trace amount of the n-type material was present, it was not responsible for the observed electrical conductivity.

The implications of this transformation are multifaceted. First, the fact that Cu_3BTC_2 can be deposited on almost any type of substrate (glass, silicon, polymers, etc.), whereas $\text{Cu}(\text{TCNQ})$ is typically grown on metallic Cu substrates and opens new routes for the integration of electrically conductive $\text{Cu}(\text{TCNQ})$ thin films with a variety of (nonplanar) substrates used to fabricate electronic devices. Second, this straightforward solution-based approach can convert insulating Cu_3BTC_2

into either a p-type semiconductor ($\text{TCNQ}@Cu_3\text{BTC}_2$ ¹²) or an n-type material ($\text{Cu}(\text{TCNQ})$ ²⁹) simply by changing the solvent. Since a number of other Cu(II)-paddlewheel MOFs are predicted by density functional theory to create (semi)-conducting TCNQ@MOF materials⁵¹ and are likely to display similar reactivity to TCNQ in protic solvents, this provides a potential route to fabricate p–n junctions with tunable chemical potentials for electronic, optoelectronic, and thermoelectric devices. Third, control of the growth morphology from nanoparticles to thin films may provide a way to probe size effects of the properties of these materials. Finally, device integration typically requires thin, uniform, defect-free films with minimal roughness. Therefore, optimizing the growth of Cu_3BTC_2 by increasing the interface energy E_{if} by, for example, using a monodentate ligand such as acetic acid as a modulator,⁵² could yield a more uniform size distribution (on polycrystalline substrates) that will likely have a positive effect on the properties of the resulting device.

■ ASSOCIATED CONTENT

Supporting Information

The Supporting Information is available free of charge on the ACS Publications website at DOI: 10.1021/acsami.8b15158.

GIXRD data and SEM images of a 50-cycle Cu₃BTC₂ film before and after reaction with TCNQ. GIXRD data of a PCN-14 film before and after reaction with TCNQ. AFM topography images, and the corresponding grain masks used for analyzing the particle size distribution (PDF)

AUTHOR INFORMATION

Corresponding Authors

*E-mail: kthurme@sandia.gov (K.T.).

*E-mail: mdallen@sandia.gov (M.D.A.).

ORCID

Konrad Thürmer: 0000-0002-3078-7372

Christian Schneider: 0000-0001-7231-3266

Vitalie Stavila: 0000-0003-0981-0432

François Léonard: 0000-0002-4973-6743

Roland A. Fischer: 0000-0002-7532-5286

Mark D. Allendorf: 0000-0001-5645-8246

A. Alec Talin: 0000-0002-1102-680X

Author Contributions

*K.T. and C.S. contributed equally.

Notes

The authors declare no competing financial interest.

ACKNOWLEDGMENTS

The authors thank Norman C. Bartelt for insightful discussions. This work was supported by the Sandia Laboratory Directed Research and Development Program. Sandia National Laboratories is a multi-mission laboratory managed and operated by National Technology and Engineering Solutions of Sandia LLC, a wholly owned subsidiary of Honeywell International Inc. for the U.S. Department of Energy's National Nuclear Security Administration under contract DE-NA0003525. C.S. acknowledges his scholarships from the German Academic Scholarship Foundation and from the German Chemical Industry Fund (FCI). This project was further supported by a PPP travel grant (project number 57314965) from the German Academic Exchange Service (DAAD) and by COORNETs (DFG, SPP 1928).

REFERENCES

- Maurin, G.; Serre, C.; Cooper, A.; Ferey, G. The New Age of MOFs and of Their Porous-Related Solids. *Chem. Soc. Rev.* **2017**, *46*, 3104–3107.
- He, Y.; Zhou, W.; Qian, G.; Chen, B. Methane Storage in Metal–Organic Frameworks. *Chem. Soc. Rev.* **2014**, *43*, 5657–5678.
- Adil, K.; Belmabkhout, Y.; Pillai, R. S.; Cadiau, A.; Bhatt, P. M.; Assen, A. H.; Maurin, G.; Eddaoudi, M. Gas/Vapour Separation Using Ultra-Microporous Metal–Organic Frameworks: Insights into the Structure/Separation Relationship. *Chem. Soc. Rev.* **2017**, *46*, 3402–3430.
- Liu, J.; Chen, L.; Cui, H.; Zhang, J.; Zhang, L.; Su, C.-Y. Applications of Metal–Organic Frameworks in Heterogeneous Supramolecular Catalysis. *Chem. Soc. Rev.* **2014**, *43*, 6011–6061.
- Stassen, I.; Burtch, N.; Talin, A.; Falcaro, P.; Allendorf, M.; Ameloot, R. An Updated Roadmap for the Integration of Metal–Organic Frameworks with Electronic Devices and Chemical Sensors. *Chem. Soc. Rev.* **2017**, *46*, 3185–3241.
- Zacher, D.; Shekha, O.; Woll, C.; Fischer, R. A. Thin Films of Metal–Organic Frameworks. *Chem. Soc. Rev.* **2009**, *38*, 1418–1429.
- Stavila, V.; Volponi, J.; Katzenmeyer, A. M.; Dixon, M. C.; Allendorf, M. D. Kinetics and Mechanism of Metal–Organic Framework Thin Film Growth: Systematic Investigation of HKUST-1 Deposition on QCM Electrodes. *Chem. Sci.* **2012**, *3*, 1531–1540.
- Nijem, N.; Fürsich, K.; Kelly, S. T.; Swain, C.; Leone, S. R.; Gilles, M. K. HKUST-1 Thin Film Layer-by-Layer Liquid Phase Epitaxial Growth: Film Properties and Stability Dependence on Layer Number. *Cryst. Growth Des.* **2015**, *15*, 2948–2957.
- Gascon, J.; Aguado, S.; Kapteijn, F. Manufacture of Dense Coatings of Cu₃(BTC)₂ (HKUST-1) on α -Alumina. *Microporous Mesoporous Mater.* **2008**, *113*, 132–138.
- Allendorf, M. D.; Foster, M. E.; Léonard, F.; Stavila, V.; Feng, P. L.; Doty, F. P.; Leong, K.; Ma, E. Y.; Johnston, S. R.; Talin, A. A. Guest-Induced Emergent Properties in Metal–Organic Frameworks. *J. Phys. Chem. Lett.* **2015**, *6*, 1182–1195.
- Talin, A. A.; Centrone, A.; Ford, A. C.; Foster, M. E.; Stavila, V.; Haney, P.; Kinney, R. A.; Szalai, V.; El Gabaly, F.; Yoon, H. P.; Léonard, F.; Allendorf, M. D. Tunable Electrical Conductivity in Metal–Organic Framework Thin-Film Devices. *Science* **2014**, *343*, 66–69.
- Erickson, K. J.; Léonard, F.; Stavila, V.; Foster, M. E.; Spataru, C. D.; Jones, R. E.; Foley, B. M.; Hopkins, P. E.; Allendorf, M. D.; Talin, A. A. Thin Film Thermoelectric Metal–Organic Framework with High Seebeck Coefficient and Low Thermal Conductivity. *Adv. Mater.* **2015**, *27*, 3453–3459.
- Hendon, C. H.; Walsh, A. Chemical Principles Underpinning the Performance of The Metal–Organic Framework HKUST-1. *Chem. Sci.* **2015**, *6*, 3674–3683.
- Neumann, T.; Liu, J.; Wächter, T.; Friederich, P.; Symalla, F.; Welle, A.; Mugnaini, V.; Meded, V.; Zharnikov, M.; Wöll, C.; Wenzel, W. Superexchange Charge Transport in Loaded Metal Organic Frameworks. *ACS Nano* **2016**, *10*, 7085–7093.
- Chen, X.; Wang, Z.; Hassan, Z. M.; Lin, P.; Zhang, K.; Baumgart, H.; Redel, E. Seebeck Coefficient Measurements of Polycrystalline and Highly Ordered Metal–Organic Framework Thin Films. *ECS J. Solid State Sci. Technol.* **2017**, *6*, P150–P153.
- Schneider, C.; Ukaj, D.; Koerver, R.; Talin, A. A.; Kieslich, G.; Pujari, S. P.; Zuillhof, H.; Janek, J.; Allendorf, M. D.; Fischer, R. A. High electrical conductivity and high porosity in a Guest@MOF material: evidence of TCNQ ordering within Cu₃BTC₂ micropores. *Chem. Sci.* **2018**, *9*, 7405–7412.
- Foster, M. E.; Sohlberg, K.; Allendorf, M. D.; Talin, A. A. Unraveling the Semiconducting/Metallic Discrepancy in Ni₃ (HITP) 2. *J. Phys. Chem. Lett.* **2018**, *9*, 481–486.
- Rohrer, G. S.; Rohrer, C. L.; Mullins, W. W. Coarsening of Faceted Crystals. *J. Am. Ceram. Soc.* **2002**, *85*, 675–682.
- Heintz, R. A.; Zhao, H.; Ouyang, X.; Grandinetti, G.; Cowen, J.; Dunbar, K. R. New Insight into the Nature of Cu(TCNQ): Solution Routes to Two Distinct Polymorphs and Their Relationship to Crystalline Films That Display Bistable Switching Behavior. *Inorg. Chem.* **1999**, *38*, 144–156.
- Lin, X.; Telepeni, I.; Blake, A. J.; Dailly, A.; Brown, C. M.; Simmons, J. M.; Zoppi, M.; Walker, G. S.; Thomas, K. M.; Mays, T. J.; et al. High Capacity Hydrogen Adsorption in Cu (II) Tetracarboxylate Framework Materials: the Role of Pore Size, Ligand Functionalization, and Exposed Metal Sites. *J. Am. Chem. Soc.* **2009**, *131*, 2159–2171.
- Potember, R. S.; Poehler, T. O.; Cowan, D. O. Electrical Switching and Memory Phenomena in Cu-TCNQ Thin Films. *Appl. Phys. Lett.* **1979**, *34*, 405–407.
- Liu, S.-G.; Liu, Y.-Q.; Wu, P.-J.; Zhu, D.-B. Multifaceted Study of CuTCNQ Thin-Film Materials. Fabrication, Morphology, and Spectral and Electrical Switching Properties. *Chem. Mater.* **1996**, *8*, 2779–2787.
- Oyamada, T.; Tanaka, H.; Matsushige, K.; Sasabe, H.; Adachi, C. Switching Effect in Cu:TCNQ Charge Transfer-Complex Thin Films by Vacuum Codeposition. *Appl. Phys. Lett.* **2003**, *83*, 1252–1254.
- Huang, W.; Wu, Y.; Gu, D.; Gan, F. In *A Novel CuTCNQ Derivative for Rewritable Optical Storage*, Seventh International Symposium on Optical Storage (ISOS 2005), 2005; p 59661G.

- (25) Shekhah, O.; Liu, J.; Fischer, R. A.; Woll, C. MOF Thin Films: Existing and Future Applications. *Chem. Soc. Rev.* **2011**, *40*, 1081–1106.
- (26) Stavila, V.; Talin, A. A.; Allendorf, M. D. MOF-Based Electronic and Opto-Electronic Devices. *Chem. Soc. Rev.* **2014**, *43*, 5994–6010.
- (27) Liu, J.; Wöll, C. Surface-Supported Metal–Organic Framework Thin Films: Fabrication Methods, Applications, and Challenges. *Chem. Soc. Rev.* **2017**, *46*, 5730–5770.
- (28) Pearson, A.; O'Mullane, A. P.; Bhargava, S. K.; Bansal, V. Effect of Imidazolium-Based Ionic Liquids on the Nanoscale Morphology of CuTCNQ (TCNQ = 7,7,8,8-Tetracyanoquinodimethane) Metal–Organic Semiconductors. *Langmuir* **2013**, *29*, 8–12.
- (29) Sun, Y.; Zhang, F.; Sun, Y.; Di, C.-a.; Xu, W.; Zhu, D. n-Type Thermoelectric Materials Based on CuTCNQ Nanocrystals and CuTCNQ Nanorod Arrays. *J. Mater. Chem. A* **2015**, *3*, 2677–2683.
- (30) Liu, Y.; Jiang, L.; Dong, H.; Tang, Z.; Hu, W. Large-Area Single-Crystalline Nanocone Arrays of an Organic Charge-Transfer Complex: Controlling Growth, Characterization, and Applications. *Small* **2011**, *7*, 1412–1415.
- (31) Fernandez, C. A.; Martin, P. C.; Schaefer, T.; Bowden, M. E.; Thallapally, P. K.; Dang, L.; Xu, W.; Chen, X.; McGrail, B. P. An Electrically Switchable Metal–Organic Framework. *Sci. Rep.* **2014**, *4*, No. 6114.
- (32) Camacho, L. G.; Mellado, J. M. R.; Mayén, M.; Rodríguez-Amaro, R. Determination of the State of Charge of TCNQ^{0/-} Mixed-Valence Complexes Based on a Spectroscopic Model. Application to Thin Films of Electrocrystallised Tetraethylammonium Complexes. *C. R. Chim.* **2015**, *18*, 630–635.
- (33) Bhunia, M. K.; Hughes, J. T.; Fettingner, J. C.; Navrotsky, A. Thermochemistry of Paddle Wheel MOFs: Cu-HKUST-1 and Zn-HKUST-1. *Langmuir* **2013**, *29*, 8140–8145.
- (34) Metzger, R. M.; Kuo, C. S.; Arafat, E. S. A Semi-Micro Rotating-Bomb Combustion Calorimeter. *J. Chem. Thermodyn.* **1983**, *15*, 841–851.
- (35) Cox, J. D.; Pilcher, G., *Thermochemistry of Organic and Organometallic Compounds*. Academic Press: New York, 1970.
- (36) Yukhno, G.; Bikkulov, A. Enthalpies of Combustion and Formation of Benzenecarboxylic Acids. *Russ. J. Phys. Chem.* **1971**, *45*, 924–925.
- (37) Chase, Jr., M. W. *NIST-JANAF Thermochemical Tables*, 4th ed.; J. Phys. Chem. Ref. Data, Monograph 9, American Institute of Physics: Woodbury, NY, 1998.
- (38) Aronson, S.; Mittelman, J. S. Free Energies of Formation of Metal-TCNQ Anion Radical Salts. *J. Solid State Chem.* **1981**, *36*, 221–224.
- (39) Rowsell, J. L. C.; Yaghi, O. M. Metal–Organic Frameworks: A New Class of Porous Materials. *Microporous Mesoporous Mater.* **2004**, *73*, 3–14.
- (40) John, N. S.; Scherb, C.; Shöäèè, M.; Anderson, M. W.; Attfield, M. P.; Bein, T. Single Layer Growth of Sub-Micron Metal–Organic Framework Crystals Observed by in Situ Atomic Force Microscopy. *Chem. Commun.* **2009**, *37*, 6294–6296.
- (41) Shöäèè, M.; Agger, J. R.; Anderson, M. W.; Attfield, M. P. Crystal Form, Defects and Growth of the Metal Organic Framework HKUST-1 revealed by Atomic Force Microscopy. *CrystEngComm* **2008**, *10*, 646–648.
- (42) Shöäèè, M.; Anderson, M. W.; Attfield, M. P. Crystal Growth of the Nanoporous Metal–Organic Framework HKUST-1 Revealed by In Situ Atomic Force Microscopy. *Angew. Chem.* **2008**, *120*, 8653–8656.
- (43) Szelagowska-Kunstman, K.; Cyganik, P.; Goryl, M.; Zacher, D.; Puterova, Z.; Fischer, R. A.; Szymanski, M. Surface Structure of Metal–Organic Framework Grown on Self-Assembled Monolayers Revealed by High-Resolution Atomic Force Microscopy. *J. Am. Chem. Soc.* **2008**, *130*, 14446–14447.
- (44) Mullins, W. W.; Rohrer, G. S. Nucleation Barrier for Volume-Conserving Shape Changes of Faceted Crystals. *J. Am. Ceram. Soc.* **2000**, *83*, 214–216.
- (45) Pimpinelli, A.; Villain, J. *Physics of Crystal Growth*; Cambridge University Press: Cambridge, 1998; Vol 19.
- (46) Rohrer, G. S.; Rohrer, C. L.; Mullins, W. W. Nucleation Energy Barriers for Volume-Conserving Shape Changes of Crystals with Nonequilibrium Morphologies. *J. Am. Ceram. Soc.* **2001**, *84*, 2099–2104.
- (47) Combe, N.; Jensen, P.; Pimpinelli, A. Changing Shapes in the Nanoworld. *Phys. Rev. Lett.* **2000**, *85*, 110.
- (48) Ling, W.; Giessel, T.; Thürmer, K.; Hwang, R.; Bartelt, N.; McCarty, K. Crucial Role of Substrate Steps in De-Wetting of Crystalline Thin Films. *Surf. Sci.* **2004**, *570*, L297–L303.
- (49) Thürmer, K.; Reutt-Robey, J.; Williams, E. D. Nucleation Limited Crystal Shape Transformations. *Surf. Sci.* **2003**, *537*, 123–133.
- (50) Summerfield, A.; Cebula, I.; Schröder, M.; Beton, P. H. Nucleation and Early Stages of Layer-by-Layer Growth of Metal Organic Frameworks on Surfaces. *J. Phys. Chem. C* **2015**, *119*, 23544–23551.
- (51) Nie, X.; Kulkarni, A.; Sholl, D. S. Computational Prediction of Metal Organic Frameworks Suitable for Molecular Infiltration as a Route to Development of Conductive Materials. *J. Phys. Chem. Lett.* **2015**, *6*, 1586–1591.
- (52) Wannapaiboon, S.; Sumida, K.; Dilchert, K.; Tu, M.; Kitagawa, S.; Furukawa, S.; Fischer, R. A. Enhanced Properties of Metal–Organic Framework Thin Films Fabricated via a Coordination Modulation-Controlled Layer-by-Layer Process. *J. Mater. Chem. A* **2017**, *5*, 13665–13673.

3.2 Study II: High Electrical Conductivity and High Porosity in a Guest@MOF Material: Evidence of TCNQ Ordering within Cu₃BTC₂ Micropores

The selection of solvents for the synthesis of TCNQ@Cu₃BTC₂ was limited to inert media (see Study I) and liquid phase impregnation, *per sé*, leads to a large parameter space that is hard to control. Thus, a new vapor phase loading synthesis was developed during this project. Stoichiometric amounts of TCNQ were mixed with activated Cu₃BTC₂, annealed in a glass ampoule under vacuum and heating at 180 °C for 72 h. The obtained solvent and water-free host-guest complexes had a composition $x\text{TCNQ@Cu}_3\text{BTC}_2$ with $0 \leq x \leq 1$. The high synthetic control of the composition and the manipulation of the samples under inert conditions allowed to study the series of materials in great detail. Powder X-ray diffractograms showed a monotonic increase of the (111) Bragg peak intensity with increasing x , being the first crystallographic evidence for the ditopic binding of TCNQ to the OMS of Cu₃BTC₂. Furthermore, the emergence of additional reflections indicated an ordering phenomenon of the guest molecule within the framework, which was associated with a symmetry reduction of the crystal structure. In addition, nitrogen adsorption measurements, IR spectroscopy, and thermogravimetric analysis (TGA) pointed at a successful and stable incorporation of TCNQ. Two-point probe conductivity measurements of pressed pellets showed an exponential increase in room temperature conductivity with increasing TCNQ amount up to $\sigma = 1.5 \cdot 10^{-4} \text{ S cm}^{-1}$ for $x = 1.0$. Importantly, SEM images revealed the formation of small nano-wires on the surface of the crystallites that were identified by AES mapping as Cu(TCNQ). It was speculated that TCNQ@Cu₃BTC₂ (volume phase) exhibits the dominant contribution to the electrical conductivity. The amount of the byproduct is apparently very low, however, the nano-wires along the grain boundaries might represent a good conduction path for charge carriers, as well, and the specific contributions of the host-guest complex and the byproduct are difficult to quantify.

The manuscript was written by the author of this thesis and edited by nine co-authors, who contributed critically to the discussion of the results. The strategy and experiments were developed by the author of this thesis under the supervision of R. A. Fischer. The synthesis and parts of the characterization were done together with D. Ukaj in the context of his Master thesis²¹⁶, supervised by the author of this thesis and Roland A. Fischer. R. Koerver helped with SEM, XPS, and electrical conductivity measurements. G. Kieslich supported the evaluation of PXRD data. S. P. Pujari and H. Zuilhof performed AES measurements. A. A. Talin helped with electrical conductivity measurements.

Reprinted with permission from *Chemical Science*. Published by the Royal Society of Chemistry.

C. Schneider, D. Ukaj, R. Koerver, A. A. Talin, G. Kieslich, S. P. Pujari, H. Zuilhof, J. Janek, M. D. Allendorf, R. A. Fischer, High Electrical Conductivity and High Porosity in a Guest@MOF Material: Evidence of TCNQ Ordering within Cu₃BTC₂ Micropores. *Chem. Sci.* **2018**, *9*, 7405-7412.

Cite this: *Chem. Sci.*, 2018, 9, 7405

All publication charges for this article have been paid for by the Royal Society of Chemistry

High electrical conductivity and high porosity in a Guest@MOF material: evidence of TCNQ ordering within Cu_3BTC_2 micropores†

Christian Schneider,^a Dardan Ukaj,^a Raimund Koerver,^b A. Alec Talin,^c Gregor Kieslich,^a Sidharam P. Pujari,^d Han Zuilhof,^{de} Jürgen Janek,^b Mark D. Allendorf^{b,*c} and Roland A. Fischer^{b,*a}

The host–guest system $\text{TCNQ@Cu}_3\text{BTC}_2$ ($\text{TCNQ} = 7,7,8,8\text{-tetracyanoquinodimethane}$, $\text{BTC} = 1,3,5\text{-benzenetricarboxylate}$) is a striking example of how semiconductivity can be introduced by guest incorporation in an otherwise insulating parent material. Exhibiting both microporosity and semiconducting behavior such materials offer exciting opportunities as next-generation sensor materials. Here, we apply a solvent-free vapor phase loading under rigorous exclusion of moisture, obtaining a series of the general formula $x\text{TCNQ@Cu}_3\text{BTC}_2$ ($0 \leq x \leq 1.0$). By using powder X-ray diffraction, infrared and X-ray absorption spectroscopy together with scanning electron microscopy and porosimetry, we provide the first structural evidence for a systematic preferential arrangement of TCNQ along the (111) lattice plane and the bridging coordination motif to two neighbouring Cu-paddlewheels, as was predicted by theory. For $1.0\text{TCNQ@Cu}_3\text{BTC}_2$ we find a specific electrical conductivity of up to $1.5 \times 10^{-4} \text{ S cm}^{-1}$ whilst maintaining a high BET surface area of $573.7 \text{ m}^2 \text{ g}^{-1}$. These values are unmatched by MOFs with equally high electrical conductivity, making the material attractive for applications such as super capacitors and chemiresistors. Our results represent the crucial missing link needed to firmly establish the structure–property relationship revealed in $\text{TCNQ@Cu}_3\text{BTC}_2$, thereby creating a sound basis for using this as a design principle for electrically conducting MOFs.

Received 5th June 2018
Accepted 7th August 2018

DOI: 10.1039/c8sc02471e

rsc.li/chemical-science

Introduction

The development of electrically (semi-)conductive metal–organic frameworks (MOFs) is of great scientific and technological interest, offering the opportunity of making electronic devices with permanent microporosity.^{1,2} MOFs are supramolecular coordination complexes composed of metal ions or clusters that are linked by polydentate organic ligands to form 2D or 3D frameworks with accessible porosity.³ By combining both long-range order found in inorganic semiconductors and high chemical tunability found in organics, semiconducting

MOFs are unique among the different classes of conducting materials. In principle, the deep understanding of coordination chemistry and crystal engineering enables rational design of MOF systems at a level that is difficult to achieve in other (particularly non-crystalline) materials.^{4,5} However, most MOFs are insulators, originating from the rather ionic coordination bonds of metal carboxylates that tend to suppress charge transfer between the metal node and linker.⁶ Typically, design strategies for electrically conductive MOFs focus on the use of organic linkers that form coordination bonds with improved orbital delocalization between metal and ligand to facilitate charge transfer, and on the use of metal ions with high-energy valance electrons such as Cu^{2+} and Fe^{2+} .^{6,7}

In 2014, some of us applied a radically new approach to impart electrical conductivity to MOFs by incorporating the redox-active molecule TCNQ (7,7,8,8-tetracyanoquinodimethane) in the pores of Cu_3BTC_2 (also known as HKUST-1; $\text{BTC} = 1,3,5\text{-benzenetricarboxylate}$).⁸ Since then, this striking observation has been confirmed by other groups;^{9,10} however, the detailed nature of the host–guest complex and the conductivity mechanism are mainly unsolved. It is proposed that TCNQ bridges two Cu dimer units *via* two geminal nitrile groups, which is strongly supported by both theory and spectroscopic data.^{8,11} Initial measurements of the Seebeck

^aDepartment of Chemistry, Technical University Munich, Lichtenbergstrasse 4, 85748 Garching, Germany. E-mail: roland.fischer@tum.de

^bInstitute of Physical Chemistry, Center for Materials Research (ZFM), Justus-Liebig-University Giessen, Heinrich-Buff-Ring 17, 35392 Giessen, Germany

^cSandia National Laboratories, Livermore, CA 94551, USA. E-mail: mdallen@sandia.gov

^dLaboratory of Organic Chemistry, Wageningen University & Research, Stippeneng 4, 6708 WE Wageningen, The Netherlands

^eSchool of Pharmaceutical Sciences and Technology, Tianjin University, 92 Weijin Road, Tianjin, P. R. China

† Electronic supplementary information (ESI) available: Experimental details, PXRD patterns, BET surface area analysis, IR spectra, thermogravimetric analysis, current–voltage curves, Auger electron spectroscopy, SEM images, XPS spectra, elemental analysis. See DOI: 10.1039/c8sc02471e

coefficient revealed that holes are the majority charge carriers,¹² and an underlying super-exchange mechanism was proposed.¹³ Neumann *et al.* reported calculations supporting this hypothesis, but required the majority carrier to be electrons, which is in apparent conflict with the abovementioned Seebeck measurements.¹⁰ Furthermore, detailed and clear structural evidence for the bridging binding motif has not been obtained, despite intense research efforts. A factor confounding interpretation of prior results is the use of solution-phase techniques for the infiltration of TCNQ into the host framework, during which solvent molecules and TCNQ compete for free Cu(II) coordination sites. This likely impedes long-range ordering of TCNQ molecules in the framework and disrupts diffusion pathways for the guest molecule. Moreover, TCNQ is easily reduced (redox potential of +0.2 V vs. Ag/AgCl),^{14,15} and in turn can react with the organic solvent and/or water molecules, preventing full control of the oxidation state of TCNQ molecules adsorbed in the Cu_3BTC_2 framework. In other words, the material obtained *via* liquid phase infiltration lacks rigorous experimental evidence possibly needed for a profound understanding of the conductivity mechanism due to a wider parameter space of compositional and structural characteristics. Is there a single type of TCNQ guest or is there a range of guest species including neutral and charged and how relevant is a homogenous long range ordering vs. short range (nanodomains) or even random and disordered distribution of TCNQ? Is the material phase pure or are their impurities to be considered? What is the role of water and solvent coordinated to Cu centers that are not occupied by TCNQ and do traces of physisorbed water or other protic impurities (*e.g.* methanol, ethanol) influence the conductivity of the material? Pristine Cu_3BTC_2 samples (bulk as well as thin film) are known to exhibit significant amounts of Cu(I) defect sites. Do these sites play a role when the material is loaded with redox non-innocent guests such as TCNQ? This more complex scenario of questions prompted us to investigate preparative concepts for loading Cu_3BTC_2 with TCNQ.

Recently, D'Alessandro and co-workers applied a vacuum vapor-phase infiltration (VPI) for the incorporation of TCNQ into Cu_3BTC_2 .¹⁶ In their approach, however, infiltrated samples were subsequently washed with solvent to remove excess, uninfiltrated TCNQ. Furthermore, samples were treated under ambient conditions, compromising efforts to keep the host-guest system free from solvent and moisture. Our study builds on their important work, applying an optimized VPI method with rigorous exclusion of moisture and solvent contaminations. Following this new protocol, we obtain samples with precise stoichiometry, having the general formula $x\text{TCNQ}@Cu_3\text{BTC}_2$ ($0 \leq x \leq 1$), that are devoid of complicating factors associated with liquid-phase infiltration. The materials were characterized by powder X-ray diffraction (PXRD), infrared (IR) and X-ray photoelectron spectroscopy (XPS) and electrical conductivity measurements, with all measurements strictly conducted under inert conditions. Strikingly, we find evidence of long-range order for $\text{TCNQ}@Cu_3\text{BTC}_2$ samples with high-loadings. Despite the observation that minor amounts of Cu(TCNQ) form as byproduct on the surface of Cu_3BTC_2

crystals, we find a relatively high electrical conductivity of these samples. Moreover, by avoiding the use of solvent and careful sample handling, our VPI method yields high permanent porosity as well – more than five times higher than achieved previously using liquid-phase infiltration⁸ – demonstrating that high electrical conductivity and large pore volume in MOFs can be compatible.

Results and discussion

The physical mixture of activated, desolvated Cu_3BTC_2 and TCNQ (ground together in a mortar) was annealed under vacuum in a glass ampule and heated for 3 days at 180 °C to yield the host-guest complex. Using the VPI approach, we produced a series of samples of the general formula $x\text{TCNQ}@Cu_3\text{BTC}_2$ ($x = n(\text{TCNQ})/n(\text{Cu}_3\text{BTC}_2)$) with $x = 0.1, 0.2, \dots, 1.0$ with precisely defined guest loadings by varying the amount of TCNQ with respect to a fixed amount of Cu_3BTC_2 . Even though a loading of $x = 1.5$ would be necessary to saturate all open Cu sites, unreacted, crystalline TCNQ was observed by powder X-ray diffraction (PXRD) and scanning electron microscopy (SEM) for samples with $x > 1.0$. This is in accordance with the maximum loading capacity of two TCNQ per large pore (one TCNQ per formula unit Cu_3BTC_2 , $x = 1$) predicted by theory.⁸ The PXRD data of the loaded series of $x\text{TCNQ}@Cu_3\text{BTC}_2$ (Fig. 1) show that the overall crystal structure of Cu_3BTC_2 is retained upon TCNQ infiltration. The largest change observed is in the intensity of the (111) reflection at $2\theta = 5.82^\circ$, which increases monotonically with the loading amount of TCNQ (highlighted in Fig. 1). Additionally, new reflections appear at higher angles, of which only the weak reflection at 15.77° matches with the principal reflection of a potential byproduct,

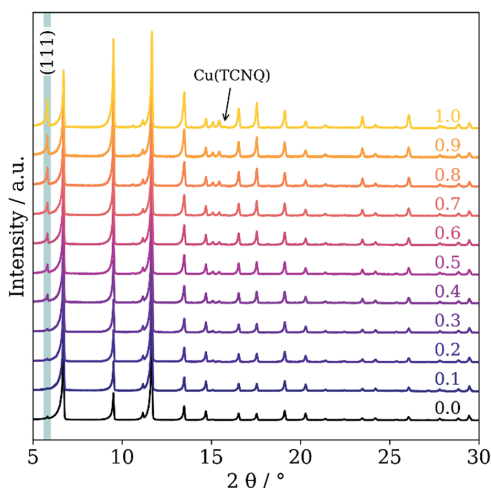


Fig. 1 PXRD patterns of pristine Cu_3BTC_2 (black) and the concentration series of TCNQ-loaded Cu_3BTC_2 . TCNQ loadings are given above each pattern as x in $x\text{TCNQ}@Cu_3\text{BTC}_2$. Traces of Cu(TCNQ) phase I can be found at high TCNQ loadings.

i.e. Cu(TCNQ) phase I (*cf.* Fig. S1†). The increase of the (111) reflection has previously been interpreted as an indicator for chemisorption of guests at the open Cu sites,¹⁷ and is here indicative of the incorporation of TCNQ into Cu₃BTC₂. Since the modified VPI method excludes any intensity changes due to solvent incorporation, this finding is consistent with the suggested bridging binding mode of TCNQ, as the Cu atoms of the paddlewheel nodes direct the planar TCNQ molecule into the (111) lattice plane (Fig. 2). Nevertheless, there will be disordered TCNQ inside of the pores considering that there are two types of large pores in Cu₃BTC₂ and only one features open Cu sites pointing to the center of the pore, *i.e.* are available for coordination of TCNQ. Furthermore, we observed weak reflections with increasing x in x TCNQ@Cu₃BTC₂ that are not in agreement with the parent face-centered cubic cell of Cu₃BTC₂, *e.g.* at 10.65°, 15.44° and 18.20°. However, they are consistent with a primitive unit cell of parent Cu₃BTC₂ having similar lattice parameters, therefore pointing to decreased lattice symmetry for the infiltrated MOF. For example, a Pawley profile fit with reduced symmetry ($Pn3m$) and maintaining the same lattice parameters as the parent Cu₃BTC₂ can account for all additional reflections (Fig. S4†). A doubling of the unit cell parameters while keeping the face-centered symmetry could similarly lead to a good profile fit, which might be in better chemical agreement, reflecting the different pores with and without available Cu sites. Determining the origin of these reflections requires additional structural analysis that is complex and extends significantly beyond the scope of the present report. However, this finding is intriguing, pointing to an ordering phenomenon related to TCNQ molecules and a subsequent symmetry reduction of the host-guest system that has not been previously observed. Based on the PXRD measurement, we therefore conclude that our modified VPI method leads to incorporation of TCNQ into Cu₃BTC₂ with the potential formation of a supercell.

In order to probe the porosity as function of x in x TCNQ@Cu₃BTC₂, we performed nitrogen adsorption experiments. As expected, a decrease of the Brunauer–Emmett–Teller (BET) surface area is observed, from 1833.0 m² g⁻¹ for pristine Cu₃BTC₂ to 573.7 m² g⁻¹ for 1.0TCNQ@Cu₃BTC₂ (Fig. 3), about

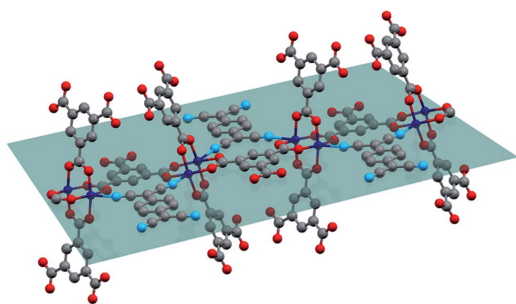


Fig. 2 Schematic representation of TCNQ binding to the apical position of two neighbouring Cu paddlewheels directing the planar molecule into the (111) lattice plane (tile). For better visualization, the cubic symmetry is not applied. Cu, C, O, and N atoms are depicted in blue, grey, red, and light blue, respectively.

two thirds of the initial BET surface area. In addition, the decrease is linear with TCNQ loading, providing additional evidence for the incorporation of the guest molecule into the framework. Importantly, the decrease cannot be explained by pore blocking or a simple adsorption of TCNQ at the crystal surface. For instance, the BET surface area of a physical mixture of both components for 1.0TCNQ@Cu₃BTC₂ would still amount to 1370.4 m² g⁻¹ (see detailed discussion in ESI†). It is further important to note that our measured surface areas considerably exceed those for TCNQ-loaded Cu₃BTC₂ samples reported in the literature. For example, the VPI 0.5TCNQ@Cu₃BTC₂ sample exhibits a surface area of 1145 m² g⁻¹, whereas the surface area of the material with the same loading synthesized *via* liquid phase infiltration is reported as 214 m² g⁻¹, which is likely due to residual adsorbed water or solvent.⁸

The microstructure and phase homogeneity of the TCNQ-loaded samples was further investigated using SEM (Fig. 4). Nanowire-like structures were discovered on the external surface of the TCNQ-loaded MOF crystallites; the amount and dimensions of these increase with the amount of TCNQ employed during the VPI. To determine the chemical nature of the nanowires, scanning Auger electron microscopy was performed. These data show a homogenous distribution of Cu, C, and N (Fig. S13†). In combination with the characteristic morphology¹⁸ and the reflection at 15.77° in the diffraction pattern, the nanowires were identified as phase I of Cu(TCNQ). For the formation of Cu(TCNQ) to occur, both TCNQ and Cu(II) must be reduced to TCNQ⁻ and Cu(I), presumably involving an oxidation (decarboxylation) of the BTC linker under the conditions of the loading experiment. In the elemental analysis data of the concentration series (Table S2†), slightly decreased carbon contents compared to the calculated values are found, whereas the nitrogen contents are slightly increased, supporting a decomposition of some BTC molecules. Moreover,

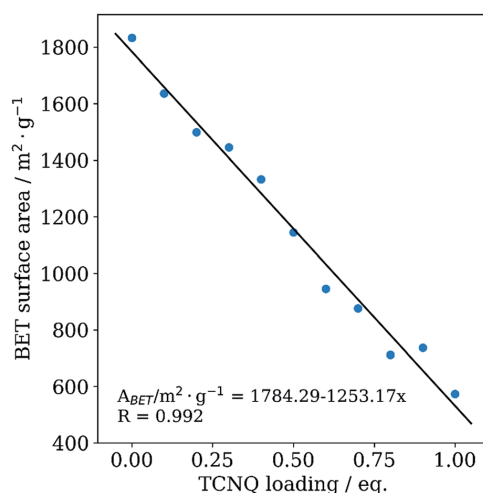


Fig. 3 BET surface area of Cu₃BTC₂ samples plotted against the TCNQ loading amount. Values of the linear fit are shown in the diagram.

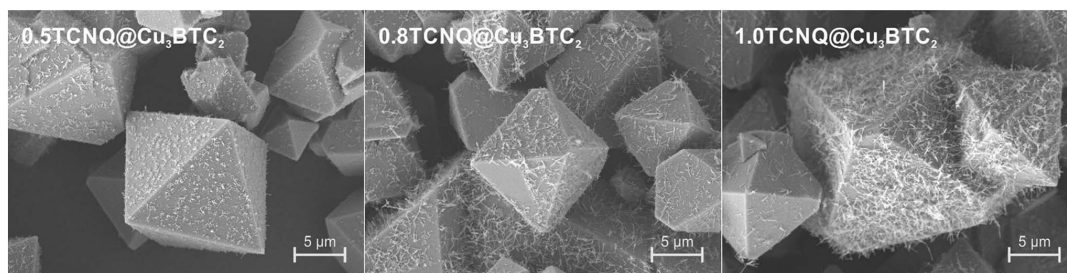


Fig. 4 SEM images of Cu_3BTC_2 loaded with 0.5 (left), 0.8 (middle), and 1.0 (right) equivalents of TCNQ. $\text{Cu}(\text{TCNQ})$ nanowires form on the surface of the octahedral Cu_3BTC_2 crystallites and their amount and dimensions increase with higher loading.

Cu_3BTC_2 is known to contain small quantities of $\text{Cu}(\text{i})$ species, which have been related to intrinsic defects and thermal treatment during activation.^{19,20} Surface sensitive XPS measurements (Fig. S19†) reveal a relatively high abundance of $\text{Cu}(\text{i})$ species at the surface of Cu_3BTC_2 crystallites. This $\text{Cu}(\text{i})$ concentration is further increased by the inevitable prolonged thermal treatment during the VPI process. The $\text{Cu}(\text{i})$ species, in turn, are able to reduce neutral TCNQ (*via* $\text{Cu}(\text{i}) \rightarrow \text{Cu}(\text{ii}) + \text{e}^-$) and thus enable the formation of the surface impurity phase $\text{Cu}(\text{TCNQ})$. The presence of several TCNQ species (*i.e.* coordinated, uncoordinated, radical anion) is suggested by the broadening of the N 1s signature in XPS (Fig. S20†). The formation of the $\text{Cu}(\text{TCNQ})$ byproduct could be reduced, but not fully inhibited, by using lower reaction temperatures (Fig. S15–S17†). However, reduced temperature also compromise the ordering of TCNQ, as evidenced by the absence of the pronounced (111) reflection in PXRD (Fig. S2†).

The loading and coordination of TCNQ to open Cu sites can also be tracked by vibrational spectroscopy. The infrared (IR) spectra of pristine and TCNQ-loaded Cu_3BTC_2 are shown in Fig. 5. Whereas in pristine Cu_3BTC_2 a band in the CN vibration region is absent, a CN vibration mode at 2222 cm^{-1} appears in TCNQ-loaded samples and becomes more pronounced with higher TCNQ loading. Notably, a second vibrational mode at 2200 cm^{-1} and a shoulder at 2170 cm^{-1} appear for samples with high TCNQ loading (*cf.* Fig. S6†). A red shift of the CN vibration was previously attributed to coordinated TCNQ involving a partial charge transfer.^{8,21} Due to the presence of the $\text{Cu}(\text{TCNQ})$ byproduct in the samples, we here also assign some contribution to the signal at 2000 cm^{-1} and the shoulder at 2170 cm^{-1} to $\text{Cu}(\text{TCNQ})$, whose IR signature is known from the literature.²² The indication of multiple TCNQ species in the IR spectra matches well with the XPS signature in the N 1s regime.

Thermogravimetric analysis (TGA) of $1.0\text{TCNQ}@Cu_3\text{BTC}_2$ (Fig. S7†) shows a decomposition that proceeds in one step with an onset at $300 \text{ }^\circ\text{C}$. This temperature is slightly lower than observed for pristine Cu_3BTC_2 , which starts to decompose at $330 \text{ }^\circ\text{C}$. The corresponding features in the differential scanning calorimetry (DSC) data are at $349.7 \text{ }^\circ\text{C}$ and $338.3 \text{ }^\circ\text{C}$ for the pristine and the loaded MOF, respectively. The $1.0\text{TCNQ}@Cu_3\text{BTC}_2$ sample shows an additional smaller peak at $314.2 \text{ }^\circ\text{C}$, indicating a step-wise decomposition.

Electrical transport measurements were performed on pressed pellets using an air-tight two-point-probe setup. I - V curves were recorded from -5 V to 5 V (Fig. S9†) and the conductivity σ was calculated using eqn (1):

$$\sigma = \frac{I d}{V A} \quad (1)$$

in which I , V , d and A are the measured electrical current, the applied voltage, the thickness of the pellet and the area of the pellet, respectively. The calculated room-temperature conductivities are plotted against the TCNQ loading (Fig. 6). We observe an exponential increase of the electrical conductivity upon TCNQ loading, starting from immeasurably small values for pristine Cu_3BTC_2 to $1.5 \times 10^{-4} \text{ S cm}^{-1}$ for $1.0\text{TCNQ}@Cu_3\text{BTC}_2$. This value is lower than the electrical conductivity reported for thin film samples infiltrated *via* the liquid phase (0.07 S cm^{-1}),⁸ pointing at additional influence of grain boundaries and particle sizes as well as at the different measurement techniques used (pressed powder *vs.* thin film).²³

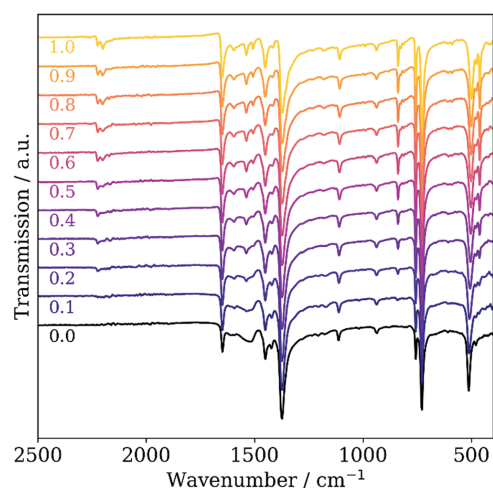


Fig. 5 IR spectra of pristine Cu_3BTC_2 (black) and the concentration series of TCNQ-loaded Cu_3BTC_2 . TCNQ loadings are given below each spectrum as x in $x\text{TCNQ}@Cu_3\text{BTC}_2$.

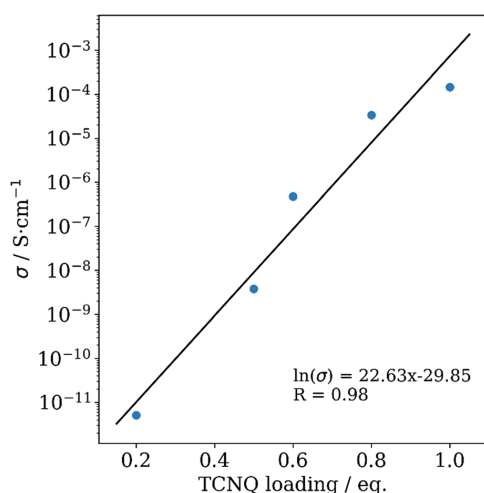


Fig. 6 Electrical conductivity of TCNQ@Cu₃BTC₂ samples plotted against their TCNQ loading amount.

The observed exponential increase of the electrical conductivity can be described by classical percolation theory.^{24,25} At low TCNQ loadings only few of the copper paddlewheel units are bridged by TCNQ and form localized conducting regions. With increasing TCNQ loading these bridged domains become interconnected and give rise to charge transport through the framework. Given the fact that TCNQ@Cu₃BTC₂ samples in the literature showed high conductivities but no pronounced (111) reflection,^{8–10} disordered TCNQ might also contribute to the charge transport through the material.

The impact of the Cu(TCNQ) byproduct on the electrical transport, however, is intrinsically difficult to assess because Cu(TCNQ) can crystallize in two different phases. Phase II is a poor conductor, whereas phase I is an electrical semiconductor with a room temperature conductivity of 0.25 S cm⁻¹.¹⁸ Mechanical removal of the nanowires by sonication was unsuccessful and led to a disordering of the TCNQ molecules and a significant decrease in the conductivity (Fig. S3, S11 and S18†). A physical mixture of 1% Cu(TCNQ)/Cu₃BTC₂ (estimated amount from SEM images) did not show any conductivity. In combination with previous findings in the literature for TCNQ@HKUST-1 in which Cu(TCNQ) as an impurity phase was not observed, we ascribe the increasing electrical conductivity as function of TCNQ loading to the formation of our host-guest system. Moreover, 1.0TCNQ@Cu₃BTC₂ exhibits one of the highest-reported electrical conductivities paired with permanent porosity reported to date, comparing with other conductive MOFs of similar porosities, such as Cd₂(TTFB).^{6,26} The synthesis of a reference sample of *x*TCNQ@Cu₃BTC₂ (*x* = 0.4 as determined by EA) *via* liquid phase infiltration revealed no indication of TCNQ ordering, but a conductivity in the order of 10⁻¹ S cm⁻¹, which is significantly higher than for samples with comparable TCNQ loading prepared *via* VPI. However, this sample shows a non-

ohmic behavior (deviation from the linear *I*-*V* curve) at high potentials that we assign to electrochemical processes of water/solvent inside the pores (Fig. S21–S24†). This finding emphasizes the importance of solvent exclusion during the guest infiltration step and highlights the need for in-depth structural and spectroscopic studies of Guest@MOF systems to develop and validate structure–property relationships.

Conclusions

We developed an optimized VPI strategy under thermodynamic control and used it to introduce stoichiometric amounts of TCNQ to obtain a concentration series of *x*TCNQ@Cu₃BTC₂ with 0 ≤ *x* ≤ 1.0 under strict inert conditions. No washing step is needed to remove excessive TCNQ, which is advantageous over the kinetically controlled loading procedure presented in previous studies.^{8–10,16} High reaction temperatures and long exposure times evidently promote an ordered, periodic arrangement of TCNQ within the (111) crystal lattice plane and the bridging coordination motif of TCNQ and the Cu atoms of two neighbouring paddle-wheel units. To our knowledge this is the first crystallographic evidence for the integration of TCNQ into the framework of Cu₃BTC₂, and further demonstrates that the introduction of a non-innocent guest molecule can be regarded as a new element of MOF property design. Additional evidence supporting the accommodation of TCNQ within the pores of the framework is the systematic decrease in the BET surface area. SEM images of the infiltrated samples show the formation of nanowires on the MOF crystal surface during VPI that were identified as Cu(TCNQ). Their formation can be reduced but not entirely suppressed at lower temperatures. IR data recorded during this work shows two nitrile vibration modes that can be attributed to TCNQ molecules inside the Cu₃BTC₂ framework and to the TCNQ anion in Cu(TCNQ). The electrical conductivity of the concentration series increases exponentially with the amount of TCNQ used in the VPI. Even though, a quantitative analysis of the contribution of the host-guest complex and the Cu(TCNQ) byproduct to the electrical conductivity of the material is difficult, the obtained material shows high conductivity values accompanied by high permanent porosity. In fact, the BET surface area of 1.0TCNQ@Cu₃BTC₂ is among the highest for electrically conductive MOFs.^{6,26} The combination of these two properties creates a high potential for using this material in sensing or electronic device fabrication where access to the pores provides an essential new function. In this respect, well defined, oriented Cu₃BTC₂ thin films deposited and infiltrated with TCNQ using solvent-free vapor phase techniques represent the ultimate goal. Pointing to the complexity of this system, further detailed analysis is required, beyond standard characterization techniques, to fully understand the ordering of TCNQ and the conductivity mechanism.

Experimental

General information

All chemicals were purchased from commercial suppliers (ABCR, Acros Organics, Alfa Aesar, Sigma Aldrich) and used

without further purification unless otherwise stated. Solvents used for the synthesis and washing steps were reagent grade or higher.

Vapor phase infiltration

Cu_3BTC_2 was synthesized following the literature procedure.²⁷ The tile crystalline product was continuously washed with ethanol and dichloromethane in a Soxhlet apparatus for one week, respectively, to rigorously remove all reactants and high-boiling solvents. The washing solution was replaced by the respective fresh solvent once. Subsequently, the blue powder was desolvated under high vacuum ($\sim 10^{-6}$ mbar) at 180 °C to yield pristine Cu_3BTC_2 . TCNQ was recrystallized three times from acetonitrile under inert conditions to yield molecular, crystalline TCNQ in high purity.

Inside an argon glovebox, 200 mg of Cu_3BTC_2 and distinct amounts of TCNQ were physically mixed and filled into borosilicate glass tubes to prepare a concentration series of $x\text{TCNQ}@Cu_3\text{BTC}_2$ ($x = n(\text{TCNQ})/n(\text{Cu}_3\text{BTC}_2)$) with $x = 0.1, 0.2, \dots, 1.0$). The glass tube was then evacuated ($\sim 10^{-3}$ mbar) and flame sealed to give a closed system for the VPI process. The sealed ampules were placed inside a convection oven at 180 °C for 72 hours allowing the TCNQ to sublime and diffuse into the MOF. After cooling down to room temperature the ampules were transferred into the glovebox and stored for further characterization.

Powder X-ray diffraction

Powder X-ray diffraction (PXRD) data was collected in a 2θ range of 5–50° in steps of 0.0016413° (2θ) on a PANalytical Empyrean equipped with a Cu X-ray tube operated at 45 kV and 40 mA. The samples were filled into borosilicate capillaries of 0.7 mm diameter and mounted onto a capillary spinner. The radiation was focused onto the sample through a focusing X-ray beam mirror equipped with a 1/8° divergence slit and 0.02 radian soller slits. The diffracted beam was detected by a PIXcel1D detector in receiving slit mode equipped with a 1/8° anti-scatter slit and 0.02 radian soller slits.

Thermogravimetric analysis/differential scanning calorimetry

TGA/DSC measurements were carried out on a Mettler Toledo TGA/DSC 1 equipped with an auto sampler unit. Aluminum crucibles (100 μL) were filled with 5–10 mg of MOF powder inside the glovebox and tightly capped with an aluminum lid. The crucible was transferred into the TGA chamber and a hole was pinched into the lid while the stream of Ar (40 mL min^{-1}) was already on. The temperature was ramped from 30 °C to 550 °C at a rate of 5 °C min^{-1} . The instrument was calibrated to a blank sample prior to the measurements.

Porosimetry measurements

Porosimetry measurements of pristine and guest-loaded MOF powders were performed using a Micromeritics 3flex to determine their BET surface area. Therefore, approximately 60 mg of a sample was filled into a BET tube and evacuated for 3 h at room

temperature prior to the measurement. Nitrogen isotherms were recorded at 77 K. The BET surface area was calculated from data points in the relative pressure range of 0.01 to 0.1.

Fourier transform infrared spectroscopy

Fourier transform infrared spectroscopy (FTIR) of powder samples was done in argon atmosphere on an ALPHA FTIR spectrometer (Bruker) equipped with a Pt attenuated total reflectance (ATR) unit at room temperature in the range of 400–4000 cm^{-1} with a resolution of 2 cm^{-1} . 64 scans were recorded per measurement.

Elemental analysis

Elemental analysis (EA) for the elements C, H, N, and S was carried out on a Hekatech EuroEA Elementaranalysator. Cu contents were determined by atom absorption spectroscopy (AAS) after decomposing the sample in a mixture of sulfuric acid and nitric acid in a CEM microwave.

Scanning electron microscopy

Top-view micrographs of MOF powders were conducted on a Merlin high-resolution scanning electron microscope (Carl Zeiss) using an acceleration voltage of 5 kV. The samples were transferred from a glove box into the analysis chamber under argon atmosphere using a transfer vessel (Leica EM VC500). To avoid charging, the sample was coated with 5 nm of Pt prior to the measurement using a Leica EM ACE600. Energy dispersive X-ray spectroscopy (EDX) analysis was conducted using an XMAX EXTREME EDX detector (Oxford Instruments). Measurements were carried out by application of an acceleration voltage of 5 kV and a probing current of 100 pA for SEM and 1000 pA for EDX.

Auger electron spectroscopy

AES measurements were performed at room temperature with a scanning Auger electron spectroscope (JEOL Ltd. JAMP-9500F field emission scanning Auger microprobe) system. Samples were prepared by spreading powder particles over a gold-coated surface. AES spectra were acquired with a primary beam of 10 keV. The take-off angle of the instrument was 0°. The differential energy spectrum was used to subtract background from the direct Auger spectrum for calculating the band-to-band intensity. The first differential $d(N(E))/d(E)$ Auger spectra were obtained by numerical derivation of the direct $N(E)$ integrated Auger data displaying an absolute scale with counts/second units by a universal Savitzky–Golay (SG) quadratic differential filter using seven points and used to calculate the band-to-band intensity of Auger electrons and derive the elemental compositions. The differential spectrum is simply the differential of the direct spectrum with respect to energy. The spectra were calibrated with the carbon band at 263.0 eV. For Auger elemental analysis an 8 nm probe diameter was used. Elemental mapping was analysed by AES. Elemental images were acquired with a primary beam of 10 keV. The take-off angle of the instrument was 0°. The coloured images are elemental

distribution maps over the area shown in the upper right image (magnification 80 000 \times).

X-ray photoelectron spectroscopy

XPS was carried out using a PHI5000 Versa Probe II (Physical Electronics GmbH) with an Al anode. To avoid air exposure, powder samples were transferred from an argon-filled glovebox to the analysis chamber using a transfer vessel filled with argon gas. The probed surface area was 100 $\mu\text{m} \times 1400 \mu\text{m}$ (*i.e.*, X-ray spot size) and an X-ray power of 100 W was used. The pass energy of the analyzer was set to 23.5 eV for detail spectra and to 187.9 eV for survey scans. The chamber pressure was in the range of 10^{-7} Pa during the measurements. All spectra were charge corrected to a binding energy of 284.8 eV for the C 1s line corresponding to adventitious aliphatic carbon. Measurements were evaluated using CasaXPS V2.3.17 software.

Electrical conductivity measurements

Inside an Ar filled glovebox, MOF powders (~ 70 mg) were filled into an air-tight press cell and compressed uniaxially at 3 t (375 MPa) for 2 minutes. The press cell was mounted into an aluminium frame and fixed with a screw applying a torque of 10 Nm (*cf.* ESI Fig. 8 \dagger).²⁸ *I-V* curves were recorded between the two stainless steel electrodes of the press cell using an EC-Lab Electrochemistry SP-300 potentiostat/galvanostat (Bio-Logic Science Instruments). Conductivity measurements were carried out at 298 K (climate chamber, Weiss Klimatechnik, 1 h equilibration time) sweeping the voltage between 5 V and -5 V at a scan rate of 100 mV s $^{-1}$.

Conflicts of interest

There are no conflicts to declare.

Acknowledgements

We thank Dr Vitalie Stavila and Dr Andrew Ullman for helpful discussions and Pia Vervoorts for help with BET measurements. Funding for this project was provided by the Sandia Laboratory Directed Research and Development (LDRD) Program. Sandia National Laboratories is a multimission laboratory managed and operated by National Technology and Engineering Solutions of Sandia, LLC, a wholly owned subsidiary of Honeywell International, Inc., for the U.S. Department of Energy's National Nuclear Security Administration under contract DE-NA-0003525. CS acknowledges his scholarships from the German Academic Scholarship Foundation and from the German Chemical Industry Fund (FCI). RK acknowledges his scholarship from the FCI. This project was further supported by a PPP travel grant from the German Academic Exchange Service (DAAD).

Notes and references

- 1 I. Stassen, N. Burtch, A. Talin, P. Falcaro, M. Allendorf and R. Ameloot, *Chem. Soc. Rev.*, 2017, **46**, 3185–3241.
- 2 V. Stavila, A. A. Talin and M. D. Allendorf, *Chem. Soc. Rev.*, 2014, **43**, 5994–6010.
- 3 G. Maurin, C. Serre, A. Cooper and G. Ferey, *Chem. Soc. Rev.*, 2017, **46**, 3104–3107.
- 4 O. M. Yaghi, M. O'Keeffe, N. W. Ockwig, H. K. Chae, M. Eddaoudi and J. Kim, *Nature*, 2003, **423**, 705–714.
- 5 M. Eddaoudi, J. Kim, N. Rosi, D. Vodak, J. Wachter, M. O'Keeffe and O. M. Yaghi, *Science*, 2002, **295**, 469–472.
- 6 L. Sun, M. G. Campbell and M. Dincă, *Angew. Chem., Int. Ed.*, 2016, **55**, 3566–3579.
- 7 L. Sun, C. H. Hendon, S. S. Park, Y. Tulchinsky, R. Wan, F. Wang, A. Walsh and M. Dincă, *Chem. Sci.*, 2017, **8**, 4450–4457.
- 8 A. A. Talin, A. Centrone, A. C. Ford, M. E. Foster, V. Stavila, P. Haney, R. A. Kinney, V. Szalai, F. El Gabaly, H. P. Yoon, F. Léonard and M. D. Allendorf, *Science*, 2014, **343**, 66–69.
- 9 X. Chen, Z. Wang, Z. M. Hassan, P. Lin, K. Zhang, H. Baumgart and E. Redel, *ECS J. Solid State Sci. Technol.*, 2017, **6**, 150–153.
- 10 T. Neumann, J. Liu, T. Wächter, P. Friederich, F. Symalla, A. Welle, V. Mugnaini, V. Meded, M. Zharnikov, C. Wöll and W. Wenzel, *ACS Nano*, 2016, **10**, 7085–7093.
- 11 C. H. Hendon and A. Walsh, *Chem. Sci.*, 2015, **6**, 3674–3683.
- 12 K. J. Erickson, F. Léonard, V. Stavila, M. E. Foster, C. D. Spataru, R. E. Jones, B. M. Foley, P. E. Hopkins, M. D. Allendorf and A. A. Talin, *Adv. Mater.*, 2015, **27**, 3453–3459.
- 13 M. D. Allendorf, M. E. Foster, F. Léonard, V. Stavila, P. L. Feng, F. P. Doty, K. Leong, E. Y. Ma, S. R. Johnston and A. A. Talin, *J. Phys. Chem. Lett.*, 2015, **6**, 1182–1195.
- 14 W. Kaim and M. Moscherosch, *Coord. Chem. Rev.*, 1994, **129**, 157–193.
- 15 M. E. Peover, *J. Chem. Soc., Faraday Trans.*, 1964, **60**, 479–483.
- 16 P. M. Usov, H. Jiang, H. Chevreau, V. K. Peterson, C. F. Leong and D. M. D'Alessandro, *J. Phys. Chem. C*, 2017, **121**, 26330–26339.
- 17 K. Schlichte, T. Kratzke and S. Kaskel, *Microporous Mesoporous Mater.*, 2004, **73**, 81–88.
- 18 R. A. Heintz, H. Zhao, X. Ouyang, G. Grandinetti, J. Cowen and K. R. Dunbar, *Inorg. Chem.*, 1999, **38**, 144–156.
- 19 N. Nijem, H. Bluhm, M. L. Ng, M. Kunz, S. R. Leone and M. K. Gilles, *Chem. Commun.*, 2014, **50**, 10144–10147.
- 20 J. Szanyi, M. Daturi, G. Clet, D. R. Baer and C. H. F. Peden, *Phys. Chem. Chem. Phys.*, 2012, **14**, 4383–4390.
- 21 J. S. Chappell, A. N. Bloch, W. A. Bryden, M. Maxfield, T. O. Poehler and D. O. Cowan, *J. Am. Chem. Soc.*, 1981, **103**, 2442–2443.
- 22 M. Inoue and M. B. Inoue, *J. Chem. Soc., Faraday Trans. 2*, 1985, **81**, 539–547.
- 23 L. Sun, S. S. Park, D. Sheberla and M. Dincă, *J. Am. Chem. Soc.*, 2016, **138**, 14772–14782.
- 24 B. Abeles, H. L. Pinch and J. I. Gittleman, *Phys. Rev. Lett.*, 1975, **35**, 247–250.
- 25 B. J. Last and D. J. Thouless, *Phys. Rev. Lett.*, 1971, **27**, 1719–1721.

- 26 M. L. Aubrey, B. M. Wiers, S. C. Andrews, T. Sakurai, S. E. Reyes-Lillo, S. M. Hamed, C.-J. Yu, L. E. Darago, J. A. Mason, J.-O. Baeg, F. Grandjean, G. J. Long, S. Seki, J. B. Neaton, P. Yang and J. R. Long, *Nat. Mater.*, 2018, **17**, 625–632.
- 27 M. K. Bhunia, J. T. Hughes, J. C. Fettinger and A. Navrotsky, *Langmuir*, 2013, **29**, 8140–8145.
- 28 W. Zhang, D. A. Weber, H. Weigand, T. Arlt, I. Manke, D. Schröder, R. Koerver, T. Leichtweiss, P. Hartmann, W. G. Zeier and J. Janek, *ACS Appl. Mater. Interfaces*, 2017, **9**, 17835–17845.

3.3 Study III: Scrutinizing the Pore Chemistry and the Importance of Cu(I) Defects in TCNQ-Loaded Cu_3BTC_2 by a Multitechnique Spectroscopic Approach

The new synthetic approach described in Study II has contributed to a better understanding of the structure-property relationships in $\text{TCNQ}@Cu_3\text{BTC}_2$. Even though, this allowed answering many questions, *e.g.* regarding the arrangement of TCNQ within the pores, a series of new questions arose due to the observed redox chemistry during the vapor phase infiltration. XPS measurements (see supporting information to Study II, chapter 6.2) point at Cu(I) surface defects to be the reducing agent for TCNQ to form Cu(TCNQ) nano-wires on the surface of the MOF crystals. However, as a surface-sensitive technique, XPS does not probe the inside of the porous material. A powerful technique that allows to study the pore chemistry, *i.e.* available coordination sites, oxidation states and the pore environment, is IR spectroscopy of adsorbed CO as a probe molecule. Supported by electron paramagnetic resonance (EPR) spectroscopy, this study provided three major findings, namely (i) the number of available Cu(II) OMS decreases monotonically with the TCNQ loading amount substantiating the coordination of TCNQ; (ii) framework Cu(I) defects in pristine Cu_3BTC_2 disappear quantitatively upon infiltration of small amounts of TCNQ and give rise to TCNQ radical anions. Notably the amount of TCNQ radical anions correlates quantitatively with Cu(I)-Cu(II) defect paddlewheels in the pristine MOF; and (iii) while the pore environment of pristine and fully TCNQ-loaded Cu_3BTC_2 is relatively well defined, intermediate loadings show a complex set of signals suggesting the co-existence of pores with 0, 1 or 2 TCNQ molecules. Interestingly, Cu_3BTC_2 loaded with TCNQ following the literature procedure (solution impregnation using DCM),¹⁰¹ unveiled the same redox chemistry between Cu(I) defects and TCNQ. In addition, TCNQ was more locally concentrated (less homogeneously distributed), underlining the potential of the vapor phase infiltration method. In conclusion, the combined spectroscopic approach helped to understand the redox chemistry during the infiltration process and sheds light on the pore chemistry of $\text{TCNQ}@Cu_3\text{BTC}_2$, serving as a model for the study of other host-guest materials.

The manuscript was written by the author of this thesis and edited by the five co-authors, who contributed critically to the discussion of the results. The strategy and experiments were developed by the author and coordinated with V. Crocellà and R. A. Fischer. The synthesis and standard characterization were done by the author of this thesis and CO probe IR measurements were performed together with V. Crocellà. M. Mendt and A. Pöpl performed and evaluated EPR measurements.

C. Schneider, M. Mendt, A. Pöpl, R. A. Fischer, V. Crocellà, Scrutinizing the Pore Chemistry and the Importance of Cu(I) Defects in TCNQ-Loaded Cu_3BTC_2 by a Multitechnique Spectroscopic Approach. *ACS Appl. Mater. Interfaces*, **2020**, *12*, 1024-1035.

Scrutinizing the Pore Chemistry and the Importance of Cu(I) Defects in TCNQ-Loaded $\text{Cu}_3(\text{BTC})_2$ by a Multitechnique Spectroscopic Approach

Christian Schneider,[†] Matthias Mendt,[‡] Andreas Pöpl,[‡] Valentina Crocellà,^{*,§} and Roland A. Fischer^{*,†}

[†]Department of Chemistry, Technical University of Munich, Lichtenbergstrasse 4, D-85748 Garching, Germany

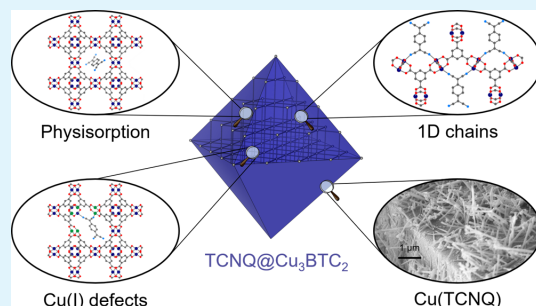
[‡]Felix Bloch Institute for Solid State Physics, University Leipzig, Linnéstrasse 5, D-04103 Leipzig, Germany

[§]Department of Chemistry, NIS and INSTM Reference Centre, Università di Torino, Via G. Quarello 15, I-10135 and Via P. Giuria 7, I-10125 Torino, Italy

Supporting Information

ABSTRACT: Host–guest interactions control the fundamental processes in porous materials for many applications such as gas storage and catalysis. The study of these processes, however, is not trivial, even if the material is crystalline. In particular, metal–organic frameworks (MOFs) represent a complex situation since guest molecules can interact with different parts of the organic linkers and the metal clusters and may alter the details of the pore structure and system properties. A prominent example is the so-called retrofitted MOF material $\text{TCNQ}@Cu_3(\text{BTC})_2$ that has attracted a lot of attention due to its electronic properties induced by the host–guest interactions. Only recently, structural evidence has been presented for a bridging binding mode of TCNQ to two Cu paddlewheel units; however, many issues regarding the redox chemistry of $\text{Cu}_3(\text{BTC})_2$ and TCNQ are currently unsolved. Herein, we report a powerful spectroscopic approach to study the host–guest chemistry of this material. Combining IR spectroscopy in the presence of CO and EPR spectroscopy, we found that the intrinsic Cu(I) defects of the host react with the guest, forming TCNQ radical anions. This chemistry has profound implications, in particular, with respect to the performance of $\text{TCNQ}@Cu_3(\text{BTC})_2$ as an electronic conductor. A decreasing availability of open Cu(II) sites with increasing TCNQ loading proves the coordinative binding of TCNQ to the paddlewheel nodes, and a heterogeneous structure is formed with different TCNQ arrangements and pore environments at low TCNQ loadings. Finally, the combined use of spectroscopic characterization techniques has proven to be, in general, a powerful approach for studying the complex chemistry of host–guest materials.

KEYWORDS: metal–organic frameworks, redox-active guests, defect chemistry, CO probe IR spectroscopy, EPR spectroscopy



INTRODUCTION

Porous materials play an important role in fundamental research and large-scale industry applications. From activated carbon in exhaust hoods to zeolites for catalytic cracking of hydrocarbons, all materials share high surface areas and pore volumes that allow guest molecules to diffuse and adsorb.¹ A newer class of porous materials named metal–organic frameworks (MOFs) has attracted tremendous attention for use in applications like gas storage, separation, and catalysis.^{2,3} Particularly, MOFs with coordinatively unsaturated metal sites, the so-called open metal sites (OMSs), bear great potential compared to their closed coordination-shell analogues as they typically feature high heats of adsorption and intrinsic reactive centers for catalysis.^{4–6} Moreover, the OMSs can serve as an anchoring point for other species that are introduced into the

MOF postsynthetically, for example, for medical applications.⁷ Recently, retrofitting was introduced as a concept, in which metal nodes with OMSs or labile monotopic ligands are bridged by additional linkers to fine-tune physicochemical properties.^{8,9} In all cases, the OMS of the MOF is involved in an interaction with the guest molecule, whose nature is typically difficult to assess. Crystallographic characterization, for example, requires a uniform distribution of the guest molecule with long-range order throughout the crystal lattice. In many cases, however, the guest occupies only a portion of the available coordination sites and thus characterizes rather as

Received: September 15, 2019

Accepted: December 6, 2019

Published: December 6, 2019

a defect to the parent structure that cannot be determined by standard single-crystal X-ray diffraction experiments. Even at high occupancies, structure determination can be challenging due to the small sizes of the crystallites. In some cases, it is possible to track the presence of guests by powder X-ray diffraction (PXRD).^{9,10} For example, $\text{Cu}_3(\text{BTC})_2$ (HKUST-1, BTC = 1,3,5-benzenetricarboxylate), which is constructed from dimeric Cu(II) paddlewheel units and tritopic BTC linkers, exposes OMSs at the Cu centers after removal of solvents through thermal treatment.^{11,12} As the Cu centers are all located in the crystallographic (111) plane, the intensity of the corresponding Bragg reflection is sensitive to adsorption of guests¹⁰ and was used to prove the bidentate binding of TCNQ (7,7,8,8-tetracyanoquinodimethane) to two neighboring Cu paddlewheels (see Figure 1a).¹³ This particular host-guest material, $\text{TCNQ}@Cu_3(\text{BTC})_2$, arose significant interest in the MOF community in the context of electrical conductivity, including various experimental and computa-

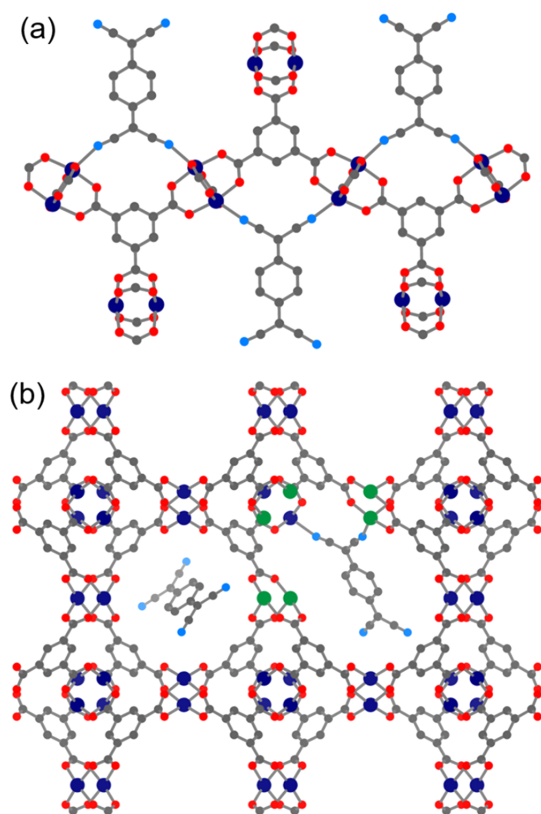


Figure 1. Pore chemistry in TCNQ-loaded $\text{Cu}_3(\text{BTC})_2$. (a) In the idealized picture, all Cu paddlewheels are bridged by TCNQ to form one-dimensional arrays along the (111) crystal lattice. (b) For a realistic description of the arrangement of TCNQ as well as noncoordinated TCNQ (left) and TCNQ in interaction with intrinsic framework defects such as missing linker defects (right) must be considered. Color code: C, gray; O, red; N, blue; Cu, dark blue or green. In particular, Cu(II)–Cu(II) and Cu(II)–Cu(I) paddlewheels are depicted in blue and green, respectively. H atoms are omitted for clarity.

tional studies aiming at elucidating the conductivity mechanism.^{14–17} However, without a profound understanding of the host-guest chemistry of the material, accurate structure-property relationships cannot be derived. In a previous study, we found that the TCNQ loading by infiltration using methanol as the solvent results in a transformation of $\text{Cu}_3(\text{BTC})_2$ to yield $\text{Cu}(\text{TCNQ})$.¹⁸ Motivated to exclude any external influences like solvent and moisture, some of us developed a vacuum loading that allows vapor-phase transport of precise molar quantities of TCNQ for adsorption into the framework. Despite the formation of a small amount of the $\text{Cu}(\text{TCNQ})$ byproduct on the surface of the MOF crystallites, this approach allows a thorough investigation of the host-guest structure.¹³ However, given the intrinsic complexity of the $\text{Cu}_3(\text{BTC})_2$ system involving framework defects such as Cu(II)–Cu(I) sites after thermal treatment (i.e., activation),^{19,20} interacting with a redox-active guest molecule (see Figure 1b), a comprehensive understanding of the obtained host-guest material in dependence of the synthesis conditions is still not available. For instance, some techniques only provide limited information; X-ray photon absorption (XPS) spectroscopy showed evidence of Cu(I) species¹³ but only probes the surface and not the bulk of the crystallites. Therefore, the use of different and more elaborate experimental techniques is necessary. One of these advanced tools is infrared (IR) spectroscopy of adsorbed probe molecules, which has shown great potential as a characterization technique,^{21,22} especially for MOFs containing OMSs such as $\text{Cu}_3(\text{BTC})_2$.^{23,24} Furthermore, electron paramagnetic resonance (EPR) spectroscopy has proven to give important insights about the nature and electronic structure of magnetic species in Cu-based MOFs.^{25–30} For example, the magnetic coupling and interactions of Cu(II)–Cu(II) paddlewheel units were characterized in detail by EPR for Cu containing MOFs.^{25,26} In addition, EPR was used to study monomeric Cu(II) defects in Cu paddlewheel-based MOFs,^{27–29} as well as the adsorption of nonmagnetic or radical species on Zn-doped and pristine $\text{Cu}_3(\text{BTC})_2$.^{31,32}

Herein, we aim to draw a clearer picture of the interactions between TCNQ and the host framework, the redox chemistry that is involved during the infiltration, and the pore chemistry of the resulting material. Therefore, we used IR spectroscopy by exploiting the power of carbon monoxide (CO) as a probe molecule to discriminate among framework Cu sites of a very similar nature. By monitoring the vibration frequencies of adsorbed CO, we were able to perform a qualitative and partially quantitative evaluation of the different Cu sites together with an assessment of the local pore environment around the metal centers. In addition, we performed continuous wave (cw) EPR spectroscopy to provide further insights into the presence of molecular radical anions of TCNQ and their correlation with different Cu(II) species, particularly with Cu(II)–Cu(I)-mixed valence paddlewheels.

EXPERIMENTAL SECTION

Synthesis. Pristine $\text{Cu}_3(\text{BTC})_2$ was synthesized following the procedure reported in the literature.¹² TCNQ-loaded $\text{Cu}_3(\text{BTC})_2$ samples were synthesized following our reported vapor-phase infiltration protocol.¹³ Briefly, after thermal activation to remove the solvent (a mixture of *N,N'*-dimethylformamide, ethanol, and H_2O) used for solvothermal synthesis and creating the characteristic OMS at the Cu paddlewheel nodes, $\text{Cu}_3(\text{BTC})_2$ was physically mixed in a mortar with TCNQ, and then, the mixture was annealed under vacuum in a sealed glass ampoule and heated for 3 days at 180 °C to

yield the host–guest complex. Distinct amounts of TCNQ were employed to prepare a set of samples with different molar fractions of TCNQ, hereafter referred to as $x\text{TCNQ}@Cu_3(\text{BTC})_2$ with $x = n(\text{TCNQ})/n(\text{Cu}_3(\text{BTC})_2) = 0.25, 0.5, \text{ and } 1.0$. During and after the synthesis, the materials were handled under inert conditions (dry Ar or vacuum) and stored in the glovebox to avoid contamination from the atmosphere.

For comparison, a sample was synthesized via solution impregnation following the published synthesis protocol of Talin et al.⁴⁴ Therefore, the parent $\text{Cu}_3(\text{BTC})_2$ was immersed in a dichloromethane (DCM) solution of TCNQ for 3 days (see the Supporting Information for details). The TCNQ-loaded sample, named $\text{sofTCNQ}@Cu_3(\text{BTC})_2$, was collected by filtration and dried under vacuum at room temperature.

In Situ IR Spectroscopy. IR spectra were collected in transmission mode on a Bruker Vertex 70 Fourier transform spectrophotometer, equipped with a KBr beamsplitter and a MCT cryodetector, accumulating 32 scans at a 2 cm^{-1} resolution. All samples were examined in the form of thin self-supporting pellets that were prepared inside the glovebox to avoid exposure to the atmosphere. The pellets, mechanically protected with a gold envelope, were placed in a special homemade quartz cell used for operations down to liquid N_2 temperature (i.e., a nominal temperature of 77 K). Transferred out of the glovebox, the cell was connected to a conventional high-vacuum glass line, equipped with a mechanical and a turbo molecular pump (capable of a residual pressure of $P < 10^{-5}$ mbar), which allows activation and in situ adsorption/desorption measurements of the employed molecular probe in a fully controlled atmosphere.³³ Before CO adsorption, each sample was heated at 150 °C under a dynamic vacuum (10^{-5} mbar) for 2 h to remove any potential residual fraction of undesired adsorbates and/or moisture. After the thermal treatment, the material was exposed to CO and cooled down to 77 K. IR spectra were recorded at this temperature, while the CO pressure was gradually decreased to 10^{-4} mbar to obtain an isothermal set of spectra.

EPR Spectroscopy. All cw EPR experiments were performed with a Bruker EMX micro (X-band, 9.4 GHz) spectrometer fitted with a Bruker ER 4119HS cylindrical cavity. Low-temperature experiments were enabled by the Oxford Instruments He cryostat ESR 900. Modulation amplitudes were always set smaller than the smallest peak-to-peak linewidth of transitions in the experimental EPR spectra. Measurements at different microwave (mw) powers ensured that no line shape distortions through saturation occurred for the signals of interest, and that, in case of quantitative experiments, EPR spectra were recorded in the nonsaturating mw power regime. The MATLAB toolbox EasySpin v. 5.2.25,³⁴ employing the exact diagonalization of the spin Hamiltonian matrix, was used for spectral simulations of the EPR signals. EPR signal intensities of various EPR active species were determined by the double integration of their simulated EPR signals, if their quantification was desired.

All TCNQ-loaded samples for EPR measurements were prepared inside the glovebox by filling the material into an X-band EPR quartz glass tube connected with a high vacuum PTFE valve. The valve was closed and transferred to a vacuum station, where the EPR tube was evacuated and then flame-sealed, keeping the material under inert conditions during each step.

RESULTS AND DISCUSSION

After the synthesis, all materials were carefully characterized to quantitatively determine the TCNQ loading in the MOF structure. Particularly, PXRD data confirmed the successful infiltration (see Figure S2). Standard characterization results of $x\text{TCNQ}@Cu_3(\text{BTC})_2$ with $x = 0.1, 1.0$ in 0.1 increments were thoroughly reported in a previous publication.⁹ In short, $\text{Cu}_3(\text{BTC})_2$ exhibits one small pore of $\sim 11\text{ \AA}$ and two types of large pores of $\sim 16\text{ \AA}$ in diameter. The Cu paddlewheel nodes are oriented in a way that the OMSs at the axial position point to the center of one large pore while being tangential relative

to the other large pore (see the Supporting Information for more information). Notably, the synthesis conditions involving noninert solvents at elevated temperatures and a thermal activation of the material promote the formation of intrinsic Cu(I) sites, the so-called modified node defects.^{19,35} During the vapor-phase infiltration reaction, TCNQ diffuses into the large pores of $\text{Cu}_3(\text{BTC})_2$ and binds preferentially to the available OMSs of two neighboring Cu paddlewheels, as evidenced by PXRD.¹⁸ At the highest possible loading ($x = 1.0$), the large pores can accommodate two molecules of TCNQ while still exhibiting a residual BET-specific surface area of $574\text{ m}^2\text{ g}^{-1}$, that is, about one-third of the pristine $\text{Cu}_3(\text{BTC})_2$, still allowing for the adsorption of smaller molecules such as N_2 or CO. During the reaction, a small amount of $\text{Cu}(\text{TCNQ})$ forms as a byproduct on the external surface of the crystallites, suggesting an electron transfer from the intrinsic Cu(I) defects of the MOF to TCNQ. The electrical conductivity of the sample correlates quasi-exponentially with the amount of TCNQ employed during the reaction and amounts to $1.5 \times 10^{-4}\text{ S cm}^{-1}$ for $1.0\text{TCNQ}@Cu_3(\text{BTC})_2$.¹³

In Situ IR Study of CO Adsorption at 77 K. $\text{Cu}_3(\text{BTC})_2$ by itself represents a complex system involving OMSs and a sophisticated defect chemistry. The introduction of TCNQ into the pores adds an additional layer of complexity as it can coordinate to the OMS and accept electrons from the framework. Therefore, the use of standard characterization techniques does not reveal the full picture of this interaction. In situ IR spectroscopy with probe molecules was used in the past and proved to be a powerful technique to shed light on complicated systems,^{21,22} such as MOFs containing open metal sites. In particular, the study of CO adsorption at 77 K is one of the more common tools employed to probe the Lewis acidic sites generated by the presence of exposed metal cations.^{36,37} For instance, the positively charged Cu(II) species in $\text{Cu}_3(\text{BTC})_2$ allow the formation of carbon end Cu(II)–CO adducts, while, in parallel, CO is able to interact with framework Cu(I) defect sites generated by missing carboxylate units (decarboxylation during thermal activation) or with extra-framework Cu(I) species deriving from Cu_2O impurities (e.g., formed during solvothermal synthesis).^{20,24,38} Finally, the framework Cu(II) cations in $\text{Cu}_3(\text{BTC})_2$ are linked to partially negatively charged carboxylate units, which could constitute a possible interaction site for CO through the formation of oxygen-end adducts as well (organic linker–OC).^{39,40} By exploiting the subtle capacity of CO to disclose the existence of sites of such different nature, it is clear how this probe molecule could be useful to clarify the host–guest structure and interactions of $x\text{TCNQ}@Cu_3(\text{BTC})_2$. As a general comment, it is worth highlighting that only the species available for interaction with CO are effectively probed, whereas fully coordinated and nonaccessible species cannot be detected. Therefore, this method is not able to probe the $\text{Cu}(\text{TCNQ})$ byphase. In addition, it is important that this technique probes the bulk volume of the porous material, and contributions from the external crystallite surface have negligible contributions to the observed IR signals due to the low external surface-to-volume ratio.

$\text{Cu}_3(\text{BTC})_2$. Before analyzing the host–guest materials, CO adsorption was carried out on the parent MOF to get a clear picture of the different Cu families. For this purpose, a thin pellet of $\text{Cu}_3(\text{BTC})_2$ was prepared inside the glovebox and placed in a homemade IR cell for low-temperature measure-

ments, as reported in the [Experimental Section](#). After a thermal activation at 150 °C for 2 h, the material was exposed to ~40 mbar CO, cooled down to 77 K, and then gradually evacuated at the same temperature. The isothermal set of spectra is reported in [Figure 2](#) (from dark blue to dark red) in the CO

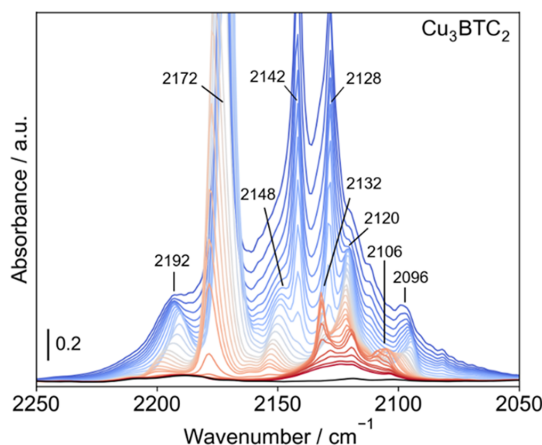


Figure 2. IR spectra of CO adsorbed at 77 K on dehydrated $\text{Cu}_3(\text{BTC})_2$ in the CO vibrational mode region. The equilibrium pressure of CO was gradually decreased from ~20 (dark blue) to 10^{-5} mbar (dark red). The spectrum before contact with CO is shown in black. The absorbance is given as a scale bar in the bottom left corner.

vibrational mode spectral range. The spectra of the materials, showing the full mid-IR spectral region before CO contact, are provided in [Figure S3](#).

The whole set of spectra is characterized by an extremely intense and complex envelope of bands due to the CO interaction with the different surface sites. A detail explanation of the various components and of their spectral behavior is reported in the Infrared Spectroscopy section of the [Supporting Information](#). However, to allow a full comprehension of the IR spectra collected after CO adsorption on the $x\text{TCNQ}@Cu_3(\text{BTC})_2$ host–guest systems, the main spectral features of CO in interaction with pristine $\text{Cu}_3(\text{BTC})_2$ are summarized in the following. (i) The out-of-scale band located at around 2172 cm^{-1} is ascribed to the formation of reversible $\text{Cu}(\text{II})\text{--CO}$ adducts. The peculiar behavior of this band during the outgassing process is due to the gradual conversion of polycarbonyl adsorbate species into monocarbonyls.^{24,38} (ii)

Considering the interpretation of Drenchev and co-workers, the band at 2192 cm^{-1} could be generated by a different $\text{Cu}(\text{II})\text{--CO}$ species, whereas the signal at 2148 cm^{-1} (probably stabilized by the presence of the 2192 cm^{-1} component) could be tentatively assigned to CO in interaction with the organic part of the framework.³⁸ (iii) The bands at around 2120 and 2096 cm^{-1} can be ascribed to the formation of monocarbonyl $\text{Cu}(\text{I})\text{--CO}$ and $\text{Cu}(\text{I})\text{--OC}$ (in which the adsorbed CO molecule interacts through the oxygen atom) adducts due to the presence of defective $\text{Cu}(\text{I})$ sites.^{38,40,41} The component at 2120 cm^{-1} is very stable, persisting until very low CO coverages. (iv) The two signals at 2132 and 2106 cm^{-1} appear in the set of spectra just at a low CO coverage when most of the $\text{Cu}(\text{II})\text{--CO}$ complexes (band at around 2172 cm^{-1}) is removed and then gradually decrease in intensity upon outgassing. These signals can be tentatively assigned to vibrational modes of bridged $\text{Cu}(\text{I})\text{--CO--Cu}(\text{II})$ carbonyls in $\text{Cu}(\text{II})\text{--Cu}(\text{I})$ dimers generated by the presence of missing carboxylate units.^{41–43} (v) The two sharp and intense signals at 2142 and 2128 cm^{-1} simultaneously decrease in intensity without any noticeable change in position and are characterized by a very labile nature (they quickly disappear at the early stages of the desorption process). Following the results proposed by Drenchev and co-workers,³⁸ these bands can be ascribed to CO in interaction with the organic linker via the formation of oxygen-end adducts, presumably with the benzene ring. This assignment is confirmed by observing the modification of some specific spectral features of the organic linker at 1912 and 1896 cm^{-1} during the CO adsorption/desorption experiments with respect to the spectrum of the material before the contact with the probe molecule (see [Figure S5](#)).³⁸ (vi) Finally, at a very low CO coverage, a broad signal appears at 2125 cm^{-1} . The frequency of the component is typical of CO adsorbed on $\text{Cu}(\text{I})$ sites of amorphous Cu_2O impurities.²³

The main IR bands resulting from the interaction of CO with pristine $\text{Cu}_3(\text{BTC})_2$ are summarized in [Table 1](#).

$x\text{TCNQ}@Cu_3(\text{BTC})_2$. After the preliminary analysis of the pristine host framework, we turned our attention to the TCNQ-loaded samples aiming to answer three questions: “What happens to the OMSs upon adsorption of TCNQ?”, “Do we observe redox processes between $\text{Cu}(\text{I})$ defects and TCNQ?”, and “How does TCNQ affect the local pore environment of $\text{Cu}_3(\text{BTC})_2$?” To this purpose, the CO adsorption at 77 K has been carried out on a series of $x\text{TCNQ}@Cu_3(\text{BTC})_2$ samples ($x = 0.25, 0.5, 1.0$) on thin pellets prepared inside the glovebox, as reported in the

Table 1. Assignments of the Main IR Bands Formed upon CO Adsorption on Pristine $\text{Cu}_3(\text{BTC})_2$ (See [Figure 2](#))

wavenumber ^a	assignment	CO coverage ^b	ref
2192–2200 ^c	polycarbonyl/monocarbonyl $\text{Cu}(\text{II})\text{--CO}$	high–low	38
2178	monocarbonyl $\text{Cu}(\text{II})\text{--CO}$	medium low	24, 38
2172	polycarbonyl $\text{Cu}(\text{II})\text{--CO}$	high–medium high	24, 38
2148 ^d	organic linker–OC	high–low	38
2142 and 2128	organic linker–OC	high–medium high	38–40
2132 and 2106	bridged $\text{Cu}(\text{I})\text{--CO--Cu}(\text{II})$	low	41–43
2120	monocarbonyl $\text{Cu}(\text{I})\text{--CO}$	high–medium low	38, 40, 41
2096	monocarbonyl $\text{Cu}(\text{I})\text{--OC}$	high–medium low	40, 41
2125	$\text{Cu}(\text{I})\text{--CO}$ (of Cu_2O impurities)	low	23

^aWavenumber (in cm^{-1}) from this work. ^bCO coverage at which the band is visible. ^c $\text{Cu}(\text{II})\text{--CO}$ adducts different from the standard ones at 2172–2178 cm^{-1} . ^dBand stabilized by the 2192 cm^{-1} component.

Experimental Section. The isothermal sets of spectra of the three materials with various TCNQ loadings are reported in Figure 3, showing the CO vibrational mode spectral range. The

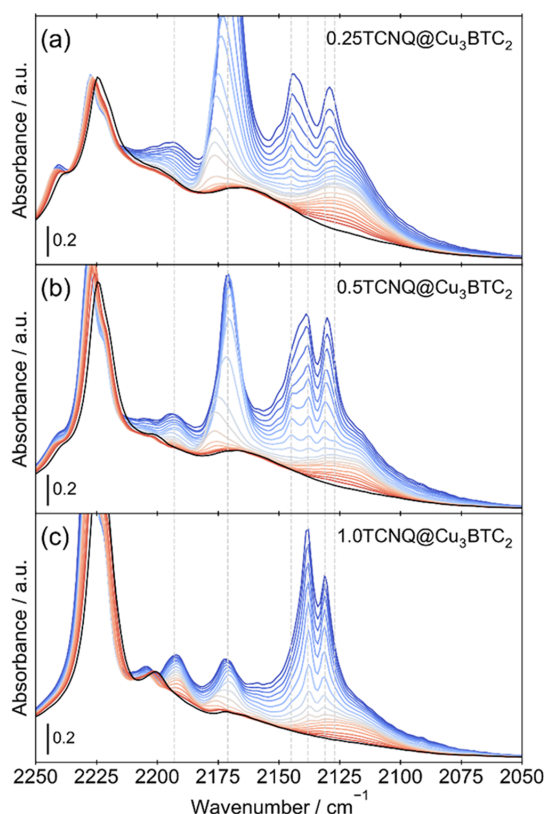


Figure 3. IR spectra of CO adsorbed at 77 K on (a) 0.25TCNQ@Cu₃(BTC)₂, (b) 0.5TCNQ@Cu₃(BTC)₂, and (c) 1.0TCNQ@Cu₃(BTC)₂ in the CO vibrational mode region. The equilibrium pressure of CO was gradually decreased from 16 (dark blue) to 10⁻⁵ mbar (dark red). The spectra before contact with CO are shown in black. The absorbance is given as a scale bar in the bottom left corner.

spectra have been collected by gradually decreasing the CO equilibrium pressure (from dark blue to dark red curves). For a better comparison, the spectra of the three materials should be normalized to take into account the different pellet thickness. However, the identification of a guest-independent IR band was not possible; unfortunately, the main signals of the host framework change, varying the TCNQ loading. On the other side, different vibration modes exhibit different IR extinction coefficients. Hence, it is clear that no absolute quantitative conclusions can be drawn but simply internal quantitative or qualitative information. Nevertheless, the simple comparison among the intensity ratios of spectral components correlated to different chemical species should allow a clear evaluation of the host–guest interactions.

The spectra of the *x*TCNQ@Cu₃(BTC)₂ samples immediately before the contact of CO are reported in Figure 3 as black curves. Regardless of the TCNQ loading, they are dominated by intense absorptions in the 2250–2180 cm⁻¹ range associated with the CN triple bond stretching modes, which

characterize the TCNQ guest molecule. Even if the spectra are not normalized, it is evident that bands coherently increase in intensity going from 0.25TCNQ@Cu₃(BTC)₂ to 1.0TCNQ@Cu₃(BTC)₂. Therefore, it can be reasonably assumed that the three pellets have similar thicknesses and densities and provide comparable results. After the gas admission in the IR cell, an envelope of signals related to the CO interaction with the different surface sites appears. Considering the assignments made for the host framework, the band at around 2170 cm⁻¹ is generated by Cu(II)–CO adducts (polycarbonyls or monocarbonyls, depending on the CO coverage). This band decreases considerably as a function of TCNQ loading, indicating a reduced number of available Cu(II) OMSs able to interact with the probe molecule. This trend clearly supports earlier experimental and computational results, suggesting the coordination of TCNQ to the Cu(II) OMSs of Cu₃(BTC)₂.^{13,44}

Concerning the formation of Cu(I)–CO and Cu(I)–OC adducts (with intrinsic Cu(I) defect sites), the sharp and well-structured bands at 2120 or 2096 cm⁻¹, which were clearly evident in pristine Cu₃(BTC)₂, are totally absent, at any CO coverage, in all three samples. The absence of these spectral components is particularly evident in Figure 4b, which compares the spectra of all the materials at a low CO pressure (1 mbar), which is probably the best situation to observe these differences due to the lower reversibility of the signals generated by Cu(I) species. It should be noted that the Cu(I) defect signals are fully absent in the sample with the lowest TCNQ loading (*x* = 0.25, compare light green and blue curves in Figure 4), suggesting a chemical reaction of these species already induced by the presence of very small amounts of TCNQ. In contrast, in all TCNQ-loaded samples, the extra-framework Cu₂O impurities are always present, as evidenced by the broad and persistent (resistant against prolonged outgassing) component at 2125 cm⁻¹, which seems completely unaffected by the presence of TCNQ. In our previous work, we observed the formation of a byphase of Cu(TCNQ), which requires transfer of an electron to TCNQ and tentatively hypothesized Cu(I) defects being the reducing agent.⁹ This previous hypothesis is now strongly supported by the spectroscopic investigation, revealing the absence of the Cu(I) species and the presence of TCNQ radical anions (see the EPR results in the following section; Figure 5).

Looking at the envelope of bands in the region between 2145 and 2125 cm⁻¹, assigned to CO in interaction with the organic backbone (presumably with the benzene ring) via the formation of oxygen-end adducts, the vibrational modes are clearly perturbed by the presence of the large guest molecule inside the MOF cavities. Indeed, at high TCNQ loadings (*x* = 1.0), the sharp components at 2142 and 2128 cm⁻¹ in pristine Cu₃(BTC)₂ shift to 2138 and 2131 cm⁻¹, respectively. In contrast, for the materials with lower TCNQ loadings (*x* = 0.25 and 0.5), these bands are distinctly broader, exhibiting an intermediate situation due to the unambiguous presence of two distinct components for each signal (upon desorption up to four bands are visible in this region). These modifications become evident in Figure 4a, where the spectra of the materials at different TCNQ loadings (from 0 to 1.0), at a medium-high CO coverage, are compared in the spectral range of CO stretching vibrations. The above described spectral changes disclose a different pore environment throughout the TCNQ loading series. While all cavities are empty in pristine Cu₃(BTC)₂ (bands at 2142 and 2128 cm⁻¹), in the sample

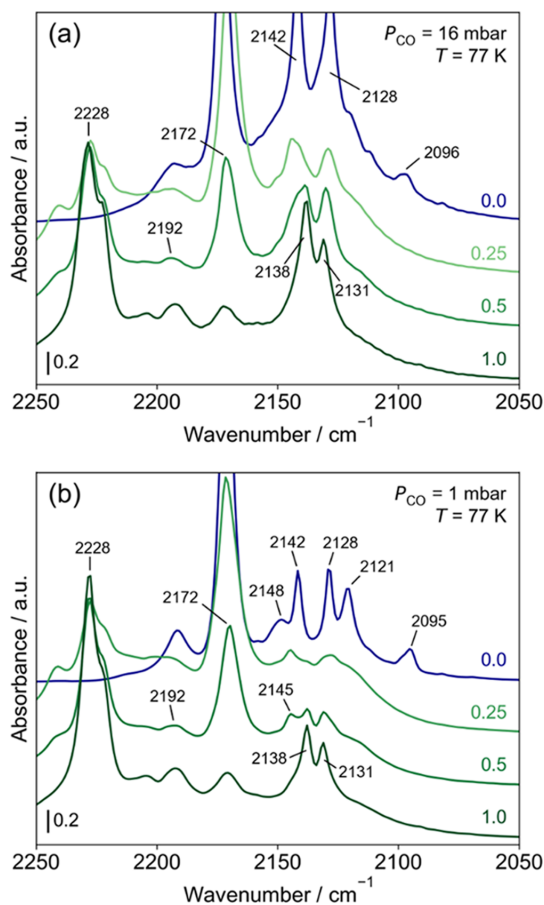


Figure 4. IR spectra of CO adsorbed on pristine $\text{Cu}_3(\text{BTC})_2$ (blue) and on different $x\text{TCNQ}@Cu_3(\text{BTC})_2$ samples (green) at 77 K in the CO vibrational mode region: comparison at different CO equilibrium pressures. (a) 16 mbar CO. (b) 1 mbar CO. The absorbance is given as a scale bar in the bottom left corner. A vertical offset is applied for clarity.

with $x = 1.0$ (bands at 2138 and 2121 cm^{-1}), all large pores are occupied with a maximum of two TCNQ molecules.^{13,15} In these two well-defined “extreme” cases, the local pore environment is therefore homogeneous. In between these two extremes, samples with $x = 0.25$ and 0.5 exhibit empty, partially, or completely filled cavities (i.e., containing 0, 1, or 2 TCNQ molecules), resulting in a more complex spectroscopic situation compared to samples with $x = 0$ and 1.0.

The unequivocal perturbation induced in the organic backbone by the guest TCNQ molecule has been also proven by directly observing the bands at 1912 and 1896 cm^{-1} (assigned to combination modes of the organic framework³⁸) in the spectra of the TCNQ loading series before the CO contact, as reported in Figure S5. These vibrations have the maximum intensity in the pristine $\text{Cu}_3(\text{BTC})_2$, whereas they gradually disappear upon increasing the TCNQ amount.

Finally, we have to spend a few words to evaluate the spectral behavior of the two IR bands at around 2192 and 2148 cm^{-1} , whose assignment has been reported to be quite

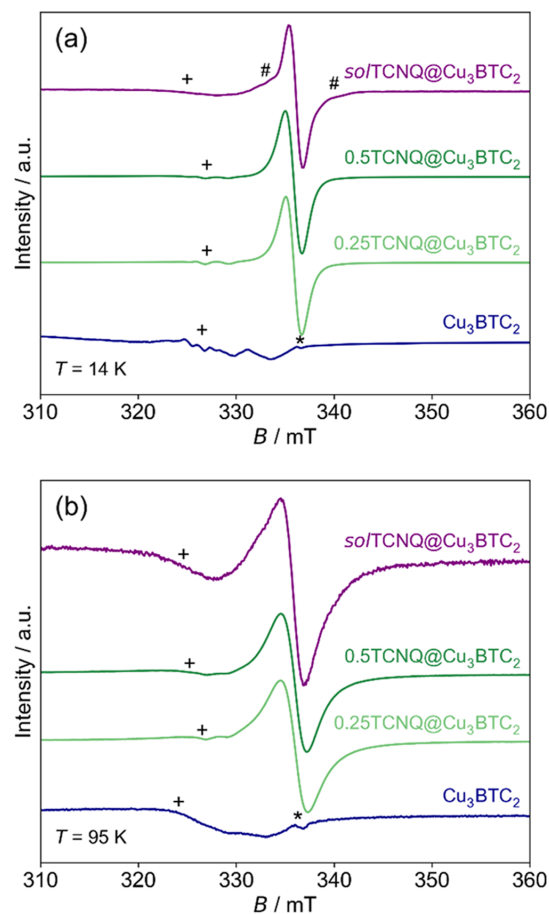


Figure 5. EPR spectra of samples $x\text{TCNQ}@Cu_3(\text{BTC})_2$ ($x = 0.25, 0.5$) (green), $so\text{TCNQ}@Cu_3(\text{BTC})_2$ (purple), and pristine $\text{Cu}_3(\text{BTC})_2$ (blue) measured at (a) $T = 14$ K and (b) $T = 95$ K at a microwave power of 0.02 mW. The maximal signal intensity of the TCNQ-loaded samples was normalized to 1 and set to 0.1 for pristine $\text{Cu}_3(\text{BTC})_2$. The pound symbol labels signals that might be attributed to a TCNQ^- species with a larger spectral linewidth. The plus signs label signals of Cu(II) monomers. The asterisk labels a signal that we assign to a free radical impurity at $g = 2.000(1)$.

controversial in the literature.^{24,38} The 2192 cm^{-1} component is always present in all TCNQ-loaded samples, whereas the 2148 cm^{-1} signal gradually disappears by increasing the guest molecule loading (see Figure 4c). This behavior demonstrates the total absence of correlation between these two spectral features, confirming the assignments proposed by Drenchev and co-workers.³⁸ The band at 2192 cm^{-1} is ascribed to the CO adsorption on a minor fraction of “different” Cu(II) sites, not involved in the interaction with the TCNQ guest molecule, as testified by the high intensity of this band compared to the signal due to standard Cu(II) species (2172 cm^{-1}), especially in the material with the highest TCNQ loading ($x = 1.0$). In contrast, the component at 2148 cm^{-1} assigned to CO attached to the organic part of the framework is no longer present in $1.0\text{TCNQ}@Cu_3(\text{BTC})_2$ due to the perturbation induced by the TCNQ molecule at its maximum loading.

Table 2. Assignments of the Main IR Bands Formed upon CO Adsorption on x TCNQ@Cu₃(BTC)₂ (See Figure 4)

wavenumber ^a	assignment	x TCNQ@Cu ₃ (BTC) ₂ ^b
2192 ^c	polycarbonyl/monocarbonyl Cu(II)–CO	0.25, 0.5, 1.0
2178	monocarbonyl Cu(II)–CO	0.25 (strong), 0.5 (medium), 1.0 (weak)
2172	polycarbonyl Cu(II)–CO	0.25 (strong), 0.5 (medium), 1.0 (weak)
2148	organic linker–OC	0.25, 0.5
2142 and 2128	organic linker–OC	0.25 (strong), 0.5 (medium)
2138 and 2131	organic linker–OC	0.25 (weak), 0.5 (medium), 0.1 (strong)
2132 and 2106	bridged Cu(I)–CO–Cu(II)	absent
2120	monocarbonyl Cu(I)–CO	absent
2096	monocarbonyl Cu(I)–CO	absent
2125	Cu(I)–CO (of Cu ₂ O impurities)	0.25, 0.5, 1.0

^aWavenumber (in cm⁻¹) from this work. ^bPresence of the band in the x TCNQ@Cu₃(BTC)₂ samples and corresponding intensity. ^cCu(II)–CO adducts different from the standard ones at 2172–2178 cm⁻¹.

The main IR bands resulting from the interaction of CO with x TCNQ@Cu₃(BTC)₂ samples are summarized in Table 2.

EPR Spectroscopy. In situ IR spectroscopy results clearly evidence the existence of Cu(I) OMSs in pristine Cu₃(BTC)₂ that vanish upon TCNQ loading, indicating a possible electron transfer from Cu(I) ions to TCNQ molecules. To distinctly elucidate the formation of paramagnetic TCNQ⁻ radicals, we decided to perform cw EPR experiments on some x TCNQ@Cu₃(BTC)₂ ($x = 0.25, 0.5$) samples and compared these results with pristine Cu₃(BTC)₂. Indeed, we unambiguously observe EPR signals of TCNQ⁻ radicals in the vapor-phase-loaded Cu₃(BTC)₂ samples, which were absent in pristine Cu₃(BTC)₂ (see Figure 5), contrasting with the results by Talin et al. who did not observe any signal of TCNQ⁻ radicals when they loaded TCNQ into Cu₃(BTC)₂ via solution impregnation (TCNQ loading, $x \approx 0.25$).⁴⁴ To scrutinize the differences between the two infiltration methods, we synthesized a reference sample, *sol*TCNQ@Cu₃(BTC)₂, following its published synthesis protocol, which was then compared with our x TCNQ@Cu₃(BTC)₂ samples obtained by vapor-phase infiltration.

The room temperature spectra of pristine Cu₃(BTC)₂, x TCNQ@Cu₃(BTC)₂ ($x = 0.25, 0.5$), and *sol*TCNQ@Cu₃(BTC)₂ exhibit an isotropic signal at $g = 2.15$ with a Lorentzian peak-to-peak linewidth of $\Delta B_{pp} = 92(3)$ mT (Figure S6). According to previous works,^{25,27} we assign these signals to the electron spin $S = 1$ state of the antiferromagnetically coupled Cu(II)–Cu(II) paddlewheel units, subjected to interdimeric exchange processes. The disappearance of this signal at $T = 14$ K in all the materials confirms its antiferromagnetic nature (Figure S7). Notably, all TCNQ-loaded samples show an isotropic signal at $g = 2.003(2)$ at $T = 14$ K (around 335 mT in Figure 5a) with an experimental linewidth of $\Delta B_{pp} \approx 1.6$ mT, typical for radical species due to the presence of TCNQ⁻.⁴⁵ According to the literature, the expected ¹⁴N hyperfine (hf) splitting of TCNQ⁻ anions is of the order of 3 MHz (~ 0.1 mT)^{46,47} which is too small to be resolved in the present case. In contrast to the x TCNQ@Cu₃(BTC)₂ samples, the TCNQ⁻ signal of *sol*TCNQ@Cu₃(BTC)₂ exhibits shoulders at the low and high field end, which we tentatively assign to TCNQ⁻ anions with a larger EPR linewidth. This larger linewidth might indicate a high local concentration of the contributing fraction of TCNQ⁻ molecules, which leads to dipolar interactions between these species, resulting in a line broadening.

TCNQ Radical Anions. Since we did not observe any signals of TCNQ⁻ radicals at room temperature (Figure S6), we performed additional EPR experiments at $T = 95$ K on all TCNQ-loaded samples. Like in the spectra obtained at $T = 14$ K, the almost isotropic signals of the TCNQ⁻ radicals at g -values of $g = 2.003(2)$ are visible (Figure 5b). However, their peak-to-peak linewidths increased from $\Delta B_{pp} = 1.56(23)$ mT at $T = 14$ K to $\Delta B_{pp} = 2.52(40)$ mT at $T = 95$ K. By increasing the temperature, the TCNQ⁻ signals further broaden (e.g., Figure S8) until they totally vanish at room temperature (Figure S6). This observation can be explained by spin–spin interactions between the TCNQ⁻ radicals with the $S = 1$ state of nearby Cu(II)–Cu(II) paddlewheel units, which becomes increasingly populated at higher temperature.²⁵ Indeed, pristine Cu₃(BTC)₂ as well as the two TCNQ-loaded x TCNQ@Cu₃(BTC)₂ ($x = 0.25, 0.5$) samples and the reference sample *sol*TCNQ@Cu₃(BTC)₂ shows the typical $S = 1$ signal of magnetically diluted Cu(II)–Cu(II) paddlewheel units at $T = 95$ K (see Figures S9 to S12),^{25,44} verifying that the excited $S = 1$ state of the paddlewheels had become significantly thermally populated at $T = 95$ K. This result strongly suggests that the TCNQ⁻ radicals are located inside the pores of the Cu₃(BTC)₂ framework, and the signal is not produced by the Cu(TCNQ) byproduct that was observed to form at the outer surface of the x TCNQ@Cu₃(BTC)₂ crystallites.¹³

To roughly estimate the amount of TCNQ⁻ radicals per paddlewheel unit, the formula for the magnetic susceptibilities χ_M of monomeric electron spin $S = 1/2$ species and χ_{PW} of dimeric electron spin $S = 1$ species of the paddlewheels were used, as given in the Supporting Information.²⁸ Here, the room temperature $S = 1$ signals of the copper paddlewheels and of the TCNQ⁻ radicals at $T = 75$ K were compared with experimental spectra of an ultramarine reference sample that was measured under the same experimental conditions. This accounts for possible differences in the EPR intensities due to different coupling conditions at different temperatures. For each sample, the amount c of TCNQ⁻ radicals per paddlewheel unit was calculated via

$$c = \frac{I_M(75 \text{ K}) \chi_{PW}(295 \text{ K})}{I_{PW}(295 \text{ K}) \chi_M(75 \text{ K})} \quad (1)$$

where $I_M(75 \text{ K})$ and $I_{PW}(295 \text{ K})$ are the EPR intensities of the TCNQ⁻ species at $T = 75$ K and of the $S = 1$ paddlewheel species at $T = 295$ K, respectively, as they have been determined by double integrating the corresponding simulated

Table 3. EPR-Derived Concentration c (Number per Paddlewheel Unit) of Different Paramagnetic Species Determined via Eq 1 and Tentative Assignments

Sample	TCNQ ⁻	species A - Cu(II)–Cu(I) paddlewheel	species B _a - defective Cu(II) monomer ^a	species B _b ^b - defective Cu(II) monomer ^a	species C - defective Cu(II) monomer
Cu ₃ (BTC) ₂	<0.0002	0.015(8)	0.0013(6)	<0.01	<0.026
0.25TCNQ@Cu ₃ (BTC) ₂	0.025(13)	<0.0004	0.0025(13)	0.0050(25)	<0.0055
0.5TCNQ@Cu ₃ (BTC) ₂	0.016(8)	<0.0012	0.0012(6)	0.012(6)	<0.0068
solTCNQ@Cu ₃ (BTC) ₂	0.010(5)	<0.0025	<0.0003	< 0.006	0.018(9)

^aPossibly assigned to a broken paddlewheel. ^bSame as species B_a but in higher local concentration.

EPR signals, normalized by means of the ultramarine reference signals. In accordance with the literature, an exchange coupling constant of $J = -370 \text{ cm}^{-1}$ was used in the Bleaney–Bowers equation for the magnetic susceptibility of the $S = 1$ spin, which had been determined for the antiferromagnetically coupled Cu paddlewheel units of Cu₃(BTC)₂·(H₂O)₃.²⁵ Following this procedure, we estimate a concentration of 0.025(13), 0.016(8), and 0.010(5) TCNQ⁻ radicals per paddlewheel units for the samples 0.25TCNQ@Cu₃(BTC)₂, 0.5TCNQ@Cu₃(BTC)₂, and solTCNQ@Cu₃(BTC)₂, respectively (Table 3). These quantitative results prove that a doubling of the TCNQ molecules per paddlewheel unit does not increase the concentration of TCNQ⁻ radicals, suggesting a scenario where all accessible framework Cu(I) (intrinsic) defects are already oxidized at low TCNQ loadings ($x = 0.25$), and additional TCNQ is adsorbed without undergoing a redox reaction. Consequently, the concentration of TCNQ⁻ radicals remains at the same order of magnitude in all TCNQ-loaded samples. In contrast to the results reported by Talin et al., we observe a significant amount of TCNQ⁻ anions in the sample prepared via solution impregnation.⁴⁴ This discrepancy could be derived by the slightly different reaction conditions, and more detailed and elaborate experiments to study the materials obtained by TCNQ solution impregnation are suggested. In this study, we show that Cu(I) defects in the crystallite volume act as the reducing agent for the TCNQ guest molecules in both samples obtained via solution impregnation or vapor-phase infiltration. Thereby, the presence of TCNQ radical anions is directly dependent on the intrinsic Cu(I) defect concentration in the pristine MOF, which, in turn, is sensible to the synthesis and activation procedure. Thus, besides the choice of the solvent, which can promote the reduction of TCNQ,¹⁸ the defect concentration of the parent MOF adds another layer of complexity to the synthesis and properties of TCNQ@Cu₃(BTC)₂.

Cu(II) Species. At low temperatures, pristine Cu₃(BTC)₂ as well as the samples x TCNQ@Cu₃(BTC)₂ and solTCNQ@Cu₃(BTC)₂ exhibits signals of monomeric Cu(II) species, which have a 3d⁹ electron configuration and, therefore, an electron spin of $S = 1/2$ (Figure 6 and Figures S13 and S14). The four measured samples display broad Cu(II) background signals with no resolved ^{63,65}Cu (nuclear spin $I = 3/2$) hf splitting, indicative for monomeric Cu(II) species in high local concentration or not well-defined coordination as they might occur at grain or outer boundaries of the MOF crystals or in extra-framework impurity species. One might expect such impurity signals since extra-framework hexaaqua Cu(II) complexes were identified in samples of Cu₃(BTC)₂ in a previous work by Pöpl et al.²⁵ The present samples were activated at higher temperatures and washed for a longer time

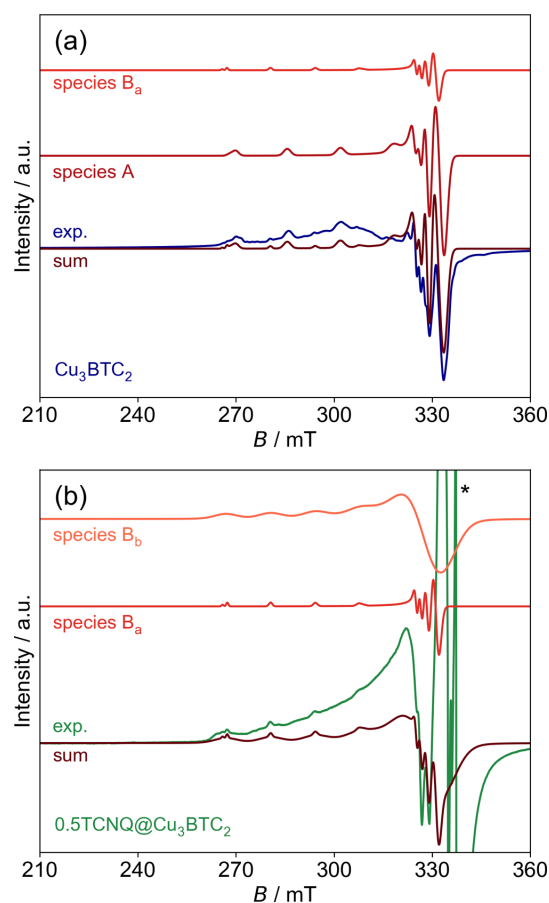


Figure 6. Experimental EPR spectra of (a) pristine Cu₃(BTC)₂ (blue) and (b) sample 0.5TCNQ@Cu₃(BTC)₂ (green) measured at $T = 14 \text{ K}$. In panel (a), the sum simulation (brown) is the superposition of the simulated signals of the monomeric Cu(II) species A (dark red) and B_a (red). In panel (b), the sum simulation (brown) is a superposition of the signals of Cu(II) species B_a (red) and B_b (light red). The asterisk labels the saturated signal of TCNQ⁻ radicals that extends outside the frame and that overlaps with the Cu(II) signals. See Table S1 for simulation parameters.

than in the work of Pöpl et al.²⁵ However, extra-framework Cu(II) species might still have remained in the present samples, even if they do not occur as hexaaqua complexes due to the potential removal of all water under the harsher

activation conditions. In addition, the EPR spectrum of pristine $\text{Cu}_3(\text{BTC})_2$ at $T = 14$ K resolves the g_z $^{63,65}\text{Cu}$ hf transitions of two Cu(II) species A and B_a between 260 and 320 mT as well as the $g_{x,y}$ $^{63,65}\text{Cu}$ hf transitions of species A between 320 and 340 mT (Figure 6a; see Table S1 for the spin Hamiltonian parameters). Further, minor g_z $^{63,65}\text{Cu}$ hf transitions of other defective Cu(II) species are resolved for pristine $\text{Cu}_3(\text{BTC})_2$ at $T = 14$ K, but their low signal intensities and their overlapping with other hf transitions of different Cu(II) species prevented their clear assignment and determination of their spin Hamiltonian parameters. However, their presence indicates a varied presence of different kinds of well-defined Cu(II) defects in pristine $\text{Cu}_3(\text{BTC})_2$.

As explained above for the TCNQ^- radicals, we have determined the concentration of species A in pristine $\text{Cu}_3(\text{BTC})_2$ at $T = 75$ K to 0.015(8) Cu(II) ions per paddlewheel unit (Table 3). Within the experimental error, this concentration is very similar to those determined for the TCNQ^- radicals in all three TCNQ -loaded samples. Importantly, the signal of species A was not observed for the TCNQ -loaded samples anymore (Figure 6b and Figures S13 and S14). The above reported observations suggest that species A represents Cu(II) ions of mixed valence Cu(II)–Cu(I) paddlewheel units in pristine $\text{Cu}_3(\text{BTC})_2$. In accordance to the IR results, all diamagnetic Cu(I) ions are oxidized to Cu(II) upon TCNQ loading, and, in parallel, a corresponding fraction of the guest molecule is reduced to TCNQ^- . Consequently, the same concentration of TCNQ^- radicals is observed in the loaded samples as Cu(II)–Cu(I) paddlewheel units occur in pristine $\text{Cu}_3(\text{BTC})_2$ (Table 3). The magnetic coupling of a potentially formed Cu(II)–Cu(II)– TCNQ^- spin triad is discussed in detail in the Supporting Information. If such spin triads are present in the TCNQ -loaded samples, then the present results indicate a weak exchange interaction between the Cu(II) ion and the axially coordinating TCNQ^- radical without significant distortion of the antiferromagnetic coupling between the two Cu(II) ions and the isotropic TCNQ^- signal. The g - and ^{63}Cu hf-tensor principal values $g_z = 2.290(3)$ and $A_z = 0.0170(7)$ cm^{-1} of species A are typical for Cu(II) ions in square planar to square pyramidal coordination as one would expect for Cu(II) ions in mixed valence paddlewheel units.^{48,49} Since Zn(II) and Cu(I) are both $3d^{10}$ ions of similar size, one might expect similar spin Hamiltonian parameters for Cu(II) ions in Cu(II)–Cu(I) and Cu(II)–Zn(II) paddlewheels. Friedländer et al. determined spin Hamiltonian parameters $g_z = 2.281(1)$ and $A_z = 0.0187(2)$ cm^{-1} for Cu(II) ions of mixed metal Cu(II)–Zn(II) paddlewheel units in activated $\text{Cu}_{2.965}\text{Zn}_{0.035}\text{BTC}_2$.²⁹ Even though they are of the same order of magnitude, they are still different to those of species A and allow no clear statement about their actual nature at this point.

Whereas the monomeric Cu(II) species A is only observed for pristine $\text{Cu}_3(\text{BTC})_2$, we observe a second Cu(II) species B_a in pristine $\text{Cu}_3(\text{BTC})_2$ as well as the two $x\text{TCNQ}@$ $\text{Cu}_3(\text{BTC})_2$ ($x = 0.25, 0.5$) samples (Figure 6 and Figure S13; see Tables S1 for spin Hamiltonian parameters). The Cu(II) concentrations derived by EPR amount to 0.0013(6), 0.0025(13), and 0.0012(6) per paddlewheel unit for pristine $\text{Cu}_3(\text{BTC})_2$, $0.25\text{TCNQ}@$ $\text{Cu}_3(\text{BTC})_2$, and $0.5\text{TCNQ}@$ $\text{Cu}_3(\text{BTC})_2$, respectively (Table 3). The concentration of species B_a is 1 order of magnitude smaller than that of species A. We can only speculate about its nature. In this specific case, species B_a might be ascribed to the single Cu(II) ion of a

broken paddlewheel node (i.e., a node with one missing Cu ion) in a well-defined coordination environment, whose presence was reported by Friedländer et al. in Cu paddlewheel-based materials.²⁸ In samples $0.25\text{TCNQ}@$ $\text{Cu}_3(\text{BTC})_2$ and $0.5\text{TCNQ}@$ $\text{Cu}_3(\text{BTC})_2$, the g_z $^{63,65}\text{Cu}$ hf transition of species B_a is superimposed by broader lines at the same field position (Figure 6b and Figure S13), which we assign to species B_b . Its identical g_z and A_z values (see Table S1) indicate that species B_b is of the same nature as species B_a but in a higher local concentration or subjected to a larger structural disorder, which leads to considerable broadening of the hf transitions. The estimated concentrations of 0.0050(25) and 0.012(6) Cu(II) ions per paddlewheel in samples $0.25\text{TCNQ}@$ $\text{Cu}_3(\text{BTC})_2$ and $0.5\text{TCNQ}@$ $\text{Cu}_3(\text{BTC})_2$, respectively (Table 3), imply a correlation between species B_b and the TCNQ loading x . In contrast, the concentration of species B_a remains almost constant, indicating that species B_a is a structural well-defined Cu(II) point defect in a small local concentration. In the spectrum of pristine $\text{Cu}_3(\text{BTC})_2$, the superposition with varied $^{63,65}\text{Cu}$ hf transitions of different Cu(II) species at $T = 14$ K does not allow clear conclusions about the presence or concentration of species B_b . Considering the high local concentration of species B_b , its quantitative correlation with the TCNQ loading amount x , and previous findings showing an increase of the Cu(TCNQ) byphase with x ,¹³ leads to the hypothesis that species B_b corresponds to the Cu(II) ion of a broken paddlewheel close to the crystallite surface. The missing Cu ion has potentially reacted with TCNQ to form the Cu(TCNQ) surface byphase. Notably, species B_a and B_b are below the detection limit in the EPR spectra of $\text{solTCNQ}@$ $\text{Cu}_3(\text{BTC})_2$ (Figure S14), while a third Cu(II) species C was observed (Figure S14; see Table S1 for spin Hamiltonian parameters). The relatively large concentration of 0.018(9) Cu(II) ions per paddlewheel unit and less-resolved hf transitions indicate that the treatment of the sample with the TCNQ/DCM solution produces a new type of Cu(II) species in high local concentration or less-defined coordination (Table 3). The above reported results evidence that the distribution of TCNQ^- radicals throughout the pore system is less homogeneous in $\text{solTCNQ}@$ $\text{Cu}_3(\text{BTC})_2$ compared to the $x\text{TCNQ}@$ $\text{Cu}_3(\text{BTC})_2$ samples. Therefore, we conclude that the vapor-phase infiltration leads to a more homogeneous TCNQ distribution compared to solution impregnation, which is likely a result of the elevated temperatures and the absence of solvents competing for the available OMSs.

For a better understanding of the different Cu(II) species, we suggest pulsed EPR experiments like electron spin echo envelope modulation (ESEEM) and electron nuclear double resonance (ENDOR) experiments, which might resolve the hf coupling between the Cu(II) electron spin $S = 1/2$ and the Cu nuclear spin $I = 3/2$ of the adjacent $^{63,65}\text{Cu}$ (I) ion. Such experiments are currently in progress. Nevertheless, a reduction of TCNQ molecules by Cu(I) ions is strongly indicated by the presented IR and EPR results.

CONCLUSIONS

An advanced spectroscopic characterization study has been carried out by means of IR spectroscopy of adsorbed probe molecules (here, CO) and EPR spectroscopy to disclose the host–guest chemistry of a series of $\text{Cu}_3(\text{BTC})_2$ samples containing increasing amounts of TCNQ .

The combined spectroscopic approach together with a comparison of solvent-free vapor-phase infiltration and

solution impregnation provides substantial answers to the three questions raised at the beginning of this study. By means of in situ IR spectroscopy, we clearly show that the amount of Cu(II) OMSs in $\text{Cu}_3(\text{BTC})_2$ decreases monotonically by increasing the guest loading because of the occupation by TCNQ. In combination with our previous powder diffraction data,¹³ the presented results dispelled any doubt about the coordination of TCNQ to the Cu(II) dimers of the paddlewheel units. Moreover, the IR data revealed a homogeneous pore environment for the pristine and fully loaded MOF ($x = 1.0$; i.e., two TCNQs per large pore), whereas intermediate samples exhibited a more heterogeneous, variegated TCNQ distribution inside the microporous cavities. In addition, both IR and EPR data evidenced the presence of intrinsic Cu(I) framework defects in the volume of pristine $\text{Cu}_3(\text{BTC})_2$ that disappear immediately upon exposure to even small TCNQ amounts. In return, the presence of TCNQ radical anions becomes evident in all TCNQ-loaded samples. Remarkably, the radical concentration in the TCNQ-loaded samples correlates quantitatively with the Cu(II)–Cu(I) defect concentration in the parent MOF, evidencing an electron transfer from the Cu(I) defects to TCNQ. Additional pulsed EPR measurements are currently in progress to get further insights into the nature of the different Cu(II) species.

The results obtained during this study have profound implication for the fabrication and the understanding of the physical origin of the electronic conductivity and performance of devices based on $\text{TCNQ}@\text{Cu}_3(\text{BTC})_2$. We find that the framework Cu(I) defect concentration directly correlates with the TCNQ radical anion concentration, thereby introducing additional charge carriers into the system, which is typically associated with an increase in electrical conductivity. In fact, the maximum TCNQ^- concentration is already reached at low loadings, which would result in a plateau of the conductivity at higher loadings if the introduced charge carrier was the only contribution to the conductivity. This contrasts with the experimental results.^{13,44} An increased charge mobility due to neutral TCNQ in the pores, or contributions from a Cu(TCNQ) surface byphase that forms under certain conditions,^{13,18} must also be taken into account when studying the electronic properties of these materials.^{14,15,17,44} The use of carefully fabricated defect-free $\text{Cu}_3(\text{BTC})_2$ thin films^{50,51} as the starting material for the infiltration reaction under very mild conditions (low temperature, inert solvent) will likely lead to a host–guest material without the formation of TCNQ radicals. In a similar way, defect-free bulk materials should be accessible by optimization of the synthetic protocol; however, mild activation procedures to generate the OMSs without Cu(I) defect formation are scarce or even absent.^{40,52–54} The present system is yet another example where the defect chemistry of MOFs has a significant impact on the material properties and underlines the importance of advancing the research field of defect-engineered MOFs.^{35,55}

At this point, we like to highlight our recent computational study on structurally retrofitting metal–organic frameworks with cross-linkers (CL), in particular, Cu paddlewheel-based systems such as $\text{CL}@\text{Cu}_3(\text{BTC})_2$ and the expansion to $\text{CL}@\text{NOTT-100}$ and $\text{CL}@\text{NOT-101}$.⁹ A library of 20 CLs with binding properties similar to TCNQ was evaluated. We suggest that the chemical interaction of these potentially noninnocent guest molecules with Cu paddlewheel-based MOFs beyond the simple coordination to the open copper sites may be as complex as the present case of $\text{Cu}_3(\text{BTC})_2$ (HKUST-1), and it

may be elucidated in detail following the methodology as we described above.

As a final, and more general, remark, it is worth highlighting that a high precision inorganic solid-state synthesis together with the application of a suite of complementary techniques of spectroscopic characterization represents a powerful approach to study the subtle, and frequently unexpectedly complex, chemistry of synergetic Guest@MOF systems,⁵⁴ in general.

■ ASSOCIATED CONTENT

Supporting Information

The Supporting Information is available free of charge at <https://pubs.acs.org/doi/10.1021/acsami.9b16663>.

Information about the synthesis, powder X-ray diffraction, IR, and EPR spectroscopy (PDF)

■ AUTHOR INFORMATION

Corresponding Authors

*E-mail: valentina.crocella@unito.it (V.C.).

*E-mail: roland.fischer@tum.de (R.A.F.).

ORCID

Matthias Mendt: 0000-0002-1295-0228

Valentina Crocella: 0000-0002-3606-8424

Roland A. Fischer: 0000-0002-7532-5286

Author Contributions

The manuscript was written through contributions of all authors. All authors have given approval to the final version of the manuscript.

Funding

DFG SPP1928 (COORNETs).

Notes

The authors declare no competing financial interest.

■ ACKNOWLEDGMENTS

The authors would like to thank Silvia Bordiga for insightful discussions. C.S. acknowledges his scholarships from the German Academic Scholarship Foundation and from the German Chemical Industry Fund (FCI). This work was supported by the German Research Foundation Priority Program 1928 “CCORNETs” (www.coornets.tum.de).

■ REFERENCES

- (1) Weckhuysen, B. M.; Yu, J. Recent Advances in Zeolite Chemistry and Catalysis. *Chem. Soc. Rev.* **2015**, *44*, 7022–7024.
- (2) Slater, A. G.; Cooper, A. I. Function-Led Design of New Porous Materials. *Science* **2015**, *348*, aaa8075.
- (3) Zhou, H.-C.; Kitagawa, S. Metal–Organic Frameworks (MOFs). *Chem. Soc. Rev.* **2014**, *43*, 5415–5418.
- (4) Chen, C.; Lee, Y.-R.; Ahn, W.-S. CO₂ Adsorption Over Metal–Organic Frameworks: A Mini Review. *J. Nanosci. Nanotechnol.* **2016**, *16*, 4291–4301.
- (5) Hall, J. N.; Bollini, P. Structure, Characterization, and Catalytic Properties of Open-Metal Sites in Metal Organic Frameworks. *React. Chem. Eng.* **2019**, *4*, 207–222.
- (6) Liu, J.; Chen, L.; Cui, H.; Zhang, J.; Zhang, L.; Su, C.-Y. Applications of Metal–Organic Frameworks in Heterogeneous Supramolecular Catalysis. *Chem. Soc. Rev.* **2014**, *43*, 6011–6061.
- (7) Souza, B. E.; Rudić, S.; Titov, K.; Babal, A. S.; Taylor, J. D.; Tan, J.-C. Guest–Host Interactions of Nanoconfined Anti-Cancer Drug in Metal–Organic Framework Exposed by Terahertz Dynamics. *Chem. Commun.* **2019**, *55*, 3868–3871.

- (8) Kapustin, E. A.; Lee, S.; Alshammari, A. S.; Yaghi, O. M. Molecular Retrofitting Adapts a Metal–Organic Framework to Extreme Pressure. *ACS Cent. Sci.* **2017**, *3*, 662–667.
- (9) Schneider, C.; Bodesheim, D.; Keupp, J.; et al. Retrofitting metal-organic frameworks. *Nat. Commun.* **2019**, *10*, 4921.
- (10) Schlichte, K.; Kratzke, T.; Kaskel, S. Improved Synthesis, Thermal Stability and Catalytic Properties of the Metal–Organic Framework Compound $\text{Cu}_3(\text{BTC})_2$. *Microporous Mesoporous Mater.* **2004**, *73*, 81–88.
- (11) Chui, S. S.-Y.; Lo, S. M.-F.; Charmant, J. P. H.; Orpen, A. G.; Williams, I. D. Chemically Functionalizable Nanoporous Material $[\text{Cu}_3(\text{TMA})_2(\text{H}_2\text{O})_3]_n$. *Science* **1999**, *283*, 1148–1150.
- (12) Bhunia, M. K.; Hughes, J. T.; Fettingler, J. C.; Navrotsky, A. Thermochemistry of Paddle Wheel MOFs: Cu-HKUST-1 and Zn-HKUST-1. *Langmuir* **2013**, *29*, 8140–8145.
- (13) Schneider, C.; Ukaj, D.; Koerver, R.; Talin, A. A.; Kieslich, G.; Pujari, S. P.; Zuilhof, H.; Janek, J.; Allendorf, M. D.; Fischer, R. A. High Electrical Conductivity and High Porosity in a Guest@MOF Material: Evidence of TCNQ Ordering within Cu_3BTC_2 Micropores. *Chem. Sci.* **2018**, *9*, 7405–7412.
- (14) Neumann, T.; Liu, J.; Wächter, T.; Friederich, P.; Symalla, F.; Welle, A.; Mugnaini, V.; Meded, V.; Zharnikov, M.; Wöll, C.; Wenzel, W. Superexchange Charge Transport in Loaded Metal Organic Frameworks. *ACS Nano* **2016**, *10*, 7085–7093.
- (15) Erickson, K. J.; Léonard, F.; Stavila, V.; Foster, M. E.; Spataru, C. D.; Jones, R. E.; Foley, B. M.; Hopkins, P. E.; Allendorf, M. D.; Talin, A. A. Thin Film Thermoelectric Metal–Organic Framework with High Seebeck Coefficient and Low Thermal Conductivity. *Adv. Mater.* **2015**, *27*, 3453–3459.
- (16) Hendon, C. H.; Walsh, A. Chemical Principles Underpinning the Performance of the Metal–Organic Framework HKUST-1. *Chem. Sci.* **2015**, *6*, 3674–3683.
- (17) Chen, X.; Wang, Z.; Hassan, Z. M.; Lin, P.; Zhang, K.; Baumgart, H.; Redel, E. Seebeck Coefficient Measurements of Polycrystalline and Highly Ordered Metal–Organic Framework Thin Films. *ECS J. Solid State Sci. Technol.* **2017**, *6*, P150–P153.
- (18) Thürmer, K.; Schneider, C.; Stavila, V.; Friddle, R. W.; Léonard, F.; Fischer, R. A.; Allendorf, M. D.; Talin, A. A. Surface Morphology and Electrical Properties of Cu_3BTC_2 Thin Films Before and After Reaction with TCNQ. *ACS Appl. Mater. Interfaces* **2018**, *10*, 39400–39410.
- (19) Nijem, N.; Bluhm, H.; Ng, M. L.; Kunz, M.; Leone, S. R.; Gilles, M. K. Cu^{1+} in HKUST-1: Selective Gas Adsorption in the Presence of Water. *Chem. Commun.* **2014**, *50*, 10144–10147.
- (20) Szanyi, J.; Daturi, M.; Clet, G.; Baer, D. R.; Peden, C. H. F. Well-Studied Cu–BTC Still Serves Surprises: Evidence for Facile $\text{Cu}^{2+}/\text{Cu}^+$ Interchange. *Phys. Chem. Chem. Phys.* **2012**, *14*, 4383.
- (21) Lamberti, C.; Zecchina, A.; Groppo, E.; Bordiga, S. Probing the Surfaces of Heterogeneous Catalysts by in Situ IR Spectroscopy. *Chem. Soc. Rev.* **2010**, *39*, 4951.
- (22) Vimont, A.; Thibault-Starzyk, F.; Daturi, M. Analysing and Understanding the Active Site by IR Spectroscopy. *Chem. Soc. Rev.* **2010**, *39*, 4928.
- (23) Prestipino, C.; Regli, L.; Vitillo, J. G.; Bonino, F.; Damin, A.; Lamberti, C.; Zecchina, A.; Solari, P. L.; Kongshaug, K. O.; Bordiga, S. Local Structure of Framework Cu(II) in HKUST-1 Metallorganic Framework: Spectroscopic Characterization upon Activation and Interaction with Adsorbates. *Chem. Mater.* **2006**, *18*, 1337–1346.
- (24) Bordiga, S.; Regli, L.; Bonino, F.; Groppo, E.; Lamberti, C.; Xiao, B.; Wheatley, P. S.; Morris, R. E.; Zecchina, A. Adsorption Properties of HKUST-1 toward Hydrogen and Other Small Molecules Monitored by IR. *Phys. Chem. Chem. Phys.* **2007**, *9*, 2676.
- (25) Pöpl, A.; Kunz, S.; Himsl, D.; Hartmann, M. CW and Pulsed ESR Spectroscopy of Cupric Ions in the Metal–Organic Framework Compound $\text{Cu}_3(\text{BTC})_2$. *J. Phys. Chem. C* **2008**, *112*, 2678–2684.
- (26) Siménas, M.; Kobalz, M.; Mendt, M.; Eckold, P.; Krautscheid, H.; Banys, J.; Pöpl, A. Synthesis, Structure, and Electron Paramagnetic Resonance Study of a Mixed Valent Metal–Organic Framework Containing Cu_2 Paddle-Wheel Units. *J. Phys. Chem. C* **2015**, *119*, 4898–4907.
- (27) Jee, B.; Eisinger, K.; Gul-E-Noor, F.; Bertmer, M.; Hartmann, M.; Himsl, D.; Pöpl, A. Continuous Wave and Pulsed Electron Spin Resonance Spectroscopy of Paramagnetic Framework Cupric Ions in the Zn(II) Doped Porous Coordination Polymer $\text{Cu}_{3-x}\text{Zn}_x(\text{BTC})_2$. *J. Phys. Chem. C* **2010**, *114*, 16630–16639.
- (28) Friedländer, S.; Siménas, M.; Kobalz, M.; Eckold, P.; Ovchar, O.; Belous, A. G.; Banys, J.; Krautscheid, H.; Pöpl, A. Single Crystal Electron Paramagnetic Resonance with Dielectric Resonators of Mononuclear Cu^{2+} Ions in a Metal–Organic Framework Containing Cu_2 Paddle Wheel Units. *J. Phys. Chem. C* **2015**, *119*, 19171–19179.
- (29) Friedländer, S.; Petkov, P. S.; Bolling, F.; Kultaeva, A.; Böhlmann, W.; Ovchar, O.; Belous, A. G.; Heine, T.; Pöpl, A. Continuous-Wave Single-Crystal Electron Paramagnetic Resonance of Adsorption of Gases to Cupric Ions in the Zn(II)-Doped Porous Coordination Polymer $\text{Cu}_{2.965}\text{Zn}_{0.035}(\text{BTC})_2$. *J. Phys. Chem. C* **2016**, *120*, 27399–27411.
- (30) Pöpl, A.; Jee, B.; Icker, M.; Hartmann, M.; Himsl, D. Untersuchungen Zur Chemischen Stabilität von $\text{Cu}_3(\text{BTC})_2$ (HKUST-1) Durch N_2 -Adsorption, Röntgenpulverdiffraktometrie Und EPR-Spektroskopie. *Chem. Ing. Tech.* **2010**, *82*, 1025–1029.
- (31) Jee, B.; Koch, K.; Moschkowitz, L.; Himsl, D.; Hartman, M.; Pöpl, A. Electron Spin Resonance Study of Nitroxide Radical Adsorption at Cupric Ions in the Metal–Organic Framework Compound $\text{Cu}_3(\text{BTC})_2$. *J. Phys. Chem. Lett.* **2011**, *2*, 357–361.
- (32) Jee, B.; St. Petkov, P.; Vayssilov, G. N.; Heine, T.; Hartmann, M.; Pöpl, A. A Combined Pulsed Electron Paramagnetic Resonance Spectroscopic and DFT Analysis of the $^{13}\text{CO}_2$ and ^{13}CO Adsorption on the Metal–Organic Framework $\text{Cu}_{2.97}\text{Zn}_{0.03}(\text{BTC})_2$. *J. Phys. Chem. C* **2013**, *117*, 8231–8240.
- (33) Crocellà, V.; Tabanelli, T.; Vitillo, J. G.; Costenaro, D.; Bisio, C.; Cavani, F.; Bordiga, S. A Multi-Technique Approach to Disclose the Reaction Mechanism of Dimethyl Carbonate Synthesis over Amino-Modified SBA-15 Catalysts. *Appl. Catal., B* **2017**, *211*, 323.
- (34) Stoll, S.; Schweiger, A. EasySpin, a Comprehensive Software Package for Spectral Simulation and Analysis in EPR. *J. Magn. Reson.* **2006**, *178*, 42–55.
- (35) Dissegna, S.; Epp, K.; Heinz, W. R.; Kieslich, G.; Fischer, R. A. Defective Metal–Organic Frameworks. *Adv. Mater.* **2018**, *30*, 1704501–1704524.
- (36) Volkringer, C.; Leclerc, H.; Lavalley, J.-C.; Loiseau, T.; Férey, G.; Daturi, M.; Vimont, A. Infrared Spectroscopy Investigation of the Acid Sites in the Metal–Organic Framework Aluminum Trimesate MIL-100(Al). *J. Phys. Chem. C* **2012**, *116*, 5710–5719.
- (37) Chavan, S.; Vitillo, J. G.; Groppo, E.; Bonino, F.; Lamberti, C.; Dietzel, P. D. C.; Bordiga, S. CO Adsorption on CPO-27-Ni Coordination Polymer: Spectroscopic Features and Interaction Energy. *J. Phys. Chem. C* **2009**, *113*, 3292–3299.
- (38) Drenchev, N.; Ivanova, E.; Mihaylov, M.; Hadjiivanov, K. CO as an IR Probe Molecule for Characterization of Copper Ions in a Basolite C300 MOF Sample. *Phys. Chem. Chem. Phys.* **2010**, *12*, 6423–6427.
- (39) Bonino, F.; Lamberti, C.; Chavan, S.; Vitillo, J. G.; Bordiga, S. Chapter 4. Characterization of MOFs. 1. Combined Vibrational and Electronic Spectroscopies. In *Metal Organic Frameworks as Heterogeneous Catalysts*; The Royal Society of Chemistry: 2013, pp 76–142.
- (40) St. Petkov, P.; Vayssilov, G. N.; Liu, J.; Shekha, O.; Wang, Y.; Wöll, C.; Heine, T. Defects in MOFs: A Thorough Characterization. *ChemPhysChem* **2012**, *13*, 2025–2029.
- (41) Areán, C. O.; Delgado, M. R.; Frolich, K.; Bulánek, R.; Pulido, A.; Bibiloni, G. F.; Nachtigall, P. Computational and Fourier Transform Infrared Spectroscopic Studies on Carbon Monoxide Adsorption on the Zeolites Na-ZSM-5 and K-ZSM-5: Evidence of Dual-Cation Sites. *J. Phys. Chem. C* **2008**, *112*, 4658–4666.
- (42) Bulánek, R.; Frolich, K.; Címanec, P.; Nachtigallova, D.; Pulido, A.; Nachtigall, P. Combined Experimental and Theoretical Investigations of Heterogeneous Dual Cation Sites in Cu,M-FER Zeolites. *J. Phys. Chem. C* **2011**, *115*, 13312–13321.

- (43) Frolich, K.; Koudelkova, E.; Frydova, E.; Bulanek, R. The Quantity of Cu⁺ Ions Forming Isolated and Bridged Carbonyl Complexes in FER Zeolites Determined by IR Spectroscopy. *Vib. Spectrosc.* **2012**, *58*, 146–152.
- (44) Talin, A. A.; Centrone, A.; Ford, A. C.; Foster, M. E.; Stavila, V.; Haney, P.; Kinney, R. A.; Szalai, V.; El Gabaly, F.; Yoon, H. P.; Léonard, F.; Allendorf, M. D. Tunable Electrical Conductivity in Metal–Organic Framework Thin-Film Devices. *Science* **2014**, *343*, 66–69.
- (45) Schwertdfeger, C. F. Low Temperature EPR Study of the “Impurity” Resonances in (TCNQ)[−] and (TCNQ)^{−2} Salts. *Solid State Commun.* **1977**, *23*, 621–622.
- (46) Bell, S. E.; Field, J. S.; Haines, R. J.; Moscherosch, M.; Matheis, W.; Kaim, W. Novel and Stable Metal–Metal-Bonded Diruthenium(I) Complexes Containing TCNXO/Bul- in Both the Inner and the Outer Coordination Sphere (TCNX = TCNE, TCNQ). A Combined EPR/ENDOR-, UV/Visible/near-IR-, and IR-Spectroscopic and Electrochemical Investigation. *Inorg. Chem.* **1992**, *31*, 3269–3276.
- (47) Flandrois, S.; Boissonade, J. EPR Fine Structure and Spin Densities in TCNQ Salts. *Chem. Phys. Lett.* **1978**, *58*, 596–600.
- (48) Hathaway, B. J.; Billing, D. E. The Electronic Properties and Stereochemistry of Mono-Nuclear Complexes of the Copper(II) Ion. *Coord. Chem. Rev.* **1970**, *5*, 143–207.
- (49) Tominaga, H.; Ono, Y.; Keii, T. Spectroscopic Study of Cu(II) Ions Supported on Silica Gel by Cation Exchange Method. *J. Catal.* **1975**, *40*, 197–202.
- (50) Gu, Z.-G.; Pfriem, A.; Hamsch, S.; Breitwieser, H.; Wohlgemuth, J.; Heinke, L.; Gliemann, H.; Wöll, C. Transparent Films of Metal–Organic Frameworks for Optical Applications. *Microporous Mesoporous Mater.* **2015**, *211*, 82–87.
- (51) Delen, G.; Ristanovic, Z.; Mandemaker, L. D. B.; Weckhuysen, B. M. Mechanistic Insights into Growth of Surface-Mounted Metal–Organic Framework Films Resolved by Infrared (Nano-) Spectroscopy. *Chem. Eur. J.* **2018**, *24*, 187–195.
- (52) Mendt, M.; Gutt, F.; Kavooosi, N.; Bon, V.; Senkovska, I.; Kaskel, S.; Pöpl, A. EPR Insights into Switchable and Rigid Derivatives of the Metal–Organic Framework DUT-8(Ni) by NO Adsorption. *J. Phys. Chem. C* **2016**, *120*, 14246–14259.
- (53) Bae, J.; Choi, J. S.; Hwang, S.; Yun, W. S.; Song, D.; Lee, J.; Jeong, N. C. Multiple Coordination Exchanges for Room-Temperature Activation of Open-Metal Sites in Metal–Organic Frameworks. *ACS Appl. Mater. Interfaces* **2017**, *9*, 24743–24752.
- (54) Allendorf, M. D.; Medishetty, R.; Fischer, R. A. Guest Molecules as a Design Element for Metal–Organic Frameworks. *MRS Bull.* **2016**, *41*, 865–869.
- (55) Fang, Z.; Bueken, B.; De Vos, D. E.; Fischer, R. A. Defect-Engineered Metal–Organic Frameworks. *Angew. Chem., Int. Ed.* **2015**, *54*, 7234–7254.

3.4 Study IV: Tuning the Negative Thermal Expansion Behavior of the Metal-Organic Framework Cu_3BTC_2 by Retrofitting

The installation of the guest molecule between the OMS of the framework represents a case of retrofitting of a MOF. In fact, the Cu_3BTC_2 framework that consists of 4-connecting metal nodes and 3-connecting linkers gains additional connectivity by (partial) linking of the metal nodes through a linear cross linker (CL). Within the timeframe of this thesis, two inspiring articles were published dealing with the mechanical properties, *i.e.* thermal expansion coefficient and bulk modulus, of MOFs as a function of the defect concentration.⁵⁶⁻⁵⁷ Following this train of thought, retrofitting of MOFs can also be regarded as a case of defect engineering in which the OMS that are not connected by CLs represent a missing linker defect to the retrofitted network with higher connectivity. Is the CL fully incorporated into the structure, the defect-free state is restored. And indeed, it was demonstrated that retrofitting effects the mechanical stability of a MOF,¹¹⁷ whereas the impact on the lattice dynamics had not been investigated. This gap is closed by Study IV in which the lattice dynamics of $\text{TCNQ}@Cu_3\text{BTC}_2$ are investigated experimentally and computationally. High quality variable temperature powder X-ray diffraction (VTPXRD) data recorded at the synchrotron revealed that the negative thermal expansion of Cu_3BTC_2 can be tuned by the amount of TCNQ introduced into the structure. This observation is confirmed by force field calculations in which TCNQ is simulated by a mechanical spring between the OMS of the framework. In general, a monotonic increase of the thermal expansion coefficient and bulk modulus is observed with increasing degree of retrofitting. The suppression (“hardening”) of low energy lattice modes was identified as the mechanistic reason behind this macroscopic observation which translates to a blue shift of the respective bands in the far infrared (FIR) spectra. Ultimately, a better understanding of the lattice modes will also contribute to create a comprehensive model the electronic properties of $\text{TCNQ}@Cu_3\text{BTC}_2$.

The manuscript was written by the author of this thesis and edited by the seven co-authors, who contributed critically to the discussion of the results. The strategy and experiments were developed by the author of this thesis under the supervision of G. Kieslich. The synthesis and characterization were carried out by the author of this thesis. D. Bodesheim performed theoretical modelling of the lattice dynamics under the supervision of K. T. Butler and G. Kieslich. J. Mink helped with the evaluation of vibrational spectroscopy data. M. G. Ehrenreich helped with the VTPXRD measurements and V. Crocellà assisted with FIR measurements.

Reprinted with permission from *The Journal of the American Chemical Society*. Copyright (2019) American Chemical Society.

C. Schneider, D. Bodesheim, M. G. Ehrenreich, V. Crocellà, J. Mink, R. A. Fischer, K. T. Butler, G. Kieslich, Tuning the Negative Thermal Expansion Behavior of the Metal-Organic Framework Cu_3BTC_2 by Retrofitting. *J. Am. Chem. Soc.* **2019**, *141*, 10504-10509.

Tuning the Negative Thermal Expansion Behavior of the Metal–Organic Framework Cu_3BTC_2 by Retrofitting

Christian Schneider,[†] David Bodesheim,[†] Michael G. Ehrenreich,[†] Valentina Crocellà,[‡] János Mink,^{§,||} Roland A. Fischer,[‡] Keith T. Butler,[⊥] and Gregor Kieslich^{*,†}

[†]Department of Chemistry, Technical University of Munich, Lichtenbergstrasse 4, Garching D-85748, Germany

[‡]Department of Chemistry, NIS and INSTM Centre of Reference, University of Turin, Via Quarello 15, Torino I-10135, Italy

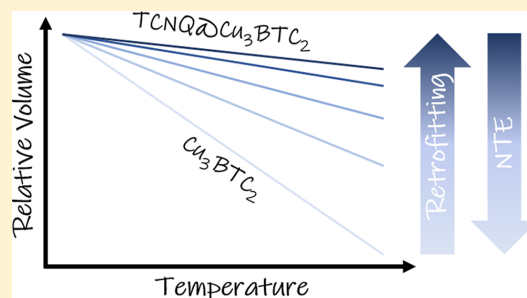
[§]Institute of Materials and Environmental Chemistry, Research Center of Natural Sciences, Hungarian Academy of Sciences, Budapest H-1519, Hungary

^{||}Research Institute for Biomolecular and Chemical Engineering, University of Pannonia, Veszprém H-8200, Hungary

[⊥]Scientific Computing Department, Rutherford Appleton Laboratory, Harwell Campus, Didcot OX11 0QX, United Kingdom

Supporting Information

ABSTRACT: The modular building principle of metal–organic frameworks (MOFs) presents an excellent platform to explore and establish structure–property relations that tie microscopic to macroscopic properties. Negative thermal expansion (NTE) is a common phenomenon in MOFs and is often ascribed to collective motions that can move through the structure at sufficiently low energies. Here, we show that the introduction of additional linkages in a parent framework, retrofitting, is an effective approach to access lattice dynamics experimentally, in turn providing researchers with a tool to alter the NTE behavior in MOFs. By introducing TCNQ (7,7,8,8-tetracyanoquinodimethane) into the prototypical MOF Cu_3BTC_2 (BTC = 1,3,5-benzenetricarboxylate; HKUST-1), NTE can be tuned between $\alpha_V = -15.3 \times 10^{-6} \text{ K}^{-1}$ (Cu_3BTC_2) and $\alpha_V = -8.4 \times 10^{-6} \text{ K}^{-1}$ (1.0TCNQ@ Cu_3BTC_2). We ascribe this phenomenon to a general stiffening of the framework as a function of TCNQ loading due to additional network connectivity, which is confirmed by computational modeling and far-infrared spectroscopy. Our findings imply that retrofitting is generally applicable to MOFs with open metal sites, opening yet another way to fine-tune properties in this versatile class of materials.



INTRODUCTION

Among the different phenomena in materials science and solid-state chemistry, it is the existence of counterintuitive materials properties that challenge our understanding of how to describe materials on a microscopic level. Properties such as negative thermal expansion (NTE),^{1–3} negative linear compressibility (NLC),^{4–6} or negative Poisson's ratio (NPR)^{7–9} tie the macroscopic world with the microscopic world, helping us continuously to sharpen our perception of how to see and understand certain phenomena in materials. Sometimes seen as scientific curiosities, such effects indeed have practical relevance. For instance, the thermal expansion (TE) behavior of a material is a crucial parameter in areas such as construction chemistry, dental care, or electrical engineering, where the fabrication, processing, and materials durability as a function of temperature variations play a critical role.^{10–13} An important example is the fabrication of optical components, such as mirrors used in big telescopes, where materials with zero thermal expansion coefficients around the typical working temperature ensure high-precision measurements.¹³

Focusing on the thermal expansion behavior of a material, we can distinguish between materials that show positive thermal expansion (PTE, $\alpha_V > 0$), zero thermal expansion (ZTE, $\alpha_V \approx 0$), and negative thermal expansion (NTE, $\alpha_V < 0$), with α_V being the volumetric thermal expansion coefficient:

$$\alpha_V = \frac{1}{V} \frac{dV}{dT} \quad (1)$$

where V is the volume of the unit cell and dV/dT the change of volume as a function of temperature. While the majority of investigated materials exhibit PTE, NTE has been discovered in a number of material classes such as metal oxides,^{14,15} metal cyanides,^{16,17} and zeolites.^{18,19} Recent research studies in this area focus on understanding the microscopic mechanism behind NTE in emerging materials, with the tunability of α_V being arguably one of the biggest challenges for experimentalists. It has been shown that α_V depends on various

Received: May 9, 2019

Published: June 11, 2019

parameters that can be accessed experimentally. For instance, the redox intercalation of Li^+ ions into ScF_3 is an effective method to control thermal expansion behavior from NTE to PTE.²⁰ Similarly, guest-dependent thermal expansion has been observed for various Prussian Blue analogues and related materials such as $\text{ZnPt}(\text{CN})_6$, $\text{Fe}_3[\text{Co}(\text{CN})_6]_2$, and $\text{Co}[(\text{Fe}(\text{CN})_5\text{NO})]$ where a complex relation exists between adsorbed H_2O or CO_2 molecules and α_V . Fundamentally, NTE in materials originates from either electronic or magnetic coupling phenomena or low energy phonons. In the latter case, collective motions are responsible for the on average shortened distances between respective building blocks.^{1,2} An elegant concept that has proved to be useful to understand NTE in various materials are rigid unit modes (RUMs). Initially developed to explain displacive phase transitions in silicates and related materials,² RUMs provide a rather intuitive approach to describe how lattice dynamics and NTE are linked on a microscopic level.

Metal-organic frameworks (MOFs) are one class of materials in which phonon-mediated NTE behavior is often observed. MOFs are coordination polymers constructed from metal nodes that are interconnected by polydentate ligands to form (porous) 2D or 3D networks.^{21,22} Notably, their building block principle as embodied in the reticular chemistry approach inherently reflects the RUM concept. In combination with the void pore space, it is easy to envision that only little energy is required for the excitation of (correlated) vibrations.²³ Examples include the iconic MOF-5 and Cu_3BTC_2 with thermal expansion coefficients of $\alpha_V = -39.3 \times 10^{-6} \text{ K}^{-1}$ and $\alpha_V = -12.3 \times 10^{-6} \text{ K}^{-1}$, respectively.^{24,25} MOF-5 is one of the better-investigated MOFs, where experimental and computational studies show that RUMs and trampoline-like vibrations of the 1,4-benzenedicarboxylate linker have a significant contribution to NTE in MOF-5.^{24,26,27} Furthermore, it was shown that lattice dynamics in MOF-5 can be accessed by adsorption of He or small organic molecules, which leads to increased thermal expansion coefficients.^{28,29} The highest NTE of a MOF to date was reported for UiO-66(Hf) ($\alpha_V = -97 \times 10^{-6} \text{ K}^{-1}$).³⁰ In general, the high degree of synthetic versatility of MOFs offers a great playground for experimentalists and physical chemists alike, providing an excellent platform for systematically investigating structure-property relationships.

In this context, the targeted incorporation of defects into a parent MOF has recently proved to be particularly exciting in the area of mechanical stability and catalysis.²⁹⁻³³ When taking a relatively broad definition for a defect, that is, defining a defect as a feature that breaks periodicity, it is possible to distinguish between point defects such as missing linker or missing node defects, and the situation where guest molecules that are incorporated into the pores break periodicity, that is, interstitial defects. Point defects in UiO-66(Hf) have recently been used to manipulate α_V , with a larger defect concentration leading to a decrease in NTE behavior. It was speculated that a volume effect together with the presence of metal-node related symmetry-breaking phenomena are responsible for this observation.³⁰ Likewise, point defects have been used to alter the mechanical response of UiO-66(Zr), where a complex relation between bulk modulus and defect concentration was found.³² It is important to note that the thermal expansion behavior and the bulk modulus are fundamentally linked through the lattice dynamics and in the big picture by entropy.² Following this thought, the postsynthetic introduc-

tion of additional connectivities between different open metal sites is intriguing and seems the natural development in the current attempts to exploit defect engineering as a tool for manipulating properties of MOFs. Only recently did Yaghi et al. report that the mechanically unstable MOF-520 can be stabilized by incorporation of a rigid 4,4'-biphenyldicarboxylate (BPDC) linker as an additional connectivity to afford a mechanically robust framework. They coined the term retrofitting, describing the postsynthetic introduction of additional network connectivity into a parent MOF. When full crystallographic occupancy of the retrofitted connectivity is obtained, the defect would have been fully incorporated into the structure motif of the network; however, only 70% occupancy was observed in the bulk powder, in principle presenting a defective state of the material. Zhou et al. followed the same approach, reporting on the incorporation of dicarboxylate ligands in the structure of the PCN-606 family with reaching occupancies of up to 56%.³⁴ Having these developments in mind, it is therefore intriguing to ask: "How does retrofitting influence the NTE behavior of a MOF?"

Here, we present a combined experimental and computational study, showing that the NTE behavior of MOFs can be tuned by retrofitting. As a model system, we focus on the MOF Cu_3BTC_2 (Figure 1a), which allows us to build on from the vast literature that exists on the host-guest chemistry in this system.³⁵⁻³⁸ It has been established that the vacant Cu coordination sites in Cu_3BTC_2 can act as anchor points for molecules such as TCNQ. These molecules bridge two adjacent metal sites, potentially creating a secondary network within Cu_3BTC_2 .³⁹ Crystallographic evidence for the ordered arrangement of TCNQ in the bridging position has recently been found when $\text{TCNQ}@Cu_3\text{BTC}_2$ is prepared by TCNQ incorporation via the vapor phase.⁴⁰ It has been observed experimentally that up to one molar equivalent of TCNQ can be introduced into the structure of Cu_3BTC_2 , confirming previous computational studies.⁴¹ The vapor phase loading of TCNQ into Cu_3BTC_2 allows for a precise control over the amount of TCNQ introduced into the framework, providing us with a tool to investigate the impact of TCNQ incorporation on the negative thermal expansion behavior. Therefore, we performed variable-temperature powder X-ray diffraction (VTPXRD) experiments as well as far-infrared (FIR) spectroscopy on a series of $\text{TCNQ}@Cu_3\text{BTC}_2$ samples. We

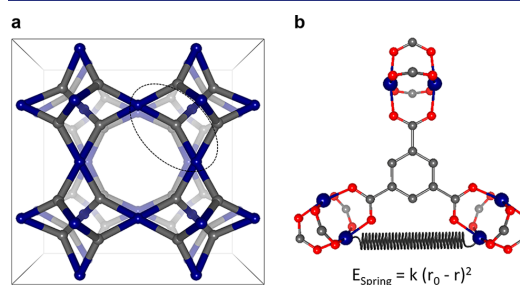


Figure 1. (a) The *tbo* topology of Cu_3BTC_2 in which blue and gray spheres represent metal nodes and linker molecules, respectively. The dashed ellipse indicates the position of the zoom-in (b), that is, three Cu paddlewheel units interconnected by BTC. Neighboring paddlewheel units can be bridged by a TCNQ molecule, which in our computational model is approximated by a mechanical spring.

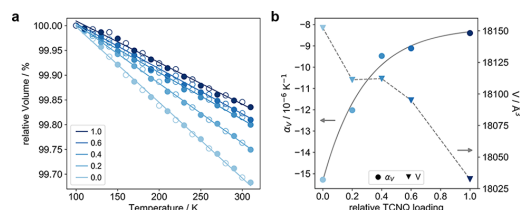


Figure 2. (a) Relative unit cell volume of $x\text{TCNQ}@Cu_3\text{BTC}_2$ (x given in the legend) plotted against the temperature. Data from cooling (empty circles) and heating (filled circles) cycle were recorded in 20 K steps. (b) Thermal expansion coefficient (α_V) and unit cell volume (V , at 100 K) of $x\text{TCNQ}@Cu_3\text{BTC}_2$ plotted against the relative TCNQ loading. The solid and dashed lines are a guide to the eyes.

combine our experimental results with model calculations, in which the bridging TCNQ is modeled by a harmonic spring (Figure 1b), allowing us insight into the phonon-based mechanism for the tunability of NTE behavior in this system qualitatively.

RESULTS AND DISCUSSION

Powder samples of $x\text{TCNQ}@Cu_3\text{BTC}_2$ with $x = 0, 0.2, 0.4, 0.6,$ and 1.0 were prepared by following an optimized vapor phase assisted synthesis; see [Experimental Section](#). We previously showed that this approach is superior to wet chemical infiltration techniques, enabling the preparation of samples that maintain a high residual BET surface area upon TCNQ incorporation,⁴⁰ for example, $865.9 \text{ m}^2/\text{g}$ for $1.0\text{TCNQ}@Cu_3\text{BTC}_2$ (see the [Supporting Information](#)). High-resolution variable-temperature powder X-ray diffractograms were recorded at the Diamond Light Source, beamline I11. Lattice parameters and volumes were extracted through a Pawley profile fit analysis within the space-group $Fm\bar{3}m$. Contour plots of all powder X-ray diffraction patterns and statistics of all refinements are given in the [Supporting Information](#). The volume as a function of temperature for different $x\text{TCNQ}@Cu_3\text{BTC}_2$ loadings is shown in Figure 2a. The thermal expansion coefficient α_V is extracted from the slope of the linear regression, following eq 1. The largest α_V is found for $x = 0$ with $\alpha_V = -15.3 \times 10^{-6} \text{ K}^{-1}$. This value is in good agreement with literature data, where an NTE coefficient of $\alpha_V = -12.3 \times 10^{-6} \text{ K}^{-1}$ has been reported for guest-free $Cu_3\text{BTC}_2$.²⁵ The slightly higher value of α_V obtained in this study likely results from a different preparation protocol, which involves very extensive solvent exchanging steps and high-vacuum activation; see the [Experimental Section](#) for details. With increasing the TCNQ loading from $x = 0.2$ to $x = 1.0$, α_V decreases monotonically to $\alpha_V = -8.4 \times 10^{-6} \text{ K}^{-1}$ for $x = 1.0$; see Figure 2b. PTE is not observed, which is different from related studies that show a guest-dependent change from NTE to PTE.^{28,29} We attribute this difference to the relatively large residual porosity at high TCNQ loadings, which seems to maintain a part of the mechanism that is responsible for NTE in $Cu_3\text{BTC}_2$. Therefore, TCNQ loading presents a valuable tool for fine-tuning the negative thermal expansion behavior of $Cu_3\text{BTC}_2$, implicating that TCNQ incorporation directly affects the underlying NTE mechanism in $Cu_3\text{BTC}_2$. We now turn our attention toward the origin for altered NTE.

Previously, it has been shown that NTE in $Cu_3\text{BTC}_2$ originates from low energy collective lattice modes and local

distortions of the linker and node, that is, trampoline-like motions of BTC and rotor-like motions of the Cu paddlewheel moiety.^{25,42,43} In other words, increasing the temperature leads to an activation of phonon modes and vibrations that lead to a volume contraction. Staying within the quasi-harmonic approximation, it has been shown that α_V can be expressed as⁴⁴

$$\alpha_V(T) = \frac{1}{KV} \sum_i \gamma_i C_{Vi}(T) \quad (2)$$

with K the bulk modulus, V the volume, γ_i the Grüneisen parameter, and $C_{Vi}(T)$ the isochoric specific heat. For the $x\text{TCNQ}@Cu_3\text{BTC}_2$ system studied here, a decrease of $|\alpha_V|$ and a decreased cell volume are observed as a function of TCNQ loading; see Figure 2b. On the basis of eq 2, such a behavior first seems contradicting; however, looking at the previous finding by Yaghi et al., who reported a significant increase of bulk modulus in MOF-520 after retrofitting, it is a reasonable assumption that any volume contributions are outweighed by a significant stiffening of the framework after TCNQ incorporation. Therefore, we ascribe the here observed decrease of $|\alpha_V|$ as a function of TCNQ loading to an allover stiffening of the $Cu_3\text{BTC}_2$ framework, that is, an increase of bulk modulus in eq 2. It is important to highlight at this point that the complexity behind the origin of NTE, particularly in materials with many different chemical interactions and open pore space such as MOFs, currently challenges our understanding. Therefore, it is worth mentioning that some results have been reported in the past, in which a correlation between the reduction of unit cell volume and a decrease of $|\alpha_V|$ has been observed.^{16,19,30,45}

While the reduced NTE in $\text{TCNQ}@Cu_3\text{BTC}_2$ is expected to have major contributions from the bulk term $1/(KV)$ in eq 2, it is also interesting to consider the summation, which contains information about the individual modes. For instance, γ_i tells us how the frequency of a mode responds to volume changes, with a negative correlation ($\gamma_i < 0$) corresponding to NTE. The factor $C_{Vi}(T)$ then only applies a weighting scheme, because lower frequency modes have higher thermal populations and in turn have a larger overall contribution. To gain insight into how collective modes are affected through TCNQ infiltration, we developed a heuristic spring model of the situation. In this model, TCNQ is simplified as a harmonic spring, which bridges the adjacent Cu coordination sites (see Figure 1b). We used this model to apply force-field-based phonon calculations within the quasi-harmonic approximation, accessing the change of lattice dynamics as a function of spring constant strength qualitatively. In a first step, we calculated the thermal expansion coefficient of the spring-free $Cu_3\text{BTC}_2$ (or similarly spring strength $k = 0 \text{ eV}/\text{\AA}^2$) to verify that the applied force field can indeed reproduce NTE behavior. Our calculations lead to $\alpha_V = -18.7 \times 10^{-6} \text{ K}^{-1}$, which is in reasonable agreement with our experimentally observed value. At this point, we want to emphasize that the applied computationally methodology is not set up to reproduce experimental results but to investigate the impact of TCNQ incorporation on the lattice dynamics qualitatively, thereby providing us with a scientific insight into the underlying changes in lattice dynamics. In a second step, we then gradually increased the force constant between $k = 0-7 \text{ eV}/\text{\AA}^2$, typical values for Cu-N force constants⁴⁶ (Figure 3a). As compared to our experiment, this increase helps us to understand the impact of TCNQ on the lattice dynamics

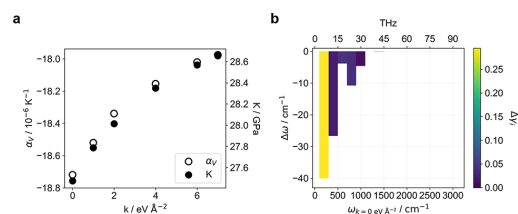


Figure 3. (a) Calculated thermal expansion coefficient α_V and bulk modulus K with variation of the spring constant k between neighboring Cu paddlewheel moieties. (b) Difference in mode frequencies between $k = 0$ and $k = 7 \text{ eV \AA}^{-2}$, with a negative value of $\Delta\omega$ indicating a stiffening of the mode and in turn a decrease in the thermal expansion coefficient α_V . The color code of the bar plot reflects the change of $\Delta\gamma_p$, with the largest changes observed for low energy modes.

and is not designed to model the increasing TCNQ content. However, we observe that $|\alpha_V|$ decreases and K increases as a function of spring constant, generally supporting our previous speculation that the reduction of NTE in TCNQ@Cu₃BTC₃ is mainly driven by a stiffening of the framework, that is, an increase of K as a function of TCNQ loading. Interestingly, α_V remains negative for all spring constants, revealing that the sum in eq 2 remains negative despite the presence of the spring. To investigate the impact of the spring on the phonon modes in more detail, we calculated the difference of frequencies $\Delta\omega = \omega_0 - \omega_7$ at $k = 7$ and 0 eV \AA^{-2} ; see Figure 3b. A mode stiffening in the low energy region can be observed, while modes at frequencies larger than approximately 1250 cm^{-1} (33 THz) show a small or vanishing change in energy. We also observe some changes in the mode-Grüneisen parameters as a function of ω ; however, the all-over summation from eq 2 remains negative, and a negative sign of α_V is maintained.

With these results on hand, we performed FIR and Raman spectroscopy to probe if any evidence for mode changes as a function of TCNQ incorporation become evident. It should be pointed out, however, that FIR and Raman spectroscopy only probe phonon dynamics at wave vectors close to 0. Moreover, only phonon changes related to optic modes are accessible due to selection rules of the method; however, previously it has been shown that optic modes can have an impact on the NTE behavior in MOFs; for instance, the above-mentioned bending mode of the benzenedicarboxylate linker in MOF-5 represents such a mode.^{24,26,27} Raman scattering of Cu₃BTC₂ before and after activation (Figure S10) is in excellent agreement with reference data,³⁵ while the Raman data provided by Ryder et al. match our as-synthesized spectra.⁴³ Note that prior to TCNQ loading, Cu₃BTC₂ powder has been thoroughly activated, limiting quantitative comparison with literature data due to the large impact of solvent or adsorbed water on the position and intensity of respective modes.³⁵ Looking at our FIR and Raman spectra, FIR measurements show several bands shifting to higher frequencies as a function of TCNQ loading, while no obvious trends are visible in our Raman data below 100 cm^{-1} (see Figure S16). For instance, all FIR bands within the frequency region $30\text{--}80 \text{ cm}^{-1}$ shift to higher frequencies; see Figure 4a for a direct comparison of FIR spectra of Cu₃BTC₂ and 1.0TCNQ@Cu₃BTC₂. The trend of FIR frequencies across the whole series is shown in Figure 4b (full FIR spectra are provided in the Supporting Information). Interestingly, for bands at higher frequencies, a small shift to

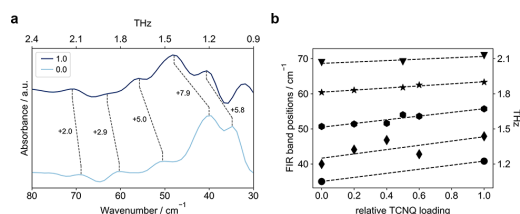


Figure 4. (a) Low-frequency FIR spectra of Cu₃BTC₂ (light blue) and 1.0TCNQ@Cu₃BTC₂ (dark blue). The spectra are normalized, and a vertical offset is applied for clarity. (b) Shift of FIR band positions with TCNQ loading. All corresponding FIR spectra are provided in the Supporting Information.

lower frequencies is observed. For instance, the band at 505 cm^{-1} for Cu₃BTC₂ shifts to 501 cm^{-1} for the sample with $x = 1.0$ (see Figure S12). The observed trend in our spectroscopic FTIR data is therefore in broad qualitative agreement with our calculations, in which the increase in frequencies in the low energy region is also observed; however, the calculations indicate mode stiffening up to frequencies of 1250 cm^{-1} , which is significantly larger than observed experimentally. Here, we would like to point out that our calculations were set up to broadly mimic the situation given by TCNQ incorporation into the Cu₃BTC₂ framework, to give insight into the general effect of TCNQ on the framework lattice dynamics.

CONCLUSION

We have shown that the postsynthetic incorporation of additional connectivity into a MOF, retrofitting, is a suitable approach to control the thermal expansion behavior. As a prototypical example, we studied the incorporation of TCNQ into Cu₃BTC₂, a host-guest system that caused some excitement in the context of electrically conductive MOFs. We show that NTE in Cu₃BTC₃ can be controlled as a function of TCNQ loading, an effect that is ascribed to a stiffening of the material. Our heuristic computational model shows, however, that a certain mode stiffening occurs at the same time, emphasizing the interrelation of the complex parameters that determine the magnitude as well as the sign of thermal expansion behavior in MOFs.

At this point, a few points are important to emphasize. First, it should be noted that examples of retrofitted MOFs were known before retrofitting as a concept was proposed in 2017;^{39,47–50} however, retrofitting per se is a useful categorization that describes a distinct approach to postsynthetically modify MOFs. Moreover, on the basis of our results, it seems that retrofitting is a universal approach to access materials properties related to lattice dynamics, which in principle can be applied to all MOFs with open metal sites or, more generally, functional groups and sites. Looking at retrofitting from a more conceptually perspective, retrofitting of MOFs leads to a defective state, when the incorporated guest exhibits only partial occupancy. It will be interesting to see if in the future full occupancy can be achieved, thereby leaving the territory of a defective state. It should be emphasized that such an introduction of defects is inherently absent in nonporous materials, highlighting the opportunities experimentalists have in manipulating materials properties of MOFs.

EXPERIMENTAL SECTION

Synthesis. Cu_3BTC_2 samples with different loadings of TCNQ were synthesized following an optimized vapor phase infiltration procedure⁴⁰ using high-vacuum glass ampoules to enhance the sublimation and diffusion of TCNQ. Stoichiometric amounts of TCNQ were thoroughly mixed with activated Cu_3BTC_2 (100 mg) and filled into high-vacuum glass ampoules, which were then evacuated to 10^{-5} mbar and flame-sealed. The ampoules were placed in a convection oven at 180 °C for 72 h to yield a series of $x\text{TCNQ}@ \text{Cu}_3\text{BTC}_2$ with $x = n(\text{TCNQ})/n(\text{Cu}_3\text{BTC}_2) = 0.2, 0.4, \dots, 1.0$. Activated and TCNQ-loaded samples were handled under argon at all times to avoid adsorption of water, which would compromise the obtained results. All measurements were performed under inert conditions.

VTPXRD. High-resolution variable-temperature powder X-ray diffraction was performed at beamline I11 of the Diamond Light Source in transmission geometry. Therefore, the samples were filled into 0.5 mm quartz capillaries inside an Ar-filled glovebox and sealed using two-component adhesive. The operating wavelength was $\lambda = 0.824945(10)$ Å, and the photosensitive detector (PSD) was used for data collection. Temperature control was applied by using an Oxford Cryosystem, in which the samples were first cooled down from rt to 100 K in 20 K steps before the temperature was increased from 110 to 310 K. Before every measurement, the temperature was allowed to stabilize for 120 s. Quantitative data analysis, that is, Pawley profile fits to extract lattice parameters, was performed by using TOPAS academic v5.

Far-Infrared Spectroscopy. Inside the glovebox, the samples were dispersed in solid paraffin wax and pressed into pellets. Far-infrared spectra were recorded under a flow of dry N_2 on a Bruker VERTEX 70 V vacuum spectrometer in the range of $600\text{--}30\text{ cm}^{-1}$. The instrument was equipped with a Si-supported beamsplitter, a ceramic source, and a DTGS detector using a GladiATR accessory (Pike, U.S.).

Raman Spectroscopy. Samples were loaded into glass capillaries under inert conditions (Ar glovebox) and sealed prior to measurements. Raman scattering was performed on a Renishaw inVia Raman microscope RE04 using an excitation wavelength of 532 nm. The data were collected with a CCD detector and evaluated using WiRE 4.2.

Calculations. Thermal expansion coefficients were calculated in a quasi-harmonic approach using the force-field code GULP⁵¹ with the UFF4MOF library⁵² by applying cell parameter deviations of $\pm 0.5\%$ in 0.1% steps. In all calculations, a free-energy optimizer was used in the approximation of only considering the first 100 modes at the Gamma point. Mode-Grüneisen parameters were calculated from the frequency and volume changes of the maximum expansion and contraction and equilibrium structure.

ASSOCIATED CONTENT

Supporting Information

The Supporting Information is available free of charge on the ACS Publications website at DOI: 10.1021/jacs.9b04755.

Further information about the synthesis, porosimetry measurements, VTPXRD measurements, and vibrational spectroscopy (PDF)

AUTHOR INFORMATION

Corresponding Author

*gregor.kieslich@tum.de

ORCID

Christian Schneider: 0000-0001-7231-3266

Valentina Crocellà: 0000-0002-3606-8424

Roland A. Fischer: 0000-0002-7532-5286

Keith T. Butler: 0000-0001-5432-5597

Gregor Kieslich: 0000-0003-2038-186X

Notes

The authors declare no competing financial interest.

ACKNOWLEDGMENTS

We like to thank Chiu Tang for support during data collection at beamline I11 at the Diamond Light Source (EE17914) and Pia Vervoorts for help with porosimetry experiments. C.S. acknowledges his scholarships from the Studienstiftung des Deutschen Volkes and from the Fonds der Chemischen Industrie. G.K. gratefully thanks the Fonds der Chemischen Industrie and the DFG SPP1928 (COORNETs) for financial support.

REFERENCES

- (1) Miller, W.; Smith, C. W.; Mackenzie, D. S.; Evans, K. E. Negative Thermal Expansion: A Review. *J. Mater. Sci.* **2009**, *44*, 5441–5451.
- (2) Dove, M. T.; Fang, H. Negative Thermal Expansion and Associated Anomalous Physical Properties: Review of the Lattice Dynamics Theoretical Foundation. *Rep. Prog. Phys.* **2016**, *79*, 066503.
- (3) Coates, C. S.; Goodwin, A. L. How to Quantify Isotropic Negative Thermal Expansion: Magnitude, Range, or Both? *Mater. Horiz.* **2019**, *6*, 211–218.
- (4) Li, W.; Probert, M. R.; Kosa, M.; Bennett, T. D.; Thirumurugan, A.; Burwood, R. P.; Parinello, M.; Howard, J. A. K.; Cheetham, A. K. Negative Linear Compressibility of a Metal–Organic Framework. *J. Am. Chem. Soc.* **2012**, *134*, 11940–11943.
- (5) Cairns, A. B.; Catafesta, J.; Levelut, C.; Rouquette, J.; van der Lee, A.; Peters, L.; Thompson, A. L.; Dmitriev, V.; Haines, J.; Goodwin, A. L. Giant Negative Linear Compressibility in Zinc Dicyanoaurate. *Nat. Mater.* **2013**, *12*, 212.
- (6) Baughman, R. H.; Stafström, S.; Cui, C.; Dantas, S. O. Materials with Negative Compressibilities in One or More Dimensions. *Science* **1998**, *279*, 1522–1524.
- (7) Huang, C.; Chen, L. Negative Poisson's Ratio in Modern Functional Materials. *Adv. Mater.* **2016**, *28*, 8079–8096.
- (8) Rothenburg, L.; Ai, Berlin, A. L.; Bathurst, R. J. Microstructure of Isotropic Materials with Negative Poisson's Ratio. *Nature* **1991**, *354*, 470–472.
- (9) Lakes, R. Foam Structures with a Negative Poisson's Ratio. *Science* **1987**, *235*, 1038–1040.
- (10) Versluis, A.; Douglas, W. H.; Sakaguchi, R. L. Thermal Expansion Coefficient of Dental Composites Measured with Strain Gauges. *Dent. Mater.* **1996**, *12*, 290–294.
- (11) Sleight, A. W. Negative Thermal Expansion Materials. *Curr. Opin. Solid State Mater. Sci.* **1998**, *3*, 128–131.
- (12) Tran, K. D.; Groshens, T. J.; Nelson, J. G. Fabrication of Near-Sero Thermal Expansion ($\text{FexSc}_{1-x}\text{2Mo}_3\text{O}_{12}\text{--MoO}_3$ Ceramic Composite using the reaction sintering process. *Mater. Sci. Eng., A* **2001**, *303*, 234–240.
- (13) Closmann, C.; Sleight, A. W.; Haygarth, J. C. Low-Temperature Synthesis of ZrW_2O_8 and Mo-Substituted ZrW_2O_8 . *J. Solid State Chem.* **1998**, *139*, 424–426.
- (14) Martinek, C.; Hummel, F. A. Linear Thermal Expansion of Three Tungstates. *J. Am. Ceram. Soc.* **1968**, *51*, 227–228.
- (15) S. O. Evans, J. Negative Thermal Expansion Materials. *J. Chem. Soc., Dalton Trans.* **1999**, 3317–3326.
- (16) Goodwin, A. L.; Kepert, C. J. Negative Thermal Expansion and Low-Frequency Modes in Cyanide-Bridged Framework Materials. *Phys. Rev. B: Condens. Matter Mater. Phys.* **2005**, *71*, 140301.
- (17) Goodwin, A. L.; Kennedy, B. J.; Kepert, C. J. Thermal Expansion Matching via Framework Flexibility in Zinc Dicyanomellates. *J. Am. Chem. Soc.* **2009**, *131*, 6334–6335.
- (18) Attfield, M. P.; Sleight, A. W. Exceptional Negative Thermal Expansion in $\text{AlPO}_4\text{--}17$. *Chem. Mater.* **1998**, *10*, 2013–2019.
- (19) Lightfoot, P.; Woodcock, D. A.; Maple, M. J.; Villaescusa, L. A.; Wright, P. A. The Widespread Occurrence of Negative Thermal Expansion in Zeolites. *J. Mater. Chem.* **2001**, *11*, 212–216.

- (20) Chen, J.; Gao, Q.; Sanson, A.; Jiang, X.; Huang, Q.; Carnera, A.; Rodriguez, C. G.; Olivi, L.; Wang, L.; Hu, L.; Lin, K.; Ren, Y.; Lin, Z.; Wang, C.; Gu, L.; Deng, J.; Attfield, J. P.; Xing, X. Tunable Thermal Expansion in Framework Materials Through Redox Intercalation. *Nat. Commun.* **2017**, *8*, 14441.
- (21) Tranchemontagne, D. J.; Mendoza-Cortes, J. L.; O'Keeffe, M.; Yaghi, O. M. Secondary Building Units, Nets and Bonding in the Chemistry of Metal-Organic Frameworks. *Chem. Soc. Rev.* **2009**, *38*, 1257–1283.
- (22) Kitagawa, S.; Kitaura, R.; Noro, S.-i. Functional porous coordination polymers. *Angew. Chem., Int. Ed.* **2004**, *43*, 2334–2375.
- (23) Lock, N.; Christensen, M.; Wu, Y.; Peterson, V. K.; Thomsen, M. K.; Piltz, R. O.; Ramirez-Cuesta, A. J.; McIntyre, G. J.; Norén, K.; Kutteh, R.; Kepert, C. J.; Kearley, G. J.; Iversen, B. B. Scrutinizing Negative Thermal Expansion in MOF-5 by Scattering Techniques and Ab Initio Calculations. *Dalton Trans.* **2013**, *42*, 1996–2007.
- (24) Lock, N.; Wu, Y.; Christensen, M.; Cameron, L. J.; Peterson, V. K.; Bridgeman, A. J.; Kepert, C. J.; Iversen, B. B. Elucidating Negative Thermal Expansion in MOF-5. *J. Phys. Chem. C* **2010**, *114*, 16181–16186.
- (25) Wu, Y.; Kobayashi, A.; Halder, G. J.; Peterson, V. K.; Chapman, K. W.; Lock, N.; Southon, P. D.; Kepert, C. J. Negative Thermal Expansion in the Metal–Organic Framework Material Cu₃(1,3,5-benzenetricarboxylate)₂. *Angew. Chem., Int. Ed.* **2008**, *47*, 8929–8932.
- (26) Zhou, W.; Wu, H.; Yildirim, T.; Simpson, J. R.; Walker, A. H. Origin of the Exceptional Negative Thermal Expansion in Metal-Organic Framework-5 Zn₄O(1,4-Benzenedicarboxylate)₃. *Phys. Rev. B: Condens. Matter Mater. Phys.* **2008**, *78*, 054114.
- (27) Rimmer, L. H. N.; Dove, M. T.; Goodwin, A. L.; Palmer, D. C. Acoustic Phonons and Negative Thermal Expansion in MOF-5. *Phys. Chem. Chem. Phys.* **2014**, *16*, 21144–21152.
- (28) Lock, N.; Christensen, M.; Kepert, C. J.; Iversen, B. B. Effect of Gas Pressure on Negative Thermal Expansion in MOF-5. *Chem. Commun.* **2013**, *49*, 789–791.
- (29) Balestra, S. R. G.; Bueno-Perez, R.; Hamad, S.; Dubbeldam, D.; Ruiz-Salvador, A. R.; Calero, S. Controlling Thermal Expansion: A Metal–Organic Frameworks Route. *Chem. Mater.* **2016**, *28*, 8296–8304.
- (30) Cliffe, M. J.; Hill, J. A.; Murray, C. A.; Coudert, F.-X.; Goodwin, A. L. Defect-Dependent Colossal Negative Thermal Expansion in UiO-66(Hf) Metal–Organic Framework. *Phys. Chem. Chem. Phys.* **2015**, *17*, 11586–11592.
- (31) Dissegna, S.; Epp, K.; Heinz, W. R.; Kieslich, G.; Fischer, R. A. Defective Metal-Organic Frameworks. *Adv. Mater.* **2018**, *30*, 1704501.
- (32) Dissegna, S.; Vervoorts, P.; Hobday, C. L.; Düren, T.; Daisenberger, D.; Smith, A. J.; Fischer, R. A.; Kieslich, G. Tuning the Mechanical Response of Metal–Organic Frameworks by Defect Engineering. *J. Am. Chem. Soc.* **2018**, *140*, 11581–11584.
- (33) Kapustin, E. A.; Lee, S.; Alshammari, A. S.; Yaghi, O. M. Molecular Retrofitting Adapts a Metal–Organic Framework to Extreme Pressure. *ACS Cent. Sci.* **2017**, *3*, 662–667.
- (34) Lollar, C. T.; Pang, J.; Qin, J.-s.; Yuan, S.; Powell, J. A.; Zhou, H.-C. Thermodynamically Controlled Linker Installation in Flexible Zirconium Metal–Organic Frameworks. *Cryst. Growth Des.* **2019**, *19*, 2069–2073.
- (35) Prestipino, C.; Regli, L.; Vitillo, J. G.; Bonino, F.; Damin, A.; Lamberti, C.; Zecchina, A.; Solari, P.; Kongshaug, K.; Bordiga, S. Local Structure of Framework Cu (II) in HKUST-1 Metallorganic Framework: Spectroscopic Characterization upon Activation and Interaction with Adsorbates. *Chem. Mater.* **2006**, *18*, 1337–1346.
- (36) Allendorf, M. D.; Foster, M. E.; Léonard, F.; Stavila, V.; Feng, P. L.; Doty, F. P.; Leong, K.; Ma, E. Y.; Johnston, S. R.; Talin, A. A. Guest-Induced Emergent Properties in Metal–Organic Frameworks. *J. Phys. Chem. Lett.* **2015**, *6*, 1182–1195.
- (37) Hendon, C. H.; Walsh, A. Chemical Principles Underpinning the Performance of The Metal-Organic Framework HKUST-1. *Chem. Sci.* **2015**, *6*, 3674–3683.
- (38) Souza, B. E.; Rudić, S.; Titov, K.; Babal, A. S.; Taylor, J. D.; Tan, J.-C. Guest–Host Interactions of Nanoconfined Anti-Cancer Drug in Metal–Organic Framework Exposed by Terahertz Dynamics. *Chem. Commun.* **2019**, *55*, 3868–3871.
- (39) Talin, A. A.; Centrone, A.; Ford, A. C.; Foster, M. E.; Stavila, V.; Haney, P.; Kinney, R. A.; Szalai, V.; El Gabaly, F.; Yoon, H. P.; Léonard, F.; Allendorf, M. D. Tunable Electrical Conductivity in Metal-Organic Framework Thin-Film Devices. *Science* **2014**, *343*, 66–69.
- (40) Schneider, C.; Ukaj, D.; Koerver, R.; Talin, A. A.; Kieslich, G.; Pujari, S. P.; Zuilhof, H.; Janek, J.; Allendorf, M. D.; Fischer, R. A. High Electrical Conductivity and High Porosity in a Guest@MOF Material: Evidence of TCNQ Ordering within Cu₃BTC₂ Micropores. *Chem. Sci.* **2018**, *9*, 7405–7412.
- (41) Erickson, K. J.; Léonard, F.; Stavila, V.; Foster, M. E.; Spataru, C. D.; Jones, R. E.; Foley, B. M.; Hopkins, P. E.; Allendorf, M. D.; Talin, A. A. Thin Film Thermoelectric Metal–Organic Framework with High Seebeck Coefficient and Low Thermal Conductivity. *Adv. Mater.* **2015**, *27*, 3453–3459.
- (42) Peterson, V. K.; Kearley, G. J.; Wu, Y.; Ramirez-Cuesta, A. J.; Kemmer, E.; Kepert, C. J. Local Vibrational Mechanism for Negative Thermal Expansion: A Combined Neutron Scattering and First-Principles Study. *Angew. Chem., Int. Ed.* **2010**, *49*, 585–588.
- (43) Ryder, M. R.; Civalieri, B.; Cinque, G.; Tan, J.-C. Discovering Connections between Terahertz Vibrations and Elasticity Underpinning the Collective Dynamics of the HKUST-1 Metal–Organic Framework. *CrystEngComm* **2016**, *18*, 4303–4312.
- (44) Wang, K.; Reeber, R. R. Mode Grüneisen Parameters and negative Thermal Expansion of Cubic ZrW₂O₈ and ZrMo₂O₈. *Appl. Phys. Lett.* **2000**, *76*, 2203–2204.
- (45) Chapman, K. W.; Chupas, P. J.; Kepert, C. J. Compositional Dependence of Negative Thermal Expansion in the Prussian Blue Analogues MIIPtIV(CN)₆ (M = Mn, Fe, Co, Ni, Cu, Zn, Cd). *J. Am. Chem. Soc.* **2006**, *128*, 7009–7014.
- (46) Wong, P. T. T.; Brewer, D. G. Nature of the Coordination Bond in Metal Complexes of Substituted Pyridine Derivatives. II. The Far Infrared Spectra and Metal–Ligand Force Constants of Copper Complexes of 4-Substituted Pyridines. *Can. J. Chem.* **1968**, *46*, 139–148.
- (47) Chen, C. X.; Wei, Z.; Jiang, J. J.; Fan, Y. Z.; Zheng, S. P.; Cao, C. C.; Li, Y. H.; Fenske, D.; Su, C. Y. Precise Modulation of the Breathing Behavior and Pore Surface in Zr-MOFs by Reversible Post-Synthetic Variable-Spacer Installation to Fine-Tune the Expansion Magnitude and Sorption Properties. *Angew. Chem., Int. Ed.* **2016**, *55*, 9932–9936.
- (48) Chen, C.-X.; Wei, Z.-W.; Jiang, J.-J.; Zheng, S.-P.; Wang, H.-P.; Qiu, Q.-F.; Cao, C.-C.; Fenske, D.; Su, C.-Y. Dynamic Spacer Installation for Multirole Metal–Organic Frameworks: A New Direction toward Multifunctional MOFs Achieving Ultrahigh Methane Storage Working Capacity. *J. Am. Chem. Soc.* **2017**, *139*, 6034–6037.
- (49) Wang, T. C.; Hod, I.; Audu, C. O.; Vermeulen, N. A.; Nguyen, S. T.; Farha, O. K.; Hupp, J. T. Rendering High Surface Area, Mesoporous Metal–Organic Frameworks Electronically Conductive. *ACS Appl. Mater. Interfaces* **2017**, *9*, 12584–12591.
- (50) Yuan, S.; Lu, W.; Chen, Y.-P.; Zhang, Q.; Liu, T.-F.; Feng, D.; Wang, X.; Qin, J.; Zhou, H.-C. Sequential Linker Installation: Precise Placement of Functional Groups in Multivariate Metal–Organic Frameworks. *J. Am. Chem. Soc.* **2015**, *137*, 3177–3180.
- (51) Gale, J. D.; Rohl, A. L. The General Utility Lattice Program (GULP). *Mol. Simul.* **2003**, *29*, 291–341.
- (52) Addicoat, M. A.; Vankova, N.; Akter, I. F.; Heine, T. Extension of the Universal Force Field to Metal–Organic Frameworks. *J. Chem. Theory Comput.* **2014**, *10*, 880–891.

3.5 Study V: Retrofitting Metal-Organic Frameworks

As described in chapter 1.3 and demonstrated in Study IV, retrofitting is a powerful new tool to post-synthetically manipulate mechanical and electronic properties of MOFs. However, to understand the full potential of this method more examples of retrofitted MOFs are necessary. For this purpose, two approaches are common, namely sophisticated theoretical modeling or trial and error experiments guided by chemical intuition. To streamline those efforts, the question arises: “Is there a rational approach to assessing the fit of a cross linker in a given MOF?” Breaking down the complex situation, in Study V three major factors were identified that determine whether a molecule qualifies as a CL to a particular MOF or not. These are (i) the geometry of the CL, (ii) the relative position of the OMS in the MOF, and (iii) the potential energy between the OMS and the donor group of the CL. Factors (i) and (ii) can simply be extracted from the DFT optimized structure of the CL and from the crystal structure of the MOF. The interaction potential between MOF and CL can be approximated by DFT calculations of a simple molecular model system. With these three input values in hand, a program based on open-source code was developed and named *RetroFit* and used to test a library of potential CLs for a particular MOF at minimal computational cost. Testing *RetroFit* for the prototypical MOF Cu_3BTC_2 , a series of suitable dinitrile-CLs were identified of which three were chosen for experimental validation. Not only the successful formation of three new CL@MOF systems could be demonstrated, also the three new materials show the same ordering phenomenon as observed in $\text{TCNQ@Cu}_3\text{BTC}_2$ (compare Study II). To show the full potential of *RetroFit*, the same library of CLs was tested for retrofitting the anisotropic MOFs $\text{Cu}_2(\text{BPTC})$ (BPTC = biphenyl-3,3',5,5'-tetracarboxylate, NOTT-100) and $\text{Cu}_2(\text{TPTC})$ (TPTC = [1,1':4',1'']terphenyl-3,3'',5,5''-tetracarboxylate, NOTT-101), which exhibit two potential binding sites of different geometries. The results show that the two different binding sites allow a distinction between CLs of different size and shape and include the possibility of retrofitting a MOF with two (or more) different CLs. Therefore, this work represents a significant contribution to the development of many further retrofitted MOFs.

The manuscript was written by the author of this thesis and edited by the four co-authors, who contributed critically to the discussion of the results. The strategy for the computational tool and the experiments were developed by the author of this thesis under the supervision of G. Kieslich. The synthesis and characterization of the materials were done by the author of this thesis. D. Bodesheim performed DFT optimization for the CL molecules and wrote the code for the *RetroFit* program under the supervision of the author of this thesis. J. Keupp performed single point DFT calculations for the Cu paddlewheel – acetonitrile complex.

C. Schneider[‡], D. Bodesheim[‡], J. Keupp, R. Schmid, G. Kieslich, Retrofitting Metal-Organic Frameworks. *Nat. Commun.* **2019**, *10*, 4921.

[‡] These authors contributed equally.



ARTICLE

<https://doi.org/10.1038/s41467-019-12876-1>

OPEN

Retrofitting metal-organic frameworks

Christian Schneider ^{1,3}, David Bodesheim^{1,3}, Julian Keupp ², Rochus Schmid ² & Gregor Kieslich ^{1*}

The post-synthetic installation of linker molecules between open-metal sites (OMSs) and undercoordinated metal-nodes in a metal-organic framework (MOF) — retrofitting — has recently been discovered as a powerful tool to manipulate macroscopic properties such as the mechanical robustness and the thermal expansion behavior. So far, the choice of cross linkers (CLs) that are used in retrofitting experiments is based on qualitative considerations. Here, we present a low-cost computational framework that provides experimentalists with a tool for evaluating various CLs for retrofitting a given MOF system with OMSs. After applying our approach to the prototypical system CL@Cu₃BTC₂ (BTC = 1,3,5-benzentricarboxylate) the methodology was expanded to NOTT-100 and NOTT-101 MOFs, identifying several promising CLs for future CL@NOTT-100 and CL@NOTT-101 retrofitting experiments. The developed model is easily adaptable to other MOFs with OMSs and is set-up to be used by experimentalists, providing a guideline for the synthesis of new retrofitted MOFs with modified physicochemical properties.

¹Department of Chemistry, Technical University of Munich, 85748 Garching, Germany. ²Computational Materials Chemistry Group, Fakultät für Chemie und Biochemie, Ruhr-Universität Bochum, Bochum, Germany. ³These authors contributed equally: Christian Schneider, David Bodesheim. *email: Gregor.Kieslich@tum.de

Metal-organic frameworks (MOFs) combine the variety of inorganic coordination chemistry with the large chemical parameter space of organic chemistry^{1–3}. At the heart of MOFs is their modular building block principle, which provides experimentalists with the control of structure and functionality through linker topology, linker chemistry and metal-node symmetry^{4,5}. In turn, MOFs show a variety of fundamentally interesting and technically relevant properties. For instance, one of the recent breakthrough discoveries is the use of MOFs as working media in highly efficient, non-toxic water recovery technologies^{6,7}. Other intriguing examples are the application of defect-engineered MOFs as Lewis-acid catalysts^{8,9}, the use of MOFs (as precursor) for the synthesis of cathode materials in the oxygen evolution reaction^{10–12} and synthesis of electrically conducting systems with remaining guest-accessible porosities to name just a few^{13,14}. In the pursuit to further optimize the physicochemical properties of MOFs for certain applications, post-synthetic modification (PSM) methods have proved to be an important tool^{15–17}. For instance, a porous but catalytic inactive MOF can be transformed into a robust heterogeneous catalyst by post-synthetic immobilization of a catalytically active iron complex at a functional group of the linker¹⁸. Likewise, breathing behavior can be introduced in a formally non-flexible MOF through post-synthetic functionalization of the linker molecules¹⁹, nicely highlighting the opportunities that come with PSM methods. Moreover, it has been shown that the properties of acid-gas degraded zeolitic imidazolate frameworks can be recovered by post-synthetic treatment with a fresh linker solution²⁰. Looking at PSM for MOFs from a more fundamental perspective, such methods are only possible due to the combination of the underlying coordination chemistry, the available functionality of the organic back-bone and the guest-accessible porosity of MOFs, representing a unique toolbox for experimentalists to fine-tune physicochemical properties.

In the search for new PSM methods, Yaghi and co-workers have recently introduced ‘retrofitting’ as a useful and intuitive categorization²¹. In the most general definition, retrofitting of a MOF describes the post-synthetic installation of additional linkers between undercoordinated metal nodes or between open metal sites (OMSs) of a MOF²¹. Subsequently, retrofitting has been discovered as a powerful approach to manipulate macroscopic physicochemical properties such as the mechanical robustness, the thermal expansion behavior and responsivity of flexible MOFs to guest adsorption^{21–23}. In a typical retrofitting experiment, a MOF with guest accessible OMSs or labile monodentate ligands is exposed to a molecule with at least two available coordination sites such as nitrile or carboxylate groups. This molecule then bridges two OMSs or two undercoordinated metal nodes, adding an additional connectivity between two different metal nodes. In the spirit of retrofitting which originally describes the addition of new components to an existing system, e.g., in construction to reinforce the structural stability of historical buildings^{24,25}, we refer to these guest molecules as *cross linkers* (CLs). It is important to note that in 2016 H. C. Zhou and co-workers demonstrated the possibility of installing two linear CLs with different lengths at two different positions in PCN-700 and referred to this approach as sequential linker installation (SLI)^{26,27} however, since retrofitting as a concept overarches several different areas of on-going research and science^{21,22,24,25,28,29}, we strongly believe that retrofitting is the more intuitive and general categorization and is used throughout this manuscript.

Today, several intriguing examples are known where retrofitting was used to manipulate the physicochemical properties of a parent MOF. For example, O. Yaghi et al. used 4,4'-biphenyldicarboxylate as ditopic CL to render the Zr-based MOF-520 more

robust towards high mechanical pressure²¹. In a similar fashion, Su and co-workers installed linear dicarboxylate CLs in a flexible Zr-based MOF to modulate the breathing behavior of the MOF and the sorption properties towards N₂ and CO₂²³. In 2014, well before ‘retrofitting’ was introduced as a concept for MOFs, A. A. Talin et al. showed that the redox-active CL TCNQ (7,7,8,8-tetracyanoquinodimethane) can bridge two OMSs in Cu₃BTC₂ (BTC = 1,3,5-benzenetricarboxylate, HKUST-1), which was observed to come with an increase in the electrical conductivity of the material³⁰. Using the same system, we recently demonstrated that retrofitting can be used as a tool to fine-tune the negative thermal expansion of Cu₃BTC₂, where an allover stiffening of the material is mainly responsible for reduced negative thermal expansion behavior as a function of TCNQ incorporation²². Looking at some general experimental considerations, the CL for a retrofitting experiment should be chosen to avoid post-synthetic linker exchange¹⁷, i.e., the binding affinity of the metal-node with the CL should be weaker than with the linker. Additionally, when trying to rationalize the underlying mechanism of CL installation, diffusion limitations are expected to play a role, since diffusion pathways through the pores are successively blocked with increasing CL installation. While longer reaction times and relatively high temperatures can overcome such diffusion barriers^{30,31}, vapor phase infiltration at elevated temperatures with CLs that exhibit low sublimation temperatures have proved most suitable in this context^{13,30,32}. It is also interesting to note that current literature examples are limited to retrofitting with ditopic CLs^{21–23,26,27,31}, with bulkier tritopic ligands further increasing concerns related to diffusion limitations. Lastly, it can be observed that retrofitting experiments mostly lead to a defective state of the CL@MOF system, with only a partial occupancy of the CL within the parent MOF network^{21,22,31}. In the big picture, this situation draws a clear line between the defect chemistry of MOFs and purely inorganic materials, with MOFs exhibiting an additional degree of freedom for creating highly defective systems.

Despite the large number of MOFs with OMSs or labile monodentate ligands, the examples of retrofitted MOFs are currently limited to only a few systems. To fully understand and unravel the synthetic opportunities that come with retrofitting as PSM, more (systematic) retrofitted MOF series are required. When designing a retrofitting experiment in the lab, immediately the question arises, “how can we assess whether a cross linker (CL) is suitable for retrofitting of a given MOF?”. D. S. Sholl and co-workers approached this question by applying a DFT-based screening study to identify Cu paddlewheel MOFs that feature OMSs for binding of TCNQ³³. While this approach is expected to provide reliable results, a screening of different combinations of MOFs and CLs comes at a high computational cost. Likewise, the use of computational screening methods based on carefully parameterized force-fields requires experience with these computational methods, typically limiting the scope for experimentalists for exploiting such screening approaches. Consequently, a robust and adaptive approach is required which is both easy to use and computationally not demanding. Additionally, as such an approach is most valuable for experimentalists, the underlying methodology should reflect the experimentalists’ chemical intuition and should be usable with a minimum of experience with computational methods.

In this work we present an easy-to-use low-cost computational framework that allows for evaluating the applicability of a certain CL for the use in a retrofitting experiment. We developed a program named RetroFit that is based on an open-source code and can guide experimentalists in the selection of suitable ditopic CLs for their retrofitting experiments. The approach is inspired by research efforts in the field of molecular modeling in the context of drug design, where molecular docking of small molecules to

macromolecular structures is predicted based on their geometry and interaction potential^{34,35}. Whilst our approach is generally applicable to MOFs with OMS, we use Cu_3BTC_2 and a library of 20 CLs (16 different molecules, 4 of them allow for more than one distinct binding mode) with nitrile groups as a test system for RetroFit. After identifying suitable CLs, the practicability of the RetroFit algorithm is shown by synthesizing the most promising $\text{CL@Cu}_3\text{BTC}_2$ systems, obtaining a set of three new retrofitted $\text{CL@Cu}_3\text{BTC}_2$ systems with $\text{CL} = \text{TCNB}$, DCNB , and DCNT ($\text{TCNB} = 1,2,4,5\text{-tetracyanobenzol}$, $\text{DCNB} = 1,2\text{-dicyanobenzol}$ and $\text{DCNT} = 2,5\text{-dicyanothiophene}$). Finally, we show that RetroFit can easily be extended to other MOF systems such as NOTT-100 and NOTT-101 , where we identify several promising CLs for the synthesis of retrofitted systems with the general formula CL@NOTT-100 and CL@NOTT-101 .

Results and discussion

The RetroFit algorithm. Staying within the realm of ditopic CLs to bridge two OMSs via retrofitting, and raising the question which CLs are suitable for creating a CL@MOF system, two main requirements for a CL can be identified: (i) the presence of two suitable electron donating groups that can bind to the OMSs of the parent MOF and (ii) a size and geometry of the CL that brings these groups into a favorable vicinity of the OMSs for bond formation. Whereas (i) can easily be fulfilled by choosing CLs with two nitrile, amino or carboxylate groups, (ii) can be approached by analyzing the CL geometry compared to the spatial arrangement of the OMSs. Combining both requirements in a screening approach is expected to provide a good measure for estimating if the synthesis of such a CL@MOF system can lead to a stable host-guest system. Based on these considerations, we developed the RetroFit program code that allows for evaluating the applicability of CLs for the use in retrofitting experiments for a given MOF with two OMSs. RetroFit is designed to avoid expensive calculations and to circumvent time-consuming trial and error experiments, in total facilitating the discovery of new retrofitted CL@MOF systems. At the core of RetroFit is a minimization routine which optimizes the position of a given CL relative to the OMS positions. The spatial minimization is based on the binding energy of the CL to the OMSs as reflected in the model interaction potential (MIP). The MIP itself is used as input for RetroFit and is obtained via single point DFT calculations of a simple test system. A schematic of the required input and output of RetroFit is shown in Fig. 1, and a detailed workflow including a how-to guide is provided in the supplementary data files. Overviewing the workflow, the required input is (i) the energies of CL coordination to the specific OMS as a function of bond lengths and angles (i.e., the MIP) of the test system which is used in the minimization process, (ii) the structure of the MOF and in particular the spatial orientation of the OMSs represented in the parameters R_{MM} and γ , and (iii) structural information about the CL that is tested which determines R_{DD} and α . The relative position of the two OMSs and the CL is defined by R_{MD} and the two angles δ and θ , as illustrated in Fig. 2. Since α , γ , and θ are interdependent (see Supplementary Note 1), the geometry of the entire host-guest system can be defined by a set of six parameters, i.e., (R_{MM} , R_{DD} , R_{MD} , α , γ , and δ) or (R_{MM} , R_{DD} , R_{MD} , α , θ , and δ), or (R_{MM} , R_{DD} , R_{MD} , α , γ , and θ). The parameters R_{MM} , γ , R_{DD} and α are extracted from the structure of the MOF and CL and treated as constants in our model, θ only depends on α and γ and can be directly computed, whereas R_{MD} , δ are variables that are optimized during the RetroFit routine. Running through the RetroFit program for one given CL@MOF combination returns an energy penalty ΔE which compares the best orientation of the CL within the MOF system to the ideal binding distance and

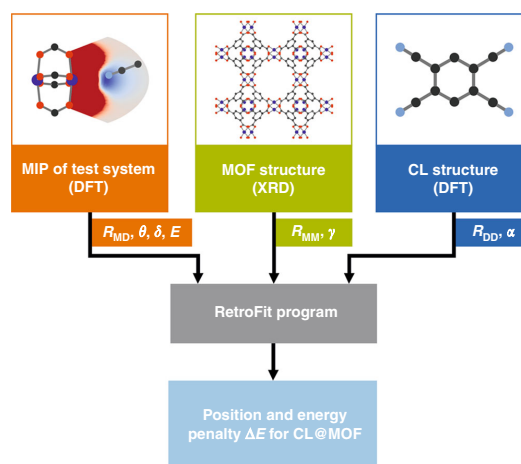


Fig. 1 General workflow of the RetroFit program. Three sets of input data, i.e., the energies from single-point DFT calculations of a test system (orange), the relative position of the OMSs in the MOF (green) and the relative position of the donor groups of the CL (blue), are used by the RetroFit program (gray) to compute the optimal position of the CL within the MOF and the corresponding energy penalty (light blue). A workflow with more technical details and a how-to guideline are provided as a part of the Supplementary data files

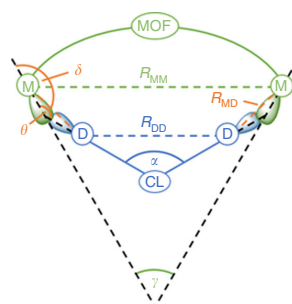


Fig. 2 Geometric parameters of a general CL@MOF system. The parameters R_{MM} and γ are determined by the spatial arrangements of the OMSs of the parent MOF (green), while R_{DD} and α are given by the CL (blue). θ is computed from α and γ , whereas the parameters R_{MD} and δ (orange) are variables and optimized with respect to the underlying MIP. The two OMSs are related to each other by mirror symmetry

angle as provided by the MIP. The application of RetroFit to various CLs allows for ranking these after their energy penalties and further allows for grouping them into three categories (good fit, medium fit, poor fit – see Supplementary Note 7). This list can guide experimentalists in the identification and prioritization for the synthesis of promising CL@MOF systems. Furthermore, RetroFit allows to identify favorable spatial arrangements of the two electron donating groups (e.g., cis, ortho, etc.) from which further CL structures can be developed.

RetroFit for $\text{CL@Cu}_3\text{BTC}_2$. After introducing the general working principle of RetroFit, we applied RetroFit to the well-established Cu_3BTC_2 system. Cu_3BTC_2 was previously used in

retrofitting experiments to obtain TCNQ@Cu₃BTC₂ and TCNE@Cu₃BTC₂^{13,22,32}. Notably, TCNQ and TCNE as prototypical CLs exhibit four nitrile groups that are available for the coordination to OMSs; however, due to the spatial orientation of the OMSs in Cu₃BTC₂ and size dependent restrictions given by the CL and MOF combination, only two nitrile groups coordinate to the MOF while the remaining two point to the center of the pore. Therefore, tetranitrile molecules such as TCNQ or TCNE are treated as bidentate CLs with two possible configurations within RetroFit. Looking at Cu₃BTC₂ in more detail, Cu₃BTC₂ crystallizes in the **tbo** topology and exhibits two types of large pores that in principle are accessible for guest molecules. In only one of these pores the Cu paddlewheels are oriented with the OMS pointing to the center of the pore to allow for retrofitting. In this pore, 12 OMSs on the axial positions of crystallographically equivalent Cu paddlewheel metal nodes point to the inside of the pore. The chemistry of such a Cu OMS shows a large propensity for the formation of Cu-N bonds, and in turn CLs with nitrile or amino groups are expected to be suitable CL candidates^{36–38}. Following the workflow in Fig. 1, a MIP for the system is required which is the basis for the calculation of the aforementioned energy penalty ΔE for a given CL@MOF system. For Cu₃BTC₂ the retrofitting experiment is meant to bridge two of the 12 available copper OMS which are related to each other by a mirror plane. Therefore, it is suitable to focus on the MIP of one Cu OMS and subsequently using the mirror symmetry to obtain the interaction potential of the whole system (see Fig. 2). In Cu₃BTC₂ the distance between the Cu OMSs (R_{CuCu}) was extracted from crystallographic data³⁹. The MIP input was obtained by single point DFT calculations (B3LYP/TZVPP level of theory, see Methods section for details) for a simple Cu(II)formate – acetonitrile complex (CH₃CN@Cu₂(HCOO)₄), where the metal to nitrile group distance (R_{CuN}), δ and θ of acetonitrile were varied. A subsequent interpolation of the 3 N dimensional data yielded the continuous MIP surface that represents one side of the CL@OMS interaction within the MOF, see Fig. 1 orange box for a representation of the MIP with fixed θ angle and Supplementary Note 6 for an extensive error analysis of the interpolation. In CH₃CN@Cu₂(HCOO)₄ the global energy minimum is reached for a linear coordination of acetonitrile ($\delta = \theta = 180^\circ$) and a distance of $R_{CuN} = 2.2 \text{ \AA}$ which we define as zero, i.e., $\Delta E = 0$. In the following, all energies for the CL@Cu₃BTC₂ system are expressed as energy difference ΔE from this ideal configuration. Lastly, the geometries of the different CLs are required, which were obtained by DFT optimization using the B3LYP hybrid functional and a 6–31 G basis set^{40,41}, see Methods section for details. The input of 20 dinitrile-CLs as *.xyz-files are given in the supplementary data files. RetroFit applied to one CL@Cu₃BTC₂ system varies the spatial orientation of the CL with respect to the OMSs within the MOF to minimize ΔE through the parameters R_{CuN} , δ and θ . In turn, the application of RetroFit to various CLs allows to rank these after their energy penalties. Based on this methodology, we have applied RetroFit to the 20 different CLs₂ which are shown in Fig. 3.

To cover a broad range of possible CLs with various geometries we tested acyclic (e.g., 7, and 10) and (hetero-)cyclic systems with 3-, 4-, 5-, and 6-membered rings (e.g., 18, 15, 9, and 5), where the nitrile groups are in geminal, cis (e.g., 1), ortho (e.g., 3) or meta (e.g., 19) positions, see Fig. 3. By using RetroFit, ΔE for the 20 tested CL@Cu₃BTC₂ combinations were calculated and are given in the energy map shown in Fig. 4 and the bar plot (see below). The global minimum of the energy map ΔE_{min} , i.e., the molecule parameters that suggest the ideal fit, is located at $R_{NN} = 5.81 \text{ \AA}$ and $\alpha = 60^\circ$. Interestingly, the dependence of ΔE on the distance between the nitrile groups within the CL (R_{NN}) is significantly stronger than on α . Therefore, molecules with similar R_{NN}

distances fit comparably well such as TCNQ (13, $R_{NN} = 4.447 \text{ \AA}$, $\Delta E = 2.24 \text{ kcal mol}^{-1}$), TCNE (2, $R_{NN} = 4.436 \text{ \AA}$, $\Delta E = 2.29 \text{ kcal mol}^{-1}$) and malononitrile (10, $R_{NN} = 4.431 \text{ \AA}$, $\Delta E = 2.32 \text{ kcal mol}^{-1}$). Looking for trends, nitriles in ortho positions of small cyclic systems as given in tetracyanobutadiene (16) as well as geminal nitriles as available in TCNQ show a good fit with Cu₃BTC₂, while ΔE increases for larger ring systems and nitrile groups in cis position. In contrast, the meta configuration in CLs with 6-membered rings (20, $R_{NN} = 6.893 \text{ \AA}$ for TCNB) shows a relatively high energy penalty of $\Delta E = 4.815 \text{ kcal mol}^{-1}$ which is therefore less favorable for retrofitting Cu₃BTC₂ (see discussion in Supplementary Note 7). TCNQ as the prototype CL has a relatively low value of $\Delta E = 2.24 \text{ kcal mol}^{-1}$, which is in good agreement with the results of previous studies^{30,42,43}. Comparing TCNQ to other tested CLs, only CLs based on 3-, and 4-membered ring systems show smaller ΔE values. Such molecules often show flashpoints below 150 °C and are therefore less suitable for retrofitting experiments which involves vapor phase infiltration at temperatures typically above 100 °C. In order to evaluate the accuracy of the RetroFit routine, the results are compared with existing computational data from the literature on TCNQ@Cu₃BTC₂. A. A. Talin et al. modeled the binding of TCNQ in Cu₃BTC₂ by using DFT (UB3LYP^{41,44}/VTZP level of theory⁴⁵) and obtained a geometry optimized crystal structure of CL@Cu₃BTC₂ with CL = TCNQ³⁰. Using their results as a benchmark and comparing these with the output values from RetroFit, we indeed observe a good correlation which is summarized in Supplementary Table 5. The largest deviations occur due to CL deformations, which are not accounted for in our model. For instance, R_{NN} of TCNQ in the literature structure of TCNQ@Cu₃BTC₂ is increased by 0.167 Å to $R_{NN}' = 4.614 \text{ \AA}$ compared to the free molecule, which results in a R_{CuN} distance which is 0.168 Å shorter and in turn leads to a stronger coordination bond. Taking the distortion of TCNQ into account by using R_{NN}' and α' from the literature as input for RetroFit, a significantly lower energy penalty of $\Delta E = 1.59 \text{ kcal mol}^{-1}$ is obtained (see Supplementary Table 5). This example shows that despite the heuristic approach of RetroFit, the binding situation is reasonably represented. It seems, however, that RetroFit slightly overestimates the energy penalty, whereas in the real CL@Cu₃BTC₂ system structural deformations can occur that further minimize the total energy of the CL@MOF system, i.e., a slight increase in energy due to unfavorable molecule deformation can be overcome through the formation of stronger coordination bonds. Therefore, CLs with low energy penalties are expected to lead to a stable CL@Cu₃BTC₂ system and structural deformations can be expected to only play a minor role. Similarly, CL@Cu₃BTC₂ systems with relatively large energy penalties can be ruled out, whilst assumptions drawn for CL@MOF combinations with intermediate energy penalties are more inconclusive. For our CL@Cu₃BTC₂ system, we observe that CL = TCNB (3), DCNB (5) and DCNT (6) are promising candidates. These combine low to medium ΔE values with experimental applicability given by the physical properties of the CLs, and the synthesis of the corresponding CL@Cu₃BTC₂ systems is described in the next paragraph.

Proof of concept – experimental validation. After having identified several promising CLs for retrofitting Cu₃BTC₂, the synthesis of new CL@Cu₃BTC₂ materials was attempted. Following the results discussed in the previous section, we selected 1,2-dicyanobenzene (5, DCNB), 1,2,4,5-tetracyanobenzene (3, TCNB) and 3,4-dicyanothiophene (6, DCNT) as promising CLs for proof-of-principle experiments. These CLs show low and intermediate ΔE values, are commercially available and easy to handle. All of these

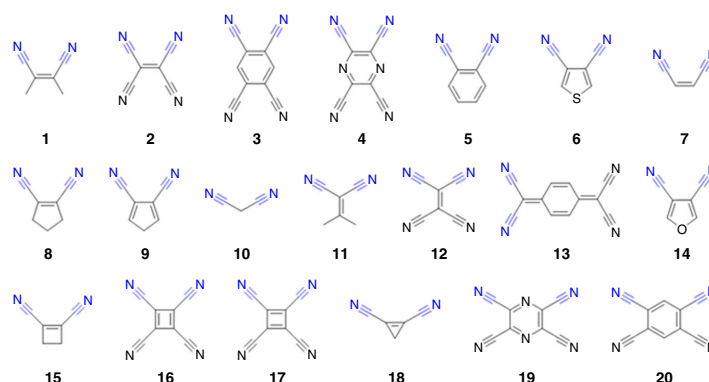


Fig. 3 Library of potential CLs evaluated with RetroFit. Structural parameters were obtained from geometry optimized structures in the gas phase. The coordinates can be found in the program package provided in the Supplementary data files

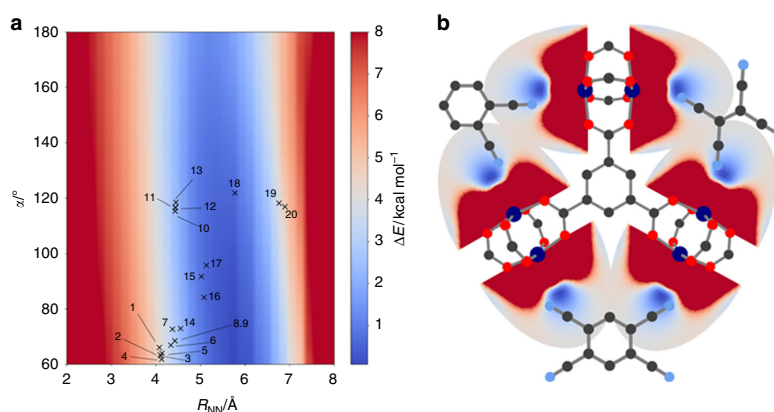


Fig. 4 RetroFit results for Cu_3BTC_2 . **a** RetroFit map for Cu_3BTC_2 and the tested dinitrile-CLs. The energy penalty ΔE for the CL parameters R_{NN} and α is given as color code and increases from blue to red. Values of ΔE , which exceed the color scale bar are set to 8 kcal mol^{-1} for better visualization. The smallest ΔE and in turn the best fit is obtained for CLs with 3 and 4-membered rings (**15**, **16**, **17** and **18**). A table overviewing the results is given in Supplementary Note 7 (Supplementary Table 3). **b** Visualization of the fit of the CLs **5**, **12**, and **20** with ortho, geminal and meta configuration, respectively. Cu, C, N, and O atoms are shown in dark blue, black, blue and red. The potential around the OMSs is illustrated as ΔE increasing from blue to red

molecules show sublimation temperatures feasible for vapor phase loading experiments that currently seem to be the preferable experimental pathway^{13,22}. Following the established solvent-free guest loading procedure¹³, we prepared $\text{CL}@\text{Cu}_3\text{BTC}_2$ compounds with one molar equivalent of DCNB, TCNB and DCNT per Cu_3BTC_2 . Such a loading situation corresponds to two CLs per large pore, which has been previously determined as the maximum loading for TCNQ^{13,46}. Details on the synthetic procedure and characterization techniques are provided in the Methods section (see below) and in the references ¹³ and ²². After infiltration of Cu_3BTC_2 with the various CLs, powder X-ray diffraction (PXRD) confirms that the crystallinity of all samples is maintained (Fig. 5). An increased intensity of the (111) reflection is observed in all cases, which has previously been attributed to the chemisorption of guest molecules to two neighboring Cu paddlewheels within the (111) plane¹³. Closer investigation of the PXRD pattern reveals new reflections which are weak in intensity, see inset in Fig. 5. These new reflections are forbidden in the face-centered cubic space group of Cu_3BTC_2 ($Fm\text{-}3m$) and have been previously observed for $\text{TCNQ}@\text{Cu}_3\text{BTC}_2$ ¹³. Indexing of the PXRD pattern

suggests a primitive space-group, such as $Pn\text{-}3m$, pointing at some sort of ordering of the guest molecules within the two chemically different pores of Cu_3BTC_2 . Notably, other symmetry-reduction pathways are possible, but when staying within the 3σ criterion, the Pawley fit with $Pn\text{-}3m$ produces the most reasonable fit in all cases. Attempts of structure solution are challenged by the expected partial occupancy and complicated ordering mechanism of CL molecules within the pores and have not been successful so far. Additional proof for the presence of the CLs are new signals in the IR spectra that are related to the guest molecules, even though the nitrile bands are less intense when compared to $\text{TCNQ}@\text{Cu}_3\text{BTC}_2$ (Supplementary Note 10). To further underpin the accommodation of the CLs inside Cu_3BTC_2 , nitrogen sorption isotherms (Fig. 6) and scanning electron microscopy images were recorded (Supplementary Note 11). From the initial slope of the type I isotherms comparable BET surface areas of $1170.3 \text{ m}^2 \text{ g}^{-1}$ (DCNT), $1151.9 \text{ m}^2 \text{ g}^{-1}$ (DCNB) and $1135.2 \text{ m}^2 \text{ g}^{-1}$ (TCNB) were determined. These values are significantly lower than for pristine Cu_3BTC_2 ($1873.8 \text{ m}^2 \text{ g}^{-1}$) but higher than for $\text{TCNQ}@\text{Cu}_3\text{BTC}_2$ ($869.9 \text{ m}^2 \text{ g}^{-1}$), which is ascribed to the smaller size of DCNT,

DCNB and TCNB compared to TCNQ. For all new CL@Cu₃BTC₂ powders, SEM images confirm the absence of unreacted CLs or the formation of amorphous byproducts (see Supplementary Note 11). This is different when compared to the case of TCNQ@Cu₃BTC₂, where the formation of CuTCNQ nano-wires on the surface of the MOF crystals was observed¹³. Comparing the electrical conductivities of DNCT@Cu₃BTC₂, DCNB@Cu₃BTC₂

and TCNB@Cu₃BTC₂, all materials are electrical insulators (see Supplementary Note 12). This might be a result of different redox potentials of the CLs and the presence of the by-phase in TCNQ@Cu₃BTC₂ (a more detailed discussion can be found in Supplementary Note 12). Lastly, we would like to note that tetracyanoethylene (TCNE), which shows an excellent fit according to RetroFit, was already employed by D'Alessandro and co-workers³² however, our attempts of the synthesis of TCNE@Cu₃BTC₂ led to an unexpected PXRD pattern that might either point to a transformation or a relatively drastic change of structure which we could not yet identify (see Supplementary Fig. 19). In summary, following the results from RetroFit, we successfully synthesized and characterized three new retrofitted CL@Cu₃BTC₂ systems namely DCNT@Cu₃BTC₂, DCNB@Cu₃BTC₂ and TCNB@Cu₃BTC₂, highlighting the applicability of the RetroFit algorithm.

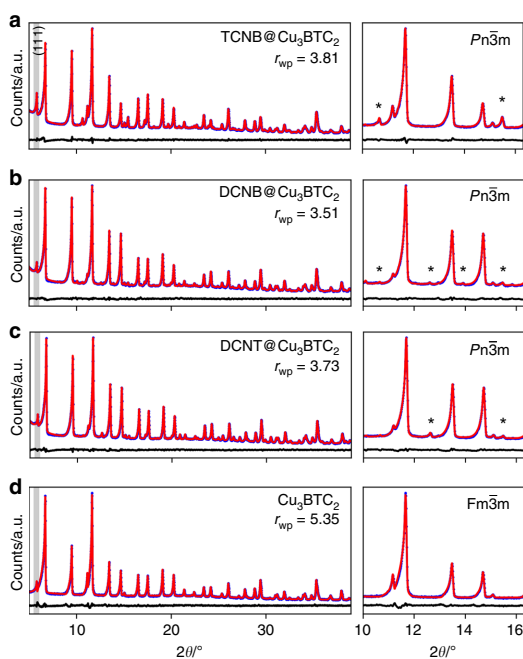


Fig. 5 PXRD data and Pawley profile fits for CL@Cu₃BTC₂. Pristine Cu₃BTC₂ **d** crystallizes in the face-centered cubic space group *Fm*-3*m*. Upon retrofitting with CL = TCNB **a**, DCNB **b**, or DCNT **c**, new reflections occur (zoom in) which can be accounted for by using the primitive space-group *Pn*-3*m*. Experimental data, Pawley profile fits and difference curves are shown in blue, red, and black, respectively. The r_{wp} fitting parameters are provided in the top right corner, respectively. The (111) reflection at 5.8° is indicated in gray

Beyond Cu₃BTC₂. To show that RetroFit is easily transferable to other CL@MOF systems, we used RetroFit to screen various dinitrile-CLs for retrofitting NOTT-100 (Cu₂(BPTC), BPTC = biphenyl-3,3',5,5'-tetracarboxylate) and NOTT-101 (Cu₂(TPTC), TPTC = [1,1':4',1'']terphenyl-3,3'',5,5''-tetracarboxylate) MOFs⁴⁷. Both MOFs crystallize in the *nbo* topology and are built from Cu paddlewheel nodes and tetratopic rectangular-shaped linkers. Since NOTT-100 and NOTT-101 have Cu-based OMSs similarly to Cu₃BTC₂, the same MIP can be used as input for RetroFit. In contrast to Cu₃BTC₂, the crystal structures of both NOTT systems exhibit two crystallographically distinct binding sites. We refer to these sites and corresponding R_{Cu-Cu} and γ values as 3,5-position and 3,3'- (NOTT-100) or 3,3''-positions (NOTT-101) which is adapted from the nomenclature of the linker molecules (see Fig. 7 for a visualization of this situation). In turn, we can generate two sets of ΔE values, which rank the different CLs after the two different binding situations. The obtained ΔE values are listed in Fig. 8 and compared with Cu₃BTC₂. For the binding site in the 3,5-position, the RetroFit maps (see Supplementary Note 8) resemble the situation previously obtained for Cu₃BTC₂ (Fig. 4) due to the similar geometry; however, significant differences can be observed for the 3,3' and 3,3'' binding site. It should be noted that in both NOTT systems, the Cu OMSs in 3,3' (or 3,3'') position exhibit a small torsion angle. In RetroFit, this torsion angle is neglected for all CLs as the routine translates a 3D multiparameter problem into 2D space. Presumably, this adds another offset to the ΔE ranking; however, as a pronounced effect of the R_{NN} distance has been found for Cu₃BTC₂, the torsion angle is expected to play only a minor role. The results of

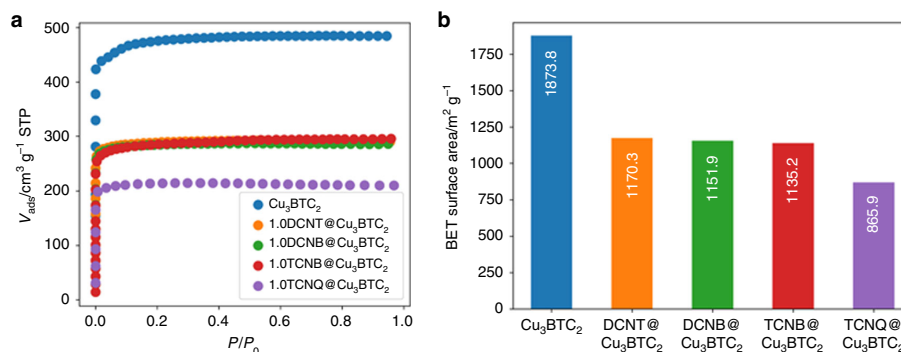


Fig. 6 Porosimetry measurements of CL@Cu₃BTC₂. Nitrogen adsorption isotherms **a** and calculated BET surface areas **b** for samples with CL = DCNT (orange), DCNB (green), TCNB (red), and pristine Cu₃BTC₂ (blue). All new materials show a high residual porosity after the retrofitting experiment

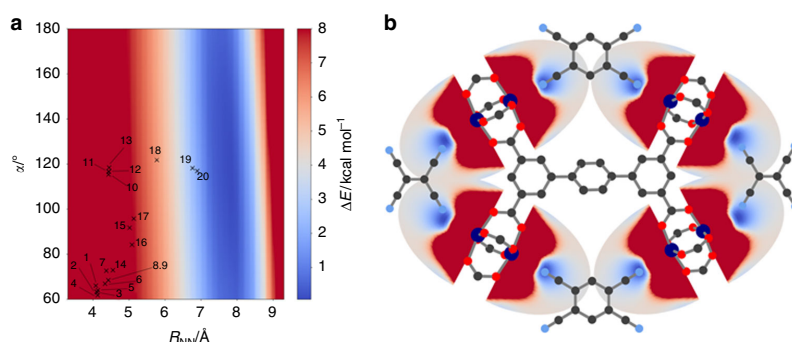


Fig. 7 RetroFit results for NOTT-101. **a** RetroFit map for the 3,3''-position and the CL library (Fig. 3). Values of ΔE , which exceed the color scale bar are set to 8 kcal mol⁻¹ for better visualization. The lowest ΔE for the 3,3''-position is obtained for CL **20** (TCNB, meta position), although CLs with even larger R_{NN} distances will show better fit. **b** Visualization of the implications for retrofitting NOTT-101. It is conceivable that two different CLs can be installed in NOTT-101, e.g., TCNB in the 3,3''-position and TCNE in the 3,5-position. Cu, C, N, and O atoms are shown in dark blue, black, blue, and red. The potential around the OMs is illustrated as ΔE increasing from blue to red

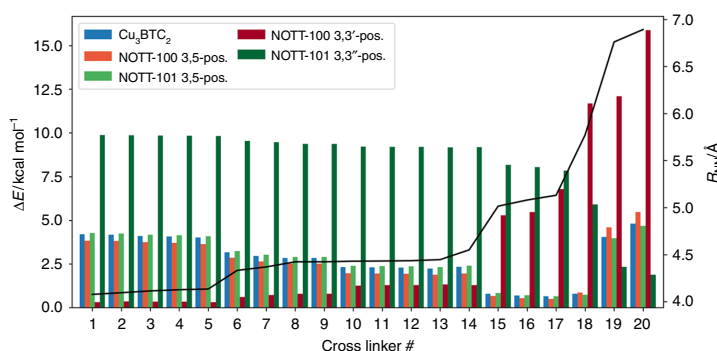


Fig. 8 Summary of the RetroFit results. The energy penalties ΔE (bars) of all CL@MOF materials studied in this work are compared. The R_{NN} distance of the CLs is visualized by the black line. Due to the anisotropy of the linker for the NOTT systems, two different positions, here referred to as 3,5 and 3,3' (or 3,3'') are possible and have been tested. For bridging two OMs in a MOF, distinct R_{NN} windows that lead to low ΔE can be identified. Cu₃BTC₂, NOTT-100 (3,5-position) and NOTT-101 (3,5-position) have very similar ΔE values with an optimum at $R_{NN} \approx 5.1$ Å. NOTT-100 (3,3'-position) shows the best fit for low R_{NN} values, whereas NOTT-101 (3,3''-position) shows the opposite trend

applying RetroFit to NOTT-100 and NOTT-101 are shown in Fig. 8 and compared to Cu₃BTC₂. In the 3,3'-position of NOTT-100, the short R_{CuCu} distance of 7.601 Å in combination with the obtuse angle of $\gamma = 145.65^\circ$ requires molecules with very short R_{NN} distances (see Supplementary Fig. 16). The isoreticular expansion from NOTT-100 to NOTT-101 results in an increase of R_{CuCu} for the 3,3' (respectively 3,3'') position to 11.607 Å. Therefore, CLs with larger R_{NN} distances, such as TCNB (**20**, meta), can be accommodated in the structure of NOTT-101 which do not fit into the structure of NOTT-100 or Cu₃BTC₂. These results suggest that a system with two distinctly different sites such as NOTT-101 can be fitted with two types of CLs, e.g., TCNE (**12**) or malononitrile (**10**) in the 3,5-position and a TCNB (**20**, meta) across the long side of the terphenyl-linker (3,3''-position), providing diffusion limitations can be minimized. Notably, TCNB is a candidate CL to bridge both the 3,5-position (ortho coordination) and the 3,3'' position (meta coordination), making it a particular interesting CL for future retrofitting experiments.

In conclusion we developed a low-cost computational framework called RetroFit which provides experimentalists with a tool to identify promising CLs for retrofitting MOFs. In a

proof-of-principle study, we used RetroFit for screening various CLs for retrofitting experiments of the iconic Cu₃BTC₂ system. The synthesis of the most promising CL@Cu₃BTC₂ candidates was approached in the laboratory, obtaining the three new retrofitted systems DNCT@Cu₃BTC₂, DCNB@Cu₃BTC₂ and TCNB@Cu₃BTC₂. To show the applicability to other systems, we applied RetroFit to the well-known NOTT-100 and NOTT-101 MOFs, testing both possible bidentate bridging modes in these systems and identifying a few promising CL@NOTT-101 and CL@NOTT-100 candidates. We would like to note that RetroFit is not aiming at a quantitative description of the possible CL@MOF systems but is designed as an easy-to-use screening tool which can be operated without a profound background in computational chemistry. A detailed how-to guide including the program code and input data for reproducing the herein presented results are given in the supplementary data files. Looking at RetroFit from a more general perspective, the routine translates a complex multiparameter 3D optimization problem to a 2D model in which only the strongest chemical interactions, i.e., the metal-coordination bonds are accounted for. With the currently available MIP for nitrile-CLs and Cu-based OMS, RetroFit can easily be applied

to all MOFs with Cu-paddlewheel motifs as OMS, such as NU-111 ($\text{Cu}_3(5,5',5''\text{-benzene-1,3,5-triyltris(buta-1,3-diyne-4,1-diyl)trisophthalate)})^{48}$, PCN-14 ($\text{Cu}_2(5,5'\text{-anthracene-9,10-diyl)diisophthalate)})^{49}$ and NOTT-115 ($\text{Cu}_3(4',4''\text{-nitrotrilo-tris}(((1''''\text{-biphenyl-3,5-dicarboxylate}))))^{50}$ to name just a few. The next step in the development of RetroFit is the creation of a library of various MIPs for different metal nodes going beyond Cu-based OMS. Likewise, currently 20 dinitrile-based CLs are contained in the database, which can be expanded to amino-based or carboxylate-based CLs in the future.

Finally, it is important to emphasize a few additional points related to the retrofitting concept. Retrofitting as relatively new categorization of PSM is an intriguing approach for accessing the structural dynamics of MOFs. Today only a limited number of retrofitted MOFs exist, a situation that makes it difficult to oversee the full potential of the concept. Most notably, retrofitting as science overarching concept is not limited to MOFs. Even in the world of covalent organic frameworks (COFs) examples exist that can be classified under the umbrella of retrofitting, i.e., when metal complexes are used to cross-link two-dimensional COF sheets or when post-synthetic modification of functional groups leads to additional framework connectivity^{28,29}. The future progress of the retrofitting concept is linked to the discovery of additional CL@MOF systems, which allows to answer open scientific questions on potential order phenomena of CLs within the parent MOFs as well as on the influence of CL size and CL-to-OMS bond strength on the macroscopic properties. With the synthesis of more retrofitted MOF systems, these questions can be approached, to which our RetroFit algorithm adds a powerful tool. Likewise, the concept itself can be extended. For instance, the incorporation of asymmetric CLs such as amino acids, or CLs that contain functional backbones such as optically active groups seem to be intriguing research directions. In these scenarios, diffusion limitations might start to play a more significant role but are difficult to estimate without experimental validation. The use of less strong donor CLs might be a solution to this problem, enabling the equilibrium to be reached at elevated temperatures. Therefore, we strongly believe the retrofitting concept has much to offer in the future, and that RetroFit can facilitate the discovery of new CL@MOFs, leaving the territory of trial and error experiments.

Methods

RetroFit algorithm. RetroFit was written in the open source programming language PythonTM (available at <http://www.python.org>) and was tested for versions 2.7 and 3.7. The algorithm uses three data sets (see Fig. 1) as input, i.e., the relative position of the OMSs within the MOF, the structural information of the CL, and a MIP representing the interaction between OMS and CL. Whereas the former is extracted from the MOF crystal structure, the geometry of the CL and the MIP are obtained by DFT calculations (see below). In the current version of RetroFit, the structural relation of the OMSs are extracted manually from the MOF crystal structure, whereas the geometry of the different CLs is provided as a library of molecular structure files (xyz-files). The continuous MIP is generated by interpolation of the input energies from single point DFT calculations of the model system. A detailed description of the algorithm is provided in Supplementary Note 3 and the workflow is shown in Supplementary Fig. 10. It should be noted that herein we release version 1.0 of RetroFit. Future developments of the code as well as a library of CLs and MIPs will be deposited on GitHub (<https://github.com/GKieslich/RetroFit>). We believe that the development of RetroFit is a task for computational scientists or users with advanced expertise on computation. On the other hand, RetroFit is designed to be applied by experimentalists with a minimum of experience with computational methods. Therefore, future developments of the program will be aiming on both to increase the capabilities of the program and to make RetroFit as user-friendly as possible.

DFT calculations. All molecule geometries were optimized with the Gaussian09 program package. Optimization was performed with DFT with a B3LYP hybrid functional and a 6–31 G basis set^{40,41}. For the optimization the ‘tight’ convergence criterion was used and the Hessian was recalculated after each optimization step. All molecules were symmetry restricted during the optimization process (CLs 2, 3, 4, 12, 13, 16, 17, 19, and 20 were restricted to D_{2h} symmetry while CLs 1, 5–11, 14, 15, and 18 were restricted to C_{2v}). The resulting Gaussian output file was converted

to the xyz-format using Open Babel (version 2.3.2) and then imported into the RetroFit tool using the Atomic Simulation Environment (ASE) (version 3.16.0) to compute R_{NN} and α .

To access energies in the host–guest system consisting of a Cu paddlewheel-based MOF and a nitrile-CL, we optimized a Cu(II) formate paddlewheel and an acetonitrile molecule, respectively, and then arranged the two entities that the nitrile group points towards the OMS of the paddlewheel ($\text{CH}_3\text{CN}@Cu_2(\text{HCOO})_4$). By varying $R_{\text{CL-OMS}}$, δ and θ according to the parameters given in Supplementary Table 2, we obtained an energy of the system for every combination of the three parameters, which allows the generation of a MIP via linear interpolation. In general, the interpolation errors can be improved by a smaller step size but for the accuracy demands herein, the chosen step sizes are sufficient (see Supplementary Note 6). The configuration with the lowest energy is defined as 0 kcal mol⁻¹ and all energies are given as energy differences ΔE . Further, a factor of 2 is applied as the host–guest complex involves two coordination bonds of nitrile groups to two OMSs. The single point calculations were done on a DFT level of theory using the TURBOMOLE (V7.1) software package⁵¹. The hybrid functional B3LYP^{41,44} was used with a TZVPP basis set⁴⁵ and a fine ‘m5’ grid⁵² for all elements. The multipole-accelerated⁵³ resolution of the identity approximation^{54,55} was used for performance reasons. Grimmes D3⁵⁶ was employed to properly account for dispersive interactions. The SCF convergence criterion was set to 10⁻⁶ Hartree. Additional details on the single point DFT calculations can be found in Supplementary Note 2.

Synthesis. Cu_3BTC_2 was synthesized following the literature procedure⁵⁷. The crystalline as-synthesized powder was solvent exchanged and activated following our previously published protocols¹³. The synthesis of CL@ Cu_3BTC_2 with CL = 1,2-dicyanobenzene (DCNB), 1,2,4,5-tetracyanobenzene (TCNB), and 3,4-dicyanophenylene (DCNT) was performed analogous to the reported procedure for $\text{TCNQ}@Cu_3\text{BTC}_2$ ¹³. Therefore, activated Cu_3BTC_2 (100 mg) and stoichiometric amounts of DCNB, TCNB, or DCNT were thoroughly mixed to yield mixtures with $x = n(\text{CL})/n(\text{Cu}_3\text{BTC}_2) = 1.0$. The mixtures were filled into a glass ampule, which then was evacuated (10⁻³ mbar) and flame-sealed. The ampules were placed in a convection oven at 180 °C for 72 h. After cooling down, the ampules were opened inside an Ar-filled glovebox and the CL@ Cu_3BTC_2 powders were stored until further characterization. For all analytic methods, the powders were handled under inert conditions (Ar or vacuum) to avoid contamination from the atmosphere.

Powder X-ray diffraction. CL@ Cu_3BTC_2 samples were filled into 0.7 mm borosilicate capillaries and sealed. The capillary was mounted onto a PANalytical Empyrean X-ray diffractometer operated in capillary mode using Cu K α radiation, a focusing beam mirror with a 1/8° slit and 0.02 rad Soller slits as the incident beam optics and a 1/8° anti-scatter slit with 0.02 rad Soller slits and a Ni filter on the diffracted beam side. Diffraction data in the 2θ range of 5–50° with a step size of 0.013° was collected using a PIXcel 1D detector in scanning line mode. Quantitative data analysis (Pawley fits) was performed using the Topas Pro v5 software. The fitting parameter, i.e., weighted-profile R -factor (r_{wp}), is provided in the respective figures.

Porosimetry measurements. Inside of an Ar glovebox, ~60 mg of a sample were filled into a glass tube and evacuated at room temperature for 3 h at ~10⁻² mbar. The exact sample mass was determined and the isotherm was recorded on a Micromeritics 3Flex at 77 K in the pressure range between 10⁻³ and 10³ mbar. The BET surface area was calculated from the initial slope (0.01 to 0.1 P/P_0) of the isotherm.

Data availability

The authors declare that all data supporting the findings of this study are available within the article and its Supplementary Information or from the corresponding author upon reasonable request.

Code availability

The RetroFit code including all required input files and a How-to-guide is freely available on GitHub, see <https://github.com/GKieslich/RetroFit> and licensed under a MIT license.

Received: 23 July 2019; Accepted: 17 September 2019;

Published online: 29 October 2019

References

1. Yaghi, O. M. et al. Reticular synthesis and the design of new materials. *Nature* **423**, 705–714 (2003).
2. Kitagawa, S., Kitaura, R. & Noro, S.-i. Functional porous coordination polymers. *Angew. Chem. Int. Ed.* **43**, 2334–2375 (2004).

Acknowledgements

We would like to thank Roland A. Fischer and Christoph Schran for insightful discussions. Mark D. Allendorf and A. Alec Talin are acknowledged for the support with electrical conductivity measurements and Pia Vervoorts and Dardan Ukaj for porosimetry measurements. C.S. acknowledges his scholarships from the Studienstiftung des Deutschen Volkes and from the Fonds der Chemischen Industrie (FCI). G.K. gratefully thanks the FCI and the DFG SPP1928 (COORNETs) for financial support.

Author contributions

C.S., D.B. and G.K. developed the concept and algorithm for RetroFit. C.S. synthesized and characterized the new $\text{CL@Cu}_3\text{BTC}_2$ materials. J.K. and R.S. calculated the model interaction potential. All authors have contributed to writing of the manuscript with C.S. and G.K. as main contributors.

Competing interests

The authors declare no competing interests.

Additional information

Supplementary information is available for this paper at <https://doi.org/10.1038/s41467-019-12876-1>.

Correspondence and requests for materials should be addressed to G.K.

Peer review information *Nature Communications* thanks Matthew Lennox, Rocio Semino and other, anonymous, reviewers for their contribution to the peer review of this work. Peer reviewer reports are available.

Reprints and permission information is available at <http://www.nature.com/reprints>

Publisher's note Springer Nature remains neutral with regard to jurisdictional claims in published maps and institutional affiliations.



Open Access This article is licensed under a Creative Commons Attribution 4.0 International License, which permits use, sharing, adaptation, distribution and reproduction in any medium or format, as long as you give appropriate credit to the original author(s) and the source, provide a link to the Creative Commons license, and indicate if changes were made. The images or other third party material in this article are included in the article's Creative Commons license, unless indicated otherwise in a credit line to the material. If material is not included in the article's Creative Commons license and your intended use is not permitted by statutory regulation or exceeds the permitted use, you will need to obtain permission directly from the copyright holder. To view a copy of this license, visit <http://creativecommons.org/licenses/by/4.0/>.

© The Author(s) 2019

4 Conclusion and Outlook

The research conducted in the context of this doctoral study can be divided into two parts, namely the in-depth investigation of the material TCNQ@Cu₃BTC₂ and the exploration of retrofitting as a new PSM method based on a simple computational model. Therefore, these two topics are addressed individually in the following two chapters.

4.1 TCNQ@Cu₃BTC₂

Despite the vast number of experimental and computational studies on TCNQ@Cu₃BTC₂, the host-guest chemistry and the associated materials properties are still not fully understood. In fact, the thorough investigations presented in this dissertation have revealed an even more complex nature of the material, emphasizing the need for more comprehensive models to accurately describe charge transport in this system. Studies I – III provided a clearer picture of the chemical processes during the infiltration reaction, the location and arrangement of TCNQ within the pore, as well as the variegated pore chemistry of the host-guest material. Therefore, it is not surprising that TCNQ@Cu₃BTC₂ prepared under different reaction conditions yielded considerably different materials properties. The reaction conditions and reported electronic properties of thin film samples prepared via solution impregnation from in the literature and studied in this thesis are summarized in Table 2. Analogously, the specifications for powder samples synthesized via solution impregnation or vapor phase loading are displayed in Table 3 and the two infiltration methods are compared in Table 4.

Table 2. Overview of the fabrication and electronic properties of TCNQ@Cu₃BTC₂ thin films reported in the literature and studied in this dissertation.

Substrate	MOF orientation	Solvent	$T / ^\circ\text{C}$	$\sigma / \text{S cm}^{-1}$	$S / \mu\text{V K}^{-1}$	Ref.
Si/SiO ₂	polycrystalline	DCM	RT	$7 \cdot 10^{-2}$	n/a	101
Si/SiO ₂	polycrystalline	MeOH	RT	$4.5 \cdot 10^{-3}$	+375	202
Au / SAM	oriented (111) [§]	EtOH	RT	$2 \cdot 10^{-10}$	n/a	203
Si/SiO ₂	polycrystalline	n/a	RT	$3 \cdot 10^{-3}$	+350	204
Au / SAM	oriented (001) [§]	n/a	RT	n/a	~0	204
quartz	polycrystalline	DCM	RT	$\sim 10^{-4}$	n/a	211
Si/SiO ₂	polycrystalline ^{&}	MeOH	RT	$\sim 10^{-1}$	n/a	217

[§] Conductivity measured perpendicular to the substrate.

[§] Conductivity measured parallel to the substrate.

[&] Cu₃BTC₂ transformed to Cu(TCNQ) during infiltration.

Table 3. Overview of the synthesis and physicochemical properties of $x\text{TCNQ}@Cu_3\text{BTC}_2$ powder samples reported in the literature and prepared via liquid phase infiltration (LPI) or vapor phase infiltration (VPI).

Infiltration method	Solvent	$T / ^\circ\text{C}$	TCNQ loading x	SSA / $\text{m}^2 \text{g}^{-1}$ (BET)	$\sigma / \text{S cm}^{-1}$	Ref.
LPI	DCM	RT	0.5	214	n/a	101
VPI	none	120	0.98	n/a	n/a	205
LPI	DCM	RT	0.5	n/a	$<10^{-12}$	§
VPI	none	180	1.0	574	$1.5 \cdot 10^{-4}$	143

§ Electrical conductivity was measured during the work towards Study II¹⁴³ but was immeasurably low. Results were not included in the publication.

Table 4. Comparison of the two infiltration methods for the synthesis of $\text{TCNQ}@Cu_3\text{BTC}_2$, *i.e.* liquid phase infiltration or vapor phase infiltration, and the physicochemical properties of the resulting materials.

	Liquid phase infiltration	Vapor phase infiltration
$T_{\text{infiltration}}$	RT	120 – 180 °C
maximum TCNQ loading $x / \text{eq.}$	0.5 ¹⁰¹	1.0 ¹⁴³
SSA (BET) / $\text{m}^2 \text{g}^{-1}$ for $0.5\text{TCNQ}@Cu_3\text{BTC}_2$	214 ¹⁰¹	1145 ¹⁴³
$\sigma / \text{S cm}^{-1}$ §	$10^{-4} - 10^{-2}$	10^{-4}
TCNQ ordering	not observed	long range order
TCNQ distribution [§]	inhomogeneous	homogeneous
TCNQ radicals [§]	yes	yes
perturbation	solvents / H_2O	$\text{Cu}(\text{TCNQ})$

§ Electrical conductivity values for thin film samples infiltrated with DCM (see Table 2).

§ According to EPR measurements from Study III.

Thin films of Cu_3BTC_2 infiltrated with TCNQ were fabricated by several different groups (see Table 2) and the increase in the electrical conductivity upon infiltration has been confirmed. Notably, with the learnings from Study I in mind, results from specimen that were made by infiltration using MeOH (or other non-inert solvents) should be treated carefully. Before discussing potential charge transport mechanisms, it is necessary to understand the microscopic structure of the material, to which this dissertation has substantially contributed.

In general, a maximum TCNQ loading of 2 TCNQ molecules per large pore could be achieved via vapor phase loading (1 TCNQ per pore via solution impregnation). In the structure of Cu_3BTC_2 , one of the large pores does not exhibit accessible Cu OMSs (pore B), which leads to a physisorption of TCNQ with no preferred orientation. The other large pore (pore A) has 12 potential binding sites (OMSs) for two TCNQ molecules. Every TCNQ molecule can only bind via two geminal nitrile groups, while the other two nitrile groups point to the center of the pore without coordination. This leads to a maximum occupation of 4 out of 12 OMSs or 33% in pore A. Notably, a simultaneous binding of two TCNQ molecules to OMSs of one pore is only possible by deviation from the ideal arrangement of TCNQ in the (111) plane due to mutual steric hindrance of the TCNQ molecules. For TCNQ loadings of $x < 1$, a preferred accommodation of TCNQ in pore A was assumed for computational modeling,²⁰² however, the monotonically increasing (111) reflection in the diffraction patterns (see Study II) and the spectroscopic trends observed in Study III suggest a homogeneous distribution between pore A and pore B. Due to the structural consideration and the absence of long range order in crystallographic experiments, it seems probable that only localized domains of 1D TCNQ-Cu paddlewheel arrays form within the pores of Cu_3BTC_2 . This is in contrast with the idealized picture of 1D polymers (“wires”) that expand through the entire crystal volume representing the major pathway for charge transport.

Another potential model to explain the charge transport in MOFs is *doping*.^{80-81, 218} In that scenario a dopant (here TCNQ or TCNQ^-) increases the charge carrier concentration of the material to enable charge transport. In this context, the concentration of TCNQ^- becomes relevant. Study III shows a quantitative correlation of the Cu(I) defect concentration in parent Cu_3BTC_2 with the amount of TCNQ^- in the loaded samples. Notably, the amount of TCNQ^- did not change with x since all Cu(I) defects had already been oxidized at low loadings. Considering the monotonic increase of the electrical conductivity in both thin films and powder samples,^{101, 143} neutral TCNQ, or the Cu(TCNQ) byphase in the vapor phase loaded samples, must have a considerable contribution to the charge transport through the material.

The strongest evidence for a significant contribution of the host-guest complex to the electrical conductivity is the positive Seebeck coefficient observed by two independent research groups, suggesting holes as the majority charge carriers.^{202, 204} This is in direct contrast to the negative Seebeck coefficient of Cu(TCNQ).¹⁹² Thermoelectric measurements on vapor phase infiltrated samples could shed light on the contributions of the Cu(TCNQ) nano-wires to the observed conductivity.

Interestingly, $\text{CL}@\text{Cu}_3\text{BTC}_2$ materials with CL = TCNE, TCNB and other nitrile-CLs showed a completely insulating character (see supporting information to Study V). This is surprising given the fact that, for example, TCNE has a very similar reduction potential as TCNQ,¹⁸¹ and the same geometry with two nitrile groups in geminal position that can bridge two Cu paddlewheel units. At the same time, no byproduct is observed by PXRD or SEM. The question arises, if TCNQ is unique in triggering electrical conductivity in Cu_3BTC_2 , and if band structure calculations for $\text{TCNE}@\text{Cu}_3\text{BTC}_2$ would suggest similar electronic properties as for TCNQ, which would be in apparent conflict with the experimental evidence.

While improved theoretical models that account for the structural specification discussed above will certainly help to understand the charge transport in TCNQ@Cu₃BTC₂, additional experiments are necessary. For example, it would be interesting to see a systematic study investigating the electronic properties as a function of the defect concentration in parent Cu₃BTC₂. This should be feasible, given the fact that strategies for varying the defect concentration in MOF films are known from the literature,^{47, 170-171, 173} or defect-engineered Cu₃BTC₂ thin films should be accessible employing a fraction of a defect-linker (e.g. isophthalic acid) during the fabrication.^{49, 51, 219} For these experiments, it is advisable to use liquid phase infiltration with inert solvents such as DCM to avoid side reactions. Potential diffusion limitations and inhomogeneity in the distribution of TCNQ could be overcome by conducting the liquid phase infiltration at elevated temperatures.

Future developments in the field may include further detailed investigations of the conductivity mechanism taking into account the newly gained insights from this thesis. With a better understanding of the properties, potential applications of TCNQ@Cu₃BTC₂ can be evaluated. While sensing experiments with 1.0TCNQ@Cu₃BTC₂ did not show a direct response of the electrical conductivity to water vapor (cf. M. Rivera-Torrente, M. Filez, C. Schneider, E. C. van der Feltz, K. Wolkersdörfer, M. Wark, R. A. Fischer, and B. M. Weckhuysen, In-Situ Micro-Spectroscopic Imaging of Guests@MOF Crystals: The Case of TCNQ-Loaded HKUST-1. *in preparation*), the material could be tested in the context of MOF supercapacitors,⁹⁰ exploiting the high porosity of the material. Furthermore, it will be interesting to see the incorporation of other guest molecules such as DCNQI that are known in the context of conductive coordination polymers and might have a similar effect as TCNQ, or other molecules that can act as a CL and bridge the OMSs in Cu₃BTC₂.

4.2 Retrofitting

During the time of this doctoral thesis study, retrofitting has emerged as a new PSM method and attracted attention as a lever to systematically tune the physicochemical properties of MOFs. Even though the concept is still in its infancy and only a handful of retrofitted MOF (CL@MOF) systems have been published so far, the potential of retrofitting is evident looking at the vast number of MOFs with OMS. In this dissertation, the existing literature dealing with the post-synthetic installation of additional linkers into MOFs was reviewed (see chapter 1.3). Importantly, among the different terminologies, *retrofitting* was proposed as the general classification and its use is encouraged in the future.

Looking at retrofitting in the context of MOF chemistry as a whole (Figure 12), retrofitting is a subgroup of PSM, on the same level with post-synthetic metal or linker exchange, linker functionalization or post-synthetic reduction or oxidation of framework constituents.

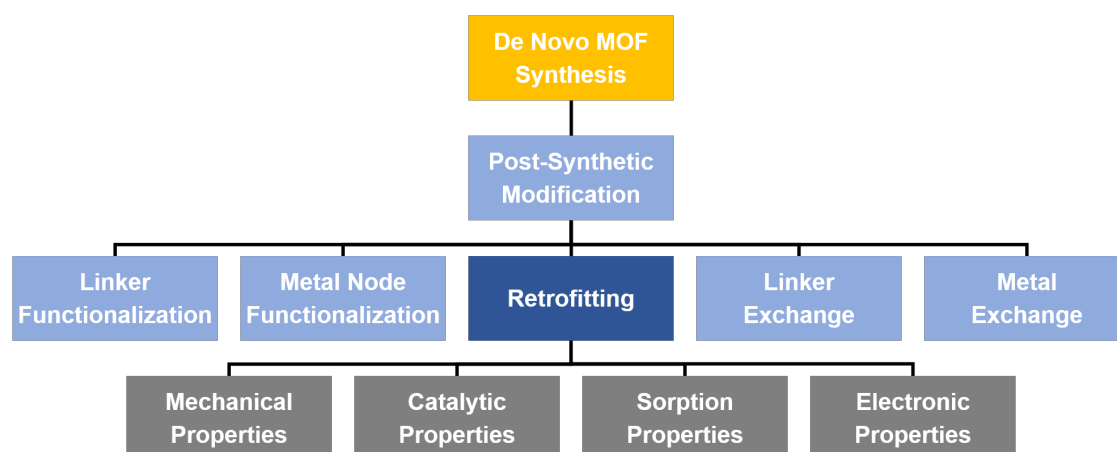


Figure 12. An updated hierarchy of the synthetic tool box of MOF chemistry. As-synthesized MOFs (yellow) can be altered via post-synthetic modification (light blue) with retrofitting (blue) representing an emerging method. At this time, physicochemical properties modified through retrofitting can be divided into four groups (grey).

Most of the CL@MOF examples examined in the introduction of this thesis were studied with respect to their mechanical, catalytic, or adsorption properties.^{117, 119-121} In addition, the use of non-innocent CLs was showed to open up the possibility of modifying the electronic structure of the MOF, as reflected in spectroscopic results and conductivity measurements.^{101, 205} Departing from here, the work presented in this thesis has made three major contributions to the field:

- (i) TCNQ@Cu₃BTC₂ was identified and categorized as a case of retrofitting. The thorough investigation in Studies I – III provides new insights into the structure-property relationships of the material. Worth highlighting are the crystallographic evidence of the ditopic binding of TCNQ to the OMSs of the framework and the observed relation between the defect chemistry of the parent MOF and the resulting redox chemistry with TCNQ during the infiltration reaction.

- (ii) Study IV highlights the possibility of tuning the mechanical properties of a MOF through retrofitting. In fact, this is the first study that investigates the lattice dynamics as a function of retrofitting. A reduction of the negative thermal expansion behavior of Cu_3BTC_2 could be induced by increasing the TCNQ loading, thereby establishing retrofitting as a tool to manipulate thermal expansion in MOFs.
- (iii) Finally, Study V provides a heuristic computational framework (*RetroFit*) for identifying further CL@MOF materials, which are necessary to advance the field and to understand the potential of the new PSM method. The practicality of the algorithm is emphasized by three new CL@ Cu_3BTC_2 materials that were successfully synthesized based on this approach and the transferability to other CL@MOF systems. Finally, *RetroFit* is available online and shall help experimentalists with the development of new materials.

It will be interesting to follow the advances in the field of retrofitting over the next years. Besides evolutionary developments describing new CL@MOF materials, fundamental developments are expected to be along two dimensions. On the one hand, new synthetic approaches will expand the library of retrofitted materials. On the other hand, existing strategies will be exploited to target further applications. For example, retrofitting of MOFs through interconnection of functional groups seems to be a logical step forward and would produce MOFs with an additional organic network (*i.e.* polymer) in the pores. While polymerization inside the pores or channels of MOFs is a research field itself,²²⁰ in this case the polymer has crystalline nature as the monomers (linkers) are at fixed positions within the MOF. This situation rather resembles a reversed approach towards polyMOFs (polymer MOFs) that were introduced by S. Cohen and co-workers and are made by reacting cross-polymerized linker molecules with metal precursors to form crystalline materials with mechanical properties of organic polymers.²²¹⁻²²² Along the second dimension, retrofitting could install CLs with target properties into a MOF and alter the chemical environment. For instance, malononitrile is a dinitrile-CL and showed a good fit between the OMS of Cu_3BTC_2 and related systems (see Study V). The highly Brønsted-acidic character of malononitrile ($\text{p}K_a = 11.1$)²²³ would render the pore environment highly acidic. Assuming structural stability of the parent framework upon retrofitting, malononitrile@MOF could promote catalytic reactions, *e.g.* acid-catalyzed isomerization, or prove advantageous for adsorption or separation applications. Another idea could be the installation of CLs with interesting (opto-)electronic properties at the confined positions within a MOF. The templated arrangement will then allow for a systematic study of the structure-property relations of the materials.

In summary, retrofitting is an intriguing concept that adds one more toy to the playground of reticular chemistry and this thesis gives a comprehensive overview of the efforts made in the field so far. Furthermore, strategies have been outlined that shall guide experimentalists to develop new CL@MOF materials with optimized properties. Developments in this field are eagerly awaited.

5 Bibliography

1. Wilson, D. M.; Hoyt, S.; Janata, J.; Booksh, K.; Obando, L., Chemical sensors for portable, handheld field instruments. *IEEE Sens. J.* **2001**, *1*, 256-274.
2. Kreno, L. E.; Van Duyne, R. P.; Hupp, J. T., Metal-organic frameworks for chemical sensing. *Abstr. Pap. Am. Chem. S.* **2013**, 245.
3. Robson, R., A net-based approach to coordination polymers *Dalton Trans.* **2000**, 3735-3744.
4. Chakrabarty, R.; Mukherjee, P. S.; Stang, P. J., Supramolecular Coordination: Self-Assembly of Finite Two- and Three-Dimensional Ensembles. *Chem. Rev.* **2011**, *111*, 6810-6918.
5. Cook, T. R.; Zheng, Y.-R.; Stang, P. J., Metal–Organic Frameworks and Self-Assembled Supramolecular Coordination Complexes: Comparing and Contrasting the Design, Synthesis, and Functionality of Metal–Organic Materials. *Chem. Rev.* **2013**, *113*, 734-777.
6. Furukawa, H.; Cordova, K. E.; O’Keeffe, M.; Yaghi, O. M., The Chemistry and Applications of Metal-Organic Frameworks. *Science* **2013**, *341*, 974-+.
7. Lin, R.-B.; Li, L.; Zhou, H.-L.; Wu, H.; He, C.; Li, S.; Krishna, R.; Li, J.; Zhou, W.; Chen, B., Molecular sieving of ethylene from ethane using a rigid metal–organic framework. *Nat. Mater.* **2018**, *17*, 1128-1133.
8. Yaghi, O. M.; O’Keeffe, M.; Ockwig, N. W.; Chae, H. K.; Eddaoudi, M.; Kim, J., Reticular Synthesis and the Design of New Materials. *Nature* **2003**, *423*, 705-714.
9. Kitagawa, S.; Kitaura, R.; Noro, S.-i., Functional Porous Coordination Polymers. *Angew. Chem., Int. Ed.* **2004**, *43*, 2334-2375.
10. Yaghi, O. M.; Kalmutzki, M. J.; Diercks, C. S., *Introduction to Reticular Chemistry: Metal-Organic Frameworks and Covalent Organic Frameworks*. John Wiley & Sons: 2019.
11. Werner, A., Beitrag zur konstitution anorganischer verbindungen. *Z. Anorg. Allg. Chem.* **1893**, *3*, 267-330.
12. Kauffman, G. B., *Alfred Werner: Founder of Coordination Chemistry*. Springer Science & Business Media: 2013.
13. Constable, E. C.; Housecroft, C. E., Coordination chemistry: the scientific legacy of Alfred Werner. *Chem. Soc. Rev.* **2013**, *42*, 1429-1439.
14. Hofmann, K.; Küspert, F., Verbindungen von kohlenwasserstoffen mit metallsalzen. *Z. Anorg. Allg. Chem.* **1897**, *15*, 204-207.
15. Rayner, J.; Powell, H. M., 67. Structure of molecular compounds. Part X. Crystal structure of the compound of benzene with an ammonia–nickel cyanide complex. *J. Chem. Soc.* **1952**, 319-328.
16. Nishikiori, S.-i.; Iwamoto, T., Crystal structure of Hofmann-dma-type benzene clathrate bis (dimethylamine) cadmium (II) tetracyanonickelate (II)-benzene (2/1). *Chem. Lett.* **1984**, *13*, 319-322.
17. Hasegawa, T.; Nishikiori, S.-i.; Iwamoto, T., The crystal structures of α , ω -diaminoalkanecadmium (II) tetracyanonickelate (II)-aromatic molecule inclusion compounds. II. 1, 6-diaminohexanecadmium (II) tetracyanonickelate (II)-o-toluidine (1/1): Cd (NH₂)₂ (CH₂)₆ (NH₂)₂ Ni (CN)₄. o-CH₃ C₆ H₄ NH₂. In *Clathrate Compounds, Molecular Inclusion Phenomena, and Cyclodextrins*, Springer: 1984; pp 351-357.
18. Nishikiori, S.-i.; Hasegawa, T.; Iwamoto, T., The crystal structures of α , ω -diaminoalkanecadmium (II) tetracyanonickelate (II)-Aromatic molecule inclusion compounds. V. Toluidine clathrates of the hosts built of the diamines, 1, 4-diaminobutane, 1,5-diaminopentane, and 1, 8-diaminooctane. *J. Incl. Phenom. Macrocycl. Chem.* **1991**, *11*, 137-152.

19. Kraft, A., Berliner Blau — ein Pigment aus dem frühen 18. Jahrhundert. *Nachr. Chem.* **2010**, *58*, 1124-1127.
20. Yaghi, O.; Li, H., Hydrothermal synthesis of a metal-organic framework containing large rectangular channels. *J. Am. Chem. Soc.* **1995**, *117*, 10401-10402.
21. Yaghi, O. M.; Li, G.; Li, H., Selective binding and removal of guests in a microporous metal-organic framework. *Nature* **1995**, *378*, 703.
22. Li, H.; Eddaoudi, M.; O'Keeffe, M.; Yaghi, O. M., Design and synthesis of an exceptionally stable and highly porous metal-organic framework. *Nature* **1999**, *402*, 276-279.
23. Horike, S.; Shimomura, S.; Kitagawa, S., Soft porous crystals. *Nat. Chem.* **2009**, *1*, 695-704.
24. Batten Stuart, R.; Champness Neil, R.; Chen, X.-M.; Garcia-Martinez, J.; Kitagawa, S.; Öhrström, L.; O'Keeffe, M.; Paik Suh, M.; Reedijk, J., Terminology of metal-organic frameworks and coordination polymers (IUPAC Recommendations 2013). In *Pure and Applied Chemistry*, 2013; Vol. 85, p 1715.
25. Batten, S. R.; Champness, N. R.; Chen, X.-M.; Garcia-Martinez, J.; Kitagawa, S.; Öhrström, L.; O'Keeffe, M.; Suh, M. P.; Reedijk, J., Coordination polymers, metal-organic frameworks and the need for terminology guidelines. *CrystEngComm* **2012**, *14*, 3001-3004.
26. Tranchemontagne, D. J.; Mendoza-Cortes, J. L.; O'Keeffe, M.; Yaghi, O. M., Secondary Building Units, Nets and Bonding in the Chemistry of Metal-Organic Frameworks. *Chem. Soc. Rev.* **2009**, *38*, 1257-1283.
27. Guillerm, V.; Kim, D.; Eubank, J. F.; Luebke, R.; Liu, X.; Adil, K.; Lah, M. S.; Eddaoudi, M., A Supramolecular Building Approach for the Design and Construction of Metal-Organic Frameworks. *Chem. Soc. Rev.* **2014**, *43*, 6141-6172.
28. Lu, W.; Wei, Z.; Gu, Z.-Y.; Liu, T.-F.; Park, J.; Park, J.; Tian, J.; Zhang, M.; Zhang, Q.; Gentle lii, T.; Bosch, M.; Zhou, H.-C., Tuning the Structure and Function of Metal-Organic Frameworks via Linker Design. *Chem. Soc. Rev.* **2014**, *43*, 5561-5593.
29. Cavka, J. H.; Jakobsen, S.; Olsbye, U.; Guillou, N.; Lamberti, C.; Bordiga, S.; Lillerud, K. P., A new zirconium inorganic building brick forming metal organic frameworks with exceptional stability. *J. Am. Chem. Soc.* **2008**, *130*, 13850-13851.
30. Rocha, J.; Carlos, L. D.; Paz, F. A. A.; Ananias, D., Luminescent multifunctional lanthanides-based metal-organic frameworks. *Chem. Soc. Rev.* **2011**, *40*, 926-940.
31. Eddaoudi, M.; Kim, J.; Rosi, N.; Vodak, D.; Wachter, J.; O'Keeffe, M.; Yaghi, O. M., Systematic Design of Pore Size and Functionality in Isoreticular MOFs and Their Application in Methane Storage. *Science* **2002**, *295*, 469-472.
32. Umemura, A.; Diring, S.; Furukawa, S.; Uehara, H.; Tsuruoka, T.; Kitagawa, S., Morphology Design of Porous Coordination Polymer Crystals by Coordination Modulation. *J. Am. Chem. Soc.* **2011**, *133*, 15506-15513.
33. Auerbach, S. M.; Carrado, K. A.; Dutta, P. K., *Handbook of Zeolite Science and Technology*. CRC Press: 2003.
34. Baerlocher, C.; McCusker, L. B.; Olson, D. H., *Atlas of zeolite framework types*. Elsevier: 2007.
35. Ribeiro, F. R.; Division, N. A. T. O. S. A., *Zeolites: Science and Technology: Science and Technology*. Springer Netherlands: 1984.
36. Guisnet, M.; Gilson, J. P., *Zeolites for Cleaner Technologies*. Imperial College Press: 2002.
37. Chen, B.; Yang, Z.; Zhu, Y.; Xia, Y., Zeolitic imidazolate framework materials: recent progress in synthesis and applications. *J. Mater. Chem. A* **2014**, *2*, 16811-16831.
38. Park, K. S.; Ni, Z.; Cote, A. P.; Choi, J. Y.; Huang, R. D.; Uribe-Romo, F. J.; Chae, H. K.; O'Keeffe, M.; Yaghi, O. M., Exceptional chemical and thermal stability of zeolitic imidazolate frameworks. *P. Natl. Acad. Sci. USA* **2006**, *103*, 10186-10191.
39. Petrovic, I.; Navrotsky, A.; Davis, M. E.; Zones, S. I., Thermochemical study of the stability of frameworks in high silica zeolites. *Chem. Mater.* **1993**, *5*, 1805-1813.

40. Ravenelle, R. M.; Schüßler, F.; D'Amico, A.; Danilina, N.; Van Bokhoven, J. A.; Lercher, J. A.; Jones, C. W.; Sievers, C., Stability of zeolites in hot liquid water. *J. Phys. Chem. C* **2010**, *114*, 19582-19595.
41. Yaghi, O. M., Reticular Chemistry—Construction, Properties, and Precision Reactions of Frameworks. *J. Am. Chem. Soc.* **2016**, *138*, 15507-15509.
42. Wells, A. F., The geometrical basis of crystal chemistry. Part 1. *Acta Cryst.* **1954**, *7*, 535-544.
43. Li, M.; Li, D.; O'Keeffe, M.; Yaghi, O. M., Topological Analysis of Metal–Organic Frameworks with Polytopic Linkers and/or Multiple Building Units and the Minimal Transitivity Principle. *Chem. Rev.* **2014**, *114*, 1343-1370.
44. Amirjalayer, S.; Schmid, R., Conformational Isomerism in the Isorecticular Metal Organic Framework Family: A Force Field Investigation. *J. Phys. Chem. C* **2008**, *112*, 14980-14987.
45. Tilley, R. J., *Defects in solids*. John Wiley & Sons: 2008; Vol. 4.
46. Busch, G., Early history of the physics and chemistry of semiconductors—from doubts to fact in a hundred years. *Eur. J. Phys.* **1989**, *10*, 254-264.
47. St. Petkov, P.; Vayssilov, G. N.; Liu, J.; Shekhah, O.; Wang, Y.; Wöll, C.; Heine, T., Defects in MOFs: A thorough characterization. *ChemPhysChem* **2012**, *13*, 2025-2029.
48. Fang, Z.; Bueken, B.; De Vos, D. E.; Fischer, R. A., Defect-engineered metal–organic frameworks. *Angew. Chem. Int. Ed.* **2015**, *54*, 7234-7254.
49. Dissegna, S.; Epp, K.; Heinz, W. R.; Kieslich, G.; Fischer, R. A., Defective Metal–Organic Frameworks. *Adv. Mater.* **2018**, *30*.
50. Cliffe, M. J.; Wan, W.; Zou, X.; Chater, P. A.; Kleppe, A. K.; Tucker, M. G.; Wilhelm, H.; Funnell, N. P.; Coudert, F.-X.; Goodwin, A. L., Correlated defect nanoregions in a metal–organic framework. *Nat. Commun.* **2014**, *5*, 4176.
51. Fang, Z.; Dürholt, J. P.; Kauer, M.; Zhang, W.; Lochenie, C.; Jee, B.; Albada, B.; Metzler-Nolte, N.; Pöpl, A.; Weber, B.; Muhler, M.; Wang, Y.; Schmid, R.; Fischer, R. A., Structural Complexity in Metal–Organic Frameworks: Simultaneous Modification of Open Metal Sites and Hierarchical Porosity by Systematic Doping with Defective Linkers. *J. Am. Chem. Soc.* **2014**, *136*, 9627-9636.
52. Shearer, G. C.; Chavan, S.; Bordiga, S.; Svelle, S.; Olsbye, U.; Lillerud, K. P., Defect Engineering: Tuning the Porosity and Composition of the Metal–Organic Framework UiO-66 via Modulated Synthesis. *Chem. Mater.* **2016**, *28*, 3749-3761.
53. Nijem, N.; Bluhm, H.; Ng, M. L.; Kunz, M.; Leone, S. R.; Gilles, M. K., Cu¹⁺ in HKUST-1: selective gas adsorption in the presence of water. *Chem. Commun.* **2014**, *50*, 10144-10147.
54. Szanyi, J.; Daturi, M.; Clet, G.; Baer, D. R.; Peden, C. H. F., Well-studied Cu-BTC still serves surprises: evidence for facile Cu²⁺/Cu⁺ interchange. *Phys. Chem. Chem. Phys.* **2012**, *14*, 4383-4390.
55. Dissegna, S.; Hardian, R.; Epp, K.; Kieslich, G.; Coulet, M.-V.; Llewellyn, P.; Fischer, R. A., Using water adsorption measurements to access the chemistry of defects in the metal–organic framework UiO-66. *CrystEngComm* **2017**, *19*, 4137-4141.
56. Dissegna, S.; Vervoorts, P.; Hobday, C. L.; Düren, T.; Daisenberger, D.; Smith, A. J.; Fischer, R. A.; Kieslich, G., Tuning the Mechanical Response of Metal–Organic Frameworks by Defect Engineering. *J. Am. Chem. Soc.* **2018**, *140*, 11581-11584.
57. Cliffe, M. J.; Hill, J. A.; Murray, C. A.; Coudert, F.-X.; Goodwin, A. L., Defect-Dependent Colossal Negative Thermal Expansion in UiO-66(Hf) Metal–Organic Framework. *Phys. Chem. Chem. Phys.* **2015**, *17*, 11586-11592.
58. Valvekens, P.; Vermoortele, F.; De Vos, D., Metal–organic frameworks as catalysts: the role of metal active sites. *Catal. Sci. Technol.* **2013**, *3*, 1435-1445.
59. Liu, Y.; Klet, R. C.; Hupp, J. T.; Farha, O., Probing the correlations between the defects in metal–organic frameworks and their catalytic activity by an epoxide ring-opening reaction. *Chem. Commun.* **2016**, *52*, 7806-7809.

60. Ye, G.; Zhang, D.; Li, X.; Leng, K.; Zhang, W.; Ma, J.; Sun, Y.; Xu, W.; Ma, S., Boosting Catalytic Performance of Metal–Organic Framework by Increasing the Defects via a Facile and Green Approach. *ACS Appl. Mater. Interfaces* **2017**, *9*, 34937-34943.
61. Cai, G.; Jiang, H.-L., A Modulator-Induced Defect-Formation Strategy to Hierarchically Porous Metal–Organic Frameworks with High Stability. *Angew. Chem. Int. Ed.* **2017**, *56*, 563-567.
62. Zhenlan, F.; Bart, B.; E., D. V. D.; A., F. R., Defect-Engineered Metal–Organic Frameworks. *Angew. Chem. Int. Ed.* **2015**, *54*, 7234-7254.
63. Brunauer, S.; Emmett, P. H.; Teller, E., Adsorption of Gases in Multimolecular Layers. *J. Am. Chem. Soc.* **1938**, *60*, 309-319.
64. Farha, O. K.; Eryazici, I.; Jeong, N. C.; Hauser, B. G.; Wilmer, C. E.; Sarjeant, A. A.; Snurr, R. Q.; Nguyen, S. T.; Yazaydin, A. O.; Hupp, J. T., Metal-Organic Framework Materials with Ultrahigh Surface Areas: Is the Sky the Limit? *J. Am. Chem. Soc.* **2012**, *134*, 15016-15021.
65. Hönicke, I. M.; Senkovska, I.; Bon, V.; Baburin, I. A.; Bönisch, N.; Raschke, S.; Evans, J. D.; Kaskel, S., Balancing Mechanical Stability and Ultrahigh Porosity in Crystalline Framework Materials. *Angew. Chem. Int. Ed.* **2018**, *57*, 13780-13783.
66. Ma, S.; Zhou, H.-C., Gas storage in porous metal–organic frameworks for clean energy applications. *Chem. Commun.* **2010**, *46*, 44-53.
67. Farrusseng, D., *Metal-organic frameworks: applications from catalysis to gas storage*. John Wiley & Sons: 2011.
68. Lee, J.; Farha, O. K.; Roberts, J.; Scheidt, K. A.; Nguyen, S. T.; Hupp, J. T., Metal–organic framework materials as catalysts. *Chem. Soc. Rev.* **2009**, *38*, 1450-1459.
69. Liu, J.; Chen, L.; Cui, H.; Zhang, J.; Zhang, L.; Su, C.-Y., Applications of Metal-Organic Frameworks in Heterogeneous Supramolecular Catalysis. *Chem. Soc. Rev.* **2014**, *43*, 6011-6061.
70. Miner, E. M.; Dincă, M., Metal-Organic Frameworks: Evolved Oxygen Evolution Catalysts. *Nat. Energy* **2016**, *1*, 16186.
71. Xia, B. Y.; Yan, Y.; Li, N.; Wu, H. B.; Lou, X. W.; Wang, X., A Metal–Organic Framework-Derived Bifunctional Oxygen Electrocatalyst. *Nat. Energy* **2016**, *1*, 15006.
72. Li, W.; Watzele, S.; El-Sayed, H. A.; Liang, Y.; Kieslich, G.; Bandarenka, A. S.; Rodewald, K.; Rieger, B.; Fischer, R. A., Unprecedented High Oxygen Evolution Activity of Electrocatalysts Derived from Surface-Mounted Metal–Organic Frameworks. *J. Am. Chem. Soc.* **2019**, *141*, 5926-5933.
73. Garlyyev, B.; Kratzl, K.; Rück, M.; Michalička, J.; Fichtner, J.; Macak, J. M.; Kratky, T.; Günther, S.; Cokoja, M.; Bandarenka, A. S., Optimizing the Size of Platinum Nanoparticles for Enhanced Mass Activity in the Electrochemical Oxygen Reduction Reaction. *Angew. Chem. Int. Ed.* **2019**, *58*, 9596-9600.
74. Arnold, L.; Averlant, G.; Marx, S.; Weickert, M.; Müller, U.; Mertel, J.; Horch, C.; Peksa, M.; Stallmach, F., Metal Organic Frameworks for Natural Gas Storage in Vehicles. *Chem. Ing. Tech.* **2013**, *85*, 1726-1733.
75. Mrasek, V. Tolle Idee! Was wurde daraus? - MOFs - zwei Gramm mit der Speicherfläche eines Fußballfelds https://www.deutschlandfunk.de/tolle-idee-was-wurde-daraus-mofs-zwei-gramm-mit-der.676.de.html?dram:article_id=451058 (accessed 28.07.2019).
76. Faust, T., MOFs move to market. *Nat. Chem.* **2016**, *8*, 990.
77. Kim, H.; Yang, S.; Rao, S. R.; Narayanan, S.; Kapustin, E. A.; Furukawa, H.; Umans, A. S.; Yaghi, O. M.; Wang, E. N., Water Harvesting From Air with Metal-Organic Frameworks Powered by Natural Sunlight. *Science* **2017**, *356*, 430-434.
78. Kim, H.; Rao, S. R.; Kapustin, E. A.; Zhao, L.; Yang, S.; Yaghi, O. M.; Wang, E. N., Adsorption-Based Atmospheric Water Harvesting Device for Arid Climates. *Nat. Commun.* **2018**, *9*, 1191.
79. Sheberla, D.; Sun, L.; Blood-Forsythe, M. A.; Er, S.; Wade, C. R.; Brozek, C. K.; Aspuru-Guzik, A.; Dincă, M., High Electrical Conductivity in Ni₃(2,3,6,7,10,11-

- hexaiminotriphenylene)₂, a Semiconducting Metal–Organic Graphene Analogue. *J. Am. Chem. Soc.* **2014**, *136*, 8859-8862.
80. Sun, L.; Campbell, M. G.; Dincă, M., Electrically Conductive Porous Metal–Organic Frameworks. *Angew. Chem. Int. Ed.* **2016**, *55*, 3566-3579.
81. Xie, L. S.; Sun, L.; Wan, R.; Park, S. S.; DeGayner, J. A.; Hendon, C. H.; Dincă, M., Tunable Mixed-Valence Doping toward Record Electrical Conductivity in a Three-Dimensional Metal–Organic Framework. *J. Am. Chem. Soc.* **2018**, *140*, 7411-7414.
82. Dincă, M.; Léonard, F., Metal–organic frameworks for electronics and photonics. *MRS Bull.* **2016**, *41*, 854-857.
83. Stassen, I.; Burtch, N.; Talin, A.; Falcaro, P.; Allendorf, M.; Ameloot, R., An Updated Roadmap for the Integration of Metal–Organic Frameworks with Electronic Devices and Chemical Sensors. *Chem. Soc. Rev.* **2017**, *46*, 3185-3241.
84. Stavila, V.; Talin, A. A.; Allendorf, M. D., MOF-Based Electronic and Opto-Electronic Devices. *Chem. Soc. Rev.* **2014**, *43*, 5994-6010.
85. Usman, M.; Mendiratta, S.; Lu, K.-L., Semiconductor Metal–Organic Frameworks: Future Low-Bandgap Materials. *Adv. Mater.* **2017**, *29*, 1605071.
86. Campbell, M. G.; Sheberla, D.; Liu, S. F.; Swager, T. M.; Dincă, M., Cu₃(hexaiminotriphenylene)₂: An Electrically Conductive 2D Metal–Organic Framework for Chemiresistive Sensing. *Angew. Chem. Int. Ed.* **2015**, *54*, 4349-4352.
87. Campbell, M. G.; Liu, S. F.; Swager, T. M.; Dincă, M., Chemiresistive Sensor Arrays from Conductive 2D Metal–Organic Frameworks. *J. Am. Chem. Soc.* **2015**, *137*, 13780-13783.
88. Campbell, M. G.; Dincă, M., Metal–Organic Frameworks as Active Materials in Electronic Sensor Devices. *Sensors* **2017**, *17*, 1108.
89. Kreno, L. E.; Leong, K.; Farha, O. K.; Allendorf, M.; Van Duyne, R. P.; Hupp, J. T., Metal–Organic Framework Materials as Chemical Sensors. *Chem. Rev.* **2011**, *112*, 1105-1125.
90. Sheberla, D.; Bachman, J. C.; Elias, J. S.; Sun, C.-J.; Shao-Horn, Y.; Dincă, M., Conductive MOF electrodes for stable supercapacitors with high areal capacitance. *Nat. Mater.* **2016**, *16*, 220.
91. Zhu, G.; Wen, H.; Ma, M.; Wang, W.; Yang, L.; Wang, L.; Shi, X.; Cheng, X.; Sun, X.; Yao, Y., A self-supported hierarchical Co-MOF as a supercapacitor electrode with ultrahigh areal capacitance and excellent rate performance. *Chem. Commun.* **2018**, *54*, 10499-10502.
92. Miner, E. M.; Fukushima, T.; Sheberla, D.; Sun, L.; Surendranath, Y.; Dincă, M., Electrochemical oxygen reduction catalysed by Ni₃(hexaiminotriphenylene)₂. *Nat. Commun.* **2016**, *7*, 10942.
93. Miner, E. M.; Gul, S.; Ricke, N. D.; Pastor, E.; Yano, J.; Yachandra, V. K.; Van Voorhis, T.; Dincă, M., Mechanistic Evidence for Ligand-Centered Electrocatalytic Oxygen Reduction with the Conductive MOF Ni₃(hexaiminotriphenylene)₂. *ACS Catal.* **2017**, *7*, 7726-7731.
94. Aiyappa, H. B.; Masa, J.; Andronesco, C.; Muhler, M.; Fischer, R. A.; Schuhmann, W., MOFs for Electrocatalysis: From Serendipity to Design Strategies. *Small Methods* **0**, 1800415.
95. Bhardwaj, S. K.; Bhardwaj, N.; Kaur, R.; Mehta, J.; Sharma, A. L.; Kim, K.-H.; Deep, A., An overview of different strategies to introduce conductivity in metal–organic frameworks and miscellaneous applications thereof. *J. Mater. Chem. A* **2018**, *6*, 14992-15009.
96. Sun, L.; Miyakai, T.; Seki, S.; Dinca, M., Mn-2(2,5-disulfhydrylbenzene-1,4-dicarboxylate): A Microporous Metal–Organic Framework with Infinite (-Mn-S-)(infinity) Chains and High Intrinsic Charge Mobility. *J. Am. Chem. Soc.* **2013**, *135*, 8185-8188.
97. Sun, L.; Hendon, C. H.; Minier, M. A.; Walsh, A.; Dinca, M., Million-Fold Electrical Conductivity Enhancement in Fe-2(DEBDC) versus Mn-2(DEBDC) (E = S, O). *J. Am. Chem. Soc.* **2015**, *137*, 6164-6167.

98. Dong, R.; Han, P.; Arora, H.; Ballabio, M.; Karakus, M.; Zhang, Z.; Shekhar, C.; Adler, P.; Petkov, P. S.; Erbe, A.; Mannsfeld, S. C. B.; Felser, C.; Heine, T.; Bonn, M.; Feng, X.; Cánovas, E., High-mobility band-like charge transport in a semiconducting two-dimensional metal–organic framework. *Nat. Mater.* **2018**, *17*, 1027-1032.
99. Sun, L.; Hendon, C. H.; Park, S. S.; Tulchinsky, Y.; Wan, R.; Wang, F.; Walsh, A.; Dinca, M., Is iron unique in promoting electrical conductivity in MOFs? *Chem. Sci.* **2017**, *8*, 4450-4457.
100. Park, S. S.; Hontz, E. R.; Sun, L.; Hendon, C. H.; Walsh, A.; Van Voorhis, T.; Dinca, M., Cation-Dependent Intrinsic Electrical Conductivity in Isostructural Tetrathiafulvalene-Based Microporous Metal-Organic Frameworks. *J. Am. Chem. Soc.* **2015**, *137*, 1774-1777.
101. Talin, A. A.; Centrone, A.; Ford, A. C.; Foster, M. E.; Stavila, V.; Haney, P.; Kinney, R. A.; Szalai, V.; El Gabaly, F.; Yoon, H. P.; Léonard, F.; Allendorf, M. D., Tunable Electrical Conductivity in Metal-Organic Framework Thin-Film Devices. *Science* **2014**, *343*, 66-69.
102. Kobayashi, Y.; Jacobs, B.; Allendorf, M. D.; Long, J. R., Conductivity, Doping, and Redox Chemistry of a Microporous Dithiolene-Based Metal-Organic Framework. *Chem. Mater.* **2010**, *22*, 4120-4122.
103. Dong, R.; Zhang, Z.; Tranca, D. C.; Zhou, S.; Wang, M.; Adler, P.; Liao, Z.; Liu, F.; Sun, Y.; Shi, W.; Zhang, Z.; Zschech, E.; Mannsfeld, S. C. B.; Felser, C.; Feng, X., A coronene-based semiconducting two-dimensional metal-organic framework with ferromagnetic behavior. *Nat. Commun.* **2018**, *9*, 2637.
104. Clough, A. J.; Skelton, J. M.; Downes, C. A.; de la Rosa, A. A.; Yoo, J. W.; Walsh, A.; Melot, B. C.; Marinescu, S. C., Metallic Conductivity in a Two-Dimensional Cobalt Dithiolene Metal–Organic Framework. *J. Am. Chem. Soc.* **2017**, *139*, 10863-10867.
105. Huang, X.; Sheng, P.; Tu, Z.; Zhang, F.; Wang, J.; Geng, H.; Zou, Y.; Di, C.-a.; Yi, Y.; Sun, Y.; Xu, W.; Zhu, D., A two-dimensional π -d conjugated coordination polymer with extremely high electrical conductivity and ambipolar transport behaviour. *Nat. Commun.* **2015**, *6*, 7408.
106. Lun, D. J.; Waterhouse, G. I. N.; Telfer, S. G., A General Thermolabile Protecting Group Strategy for Organocatalytic Metal-Organic Frameworks. *J. Am. Chem. Soc.* **2011**, *133*, 5806-5809.
107. Wang, Z.; Cohen, S. M., Postsynthetic Modification of Metal–Organic Frameworks. *Chem. Soc. Rev.* **2009**, *38*, 1315-1329.
108. Cohen, S. M., Postsynthetic Methods for the Functionalization of Metal–Organic Frameworks. *Chem. Rev.* **2011**, *112*, 970-1000.
109. Kim, M.; Cahill, J. F.; Fei, H.; Prather, K. A.; Cohen, S. M., Postsynthetic Ligand and Cation Exchange in Robust Metal–Organic Frameworks. *J. Am. Chem. Soc.* **2012**, *134*, 18082-18088.
110. Tanabe, K. K.; Cohen, S. M., Engineering a Metal–Organic Framework Catalyst by Using Postsynthetic Modification. *Angew. Chem. Int. Ed.* **2009**, *48*, 7424-7427.
111. Wang, Z.; Cohen, S. M., Modulating Metal–Organic Frameworks To Breathe: A Postsynthetic Covalent Modification Approach. *J. Am. Chem. Soc.* **2009**, *131*, 16675-16677.
112. Banerjee, M.; Das, S.; Yoon, M.; Choi, H. J.; Hyun, M. H.; Park, S. M.; Seo, G.; Kim, K., Postsynthetic Modification Switches an Achiral Framework to Catalytically Active Homochiral Metal–Organic Porous Materials. *J. Am. Chem. Soc.* **2009**, *131*, 7524-7525.
113. Deria, P.; Mondloch, J. E.; Karagiari, O.; Bury, W.; Hupp, J. T.; Farha, O. K., Beyond Post-Synthesis Modification: Evolution of Metal–Organic Frameworks via Building Block Replacement. *Chem. Soc. Rev.* **2014**, *43*, 5896-5912.
114. Karagiari, O.; Bury, W.; Mondloch, J. E.; Hupp, J. T.; Farha, O. K., Solvent-Assisted Linker Exchange: An Alternative to the De Novo Synthesis of Unattainable Metal–Organic Frameworks. *Angew. Chem. Int. Ed.* **2014**, *53*, 4530-4540.

115. Karagiari, O.; Bury, W.; Tylanakis, E.; Sarjeant, A. A.; Hupp, J. T.; Farha, O. K., Opening Metal–Organic Frameworks Vol. 2: Inserting Longer Pillars into Pillared-Paddlewheel Structures through Solvent-Assisted Linker Exchange. *Chem. Mater.* **2013**, *25*, 3499-3503.
116. Burnett, B. J.; Barron, P. M.; Hu, C.; Choe, W., Stepwise Synthesis of Metal–Organic Frameworks: Replacement of Structural Organic Linkers. *J. Am. Chem. Soc.* **2011**, *133*, 9984-9987.
117. Kapustin, E. A.; Lee, S.; Alshammari, A. S.; Yaghi, O. M., Molecular Retrofitting Adapts a Metal–Organic Framework to Extreme Pressure. *ACS Cent. Sci.* **2017**, *3*, 662-667.
118. Yuan, S.; Lu, W.; Chen, Y.-P.; Zhang, Q.; Liu, T.-F.; Feng, D.; Wang, X.; Qin, J.; Zhou, H.-C., Sequential Linker Installation: Precise Placement of Functional Groups in Multivariate Metal–Organic Frameworks. *J. Am. Chem. Soc.* **2015**, *137*, 3177-3180.
119. Yuan, S.; Chen, Y.-P.; Qin, J.-S.; Lu, W.; Zou, L.; Zhang, Q.; Wang, X.; Sun, X.; Zhou, H.-C., Linker Installation: Engineering Pore Environment with Precisely Placed Functionalities in Zirconium MOFs. *J. Am. Chem. Soc.* **2016**, *138*, 8912-8919.
120. Chen, C. X.; Wei, Z.; Jiang, J. J.; Fan, Y. Z.; Zheng, S. P.; Cao, C. C.; Li, Y. H.; Fenske, D.; Su, C. Y., Precise Modulation of the Breathing Behavior and Pore Surface in Zr-MOFs by Reversible Post-Synthetic Variable-Spacer Installation to Fine-Tune the Expansion Magnitude and Sorption Properties. *Angew. Chem. Int. Ed.* **2016**, *55*, 9932-9936.
121. Chen, C.-X.; Wei, Z.-W.; Jiang, J.-J.; Zheng, S.-P.; Wang, H.-P.; Qiu, Q.-F.; Cao, C.-C.; Fenske, D.; Su, C.-Y., Dynamic Spacer Installation for Multirole Metal–Organic Frameworks: A New Direction toward Multifunctional MOFs Achieving Ultrahigh Methane Storage Working Capacity. *J. Am. Chem. Soc.* **2017**, *139*, 6034-6037.
122. Lollar, C. T.; Pang, J.; Qin, J.-s.; Yuan, S.; Powell, J. A.; Zhou, H.-C., Thermodynamically Controlled Linker Installation in Flexible Zirconium Metal–Organic Frameworks. *Cryst. Growth Des.* **2019**, *19*, 2069-2073.
123. Allendorf, M. D.; Medishetty, R.; Fischer, R. A., Guest molecules as a design element for metal–organic frameworks. *MRS Bull.* **2016**, *41*, 865-869.
124. Bhattacharya, S.; Nayak, S.; Dutta, S. C., A Critical Review of Retrofitting Methods for Unreinforced Masonry Structures. *Int. J. Disaster Risk Reduct.* **2014**, *7*, 51-67.
125. Dadras Eslamlou, S.; Masia, M. J.; Totoev, Y. Z.; Page, A. W., Effect of Retrofitting on the Structural Factors for Seismic Assessment of Unreinforced Masonry Structures: A Review. *Aust. J. Struct. Eng.* **2019**, *20*, 26-53.
126. Mitra, S.; Sasmal, H. S.; Kundu, T.; Kandambeth, S.; Illath, K.; Díaz Díaz, D.; Banerjee, R., Targeted Drug Delivery in Covalent Organic Nanosheets (CONs) via Sequential Postsynthetic Modification. *J. Am. Chem. Soc.* **2017**, *139*, 4513-4520.
127. Segura, J. L.; Royuela, S.; Mar Ramos, M., Post-Synthetic Modification of Covalent Organic Frameworks. *Chem. Soc. Rev.* **2019**, *48*, 3903-3945.
128. Gineli, W.; Uriel Jr, C.; Tolles, E. L.; Webster, F. A., Seismic Stabilization of Historic Adobe Buildings. *WIT Trans. Built Env.* **1970**, *17*.
129. Priestley, M. N.; Seible, F.; Calvi, G. M., *Seismic design and retrofit of bridges*. John Wiley & Sons: 1996.
130. Castleton, H. F.; Stovin, V.; Beck, S. B.; Davison, J. B., Green roofs; building energy savings and the potential for retrofit. *Energ. Buildings* **2010**, *42*, 1582-1591.
131. Asadi, E.; Da Silva, M. G.; Antunes, C. H.; Dias, L., Multi-objective optimization for building retrofit strategies: A model and an application. *Energ. Buildings* **2012**, *44*, 81-87.
132. Sanhudo, L.; Ramos, N. M. M.; Poças Martins, J.; Almeida, R. M. S. F.; Barreira, E.; Simões, M. L.; Cardoso, V., Building information modeling for energy retrofitting – A review. *Renew. Sust. Energ. Rev.* **2018**, *89*, 249-260.
133. Smith, R.; Jobson, M.; Chen, L., Recent development in the retrofit of heat exchanger networks. *Appl. Therm. Eng.* **2010**, *30*, 2281-2289.

134. Jegla, Z.; Stehlík, P.; Kohoutek, J., Plant energy saving through efficient retrofit of furnaces. *Appl. Therm. Eng.* **2000**, *20*, 1545-1560.
135. Errico, M.; Rong, B.-G.; Tola, G.; Turunen, I., Process intensification for the retrofit of a multicomponent distillation plant an industrial case study. *Ind. Eng. Chem. Res.* **2008**, *47*, 1975-1980.
136. Necula, G. C.; McPeak, S.; Weimer, W. In *CCured: Type-safe retrofitting of legacy code*, ACM SIGPLAN Notices, ACM: 2002; pp 128-139.
137. Kim, J.; Batory, D.; Dig, D. In *Scripting parametric refactorings in Java to retrofit design patterns*, 2015 IEEE International Conference on Software Maintenance and Evolution (ICSME), IEEE: 2015; pp 211-220.
138. Pearson, R. G., Hard and Soft Acids and Bases. *J. Am. Chem. Soc.* **1963**, *85*, 3533-3539.
139. Chui, S. S.-Y.; Lo, S. M.-F.; Charmant, J. P. H.; Orpen, A. G.; Williams, I. D., A Chemically Functionalizable Nanoporous Material [Cu₃(TMA)₂(H₂O)₃]_n. *Science* **1999**, *283*, 1148-1150.
140. Holleman, A. F.; Wiberg, E.; Wiberg, N., *Lehrbuch der anorganischen Chemie*. Walter de Gruyter: 2007.
141. Moosavi, S. M.; Chidambaram, A.; Talirz, L.; Haranczyk, M.; Stylianou, K. C.; Smit, B., Capturing chemical intuition in synthesis of metal-organic frameworks. *Nat. Commun.* **2019**, *10*, 539.
142. Schneider, C.; Bodesheim, D.; Ehrenreich, M. G.; Crocellà, V.; Mink, J.; Fischer, R. A.; Butler, K. T.; Kieslich, G., Tuning the Negative Thermal Expansion Behavior of the Metal-Organic Framework Cu₃BTC₂ by Retrofitting. *J. Am. Chem. Soc.* **2019**, *141*, 10504-10509.
143. Schneider, C.; Ukaj, D.; Koerver, R.; Talin, A. A.; Kieslich, G.; Pujari, S. P.; Zuilhof, H.; Janek, J.; Allendorf, M. D.; Fischer, R. A., High Electrical Conductivity and High Porosity in a Guest@MOF Material: Evidence of TCNQ Ordering within Cu₃BTC₂ Micropores. *Chem. Sci.* **2018**, *9*, 7405-7412.
144. Dubbeldam, D.; Walton, K. S.; Ellis, D. E.; Snurr, R. Q., Exceptional Negative Thermal Expansion in Isoreticular Metal–Organic Frameworks. *Angew. Chem. Int. Ed.* **2007**, *46*, 4496-4499.
145. Wu, Y.; Kobayashi, A.; Halder, G. J.; Peterson, V. K.; Chapman, K. W.; Lock, N.; Southon, P. D.; Kepert, C. J., Negative Thermal Expansion in the Metal–Organic Framework Material Cu₃(1,3,5-benzenetricarboxylate)₂. *Angew. Chem. Int. Ed.* **2008**, *47*, 8929-8932.
146. Miller, W.; Smith, C. W.; Mackenzie, D. S.; Evans, K. E., Negative Thermal Expansion: A Review. *J. Mater. Sci.* **2009**, *44*, 5441-5451.
147. Dove, M. T.; Fang, H., Negative Thermal Expansion and Associated Anomalous Physical Properties: Review of the Lattice Dynamics Theoretical Foundation. *Rep. Prog. Phys.* **2016**, *79*, 066503.
148. Coates, C. S.; Goodwin, A. L., How to Quantify Isotropic Negative Thermal Expansion: Magnitude, Range, or Both? *Mater Horiz.* **2019**, *6*, 211-218.
149. Martinek, C.; Hummel, F. A., Linear Thermal Expansion of Three Tungstates. *J. Am. Ceram. Soc.* **1968**, *51*, 227-228.
150. S. O. Evans, J., Negative Thermal Expansion Materials *Dalton Trans.* **1999**, 3317-3326.
151. Goodwin, A. L.; Kepert, C. J., Negative Thermal Expansion and Low-Frequency Modes in Cyanide-Bridged Framework Materials. *Phys. Rev. B* **2005**, *71*, 140301.
152. Goodwin, A. L.; Kennedy, B. J.; Kepert, C. J., Thermal Expansion Matching via Framework Flexibility in Zinc Dicyanometallates. *J. Am. Chem. Soc.* **2009**, *131*, 6334-6335.
153. Atfield, M. P.; Sleight, A. W., Exceptional Negative Thermal Expansion in AlPO₄-17. *Chem. Mater.* **1998**, *10*, 2013-2019.

154. Lightfoot, P.; Woodcock, D. A.; Maple, M. J.; Villaescusa, L. A.; Wright, P. A., The Widespread Occurrence of Negative Thermal Expansion in Zeolites. *J. Mater. Chem.* **2001**, *11*, 212-216.
155. Lock, N.; Christensen, M.; Wu, Y.; Peterson, V. K.; Thomsen, M. K.; Piltz, R. O.; Ramirez-Cuesta, A. J.; McIntyre, G. J.; Norén, K.; Kutteh, R.; Kepert, C. J.; Kearley, G. J.; Iversen, B. B., Scrutinizing Negative Thermal Expansion in MOF-5 by Scattering Techniques and Ab Initio Calculations. *Dalton Trans.* **2013**, *42*, 1996-2007.
156. Zhou, W.; Wu, H.; Yildirim, T.; Simpson, J. R.; Walker, A. H., Origin of the Exceptional Negative Thermal Expansion in Metal-Organic Framework-5 Zn₄O(1,4-Benzenedicarboxylate)₃. *Phys. Rev. B* **2008**, *78*, 054114.
157. Lock, N.; Wu, Y.; Christensen, M.; Cameron, L. J.; Peterson, V. K.; Bridgeman, A. J.; Kepert, C. J.; Iversen, B. B., Elucidating Negative Thermal Expansion in MOF-5. *J. Phys. Chem. C* **2010**, *114*, 16181-16186.
158. Peterson, V. K.; Kearley, G. J.; Wu, Y.; Ramirez-Cuesta, A. J.; Kemner, E.; Kepert, C. J., Local Vibrational Mechanism for Negative Thermal Expansion: A Combined Neutron Scattering and First-Principles Study. *Angew. Chem. Int. Ed.* **2010**, *49*, 585-588.
159. Ryder, M. R.; Civalleri, B.; Cinque, G.; Tan, J.-C., Discovering Connections between Terahertz Vibrations and Elasticity Underpinning the Collective Dynamics of the HKUST-1 Metal-Organic Framework. *CrystEngComm* **2016**, *18*, 4303-4312.
160. Bhunia, M. K.; Hughes, J. T.; Fettingner, J. C.; Navrotsky, A., Thermochemistry of Paddle Wheel MOFs: Cu-HKUST-1 and Zn-HKUST-1. *Langmuir* **2013**, *29*, 8140-8145.
161. Müller, K.; Fink, K.; Schöttner, L.; Koenig, M.; Heinke, L.; Wöll, C., Defects as Color Centers: The Apparent Color of Metal-Organic Frameworks Containing Cu²⁺-Based Paddle-Wheel Units. *ACS Appl. Mater. Interfaces* **2017**, *9*, 37463-37467.
162. Stavila, V.; Volponi, J.; Katzenmeyer, A. M.; Dixon, M. C.; Allendorf, M. D., Kinetics and Mechanism of Metal-Organic Framework Thin Film Growth: Systematic Investigation of HKUST-1 Deposition on QCM Electrodes. *Chem. Sci.* **2012**, *3*, 1531-1540.
163. Shekhah, O.; Wang, H.; Kowarik, S.; Schreiber, F.; Paulus, M.; Tolan, M.; Sternemann, C.; Evers, F.; Zacher, D.; Fischer, R. A.; Woll, C., Step-by-step route for the synthesis of metal-organic frameworks. *J. Am. Chem. Soc.* **2007**, *129*, 15118-9.
164. Zacher, D.; Shekhah, O.; Woll, C.; Fischer, R. A., Thin Films of Metal-Organic Frameworks. *Chem. Soc. Rev.* **2009**, *38*, 1418-1429.
165. Bétard, A.; Fischer, R. A., Metal-Organic Framework Thin Films: From Fundamentals to Applications. *Chem. Rev.* **2011**, *112*, 1055-1083.
166. Heinke, L.; Tu, M.; Wannapaiboon, S.; Fischer, R. A.; Wöll, C., Surface-mounted metal-organic frameworks for applications in sensing and separation. *Microporous Mesoporous Mater.* **2015**, *216*, 200-215.
167. Liu, J.; Wöll, C., Surface-Supported Metal-Organic Framework Thin Films: Fabrication Methods, Applications, and Challenges. *Chem. Soc. Rev.* **2017**, *46*, 5730-5770.
168. Kreno, L. E.; Leong, K.; Farha, O. K.; Allendorf, M.; Van Duyne, R. P.; Hupp, J. T., Metal-Organic Framework Materials as Chemical Sensors. *Chem. Rev.* **2012**, *112*, 1105.
169. Stavila, V.; Schneider, C.; Mowry, C.; Zeitler, T. R.; Greathouse, J. A.; Robinson, A. L.; Denning, J. M.; Volponi, J.; Leong, K.; Quan, W.; Tu, M.; Fischer, R. A.; Allendorf, M. D., Thin Film Growth of nbo MOFs and their Integration with Electroacoustic Devices. *Adv. Funct. Mater.* **2016**, *26*, 1699-1707.
170. Gu, Z.-G.; Pfriem, A.; Hamsch, S.; Breitwieser, H.; Wohlgemuth, J.; Heinke, L.; Gliemann, H.; Wöll, C., Transparent films of metal-organic frameworks for optical applications. *Microporous Mesoporous Mater.* **2015**, *211*, 82-87.
171. Müller, K.; Singh Malhi, J.; Wohlgemuth, J.; Fischer, R. A.; Wöll, C.; Gliemann, H.; Heinke, L., Water as a modulator in the synthesis of surface-mounted metal-organic framework films of type HKUST-1. *Dalton Trans.* **2018**, *47*, 16474-16479.

172. Wang, Z.; Rodewald, K.; Medishetty, R.; Rieger, B.; Fischer, R. A., Control of Water Content for Enhancing the Quality of Copper Paddle-Wheel-Based Metal–Organic Framework Thin Films Grown by Layer-by-Layer Liquid-Phase Epitaxy. *Cryst. Growth Des.* **2018**, *18*, 7451-7459.
173. Delen, G.; Ristanović, Z.; Mandemaker, L. D. B.; Weckhuysen, B. M., Mechanistic Insights into Growth of Surface-Mounted Metal-Organic Framework Films Resolved by Infrared (Nano-) Spectroscopy. *Chemistry* **2018**, *24*, 187-195.
174. Liu, J.; Wang, Y.; Benin, A. I.; Jakubczak, P.; Willis, R. R.; LeVan, M. D., CO₂/H₂O adsorption equilibrium and rates on metal– organic frameworks: HKUST-1 and Ni/DOBDC. *Langmuir* **2010**, *26*, 14301-14307.
175. Moellmer, J.; Moeller, A.; Dreisbach, F.; Glaeser, R.; Staudt, R., High pressure adsorption of hydrogen, nitrogen, carbon dioxide and methane on the metal–organic framework HKUST-1. *Microporous Mesoporous Mater.* **2011**, *138*, 140-148.
176. Bordiga, S.; Regli, L.; Bonino, F.; Groppo, E.; Lamberti, C.; Xiao, B.; Wheatley, P. S.; Morris, R. E.; Zecchina, A., Adsorption Properties of HKUST-1 Toward Hydrogen and Other Small Molecules Monitored by IR. *Phys. Chem. Chem. Phys.* **2007**, *9*, 2676-2685.
177. Hendon, C. H.; Walsh, A., Chemical Principles Underpinning the Performance of The Metal-Organic Framework HKUST-1. *Chem. Sci.* **2015**, *6*, 3674-3683.
178. Schlichte, K.; Kratzke, T.; Kaskel, S., Improved Synthesis, Thermal Stability and Catalytic Properties of the Metal-Organic Framework Compound Cu₃(BTC)₂. *Microporous Mesoporous Mater.* **2004**, *73*, 81-88.
179. Acker, D. S.; Harder, R. J.; Hertler, W. R.; Mahler, W.; Melby, L. R.; Benson, R. E.; Mochel, W. E., 7,7,8,8-Tetracyanoquinodimethane and its Electrically Conducting Anion-Radical Derivatives. *J. Am. Chem. Soc.* **1960**, *82*, 6408-6409.
180. Acker, D. S.; Hertler, W. R., Substituted Quinodimethans. I. Preparation and Chemistry of 7,7,8,8-Tetracyanoquinodimethan. *J. Am. Chem. Soc.* **1962**, *84*, 3370-3374.
181. Peover, M. E., Reduction potentials and intermolecular charge-transfer spectra of organic acceptor molecules. Part 4.-Nitrobenzenes. *J. Chem. Soc. Faraday Trans.* **1964**, *60*, 479-483.
182. Deuchert, K.; Hünig, S., Multistage Organic Redox Systems—A General Structural Principle. *Angewandte Chemie International Edition in English* **1978**, *17*, 875-886.
183. Beverina, L.; Pagani, G. A.; Sassi, M., Multichromophoric electrochromic polymers: colour tuning of conjugated polymers through the side chain functionalization approach. *Chem. Commun.* **2014**, *50*, 5413-5430.
184. Ferraris, J.; Cowan, D. O.; Walatka, V.; Perlstein, J. H., Electron transfer in a new highly conducting donor-acceptor complex. *J. Am. Chem. Soc.* **1973**, *95*, 948-949.
185. Cohen, M. J.; Coleman, L.; Garito, A.; Heeger, A., Electrical conductivity of tetrathiofulvalinium tetracyanoquinodimethan (TTF)(TCNQ). *Phys. Rev. B* **1974**, *10*, 1298.
186. Melby, L. R.; Harder, R. J.; Hertler, W. R.; Mahler, W.; Benson, R. E.; Mochel, W. E., Substituted Quinodimethans. II. Anion-radical Derivatives and Complexes of 7,7,8,8-Tetracyanoquinodimethan. *J. Am. Chem. Soc.* **1962**, *84*, 3374-3387.
187. Kepler, R. G.; Bierstedt, P. E.; Merrifield, R. E., Electronic Conduction and Exchange Interaction in a New Class of Conductive Organic Solids. *Phys. Rev. Lett.* **1960**, *5*, 503-504.
188. Inoue, M.; Inoue, M. B., Infrared spectroscopic study of electrically conducting tetracyanoquinodimethane salts of copper chelates with ethylenediamine. *J. Chem. Soc., Faraday Trans. 2* **1985**, *81*, 539-547.
189. Aronson, S.; Mittelman, J. S., Free Energies of Formation of Metal-TCNQ Anion Radical Salts. *J. Solid State Chem.* **1981**, *36*, 221-224.
190. Potember, R. S.; Poehler, T. O.; Cowan, D. O., Electrical switching and memory phenomena in Cu-TCNQ thin films. *Appl. Phys. Lett.* **1979**, *34*, 405-407.

191. Heintz, R. A.; Zhao, H.; Ouyang, X.; Grandinetti, G.; Cowen, J.; Dunbar, K. R., New Insight into the Nature of Cu(TCNQ): Solution Routes to Two Distinct Polymorphs and Their Relationship to Crystalline Films That Display Bistable Switching Behavior. *Inorg. Chem.* **1999**, *38*, 144-156.
192. Sun, Y.; Zhang, F.; Sun, Y.; Di, C.-a.; Xu, W.; Zhu, D., n-Type Thermoelectric Materials Based on CuTCNQ Nanocrystals and CuTCNQ Nanorod Arrays. *J. Mater. Chem. A* **2015**, *3*, 2677-2683.
193. Wheland, R. C.; Martin, E. L., Synthesis of substituted 7,7,8,8-tetracyanoquinodimethanes. *The Journal of Organic Chemistry* **1975**, *40*, 3101-3109.
194. Wheland, R. C.; Gillson, J. L., Synthesis of electrically conductive organic solids. *J. Am. Chem. Soc.* **1976**, *98*, 3916-3925.
195. Kaim, W.; Moscherosch, M., The coordination chemistry of TCNE, TCNQ and related polynitrile π acceptors. *Coord. Chem. Rev.* **1994**, *129*, 157-193.
196. Aumüller, A.; Erk, P.; Klebe, G.; Hünig, S.; von Schütz, J. U.; Werner, H.-P., A Radical Anion Salt of 2,5-Dimethyl-N,N'-dicyanoquinonedimine with Extremely High Electrical Conductivity. *Angewandte Chemie International Edition in English* **1986**, *25*, 740-741.
197. Aumüller, A.; Hünig, S., One-Step Entry to N-Cyanimines and to N,N'-Dicyanoquinonedimines, a Novel Class of Electron-Acceptors. *Angewandte Chemie International Edition in English* **1984**, *23*, 447-448.
198. Peover, M. E., Reduction potentials and intermolecular charge-transfer spectra of organic acceptor molecules. Part 1.—Quinones. *J. Chem. Soc. Faraday Trans.* **1962**, *58*, 1656-1660.
199. Weitz, R. T.; Walter, A.; Engl, R.; Sezi, R.; Dehm, C., New Charge-Transfer Salts for Reversible Resistive Memory Switching. *Nano Lett.* **2006**, *6*, 2810-2813.
200. Chappell, J. S.; Bloch, A. N.; Bryden, W. A.; Maxfield, M.; Poehler, T. O.; Cowan, D. O., Degree of charge transfer in organic conductors by infrared absorption spectroscopy. *J. Am. Chem. Soc.* **1981**, *103*, 2442-2443.
201. Allendorf, M. D.; Foster, M. E.; Léonard, F.; Stavila, V.; Feng, P. L.; Doty, F. P.; Leong, K.; Ma, E. Y.; Johnston, S. R.; Talin, A. A., Guest-Induced Emergent Properties in Metal–Organic Frameworks. *J. Phys. Chem. Lett.* **2015**, *6*, 1182-1195.
202. Erickson, K. J.; Léonard, F.; Stavila, V.; Foster, M. E.; Spataru, C. D.; Jones, R. E.; Foley, B. M.; Hopkins, P. E.; Allendorf, M. D.; Talin, A. A., Thin Film Thermoelectric Metal–Organic Framework with High Seebeck Coefficient and Low Thermal Conductivity. *Adv. Mater.* **2015**, *27*, 3453-3459.
203. Neumann, T.; Liu, J.; Wächter, T.; Friederich, P.; Symalla, F.; Welle, A.; Mugnaini, V.; Meded, V.; Zharnikov, M.; Wöll, C.; Wenzel, W., Superexchange Charge Transport in Loaded Metal Organic Frameworks. *ACS Nano* **2016**, *10*, 7085-7093.
204. Chen, X.; Wang, Z.; Hassan, Z. M.; Lin, P.; Zhang, K.; Baumgart, H.; Redel, E., Seebeck Coefficient Measurements of Polycrystalline and Highly Ordered Metal–Organic Framework Thin Films. *ECS J. Solid State Sci. Technol.* **2017**, *6*, 150-153.
205. Usov, P. M.; Jiang, H.; Chevreau, H.; Peterson, V. K.; Leong, C. F.; D'Alessandro, D. M., Guest–Host Complexes of TCNQ and TCNE with Cu₃(1,3,5-benzenetricarboxylate)₂. *J. Phys. Chem. C* **2017**, *121*, 26330-26339.
206. Pöpl, A.; Kunz, S.; Himsl, D.; Hartmann, M., CW and Pulsed ESR Spectroscopy of Cupric Ions in the Metal–Organic Framework Compound Cu₃(BTC)₂. *J. Phys. Chem. C* **2008**, *112*, 2678-2684.
207. Zhang, X. X.; Chui, S. S.-Y.; Williams, I. D., Cooperative magnetic behavior in the coordination polymers [Cu₃(TMA)₂L₃] (L=H₂O, pyridine). *J. Appl. Phys.* **2000**, *87*, 6007-6009.
208. Last, B. J.; Thouless, D. J., Percolation Theory and Electrical Conductivity. *Phys. Rev. Lett.* **1971**, *27*, 1719-1721.
209. Tominaka, S.; Cheetham, A. K., Intrinsic and extrinsic proton conductivity in metal-organic frameworks. *RSC Adv.* **2014**, *4*, 54382-54387.

210. Sun, L.; Park, S. S.; Sheberla, D.; Dincă, M., Measuring and Reporting Electrical Conductivity in Metal–Organic Frameworks: Cd₂(TTFTB) as a Case Study. *J. Am. Chem. Soc.* **2016**, *138*, 14772-14782.
211. Schneider, C. Thin Film Synthesis and Guest Molecule Interactions in Copper Paddlewheel Metal-Organic Frameworks. Master Thesis, Ruhr-University Bochum, 2015.
212. Nie, X.; Kulkarni, A.; Sholl, D. S., Computational Prediction of Metal Organic Frameworks Suitable for Molecular Infiltration as a Route to Development of Conductive Materials. *J. Phys. Chem. Lett.* **2015**, *6*, 1586-1591.
213. Sengupta, A.; Datta, S.; Su, C.; Heng, T. S.; Ding, J.; Vittal, J. J.; Loh, K. P., Tunable Electrical Conductivity and Magnetic Property of the Two Dimensional Metal Organic Framework [Cu(TPyP)Cu₂(O₂CCH₃)₄]. *ACS Appl. Mater. Interfaces* **2016**, *8*, 16154-16159.
214. Goswami, S.; Ray, D.; Otake, K.-i.; Kung, C.-W.; Garibay, S. J.; Islamoglu, T.; Atilgan, A.; Cui, Y.; Cramer, C. J.; Farha, O. K.; Hupp, J. T., A porous, electrically conductive hexa-zirconium(iv) metal–organic framework. *Chem. Sci.* **2018**, *9*, 4477-4482.
215. Liu, X.; Kozłowska, M.; Okkali, T.; Wagner, D.; Higashino, T.; Brenner-Weiß, G.; Marschner, S. M.; Fu, Z.; Zhang, Q.; Imahori, H.; Bräse, S.; Wenzel, W.; Wöll, C.; Heinke, L., Photoconductivity in Metal–Organic Framework (MOF) Thin Films. *Angew. Chem. Int. Ed.* **2019**, *58*, 9590-9595.
216. Ukaj, D. Solvent-free Synthesis and Electrical Conductivity in Guest-Loaded Metal-Organic Frameworks. Master Thesis, Technical University of Munich, 2017.
217. Thürmer, K.; Schneider, C.; Stavila, V.; Friddle, R. W.; Léonard, F.; Fischer, R. A.; Allendorf, M. D.; Talin, A. A., Surface Morphology and Electrical Properties of Cu₃BTC₂ Thin Films Before and After Reaction with TCNQ. *ACS Appl. Mater. Interfaces* **2018**, *10*, 39400-39410.
218. Shiozawa, H.; Bayer, B. C.; Peterlik, H.; Meyer, J. C.; Lang, W.; Pichler, T., Doping of metal–organic frameworks towards resistive sensing. *Sci. Rep.* **2017**, *7*, 2439.
219. Wang, Z.; Wannapaiboon, S.; Rodewald, K.; Tu, M.; Rieger, B.; Fischer, R. A., Directing the hetero-growth of lattice-mismatched surface-mounted metal–organic frameworks by functionalizing the interface. *J. Mater. Chem. A* **2018**, *6*, 21295-21303.
220. Uemura, T.; Yanai, N.; Kitagawa, S., Polymerization reactions in porous coordination polymers. *Chem. Soc. Rev.* **2009**, *38*, 1228-1236.
221. Zhang, Z.; Nguyen, H. T. H.; Miller, S. A.; Cohen, S. M., polyMOFs: A Class of Interconvertible Polymer-Metal-Organic-Framework Hybrid Materials. *Angew. Chem. Int. Ed.* **2015**, *54*, 6152-6157.
222. Zhang, Z.; Nguyen, H. T. H.; Miller, S. A.; Ploskonka, A. M.; DeCoste, J. B.; Cohen, S. M., Polymer–Metal–Organic Frameworks (polyMOFs) as Water Tolerant Materials for Selective Carbon Dioxide Separations. *J. Am. Chem. Soc.* **2016**, *138*, 920-925.
223. Matthews, W. S.; Bares, J. E.; Bartmess, J. E.; Bordwell, F. G.; Cornforth, F. J.; Drucker, G. E.; Margolin, Z.; McCallum, R. J.; McCollum, G. J.; Vanier, N. R., Equilibrium acidities of carbon acids. VI. Establishment of an absolute scale of acidities in dimethyl sulfoxide solution. *J. Am. Chem. Soc.* **1975**, *97*, 7006-7014.

6 Supporting Information

6.1 Supporting Information Study I

SUPPORTING INFORMATION

Surface morphology and electrical properties of Cu_3BTC_2 thin films before and after reaction with TCNQ

Konrad Thürmer^{a†}, Christian Schneider^{b‡}, Vitalie Stavila^a, Raymond W. Friddle^a, François
Léonard^a, Roland A. Fischer^b, Mark D. Allendorf^{a*}, A. Alec Talin^a*

^a Sandia National Laboratories, Livermore, CA 94551, USA

^b Department of Chemistry, Technical University Munich, Lichtenbergstrasse 4, 85748 Garching,
Germany

[†] *These authors contributed equally.*

Corresponding Authors

* E-mail: kthurme@sandia.gov

* E-mail: mdallen@sandia.gov

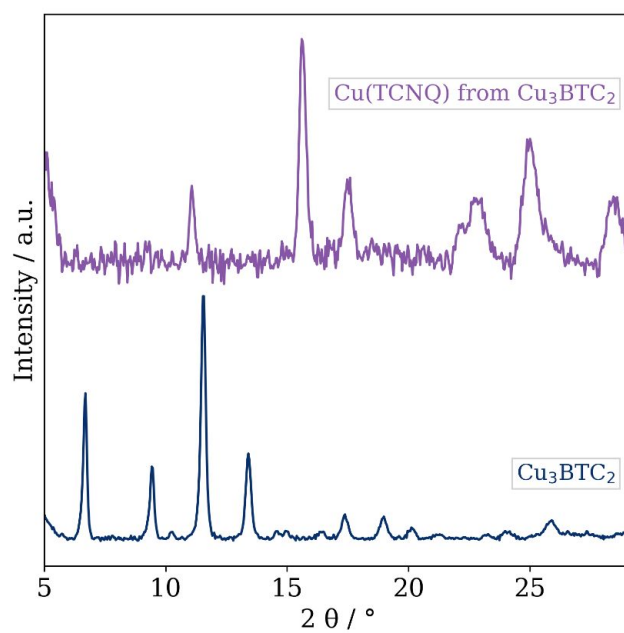


Figure S1: GIXRD pattern of a 50 cycles Cu₃BTC₂ film on SiO₂/Si(001) before and after infiltration with TCNQ in a MeOH solution.

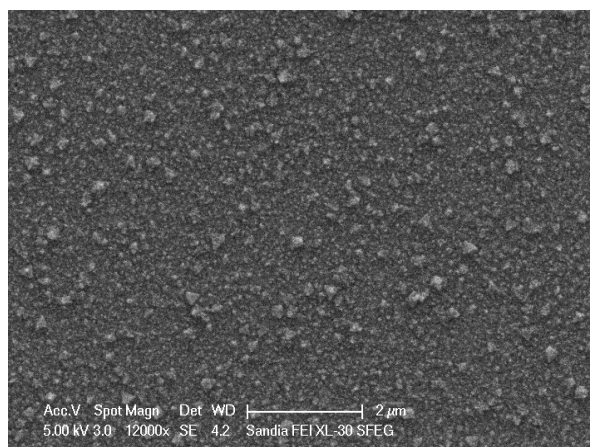


Figure S2: SEM image of a 50 cycles Cu₃BTC₂ film on SiO₂/Si(001). Similar to the films grown on ITO, a large size distribution (many small and few large crystallites) can be observed.

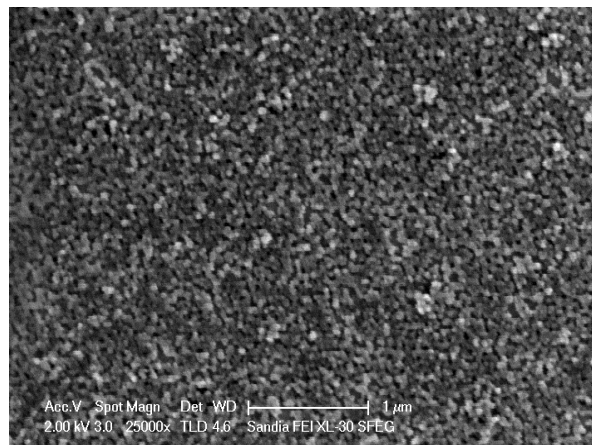


Figure S3: SEM image of a 50 cycles Cu_3BTC_2 film on $\text{SiO}_2/\text{Si}(001)$ after immersion in a saturated TCNQ solution in MeOH. A conversion of the film is evidenced by the morphology change.

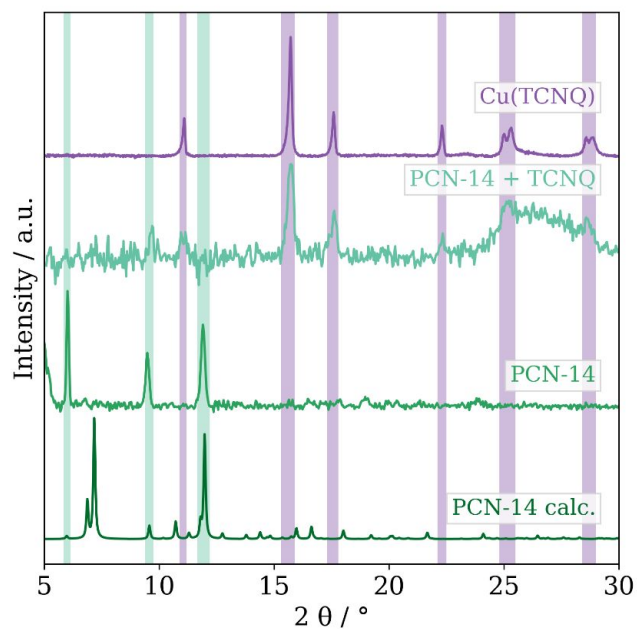
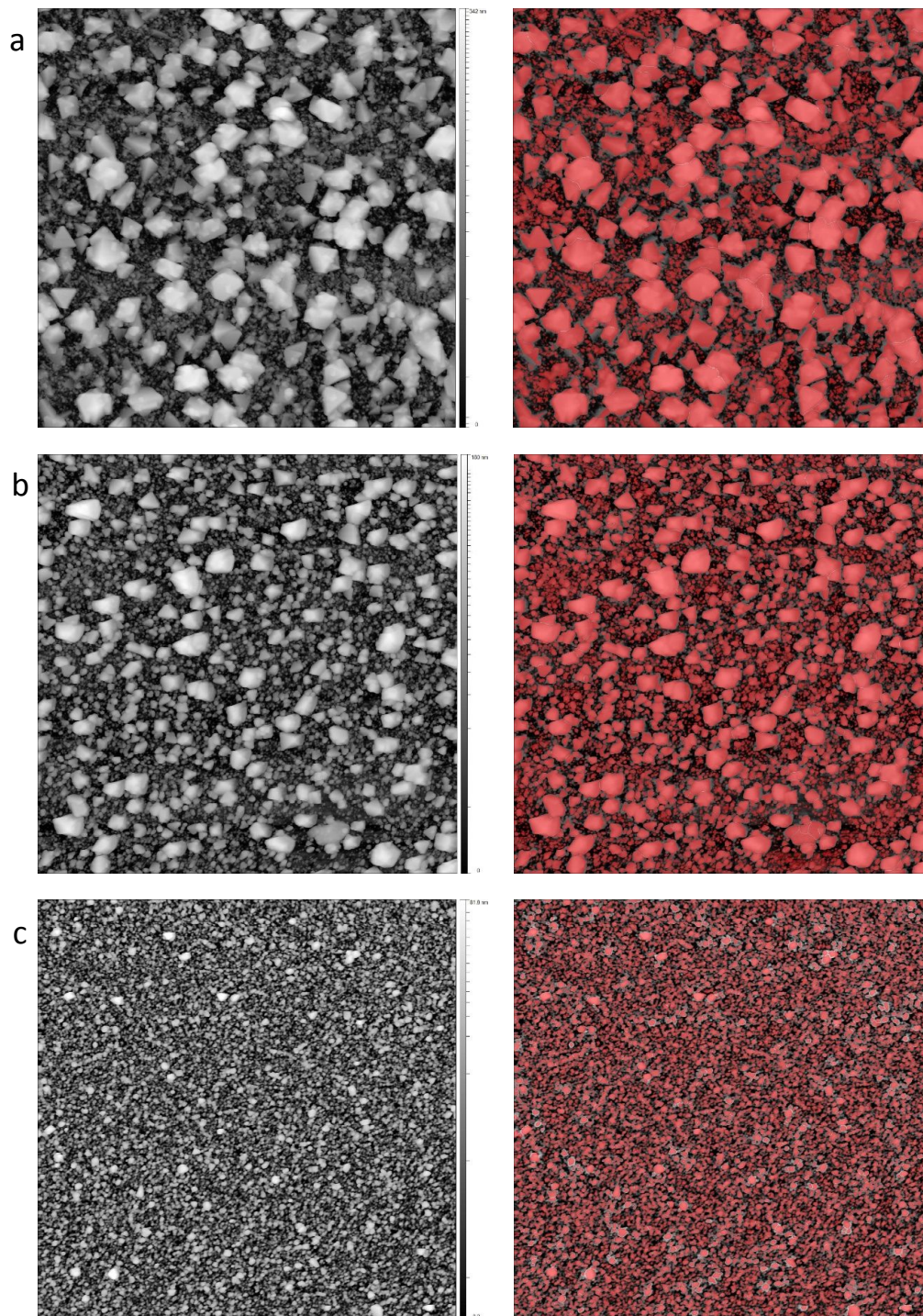


Figure S4: GIXRD patterns of a solvothermally synthesized PCN-14 film before and after infiltration with TCNQ in MeOH. The reference pattern for PCN-14 and Cu(TCNQ) are shown at the bottom and top, respectively. Peak positions are indicated by vertical boxes.



S-4

Figure S5: AFM topography images (left column) and corresponding grain masks (right column) used for analyzing particle size distributions. a, HKUST-1 after 20 cycles on ITO substrate. b, HKUST-1 after 4 cycles on ITO substrate. c, HKUST after 4 cycles on SiO₂ substrate. Masking of small particles was carried out by a watershed algorithm, while larger particles were masked by height thresholding with joined particles separated by manual editing. All masking operations have been performed in Gwyddion SPM analysis software. Topography is displayed by non-linear adaptive false color mapping. Image sizes are 5 μm x 5 μm.

6.2 Supporting Information Study II

High electrical conductivity and high porosity in a Guest@MOF material: evidence of TCNQ ordering within Cu₃BTC₂ micropores

Christian Schneider^a, Dardan Ukaj^a, Raimund Koerver^b, A. Alec Talin^c, Gregor Kieslich^a, Sidharam P. Pujari^d, Han Zuilhof^{d,e}, Jürgen Janek^b, Mark D. Allendorf^c, Roland A. Fischer^{*a}

a Department of Chemistry, Technical University Munich, Lichtenbergstrasse 4, D-85748 Garching, Germany

b Institute of Physical Chemistry & Center for Materials Research (ZFM), Justus-Liebig-University Giessen, Heinrich-Buff-Ring 17, 35392 Giessen, Germany

c Sandia National Laboratories, Livermore, CA 94551, USA

d Laboratory of Organic Chemistry, Wageningen University & Research, Stippeneng 4, 6708 WE Wageningen, The Netherlands

e School of Pharmaceutical Sciences and Technology, Tianjin University, 92 Weijin Road, Tianjin, P.R. China

Contents

Powder X-ray diffraction (PXRD).....	2
Theoretical BET surface area if TCNQ does not penetrate the MOF	4
Infrared (IR) spectroscopy.....	4
Thermogravimetric analysis (TGA) and differential scanning calorimetry (DSC)	5
Electrical conductivity measurements	5
Auger electron spectroscopy (AES).....	9
Scanning electron microscopy (SEM) images	10
X-ray photon absorption spectroscopy (XPS)	12
Elemental analysis.....	15
Liquid phase infiltration	15
References	18

Powder X-ray diffraction (PXRD)

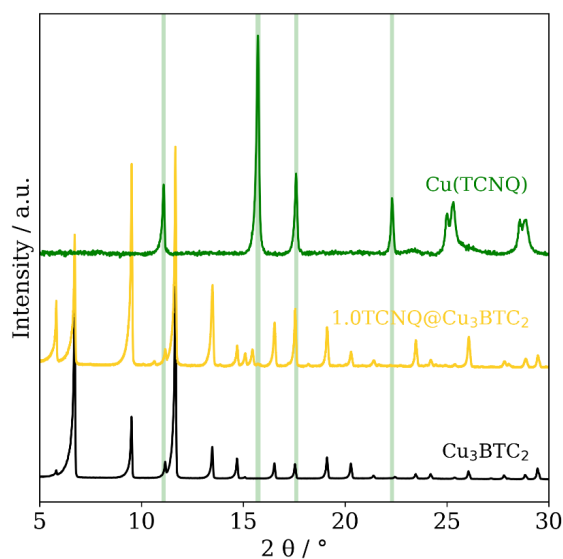


Figure S 1: Powder X-ray diffraction (PXRD) pattern of pristine Cu_3BTC_2 (black), $1.0\text{TCNQ}@Cu_3\text{BTC}_2$ and $\text{Cu}(\text{TCNQ})$ prepared following the literature procedure.^[1] Vertical lines indicate the reflection positions of $\text{Cu}(\text{TCNQ})$. The principal reflection of $\text{Cu}(\text{TCNQ})$ can be found in the diffraction pattern of $1.0\text{TCNQ}@Cu_3\text{BTC}_2$.

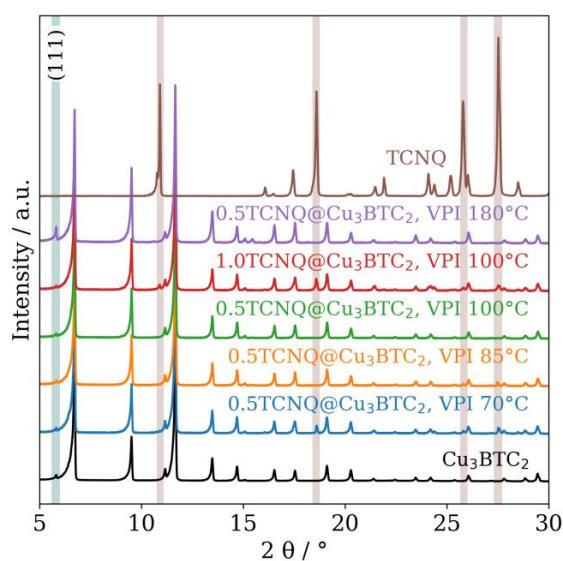


Figure S 2: PXRD pattern of pristine Cu_3BTC_2 (black), Cu_3BTC_2 loaded with TCNQ at different reaction temperatures and TCNQ (brown). The pronounced (111) reflection is absent for samples infiltrated at low temperatures. Instead, new reflections attributed to unreacted TCNQ become apparent.

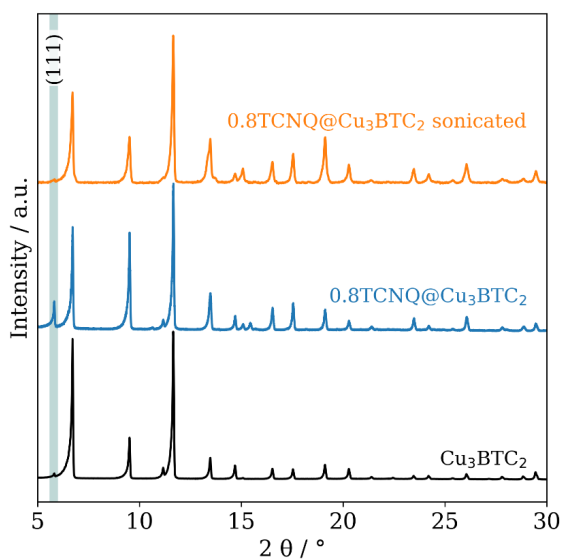


Figure S 3: Powder X-ray diffraction (PXRD) pattern of pristine Cu_3BTC_2 (black), $0.8\text{TCNQ}@Cu_3\text{BTC}_2$ before (blue) and after sonication in hexane (orange). The crystal structure of the MOF remains intact after sonication, but the intensity of the (111) reflection and additional reflections attributed to a systematic arrangement of TCNQ vanish.

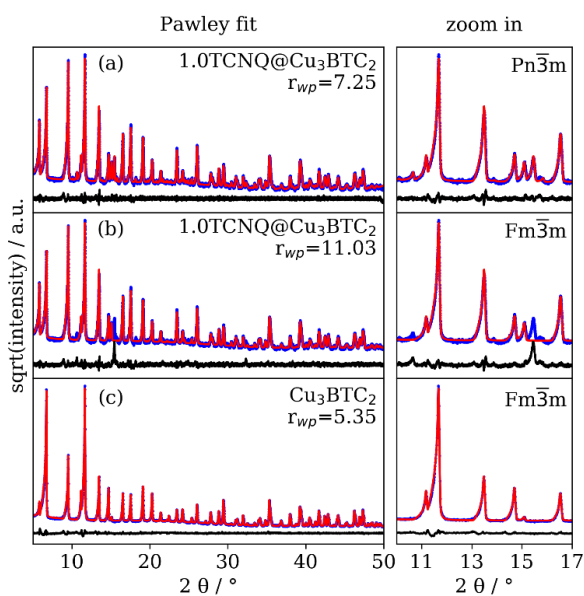


Figure S 4: Pawley profile fit $1.0\text{TCNQ}@Cu_3\text{BTC}_2$ using the space group $\text{Pn}\bar{3}\text{m}$ (a) and $\text{Fm}\bar{3}\text{m}$ (b) and of Cu_3BTC_2 (c). The experimental data, profile fit and their difference are plotted in blue, red, and black, respectively. The weighted profile R-factor (r_{wp}) for each fit is shown in each diagram. A zoom in is shown on the right-hand side. Although the diffraction pattern of Cu_3BTC_2 can be fitted in the space group $\text{Fm}\bar{3}\text{m}$, not all reflections of $1.0\text{TCNQ}@Cu_3\text{BTC}_2$ can be indexed using the same space group. A profile fit using the primitive space group $\text{Pn}\bar{3}\text{m}$, however, can account for all new reflections.

Theoretical BET surface area if TCNQ does not penetrate the MOF

The accessible pore volume of the MOF would remain unchanged in a physical mixture of Cu_3BTC_2 and TCNQ if TCNQ was not capable of diffusing into the MOF pores during the VPI process. Consequently, during a porosimetry measurement, only the additional mass of the non-porous TCNQ would contribute to the decrease of the BET surface area compared to the pristine MOF. The measured BET surface area of pristine Cu_3BTC_2 (BTC = 1,3,5-benzenetricarboxylate) amounts to $1833.0 \text{ m}^2/\text{g}$. For a sample with the composition $n(\text{TCNQ}) / n(\text{Cu}_3\text{BTC}_2) = 1$, denoted as $1.0\text{TCNQ}@Cu_3\text{BTC}_2$, the relative weight percentage of TCNQ amounts to 25.2%. In case of a physical mixture, the presence of TCNQ would result in a loss in BET surface area of $463.6 \text{ m}^2/\text{g}$ to $1370.4 \text{ m}^2/\text{g}$. The prepared sample $1.0\text{TCNQ}@Cu_3\text{BTC}_2$, however, has a BET surface area of only $574 \text{ m}^2/\text{g}$, which is clear evidence for the incorporation of TCNQ in Cu_3BTC_2 .

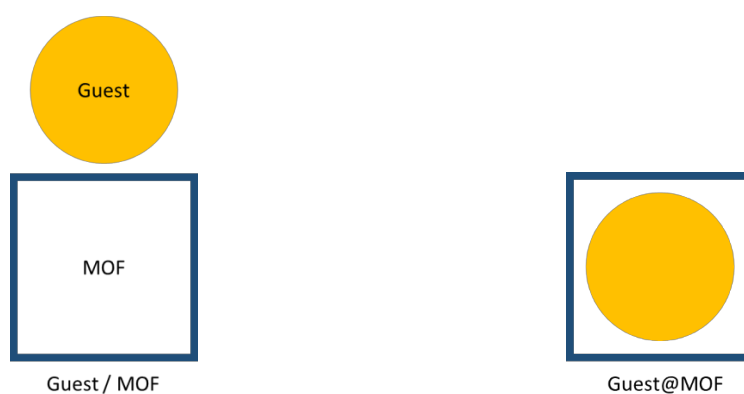


Figure S 5: Schematic illustration of the difference between a physical mixture of a MOF plus a guest material (left) and a Guest@MOF material (right) to illustrate the implication of the two scenarios on the BET surface area.

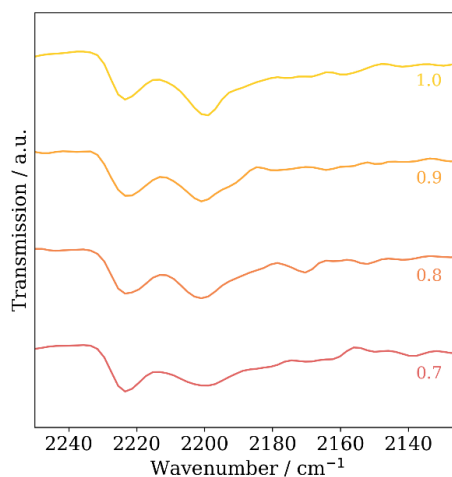
Infrared (IR) spectroscopy

Figure S 6: IR spectra in the CN vibration region of $x\text{TCNQ}@Cu_3\text{BTC}_2$ with high loadings (value for x indicated below spectrum).

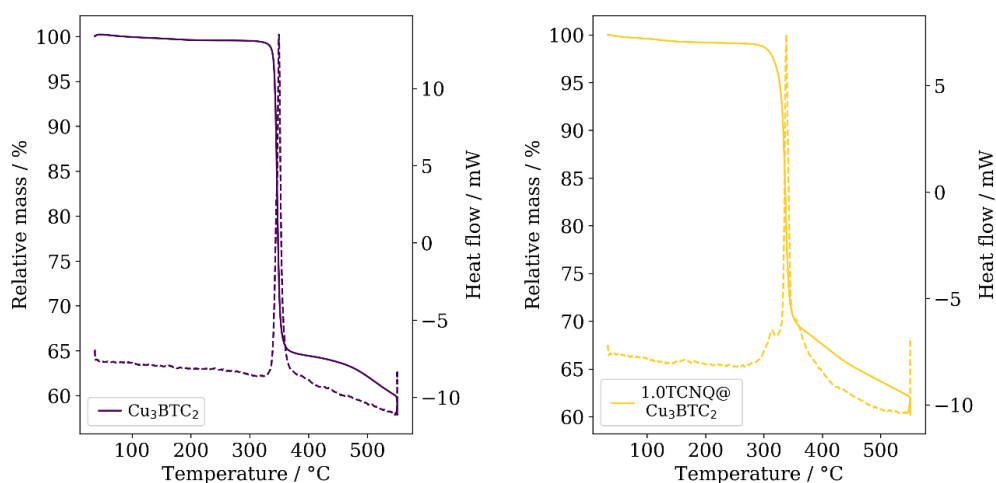
Thermogravimetric analysis (TGA) and differential scanning calorimetry (DSC)

Figure S 7: TGA (solid line) and DSC (dashed line) of pristine Cu_3BTC_2 (left) and 1.0TCNQ@ Cu_3BTC_2 (right).

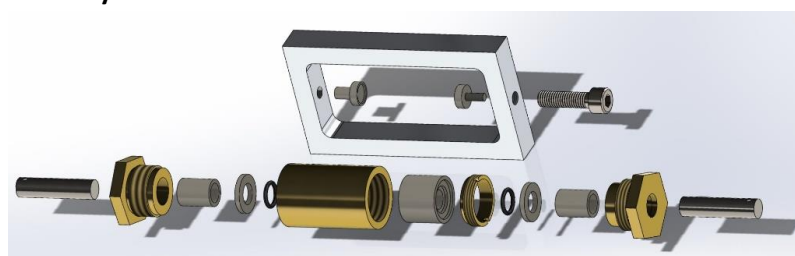
Electrical conductivity measurements

Figure S 8: Schematic of the air-tight press cell used for electrical conductivity measurements. MOF powder is filled into the assembled cell compressed between the two outer stainless steel pistons. PEEK elements serve as electrical insulation from the brass parts. After the powder is pressed to a pellet, the cell is mounted into an aluminum frame and fixed with a screw applying a torque of 10 Nm to maintain pressure on the pressed pellet. The stainless steel cylinders serve as electrodes for the conductivity measurements.

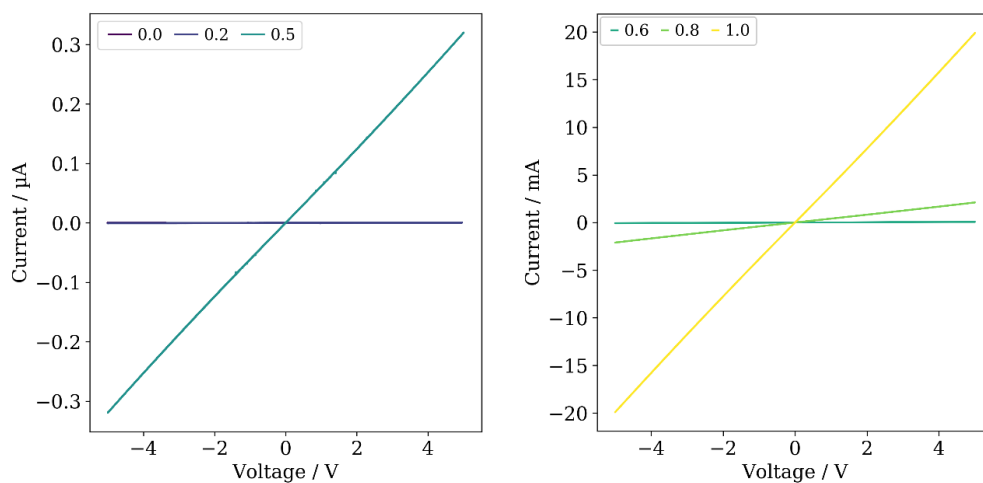


Figure S 9: I/V -curves of TCNQ-loaded Cu_3BTC_2 samples. Figure divided into two plots for clarity (different scale of y-axis).

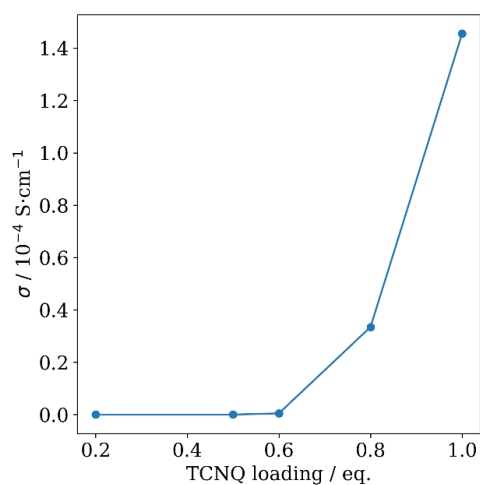


Figure S 10: Calculated conductivities of TCNQ-loaded Cu_3BTC_2 samples plotted versus loading amount.

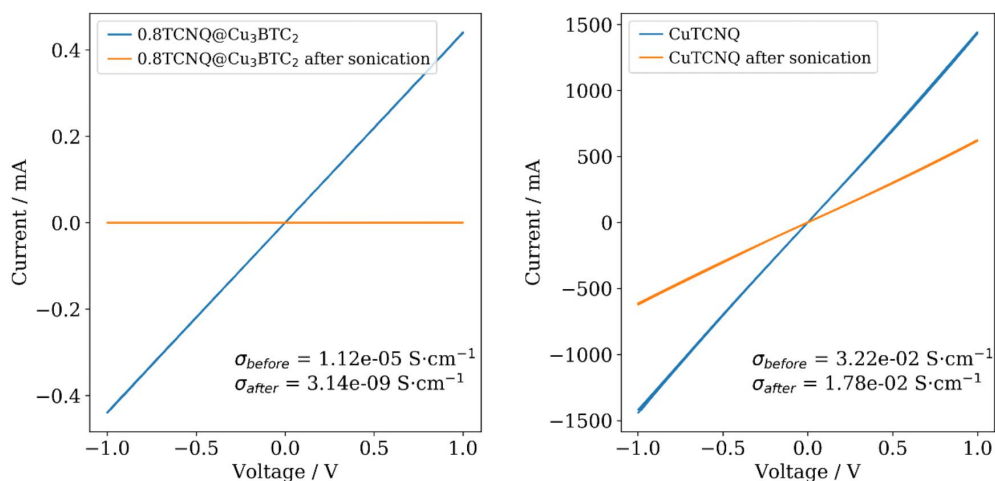


Figure S 11: *IV*-curves of 0.8TCNQ@Cu₃BTC₂ and pristine Cu(TCNQ) before and after 1 hour sonication in hexane. Conductivity of 0.8TCNQ@Cu₃BTC₂ drops by four orders of magnitude while the conductivity of pristine Cu(TCNQ) shows only small changes.

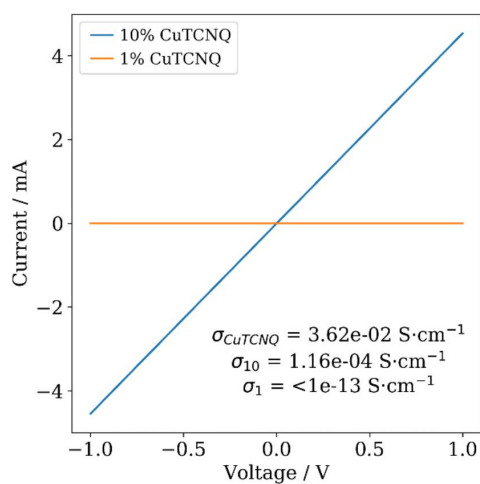


Figure S 12: *IV* curves of pressed pellets of physical mixtures of 1% and 10% CuTCNQ mixed with pristine Cu₃BTC₂. Conductivities of both mixtures and of pristine CuTCNQ are given in the diagram.

Table S 1: Pellet thicknesses for the calculation of the conductivity.

Sample	pellet thickness / mm
Cu ₃ BTC ₂	0.30
0.2TCNQ@ Cu ₃ BTC ₂	0.37
0.5TCNQ@ Cu ₃ BTC ₂	0.47
0.6TCNQ@ Cu ₃ BTC ₂	0.28
0.8TCNQ@ Cu ₃ BTC ₂	0.63
1.0TCNQ@ Cu ₃ BTC ₂	0.29
Cu(TCNQ)	0.18
0.8TCNQ@ Cu ₃ BTC ₂ (sonnication)	0.20
Cu(TCNQ) (sonnication)	0.18
CuTCNQ/ Cu ₃ BTC ₂ 99:1	0.053
CuTCNQ/ Cu ₃ BTC ₂ 9:1	0.043

Auger electron spectroscopy (AES)

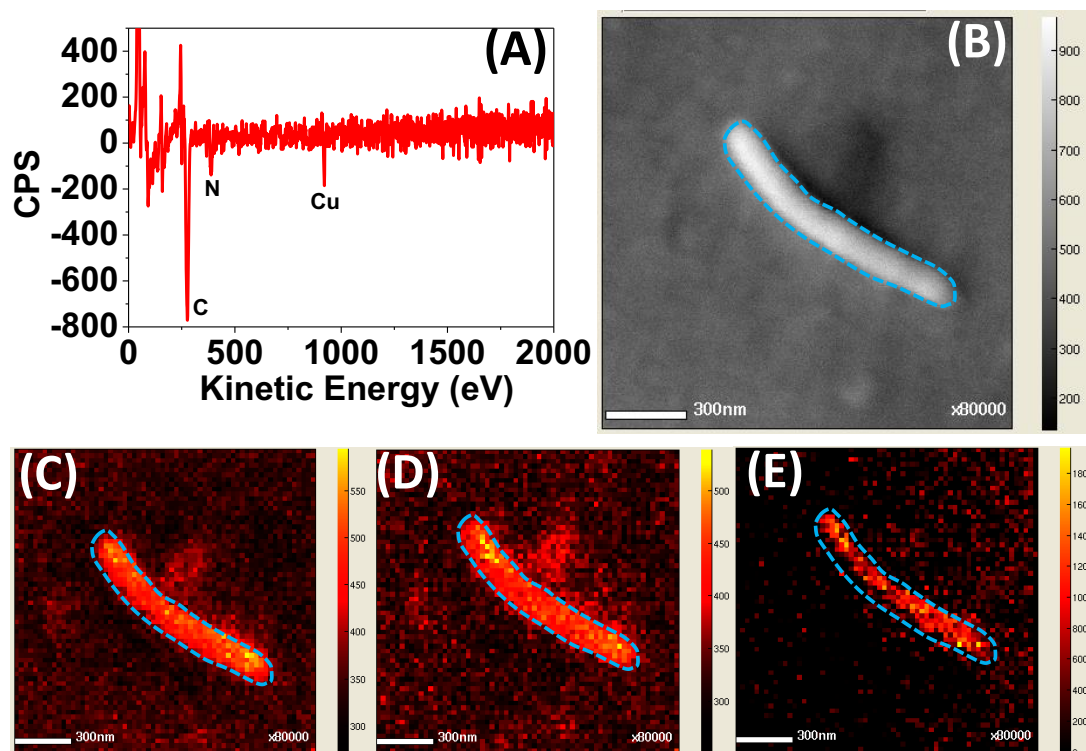


Figure S 13: AES spectra (A), SEM image (B) and AES image of a Cu(TCNQ) nano-wire that has formed on the surface of a Cu_3BTC_2 crystal during the VPI process. Bottom images showing a homogeneous distribution of C (C), N (D), and Cu (E).

Scanning electron microscopy (SEM) images

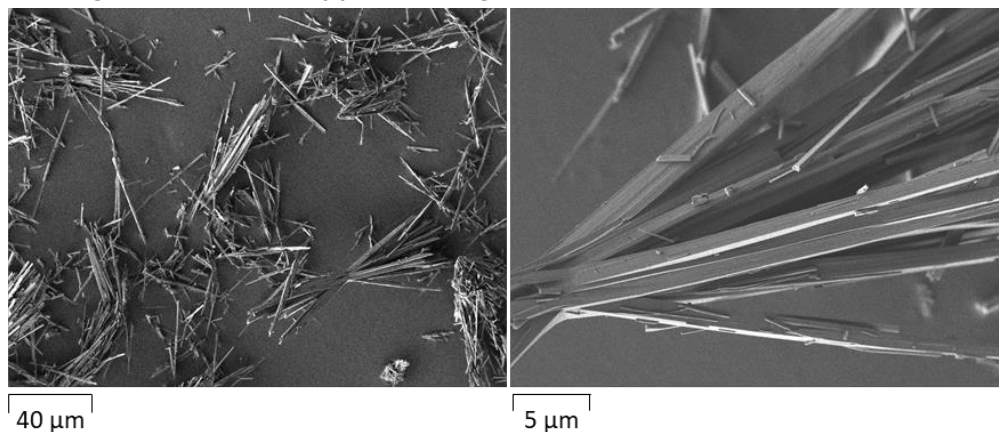


Figure S 14: SEM images of needle-shaped Cu(TCNQ) crystals prepared following the literature procedure.^[1]

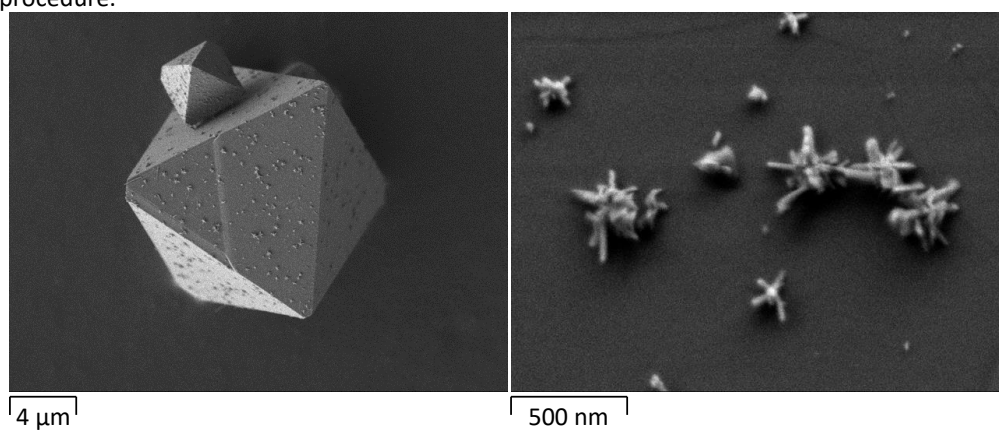


Figure S 15: SEM images of 0.5 TCNQ@Cu₃BTC₂ synthesized at 100 °C.

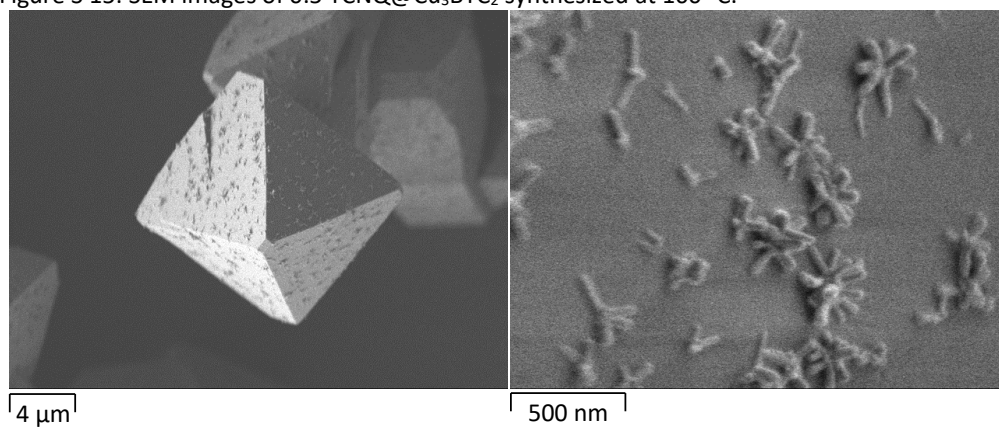


Figure S 16: SEM images of 1.0 TCNQ@Cu₃BTC₂ synthesized at 100 °C.

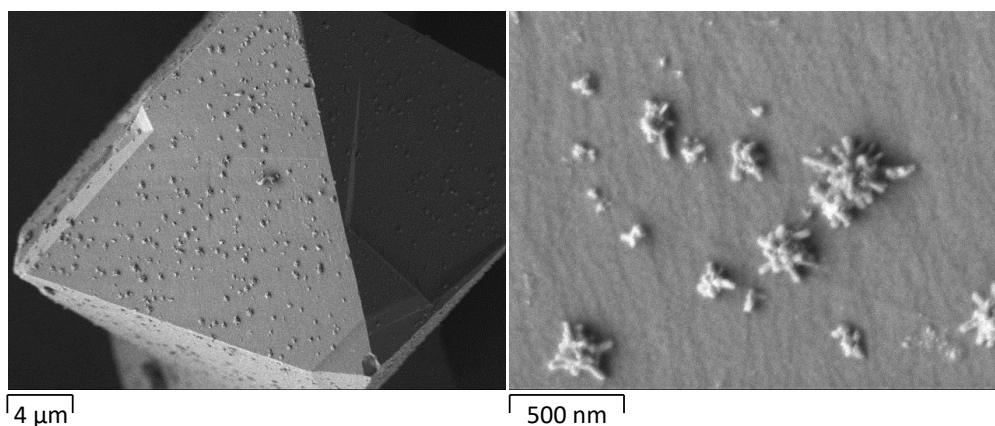


Figure S 17: SEM images of 0.5 TCNQ@Cu₃BTC₂ synthesized at 70 °C. To overcome the low vapor pressure of TCNQ at these low temperatures, the synthesis was performed in high-vacuum flame sealed glass ampoules at a pressure of 10⁻⁵ mbar.

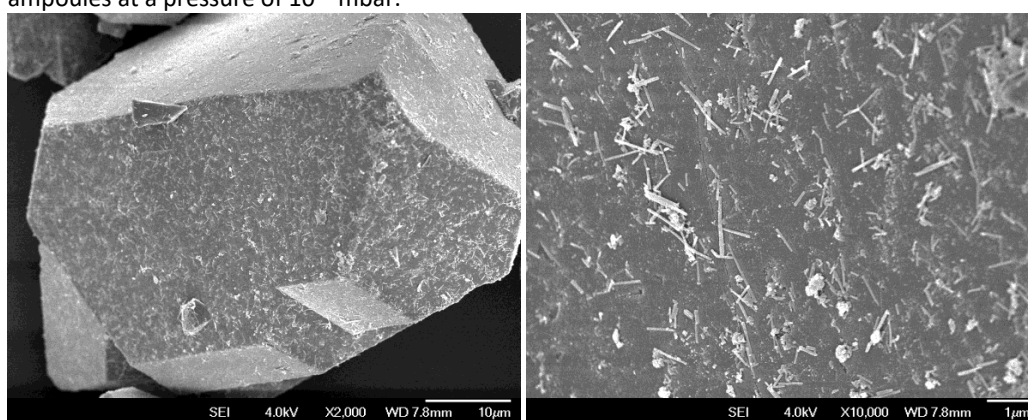


Figure S 18: SEM images of 0.8 TCNQ@Cu₃BTC₂ synthesized at 180 °C after sonication in hexane for 1 hour.

X-ray photoelectron spectroscopy (XPS)

We acknowledge the constructive referee comments which have motivated us do a thorough analysis of the XPS data. XPS is a highly surface sensitive method that is used to probe the binding energy and thus the oxidation state of Cu and N present in the sample. It has to be noted, that this technique does not provide localized information but rather an average over the sample.

The Cu 2p_{3/2} regime of the XPS spectra of Cu₃BTC₂ (a) and samples loaded with 0.5 (b) and 1.0 equivalents of TCNQ (c) are shown in Figure S 19. Integration of the Cu(I) and Cu(II) peak fits reveals Cu(I)/Cu(II) ratios of 1.50, 2.62, and 2.36, respectively. From the literature,^[2-3] we know that thermal activation (vacuum, elevated temperatures) causes reduction of Cu(II) species in Cu₃BTC₂. Cu(I) species are likely to form at the surface of the crystallites due to an incomplete coordination shell and according charge compensation of the exposed Cu ions. This explains the high Cu(I)/Cu(II) ratio at the surface of pristine Cu₃BTC₂. The prolonged thermal treatment during the VPI process (3 days at 180 °C) causes the formation of further Cu(I) species and hence higher Cu(I)/Cu(II) ratios for the infiltrated samples. The amount of Cu(I) formed during the treatment is assumed to be the same for all samples and independent of the amount of TCNQ used in the VPI reaction. However, TCNQ is a good electron acceptor and can thus serve as an oxidizing agent. As a result, neutral TCNQ can oxidize Cu(I) species back to Cu(II) giving rise to the formation of CuTCNQ at the surface of the crystallites ($2 \text{Cu}^{\text{I}} + \text{TCNQ}^{\text{0}} \rightarrow \text{Cu}^{\text{II}} + \text{Cu}^{\text{I}}\text{TCNQ}^{\text{-1}}$). From SEM data we see that this reaction occurs increasingly with increasing amount of TCNQ provided in the synthesis. Consequently, a decreasing Cu(I)/Cu(II) ratio is expected for samples with higher TCNQ loading, which is exactly what we see comparing the results for 0.5TCNQ@Cu₃BTC₂ and 1.0TCNQ@Cu₃BTC₂. It is important to note, that XPS detects Cu(I) species from both Cu(TCNQ) and surface defects of the MOF. Therefore, the amount of CuTCNQ nanowires seen in SEM images cannot be directly correlated with the amount of Cu(I) found by analysis of the XPS data.

The XPS signature in the N1s regime for TCNQ matches well with the literature reference,^[4] and changes upon infiltration with TCNQ (Figure S 20). While the spectra of TCNQ could be easily fitted by two Gauss-Lorentz peak shapes, the spectra for 0.5TCNQ@Cu₃BTC₂ and 1.0TCNQ@Cu₃BTC₂ are more complex. The most plausible fit could be achieved using two peaks that, however, show a significant broadening compared to the fits for pristine TCNQ. Moreover, the position of the green peak is shifted to slightly lower binding energies. As the XPS spectra represent the chemical environment at the surface of the particles, significant contributions of the TCNQ radical anion of CuTCNQ can be assumed. Moreover, coordinated and uncoordinated nitrile groups of TCNQ molecules (ordered and disordered) will give a different signal. Therefore, we believe that the peak at higher binding energies, which was assigned as a shake-up in the spectrum of TCNQ,^[4] here consists of contributions from the different TCNQ species, which account for the significant broadening of the fitted peaks.

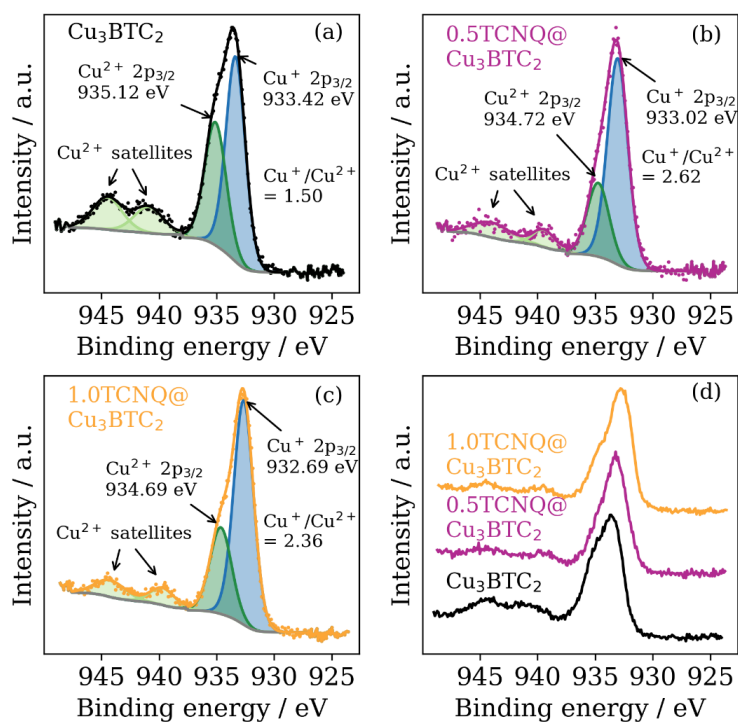


Figure S 19: XPS analysis of the Cu 2p region of Cu_3BTC_2 (a), $0.5\text{TCNQ}@Cu_3\text{BTC}_2$ (b), and $1.0\text{TCNQ}@Cu_3\text{BTC}_2$ (c) and a comparison plot of the normalized spectra (d). Cu(I)/Cu(II) ratios based on the peak integrals are given in the diagram.

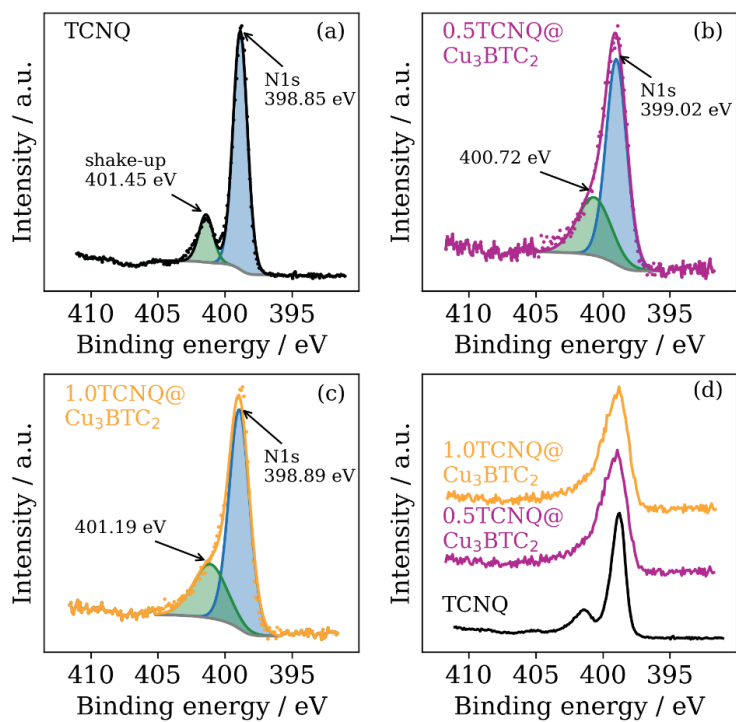


Figure S 20: XPS analysis of the N 1s region of Cu₃BTC₂ (a), 0.5 TCNQ@Cu₃BTC₂ (b), and 1.0 TCNQ@Cu₃BTC₂ (c) and a comparison plot of the normalized spectra (d).

Elemental analysisTable S 2 Elemental analysis of the concentration series of TCNQ@Cu₃BTC₂.

Compound		Weight% of elements				
		C	H	N	Cu	O
Cu ₃ BTC ₂	calc.	35.74	1.00	0	31.52	31.74
	found	35.45	1.03	0.00	31.1	
0.1 TCNQ@Cu ₃ BTC ₂	calc.	36.88	1.03	0.90	30.49	30.70
	found	35.82	1.01	1.17	28.6	
0.2 TCNQ@Cu ₃ BTC ₂	calc.	37.95	1.06	1.74	29.52	29.73
	found	36.98	1.09	2.21	28.0	
0.3 TCNQ@Cu ₃ BTC ₂	calc.	38.95	1.09	2.52	28.62	28.82
	found	38.11	1.12	2.81	27.3	
0.4 TCNQ@Cu ₃ BTC ₂	calc.	39.89	1.12	3.26	27.77	27.96
	found	39.13	1.13	3.71	25.9	
0.5 TCNQ@Cu ₃ BTC ₂	calc.	40.77	1.14	3.96	26.97	27.16
	found	39.87	1.15	4.52	24.8	
0.6 TCNQ@Cu ₃ BTC ₂	calc.	41.61	1.16	4.62	26.21	26.39
	found	41.42	1.19	5.23	24.3	
0.7 TCNQ@Cu ₃ BTC ₂	calc.	42.40	1.19	5.24	25.94	25.67
	found	42.10	1.28	5.72	24.2	
0.8 TCNQ@Cu ₃ BTC ₂	calc.	43.15	1.21	5.83	24.82	24.99
	found	43.27	1.27	6.84	22.5	
0.9 TCNQ@Cu ₃ BTC ₂	calc.	43.86	1.23	6.39	24.17	24.34
	found	43.61	1.21	6.97	22.5	
1.0 TCNQ@Cu ₃ BTC ₂	calc.	44.54	1.25	6.92	23.56	23.73
	found	45.12	1.38	8.08	21.2	

Liquid phase infiltration

Pristine, activated Cu₃BTC₂ (150 mg) was immersed in a saturated TCNQ solution in DCM (100mL) and stirred for 5 days. The resulting green powder was collected via filtration and dried in ambient air.

The PXRD pattern (Figure S 21) of TCNQ@Cu₃BTC₂ shows that the overall crystal structure of the MOF is retained and no new reflections appear, as was seen for material synthesized via the vapor phase. Moreover, the (111) reflection is not pronounced suggesting that the TCNQ molecules are not preferentially accommodated in the (111) lattice plane due to the presence of solvent molecules in the pores. Elemental analysis (Table S 3) reveals overall lower weight percentages due to the adsorption of water in the pores and a C/N ratio that matches with a loading of $x = 0.4$ TCNQ molecules per formula unit Cu₃BTC₂. SEM images (Figure S 22) show octahedral MOF crystallites surrounded by further smaller fragments and no indication for the formation of CuTCNQ. EDX mapping (Figure S 23) shows a homogenous element distribution indicating that the material around the octahedra are fragments of the MOF crystallites that have formed due to the mechanical stress while stirring. *IV* curves of a pressed pellet of the material show a conductivity in the order of 10^{-4} S·cm⁻¹. This is higher than for material with equivalent loading synthesized via the vapor phase which is likely due to different particle sizes and the

presence of additional solvent and water molecules inside the pores, which causes a non-linear (non-ohmic) behavior of the IV curve.

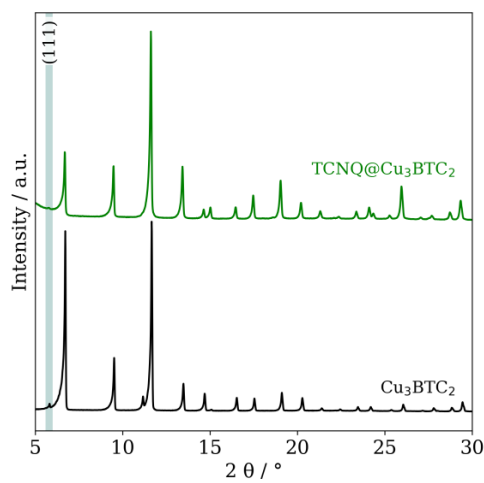


Figure S 21: PXRD of pristine Cu₃BTC₂ (black) and TCNQ@Cu₃BTC₂ synthesized via liquid phase infiltration (green).

Table S 3: Elemental analysis of the concentration series of TCNQ@Cu₃BTC₂.

Compound	Weight% of elements			
	C	H	N	Cu
0.4TCNQ@Cu ₃ BTC ₂ + n H ₂ O	27.42	3.98	2.20	18.3

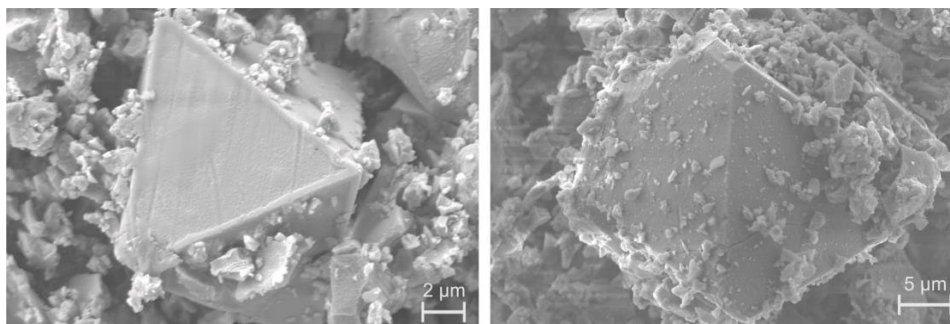


Figure S 22: SEM images of TCNQ@Cu₃BTC₂ synthesized via liquid phase infiltration.

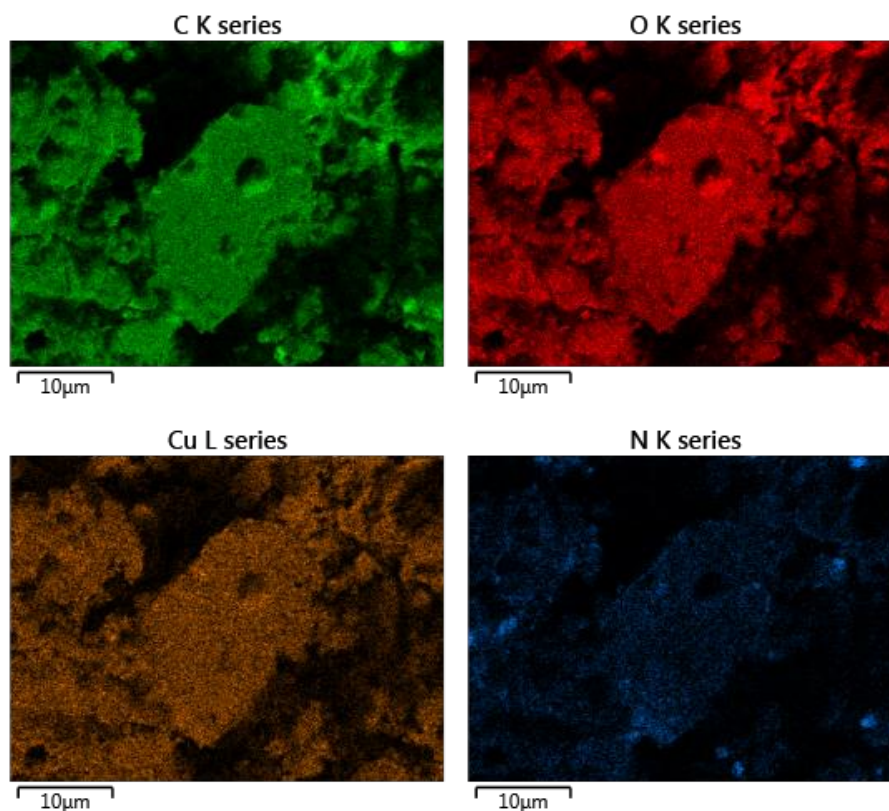


Figure S 23: EDX elemental mapping of TCNQ@Cu₃BTC₂ synthesized via liquid phase infiltration.

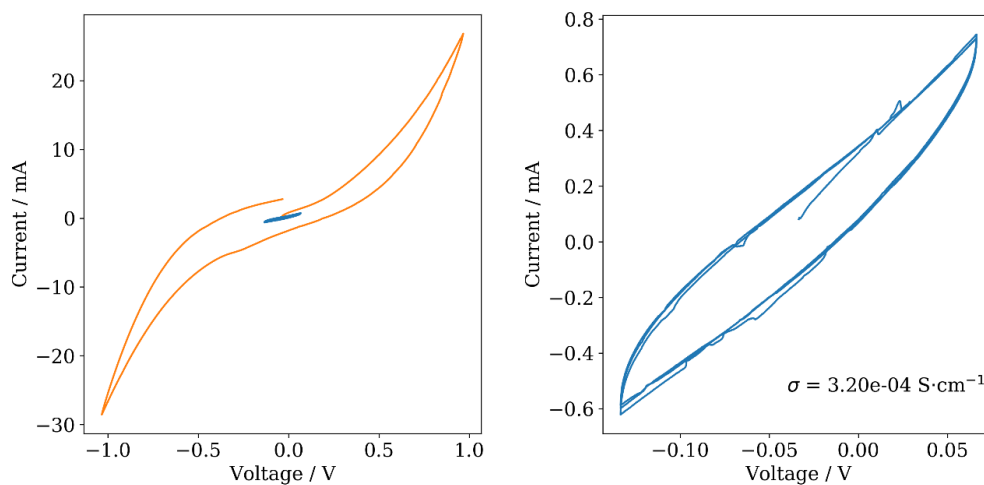


Figure S 24: IV curves of TCNQ@Cu₃BTC₂ synthesized via liquid phase infiltration. Orange curve shows non-ohmic behavior at potentials of ± 1 V. Measurement at low potentials (blue) was used to calculate the conductivity of the material. Pellet thickness is 0.44 mm.

References

- [1] R. A. Heintz, H. Zhao, X. Ouyang, G. Grandinetti, J. Cowen, K. R. Dunbar, *Inorg. Chem.* **1999**, *38*, 144-156.
- [2] N. Nijem, H. Bluhm, M. L. Ng, M. Kunz, S. R. Leone, M. K. Gilles, *Chem. Commun.* **2014**, *50*, 10144-10147.
- [3] J. Szanyi, M. Daturi, G. Clet, D. R. Baer, C. H. F. Peden, *Phys Chem Chem Phys* **2012**, *14*, 4383-4390.
- [4] M. J. Capitán, J. Álvarez, C. Navio, *Phys Chem Chem Phys* **2018**, *20*, 10450-10459.

6.3 Supporting Information Study III

Supporting Information

Scrutinizing the Pore Chemistry and the Importance of Cu(I) Defects in TCNQ-loaded Cu_3BTC_2 by a Multi-Technique Spectroscopic Approach

Christian Schneider^a, Matthias Mendt^b, Andreas Pöppl^b, Valentina Crocella^{c*}, Roland A. Fischer^{a*}

^a Department of Chemistry, Technical University of Munich, Lichtenbergstrasse 4, D-85748 Garching, Germany.

^b Felix Bloch Institute for Solid State Physics, University Leipzig, Linnéstrasse 5, D-04103 Leipzig, Germany.

^c Department of Chemistry, NIS and INSTM Reference Centre, Università di Torino, Via G. Quarello 15, I-10135 and Via P. Giuria 7, I-10125, Torino, Italy.

*Corresponding authors: roland.fischer@tum.de and valentina.crocella@unito.it

Table of content:

Synthesis of TCNQ@ Cu_3BTC_2	S-2
Structure of Cu_3BTC_2 and implications for TCNQ adsorption	S-3
Powder X-ray diffraction	S-4
Infrared spectroscopy	S-5
EPR spectroscopy	S-9
References	S-18

Synthesis of TCNQ@Cu₃BTC₂

Cu₃BTC₂: Cu₃BTC₂ was prepared following the literature procedure.¹ Cu(NO₃)₂·3H₂O (1 g) and trimesic acid (500 mg) was dissolved in a solvent mixture of N,N-dimethylformamide (DMF), ethanol (1:1:1 v/v/v, 25 mL total) and filled into a screw-capped jar. The mixture was heated at 85°C for 20 h. The tile crystalline product was collected by filtration when it was still hot and immersed in fresh DMF overnight. Afterwards, the powder was placed in a Soxhlett extraction apparatus and washed with ethanol for 4 days before replacing the solvent with dichloromethane (DCM) for additional 4 days. Subsequently, the material was desolvated *in vacuo* ($P = 10^{-6}$ mbar) at 180°C for 24 h. The activated sample was transferred to a glovebox with argon atmosphere until further use.

xTCNQ@Cu₃BTC₂: Cu₃BTC₂ with varying molar fractions of TCNQ (7,7,8,8-tetracyanoquinodimethane), *i.e.* xTCNQ@ Cu₃BTC₂ with $x = 0.25, 0.5$ and 1.0 , were prepared following our reported vapor phase loading protocol.² Therefore, both activated Cu₃BTC₂ and stoichiometric amounts of TCNQ were mixed inside the glovebox and filled into a glass ampule that was tentatively evacuated to $P = 10^{-3}$ mbar and flame sealed. The ampule was then placed in a convection oven at 180 °C for 72 h. After cooling down to room temperature, the ampule was opened inside the glove box and the material was stored until further use.

so/TCNQ@Cu₃BTC₂: Liquid phase infiltration of TCNQ into Cu₃BTC₂ was done following the literature protocol.³ Therefore, activated Cu₃BTC₂ (100 mg) was immersed in a saturated solution of TCNQ in dichloromethane (reagent grade) for 3 days at room temperature. Notably, the TCNQ solution was prepared under atmospheric conditions as in the literature example. The powder was collected by filtration and was dried *in vacuo* ($P = 10^{-3}$ mbar) at room temperature.

Structure of Cu_3BTC_2 and implications for TCNQ adsorption

Cu_3BTC_2 crystallizes in the face-centered cubic space group $Fm-3m$ and contains 48 Cu atoms and 32 BTC molecules per unit cell, which enclose eight small pores of 1.0 nm and eight large pores of 1.6 nm in diameter. Cu paddlewheel units are located at the interface between four large pores. Therefore, the large pores can be distinguished based on their chemical environment; while 50% of the large pores feature 12 open metal sites (OMSs) that point to the center of the pore and allow chemisorption of guest molecules (Pore A), in the other half of the pores the Cu paddlewheels are arranged tangentially to the pore and are therefore inaccessible for guest molecules (Pore B). The crystal structure of Cu_3BTC_2 is shown in Figure S 1.

The maximum TCNQ loading as predicted by computational modeling,⁴ and experiments,² is 1.0 equivalents TCNQ per formula unit Cu_3BTC_2 . This corresponds to 2 TCNQ molecules per large pore. While TCNQ molecules can bind to the OMSs of Pore A, the TCNQ molecules in Pore B are presumably randomly oriented in Pore B. The 2 TCNQ molecules in Pore A can bridge 4 of the 12 OMSs, therefore allowing for different permutations of the binding situation within one pore. In all cases, the TCNQ molecules will be located in the (111) lattice plane as a result of the cubic symmetry. This is reflected in the increasing (111) Bragg peak as a function of TCNQ loading as observed in Figure S 2 and in the literature.^{2,5}

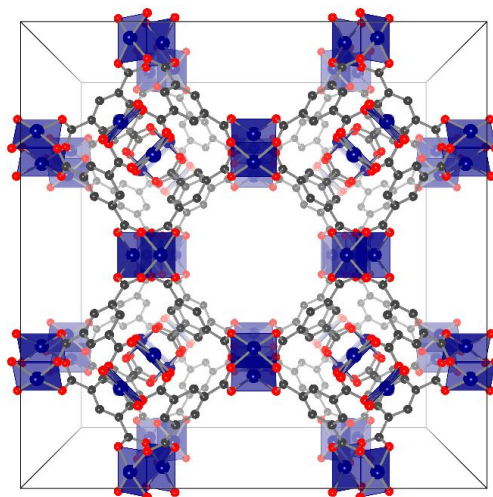


Figure S 1. The crystal structure of Cu_3BTC_2 viewed along the a-axis. Cu, O, and C atoms are depicted in blue, red, and grey, respectively. The blue squares indicate the square-planar coordination environment around each Cu atom. H atoms are omitted for clarity.

Powder X-ray diffraction

Inside the Ar-filled glovebox, activated or TCNQ-loaded powder samples were filled into 0.7 mm glass capillaries and sealed for collecting powder X-ray diffraction data on a PANalytical Empyrean X-ray diffractometer. The instrument was equipped with a Cu $K\alpha$ radiation source, a focusing beam mirror with a $1/8^\circ$ slit and 0.02 rad Soller slits as the incident beam optics and a $1/8^\circ$ anti-scatter slit with 0.02 rad Soller slits and a Ni filter on the diffracted beam side. To confirm crystallinity and quality of the sample, diffraction data in the 2θ range of 5 – 27° with a step size of 0.013° was collected using a PIXcel 1D detector in scanning line mode.

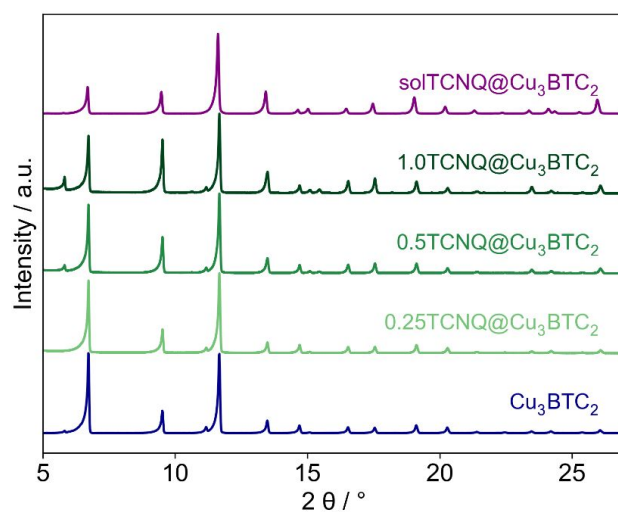


Figure S 2: Powder X-ray diffraction patterns of pristine Cu_3BTC_2 (blue), $xTCNQ@Cu_3BTC_2$ (greens) and $so/TCNQ@Cu_3BTC_2$ (purple).

Infrared spectroscopy

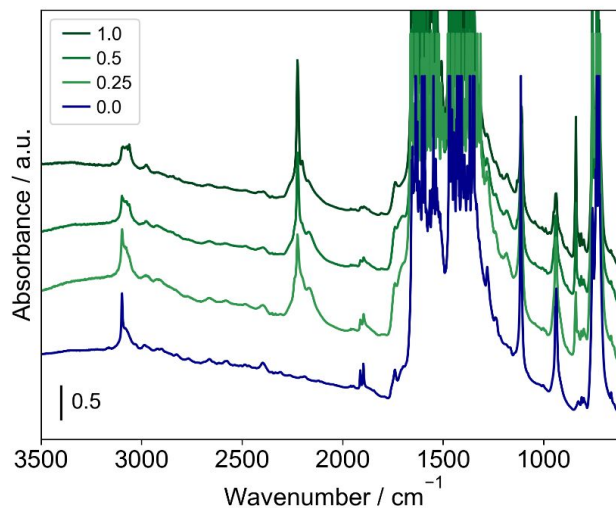


Figure S 3: IR spectra of pristine Cu_3BTC_2 (blue) and $x\text{TCNQ}@Cu_3\text{BTC}_2$ (greens) in vacuum at room temperature. The absorbance is given as a scale bar in the bottom left corner. A vertical offset is applied for clarity.

CO adsorption was carried out on the parent MOF to get a clear picture of the different Cu families. For this purpose, a thin pellet of $\text{Cu}_3(\text{BTC})_2$ was prepared inside the glovebox and placed in a homemade IR cell for low temperature measurements, as reported in the experimental section. After a thermal activation at $150\text{ }^\circ\text{C}$ for 2 h, the material was exposed to ~ 40 mbar CO, cooled down to 77 K and then gradually evacuated at the same temperature. The isothermal set of spectra is reported in the main text in **Error! Reference source not found.** (from dark blue to dark red) in the CO vibrational modes spectral range. The whole set of spectra is characterized by an extremely intense and complex envelope of bands due to the CO interaction with the different surface sites. The following main signals can be recognized:

- (i) an out of scale band at around 2172 cm^{-1} ascribed to the formation of reversible $\text{Cu(II)}\text{---CO}$ adducts (σ -donation interactions) which progressively undergoes a shift to 2178 cm^{-1} by decreasing the CO equilibrium pressure. Such adducts form due to σ -donation of the CO lone pair in the weakly antibonding 3σ molecular orbital with the Cu(II) OMSs of the nodes, yielding a slightly stronger C-O bond, which reflects in an upward shift of the CO stretching mode compared to the free gaseous molecule (2143 cm^{-1}). The peculiar behavior of this band during the outgassing process is due to the gradual conversion of polycarbonyl adsorbate species into monocarbonyls.^{6,7}
- (ii) The assignment of the two IR bands, at 2192 and 2148 cm^{-1} is quite controversial. First, they were assigned by Bordiga et al. to the symmetric and antisymmetric modes of $\text{Cu(II)}\text{---}(\text{CO})_2$ dicarbonyls, respectively.⁷ Then, Drenchev and co-workers associated the same

components to other carbonyls species.⁶ In particular, the band at 2192 cm⁻¹ was ascribed to a different Cu(II)---CO species, whereas the signal at 2148 cm⁻¹ (in some way stabilized by the 2192 cm⁻¹ component) was tentatively assigned to CO in interaction with the organic part of the framework.

- (iii) The bands at around 2120 and 2096 cm⁻¹ can be ascribed to the formation of monocarbonyl Cu(I)---CO and Cu(I)---OC (in which the adsorbed CO molecule interacts through the oxygen atom) adducts due to the presence of defective Cu(I) sites.^{6,8,9} As expected, the Cu(I)---CO component at 2120 cm⁻¹ is clearly more resistant (less reversible upon outgassing) if compared to the corresponding signals of CO in interaction with Cu(II) ions. This spectral behavior is correlated with the nature of the component generated by at least two simultaneous effects: an upward shift due to σ -coordination between the filled CO 3 σ orbital (C-end lone pair) and empty orbital of suitable energy of Cu(I) ion, and a downward shift due to π back-donation of electrons from partially filled d orbitals of Cu(I) to the π^* antibonding molecular orbitals of CO. As a consequence, the resulting CO stretching band is more stable persisting until very low CO coverages.
- (iv) The two signals at 2132 and 2106 cm⁻¹ appear in the isothermal set of spectra just at low CO coverage, when most of the Cu(II)---CO complexes was removed, and then gradually decrease in intensity upon outgassing. Considering their peculiar spectral behavior and the literature data concerning carbonyl complexes formed on dual cation sites in metal-exchanged zeolites,⁹⁻¹¹ these signals can be tentatively assigned to vibrational modes of bridged Cu(I)---CO---Cu(II) carbonyls in Cu(II)-Cu(I) dimers generated by the presence of missing carboxylate units. It is worth noting that these bridged species form just when a fraction of dimeric Cu(II)-Cu(I) species are no more involved in the formation of standard monocarbonyls, due to the decrease of CO coverage. Moreover, after a brief initial intensity increment, the bridged carbonyl bands gradually disappear by further decreasing the CO partial pressure.
- (v) The two sharp and intense signals at 2142 and 2128 cm⁻¹ simultaneously decrease in intensity without any noticeable change in position and are characterized by a very labile nature (they quickly disappear at the early stages of the desorption process). Following the results proposed by Drenchev and co-workers,⁶ these bands can be ascribed to CO in interaction with the organic linker via the formation of oxygen-end adducts, presumably with the benzene ring. This assignment is confirmed by observing the modification of some specific spectral features of the organic linker at 1912 and 1896 cm⁻¹ during the CO adsorption/desorption experiments with respect to the spectrum of the material before the contact with the probe molecule (see Figure S5).⁶ These spectral modifications prove the existence of a not negligible perturbation of the organic part of the framework (well evident also at low CO coverages, i.e. in the presence of CO coordinated only to Cu ions) possibly due to (lateral) O-end interactions with the benzene ring.
- (vi) At very low CO coverage, a broad and ill-defined signal appears at 2125 cm⁻¹, which persists upon prolonged outgassing. The frequency of the component is typical of CO adsorbed on Cu(I) sites of amorphous Cu₂O impurities.¹² Considering the negligible intensity of this signal and the very high IR extinction coefficients of Cu(I)---(CO)_n

complexes,¹³ it can be concluded that the fraction of this extra framework Cu_2O phase should be very low.

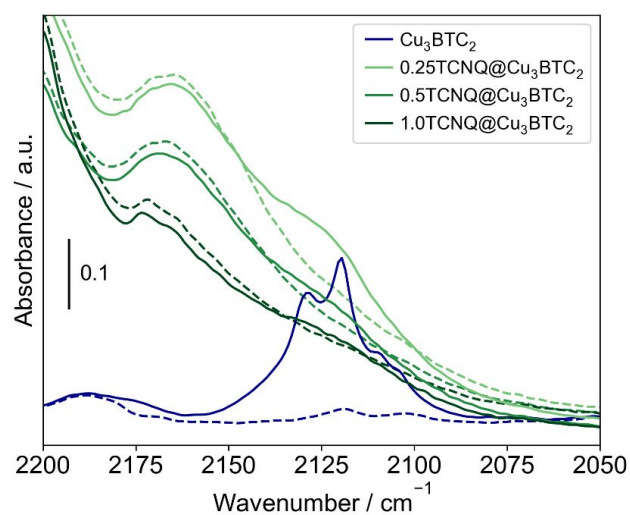


Figure S4: IR spectra of CO adsorbed on pristine Cu_3BTC_2 (blue) and $x\text{TCNQ}@Cu_3\text{BTC}_2$ (greens) at room temperature after vacuum activation (dashed line) and contact with ~16 mbar CO (solid line). The roto-vibrational spectrum of gaseous CO is subtracted from the spectra in the presence of CO. The absorbance is given as a scale bar on the left.

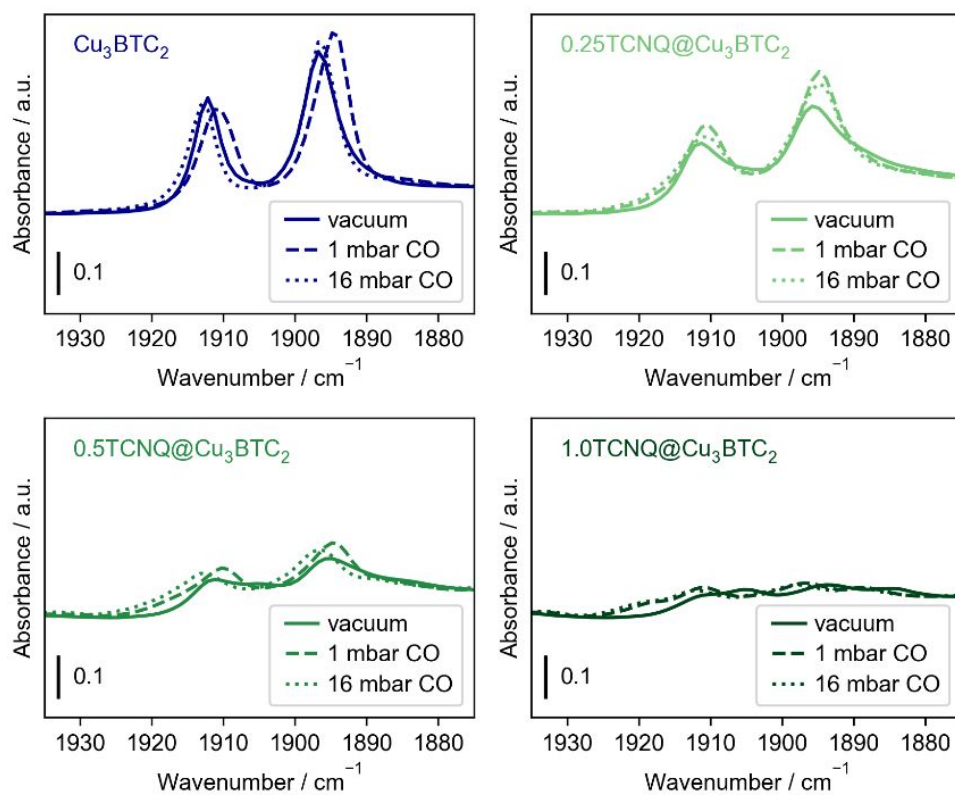


Figure S5: IR spectra of pristine Cu₃BTC₂ (blue) and xTCNQ@Cu₃BTC₂ (greens) at room temperature after vacuum activation (solid line) and at 77 K after contact with 1 mbar CO (dashed line) and 16 mbar CO (dotted line). The absorbance is given as a scale bar on the left. The two bands at 1912 and 1896 cm⁻¹, which are associated with the BTC linker,⁶ are gradually suppressed with increasing TCNQ loading.

EPR spectroscopy

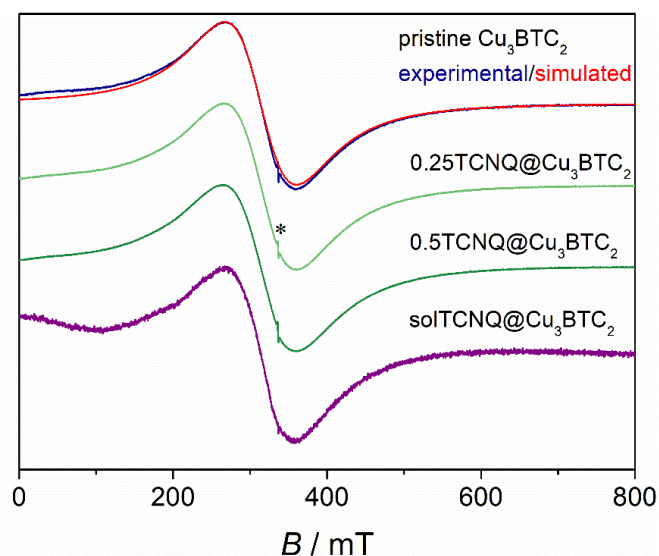


Figure S6: Experimental (blue, green, purple) and simulated (red) room temperature ($T = 295$ K) EPR spectra of different samples (see manuscript), all showing the typical isotropic room temperature signal of antiferromagnetically coupled Cu^{2+} - Cu^{2+} paddlewheel units ($S = 1$)¹⁴ at the isotropic (averaged) g -values $g = 2.145(10)$ (samples pristine Cu_3BTC_2 , $0.25\text{TCNQ}@Cu_3\text{BTC}_2$ and $so\text{TCNQ}@Cu_3\text{BTC}_2$) and $g = 2.151(10)$ (sample $0.5\text{TCNQ}@Cu_3\text{BTC}_2$) and isotropic convolutional Lorentzian peak-to-peak line widths $\Delta B_{pp} = 93(2)$ mT (samples pristine Cu_3BTC_2 , $0.25\text{TCNQ}@Cu_3\text{BTC}_2$ and $so\text{TCNQ}@Cu_3\text{BTC}_2$) and $\Delta B_{pp} = 95(2)$ mT (sample $0.5\text{TCNQ}@Cu_3\text{BTC}_2$) as determined by spectral simulation (like shown in red for pristine Cu_3BTC_2). All spectra are divided by the maximal signal intensity. Differences in the signal to noise ratio reflect the different material amount in the EPR sample tubes which was lowest for sample $so\text{TCNQ}@Cu_3\text{BTC}_2$. The asterisk marks a signal of a free radical impurity of the sample at $g = 2.0002(3)$.

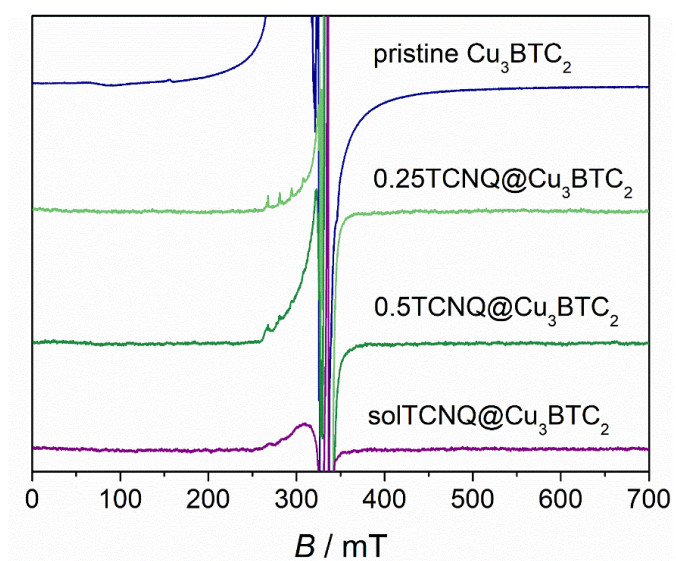


Figure S7: EPR spectra of samples pristine Cu₃BTC₂ (blue), x TCNQ@Cu₃BTC₂ ($x = 0.25, 0.5$) (green) and soTCNQ@Cu₃BTC₂ (purple), measured at $T = 14$ K, showing that no $S = 1$ signal contributes like at higher temperatures (see Figure S8 to Figure S12).

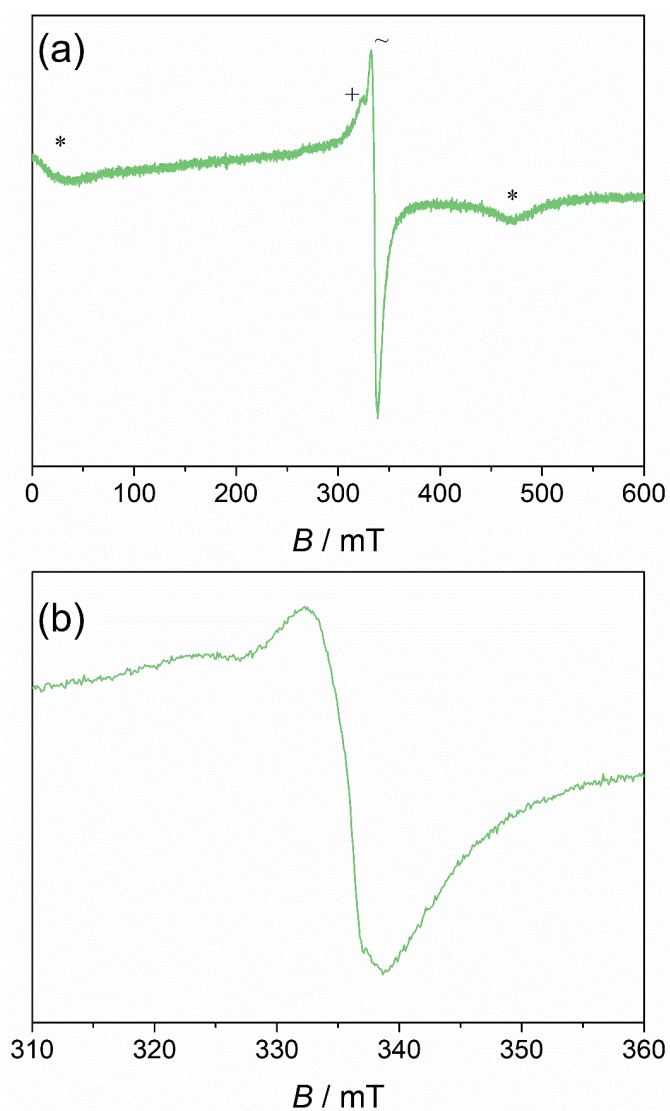


Figure S8: (a) EPR spectrum of sample $0.25\text{TCNQ}@Cu_3\text{BTC}_2$ measured at $T = 125$ K. They symbols *, + and ~ label signals of the $S = 1$ state of the $\text{Cu}^{2+}\text{-Cu}^{2+}$ paddlewheels, of monomeric Cu^{2+} species and of TCNQ^- radicals, respectively. (b) Enlargement of subfigure (a).

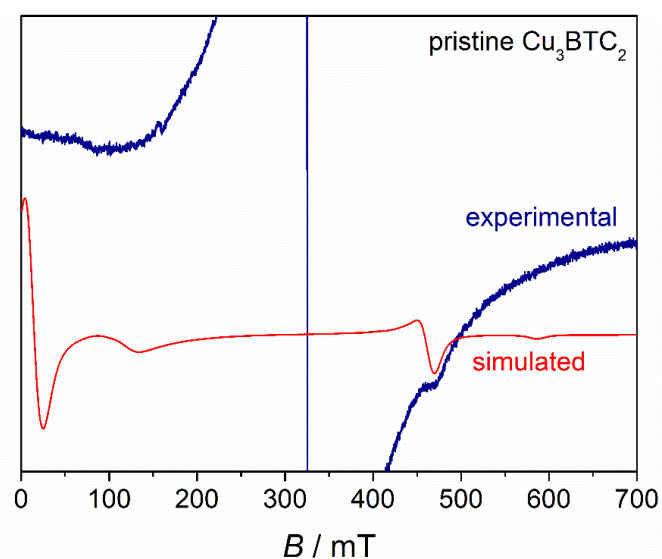


Figure S9: Experimental (blue) and simulated (red) EPR spectra of pristine Cu_3BTC_2 at $T = 95$ K. The latter simulates an electron spin $S = 1$ signal with g-tensor principal values $g_{x,y} = 2.060$, $g_z = 2.330$, an axial zerofield splitting parameter $D = 0.324$ cm^{-1} and an orthorhombic zerofield splitting parameter $E < 0.007$ cm^{-1} .

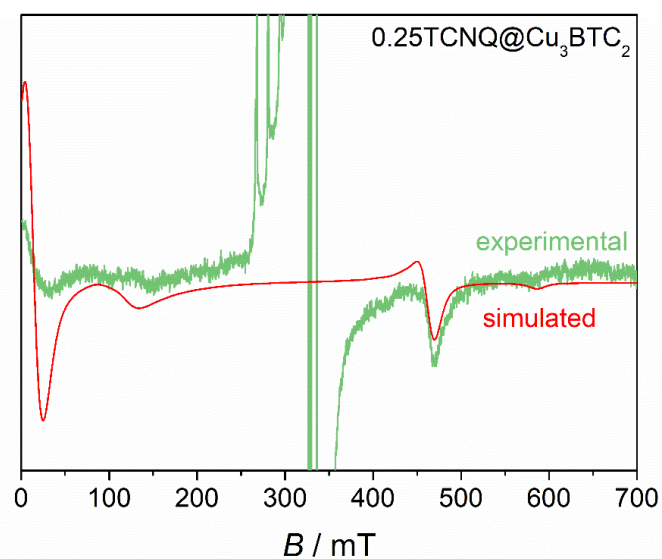


Figure S10: Experimental (green) and simulated (red) EPR spectra of $0.25\text{TCNQ}@Cu_3\text{BTC}_2$ at $T = 95$ K. The latter simulates an electron spin $S = 1$ signal with g-tensor principal values $g_{x,y} = 2.060$, $g_z = 2.330$, an axial zerofield splitting parameter $D = 0.324$ cm^{-1} and an orthorhombic zerofield splitting parameter $E < 0.004$ cm^{-1} .

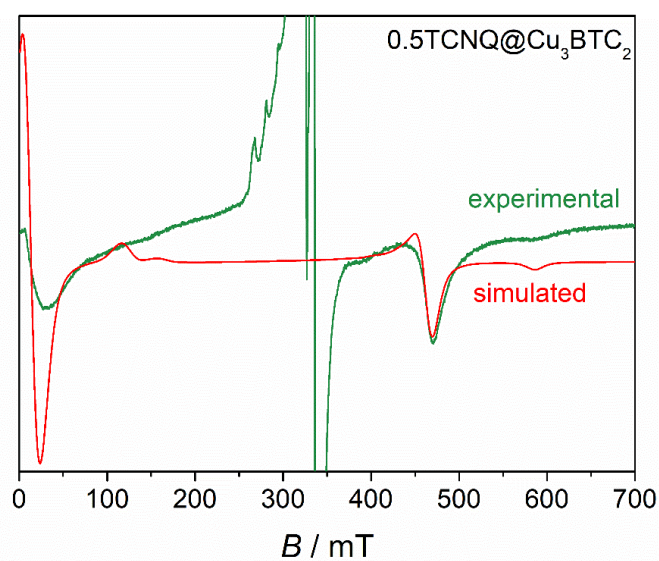


Figure S11: Experimental (green) and simulated (red) EPR spectra of $0.5\text{TCNQ}@Cu_3\text{BTC}_2$ at $T = 95$ K. The latter simulates an electron spin $S = 1$ signal with g-tensor principal values $g_{x,y} = 2.060$, $g_z = 2.330$, an axial zerofield splitting parameter $D = 0.324$ cm^{-1} and an orthorhombic zerofield splitting parameter $E < 0.004$ cm^{-1} .

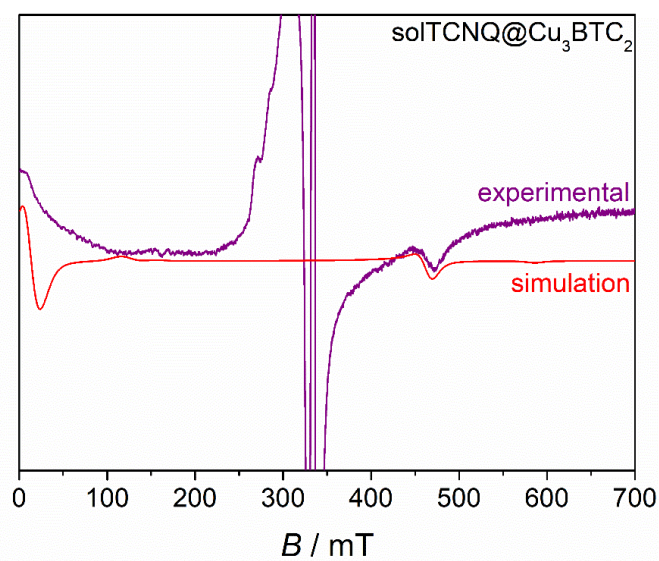


Figure S12: Experimental (purple) and simulated (red) EPR spectra of $so/TCNQ@Cu_3\text{BTC}_2$ at $T = 95$ K. The latter simulates an electron spin $S = 1$ signal with g-tensor principal values $g_{x,y} = 2.060$, $g_z = 2.330$, an axial zerofield splitting parameter $D = 0.324$ cm^{-1} and an orthorhombic zerofield splitting parameter $E < 0.004$ cm^{-1} .

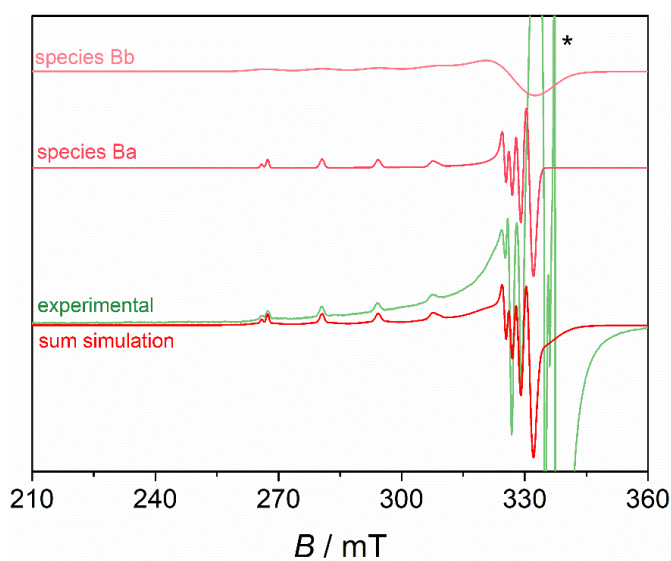


Figure S13: Experimental (green) spectrum of sample $0.25\text{TCNQ}@Cu_3\text{BTC}_2$ measured at $T = 14$ K and simulated EPR signal of species Bb, Ba and their sum (red). The asterisk labels the saturated signal of TCNQ^- radicals that extends outside the frame and that overlaps with the Cu^{2+} signals.

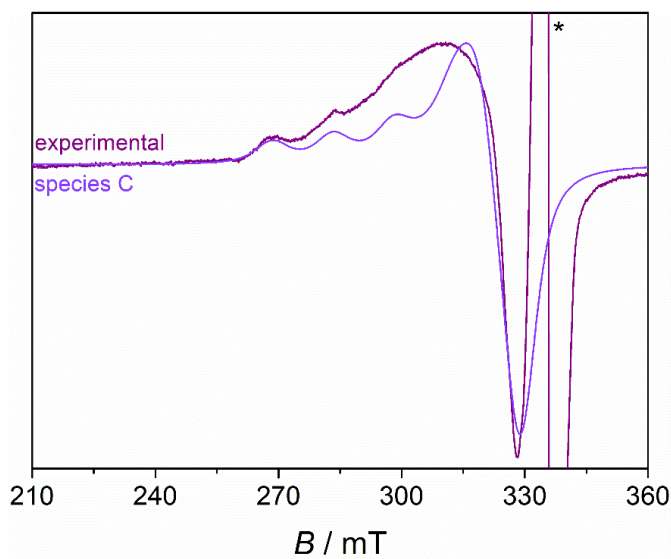


Figure S14: Experimental (dark purple) spectrum of sample $so/\text{TCNQ}@Cu_3\text{BTC}_2$ measured at $T = 14$ K and the simulated EPR signal of species C (light purple). The asterisk labels the signal of TCNQ^- radicals that extends outside the frame and that overlaps with the Cu^{2+} signals.

Table S 1: Experimentally derived g-tensor principal values g_z and $g_{x,y}$ and the principal values A_z and $A_{x,y}$ of the ^{63}Cu isotope hyperfine interaction tensor of different Cu^{2+} monomer species with electron spin $S = 1/2$ observed in the present work by EPR spectroscopy.

	g_z	$g_{x,y}$	A_z / cm^{-1}	$A_{x,y} / \text{cm}^{-1}$
Species A	2.290(3)	2.050(3)	0.0170(7)	0.0020(7)
Species Ba	2.341(3)	2.050(3)	0.0146(7)	0.0020(7)
Species Bb	2.341(6)	2.050(6)	0.0146(14)	0.0020(14)
Species C	2.315(6)	2.08(6)	0.0157(14)	0.0020(14)

$$\chi_M = \frac{N_M \beta_e^2 g_M^2}{4 k_B T}$$

$$\chi_{PW} = 2N_{PW} \frac{\beta_e^2 g_{PW}^2}{k_B T} \left[3 + \exp\left(\frac{-J}{k_B T}\right) \right]^{-1}$$

Formula for the magnetic susceptibilities χ_M of a mononuclear electron $S = 1/2$ species and χ_{PW} of Cu(II)-Cu(II) paddlewheels with electron spin $S = 1$.¹⁵ N_M – number of the mononuclear $S = 1/2$ species, N_{PW} – number of Cu(II)-Cu(II) paddlewheel units, g_M – isotropic g value of the mononuclear $S = 1/2$ species, g_{PW} – isotropic g value of the dimeric $S = 1$ species, J – exchange coupling constant of the exchange Hamiltonian $\hat{H} = -J\hat{S}_1\hat{S}_2$ of two electron spins S_1 and S_2 , β_e – Bohr magneton, k_B – Boltzmann constant, T – temperature

Discussion of the magnetism of a Cu(II)-Cu(II)-TCNQ⁻ spin triad

The present results indicate a reduction of TCNQ molecules by mixed valence Cu(II)-Cu(I) paddlewheel units which might lead to the formation of Cu(II)-Cu(II)-TCNQ⁻ complexes where each Cu(II) ion as well as the TCNQ⁻ anion have an electron spin $S = 1/2$. According to previous works, both Cu(II) ions couple antiferromagnetically with an exchange coupling constant $J_1 \approx -370 \text{ cm}^{-1}$.¹⁴ However, in dependence of the exchange coupling constant J_2 describing the interaction between the Cu(II) ion and the axially coordinating TCNQ⁻ radical, different coupling scenarios are possible. The range of exchange interactions between radicals and Cu(II) ions, reported in literature, spans from small values ($|J| < 20 \text{ cm}^{-1}$)^{16,17} to large values ($|J| > 150 \text{ cm}^{-1}$)¹⁷ in dependence of the geometric arrangement and the overlap of the molecular orbitals. Couplings between Cu(II) and nitric oxide molecules were reported which might be such large that the Cu(II)-radical complex is EPR silent even at room temperature.¹⁸ Thus, to our best knowledge the literature gives no clear hint for a specific size of J_2 describing the coupling between Cu(II) and the TCNQ⁻ anion. Therefore, we have addressed different coupling cases by spectral simulations of the EPR signal of three electron spins $S_{\text{Cu1}} = S_{\text{Cu2}} = S_{\text{TCNQ}} = 1/2$ at $T = 14 \text{ K}$ in dependence of an isotropic Cu(II)-TCNQ⁻ exchange with coupling constant J_2 , assuming for both Cu(II) ions same g - and ⁶³Cu hfi tensors with principal values of species A (Table S 1), an isotropic g -value of $g = 2.003$ for the TCNQ⁻ ion,¹⁹ an intra-dimeric Cu(II)-Cu(II) exchange coupling constant $J = -370 \text{ cm}^{-1}$ and neglecting any magnetic coupling between the TCNQ⁻ and the second Cu(II) ion not coordinating to the TCNQ⁻ radical.

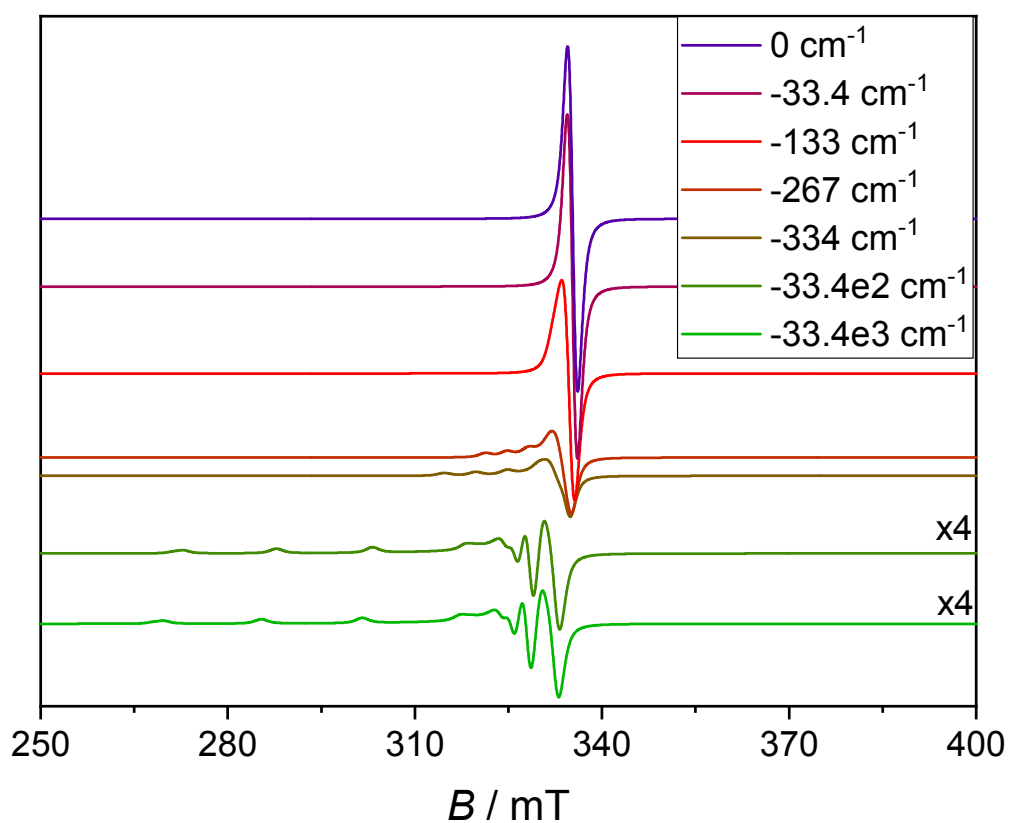


Figure S15. Simulated EPR powder spectra of a spin triad Cu1-Cu2-TCNQ⁻ at T = 14 K, where the S = 1/2 species Cu1 and Cu2 have g-tensor and ⁶³Cu hf interaction principal values of the Cu(II) species A discussed in the manuscript (Table S 1), the TCNQ⁻ has an isotropic g value g = 2.003 and the isotropic exchange coupling constants are $J_{\text{Cu1-Cu2}} = -370 \text{ cm}^{-1}$, $J_{\text{TCNQ-Cu1}} = 0$ and $J_{\text{Cu2-TCNQ}} = J_2$.

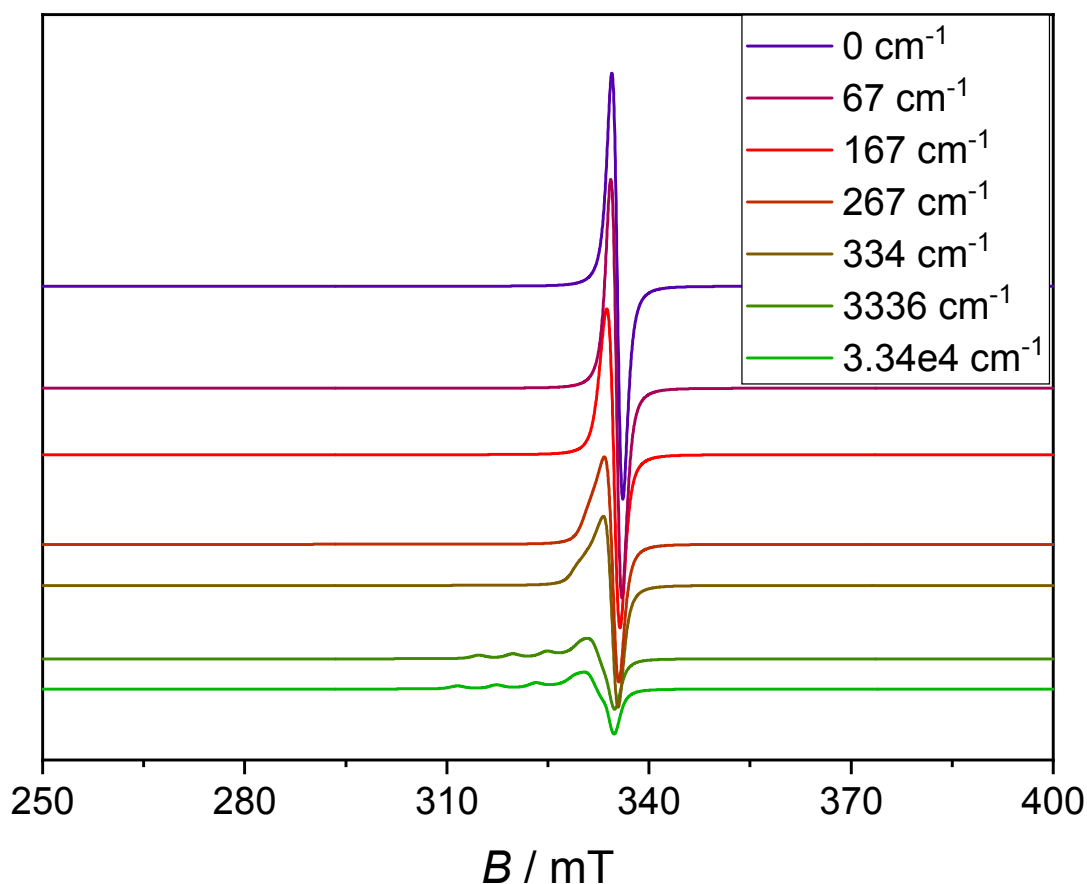


Figure S16. Simulated EPR powder spectra of a spin triad Cu1-Cu2-TCNQ⁻ at T = 14 K, where the S = 1/2 species Cu1 and Cu2 have g-tensor and ⁶³Cu hf interaction principal values of the Cu(II) species A discussed in the manuscript (Table S 1), the TCNQ⁻ has an isotropic g value g = 2.003 and the isotropic exchange coupling constants are $J_{\text{Cu1-Cu2}} = -370 \text{ cm}^{-1}$, $J_{\text{TCNQ-Cu1}} = 0$ and $J_{\text{Cu2-TCNQ}} = J_2$.

In case of a strong antiferromagnetic coupling between the Cu(II) ion Cu2 and the axially coordinating TCNQ⁻ anion the spin triad should show the signal of the monomeric second Cu(II) ion (Cu1) like it is verified by spectral simulations ($J_2 = -33.4\text{e}3 \text{ cm}^{-1}$, Figure S15). In case of a strong ferromagnetic coupling, spectral simulations suggest the occurrence of an anisotropic S = 1/2 signal with g-values between those of species A and that of the TCNQ⁻ anion ($J_2 = -33.4\text{e}3 \text{ cm}^{-1}$, Figure S16). For corresponding intermediate couplings anisotropic S = 1/2 signals are expected at smaller g-values which are still larger than those of the isolated TCNQ⁻ anion (Figure S15, Figure S16). But, we did not observe any clear indication for such signals in the EPR spectra of the TCNQ loaded samples. Nevertheless, such anisotropic signals might contribute to the broad background signal of ill-defined Cu(II) species in the TCNQ loaded samples (Figure 6, Figure S13, Figure S14). However, the equality of the EPR derived amounts of TCNQ⁻ radicals in

the TCNQ loaded sample and the Cu(II) species A in the pristine Cu₃BTC₂ samples supports a scenario where most of the TCNQ⁻ radicals contribute to the observed isotropic line at $g = 2.003$. There might be the possibility that TCNQ⁻ anions coordinating to the Cu(II) exhibit a large J_2 but we measure with EPR only signals of non-coordinating TCNQ⁻. But, if those anions which contribute to the observed isotropic signal coordinate to the Cu(II)-Cu(II) PW units, spectral simulations like shown in Figure S15 and Figure S16 demonstrate that the exchange coupling between the Cu(II) ion and the axially coordinating TCNQ⁻ radical should be in the range $-150 \text{ cm}^{-1} < J_2 < 250 \text{ cm}^{-1}$, a range where the simulated isotropic EPR signal of TCNQ⁻ ions is hardly disturbed. Such a scenario is reasonable, since the unpaired electron of the Cu(II) ion is expected to be mainly localized in the $d_{x^2-y^2}$ orbital²⁰ and the unpaired spin density at the axially coordinating nitrogen atom of the TCNQ⁻ radical is expected to be smaller than 0.1,²¹ which is also reflected by the small ¹⁴N hf interaction parameter which was reported to be for TCNQ⁻ of the order of 3 MHz.²² Thus, the overlap of molecular orbitals of the Cu(II) ion and the TCNQ⁻ including such with unpaired spin density is expected to be small leading to rather small values of J_2 .²³ In conclusion, the present experimental results suggest the most likely scenario, where the coupling between the TNCQ⁻ radicals and the Cu(II)-Cu(II) PW units is too small to disturb the antiferromagnetic coupling of both Cu(II) ions and to disturb significantly the isotropic signal of the TCNQ⁻ anion.

References

- (1) Bhunia, M. K.; Hughes, J. T.; Fetting, J. C.; Navrotsky, A. Thermochemistry of Paddle Wheel MOFs: Cu-HKUST-1 and Zn-HKUST-1. *Langmuir* **2013**, *29* (25), 8140–8145.
- (2) Schneider, C.; Ukaj, D.; Koerver, R.; Talin, A. A.; Kieslich, G.; Pujari, S. P.; Zuillhof, H.; Janek, J.; Allendorf, M. D.; Fischer, R. A. High Electrical Conductivity and High Porosity in a Guest@MOF Material: Evidence of TCNQ Ordering within Cu₃BTC₂ Micropores. *Chem. Sci.* **2018**, *9* (37), 7405–7412.
- (3) Talin, A. A.; Centrone, A.; Ford, A. C.; Foster, M. E.; Stavila, V.; Haney, P.; Kinney, R. A.; Szalai, V.; El Gabaly, F.; Yoon, H. P.; Léonard, F.; Allendorf, M. D. Tunable Electrical Conductivity in Metal-Organic Framework Thin-Film Devices. *Science* **2014**, *343* (6166), 66–69.
- (4) Erickson, K. J.; Léonard, F.; Stavila, V.; Foster, M. E.; Spataru, C. D.; Jones, R. E.; Foley, B. M.; Hopkins, P. E.; Allendorf, M. D.; Talin, A. A. Thin Film Thermoelectric Metal-Organic Framework with High Seebeck Coefficient and Low Thermal Conductivity. *Adv. Mater.* **2015**, *27* (22), 3453–3459.
- (5) Schneider, C.; Bodesheim, D.; Ehrenreich, M. G.; Crocellà, V.; Mink, J.; Fischer, R. A.; Butler, K. T.; Kieslich, G. Tuning the Negative Thermal Expansion Behavior of the Metal-Organic Framework Cu₃BTC₂ by Retrofitting. *J. Am. Chem. Soc.* **2019**, *141* (26), 10504–10509.
- (6) Drenchev, N.; Ivanova, E.; Mihaylov, M.; Hadjiivanov, K. CO as an IR Probe Molecule for Characterization of Copper Ions in a Basolite C300 MOF Sample. *Phys. Chem. Chem. Phys.* **2010**, *12* (24), 6423.
- (7) Bordiga, S.; Regli, L.; Bonino, F.; Groppo, E.; Lamberti, C.; Xiao, B.; Wheatley, P. S.; Morris, R. E.; Zecchina, A. Adsorption Properties of HKUST-1 toward Hydrogen and Other Small Molecules Monitored by IR. *Phys. Chem. Chem. Phys.* **2007**, *9* (21), 2676.
- (8) St. Petkov, P.; Vayssilov, G. N.; Liu, J.; Shekhah, O.; Wang, Y.; Wöll, C.; Heine, T. Defects in MOFs: A Thorough Characterization. *ChemPhysChem* **2012**, *13* (8), 2025–2029.

- (9) Areán, C. O.; Delgado, M. R.; Frolich, K.; Bulánek, R.; Pulido, A.; Bibiloni, G. F.; Nachtigall, P. Computational and Fourier Transform Infrared Spectroscopic Studies on Carbon Monoxide Adsorption on the Zeolites Na-ZSM-5 and K-ZSM-5: Evidence of Dual-Cation Sites. *J. Phys. Chem. C* **2008**, *112* (12), 4658–4666.
- (10) Bulanek, R.; Frolich, K.; Cicmanec, P.; Nachtigallova, D.; Pulido, A.; Nachtigall, P. Combined Experimental and Theoretical Investigations of Heterogeneous Dual Cation Sites in Cu,M-FER Zeolites. *J. Phys. Chem. C* **2011**, *115* (27), 13312–13321.
- (11) Frolich, K.; Koudelkova, E.; Frydova, E.; Bulanek, R. The Quantity of Cu⁺ Ions Forming Isolated and Bridged Carbonyl Complexes in FER Zeolites Determined by IR Spectroscopy. *Vib. Spectrosc.* **2012**, *58*, 146–152.
- (12) Prestipino, C.; Regli, L.; Vitillo, J. G.; Bonino, F.; Damin, A.; Lamberti, C.; Zecchina, A.; Solari, P. L.; Kongshaug, K. O.; Bordiga, S. Local Structure of Framework Cu(II) in HKUST-1 Metallorganic Framework: Spectroscopic Characterization upon Activation and Interaction with Adsorbates. *Chem. Mater.* **2006**, *18* (5), 1337–1346.
- (13) Zecchina, A.; Scarano, D.; Bordiga, S.; Spoto, G.; Lamberti, C. Surface Structures of Oxides and Halides and Their Relationships to Catalytic Properties; 2001; pp 265–397.
- (14) Pöppl, A.; Kunz, S.; Himsl, D.; Hartmann, M. CW and Pulsed ESR Spectroscopy of Cupric Ions in the Metal–Organic Framework Compound Cu₃ (BTC) 2. *J. Phys. Chem. C* **2008**, *112* (7), 2678–2684.
- (15) Friedländer, S.; Šiménas, M.; Kobalz, M.; Eckold, P.; Ovchar, O.; Belous, A. G.; Banyš, J.; Krautscheid, H.; Pöppl, A. Single Crystal Electron Paramagnetic Resonance with Dielectric Resonators of Mononuclear Cu²⁺ Ions in a Metal–Organic Framework Containing Cu₂ Paddle Wheel Units. *J. Phys. Chem. C* **2015**, *119* (33), 19171–19179.
- (16) Gautam, R.; Astashkin, A. V.; Chang, T. M.; Shearer, J.; Tomat, E. Interactions of Metal-Based and Ligand-Based Electronic Spins in Neutral Tripyrindione π Dimers. *Inorg. Chem.* **2017**, *56* (11), 6755–6762.
- (17) Fedin, M.; Veber, S.; Gromov, I.; Maryunina, K.; Fokin, S.; Romanenko, G.; Sagdeev, R.; Ovcharenko, V.; Bagryanskaya, E. Thermally Induced Spin Transitions in Nitroxide–Copper(II)–Nitroxide Spin Triads Studied by EPR. *Inorg. Chem.* **2007**, *46* (26), 11405–11415.
- (18) Sarma, M.; Mondal, B. Nitric Oxide Reduction of Copper(II) Complexes: Spectroscopic Evidence of Copper(II)–Nitrosyl Intermediate. *Inorg. Chem.* **2011**, *50* (8), 3206–3212.
- (19) Schwertfeger, C. F. Low Temperature EPR Study of the “Impurity” Resonances in (TCNQ)- and (TCNQ)₂ Salts. *Solid State Commun.* **1977**, *23* (9), 621–622.
- (20) Hathaway, B. J.; Billing, D. E. The Electronic Properties and Stereochemistry of Mono-Nuclear Complexes of the Copper(II) Ion. *Coord. Chem. Rev.* **1970**, *5* (2), 143–207.
- (21) Flandrois, S.; Boissonade, J. EPR Fine Structure and Spin Densities in TCNQ Salts. *Chem. Phys. Lett.* **1978**, *58* (4), 596–600.
- (22) Bell, S. E.; Field, J. S.; Haines, R. J.; Moscherosch, M.; Matheis, W.; Kaim, W. Novel and Stable Metal–Metal-Bonded Diruthenium(I) Complexes Containing TCNX₀/Bul.- in Both the Inner and the Outer Coordination Sphere (TCNX = TCNE, TCNQ). A Combined EPR/ENDOR-, UV/Visible/near-IR-, and IR-Spectroscopic and Electrochemical Investigation. *Inorg. Chem.* **1992**, *31* (15), 3269–3276.
- (23) Bencini, A.; Gatteschi, D. *Electron Paramagnetic Resonance of Exchange Coupled Systems*; Springer Berlin Heidelberg: Berlin, Heidelberg, 1990.

6.4 Supporting Information Study IV

Supporting Information

Tuning the Negative Thermal Expansion Behavior of the Metal-Organic Framework Cu_3BTC_2 by Retrofitting

Christian Schneider,^a David Bodesheim,^a Michael G. Ehrenreich,^a Valentina Crocellà,^b János Mink,^{c,d} Roland A. Fischer,^a Keith T. Butler,^e Gregor Kieslich^a

^a Department of Chemistry, Technical University Munich, Lichtenbergstrasse 4, D-85748 Garching, Germany.

^b Department of Chemistry, NIS and INSTM Centre of Reference, University of Turin, Via Quarello 15, I-10135 Torino, Italy.

^c Institute of Materials and Environmental Chemistry, Research Center of Natural Sciences, Hungarian Academy of Sciences, H-1519 Budapest, Hungary.

^d Research Institute for Biomolecular and Chemical Engineering, University of Pannonia, H-8200 Veszprém, Hungary.

^e Scientific Computing Department, Rutherford Appleton Laboratory, Harwell Campus, Didcot OX11 0QX, United Kingdom.

Table of content:

Synthesis of $x\text{TCNQ}@Cu_3\text{BTC}_2$	2
Porosimetry measurements	3
Variable temperature XRD measurements.....	4
Raman spectroscopy	10
Far infrared spectroscopy.....	10
References.....	12

Synthesis of $x\text{TCNQ}@Cu_3\text{BTC}_2$

The synthesis of TCNQ-loaded $Cu_3\text{BTC}_2$ was adapted from our previous work.¹ For the vapor phase infiltration of TCNQ into $Cu_3\text{BTC}_2$, we used new high-vacuum glass ampules to enhance the sublimation and diffusion of TCNQ.

$Cu_3\text{BTC}_2$ was synthesized in a solvothermal synthesis from $Cu(\text{NO}_3)_2 \cdot 3\text{H}_2\text{O}$ (1 g) and H_3BTC (500 mg) in a solvent mixture of N,N-dimethylformamide (DMF), ethanol and water of equal volumetric parts (25 mL total) at 85°C for 20 h.² The tile crystalline product was collected by filtration and immersed in fresh DMF overnight. Afterwards, the powder was placed in a Soxhlett extraction apparatus and washed with ethanol for four days before replacing the solvent with dichloromethane for additional 4 days. Subsequently, adsorbed solvent and water was removed *in vacuo* ($\sim 10^{-6}$ mbar) at 180°C for 24 h. The activated sample was transferred to a glovebox with argon atmosphere until further use.

TCNQ-loaded samples were prepared via vapor-phase infiltration. Therefore, stoichiometric amounts of TCNQ were thoroughly mixed with activated $Cu_3\text{BTC}_2$ (100 mg) to prepare a series of $x\text{TCNQ}@Cu_3\text{BTC}_2$ with $x = n(\text{TCNQ})/n(Cu_3\text{BTC}_2) = 0.2, 0.4, \dots, 1.0$. The mixtures were filled into high-vacuum glass ampules, evacuated to 10^{-5} mbar, and flame sealed. The ampules were placed in a convection oven at 180 °C for 72 h. Inside of the glovebox, the ampules were opened and the TCNQ-loaded MOF samples were stored for further characterization.

Porosimetry measurements

BET surface areas were extracted from N₂ sorption isotherms recorded on a Micromeritics 3flex at 77 K. Inside of an Ar glovebox, approximately 60 mg of a sample were filled into a glass tube and evacuated for 3 h at $\sim 10^{-5}$ mbar. The exact sample mass was determined and the isotherm was recorded in the pressure range between 10^{-3} and 10^3 mbar. The BET surface area was calculated from the initial slope (0.01 to 0.1 P/P₀) of the isotherm.

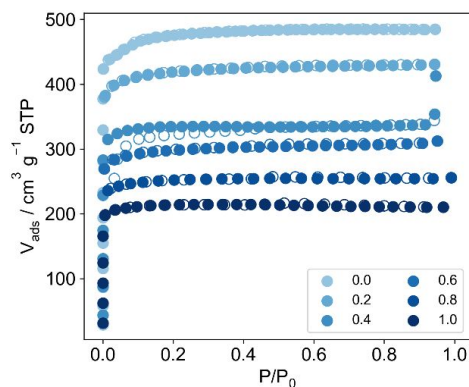


Figure S 1: Nitrogen sorption isotherms of the concentration series $x\text{TCNQ}@Cu_3\text{BTC}_2$ recorded at 77 K. Guest loading amount x for each sample is shown in the legend. Filled and empty circles indicate adsorption and desorption branches, respectively.

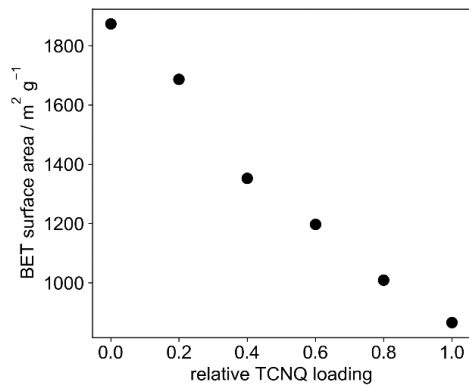


Figure S 2: Brunauer-Emmet-Teller (BET) surface area calculated from the initial slope of the nitrogen sorption measurement of each sample plotted against the TCNQ loading amount. The BET surface area decreases monotonically with the relative TCNQ loading to a value of 865.9 m²/g for 1.0TCNQ@Cu₃BTC₂.

Variable temperature XRD measurements

VTPXRD data was recorded for pristine and TCNQ-loaded Cu_3BTC_2 samples at the Diamond Light Source beam line I11. Diffraction patterns were recorded in 20 K steps while cooling the sample from 300 K to 100 K and heating the sample back up from 110 K to 310 K using X-ray radiation with a wavelength of $\lambda = 0.824945(10)$ Å. The diffraction patterns for the cooling and heating branch of all samples are shown in stack plots below. All patterns were normalized to the most intense reflection and a vertical offset is applied for visualization.

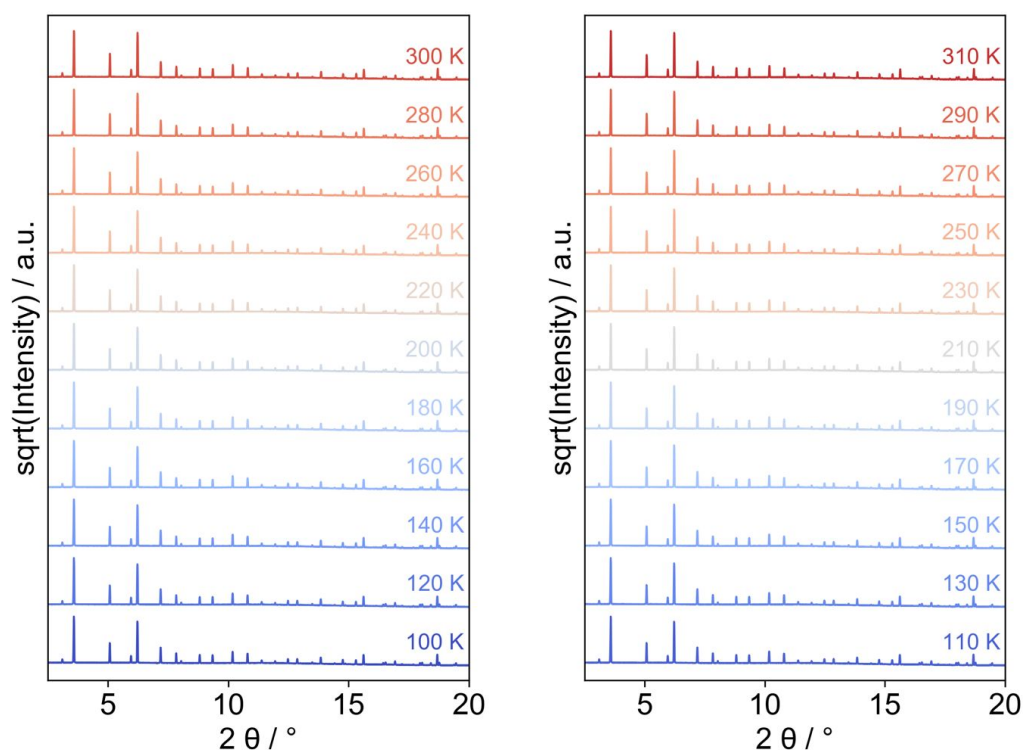


Figure S 3: Stack plots for the cooling (left) and heating (right) branch of the VTPXRD data of Cu_3BTC_2 .

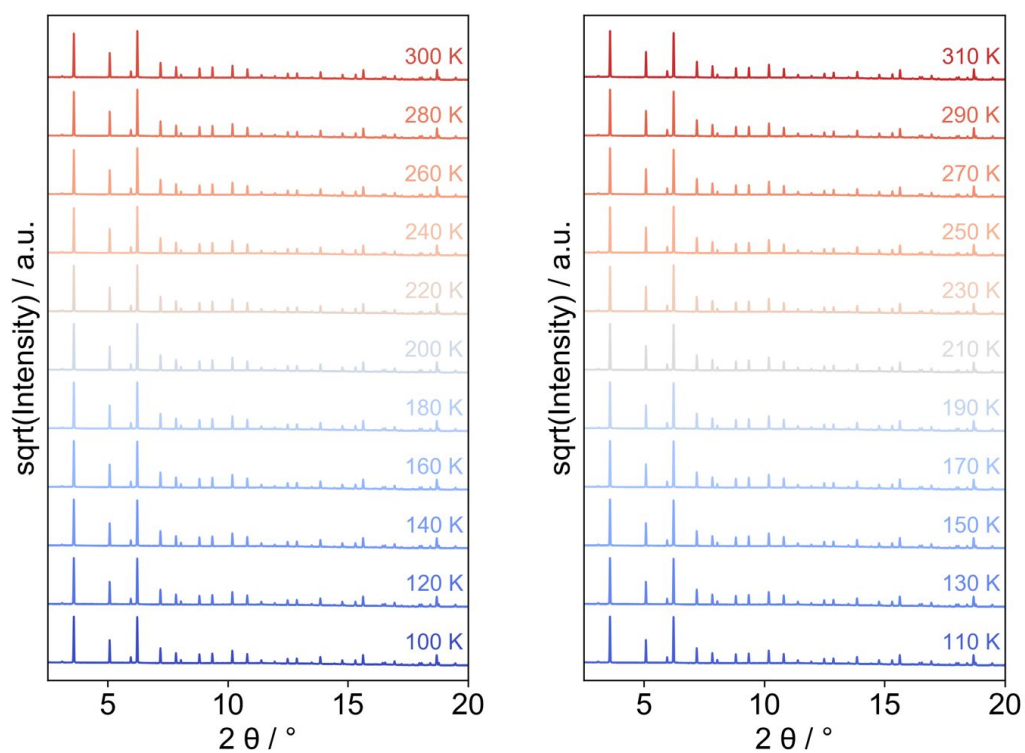


Figure S 4: Stack plots for the cooling (left) and heating (right) branch of the VTPXRD data of 0.2TCNQ@Cu₃BTC₂.

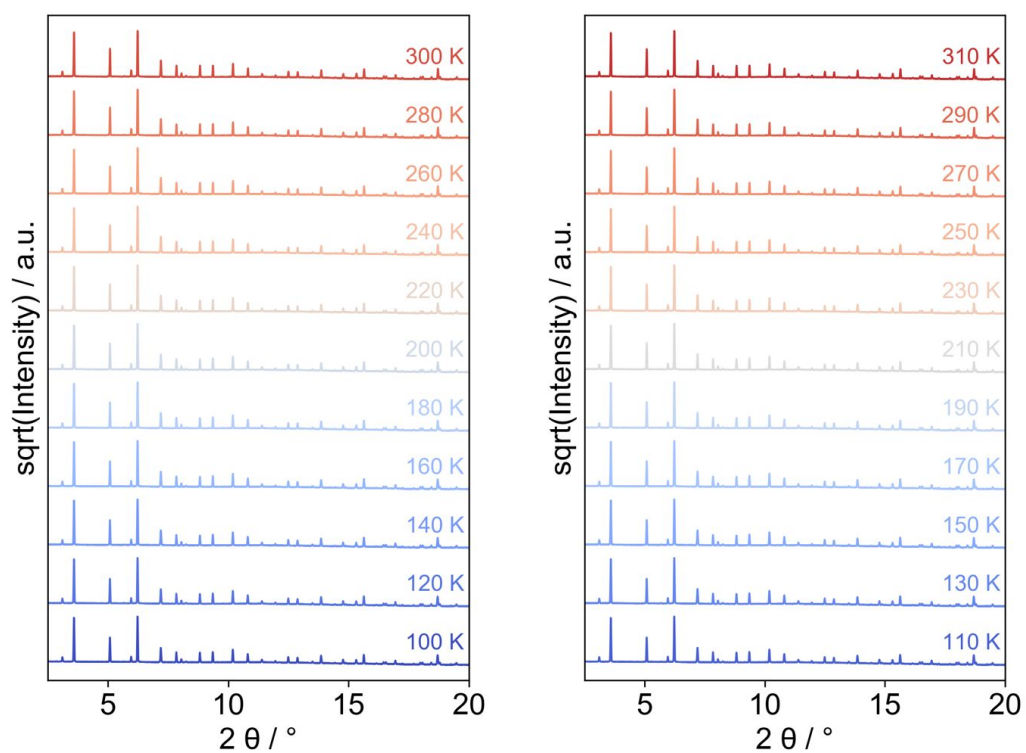


Figure S 5: Stack plots for the cooling (left) and heating (right) branch of the VTPXRD data of $0.4\text{TCNQ}@Cu_3\text{BTC}_2$.

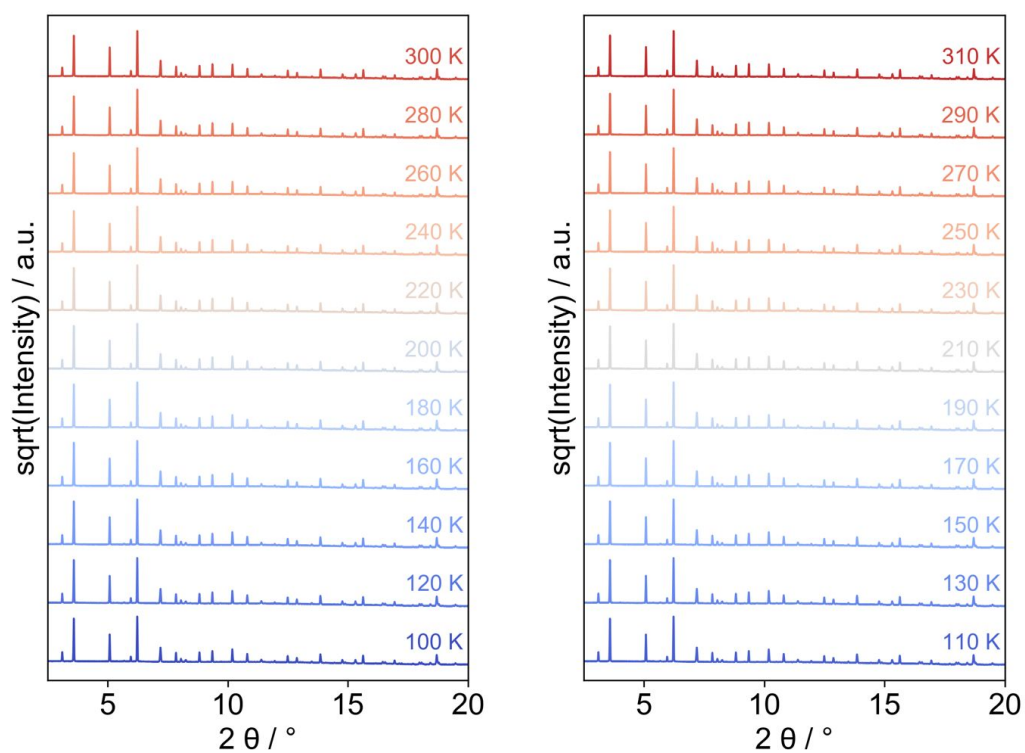


Figure S 6: Stack plots for the cooling (left) and heating (right) branch of the VTPXRD data of 0.6TCNQ@Cu₃BTC₂.

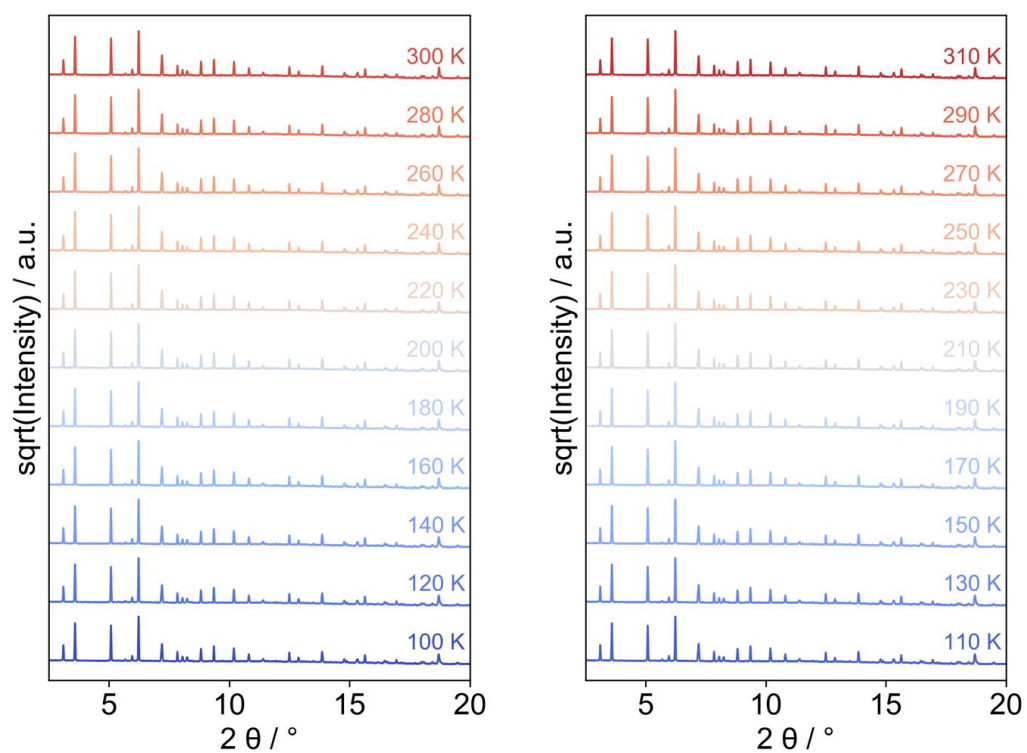


Figure S 7: Stack plots for the cooling (left) and heating (right) branch of the VTPXRD data of 1.0TCNQ@Cu₃BTC₂.

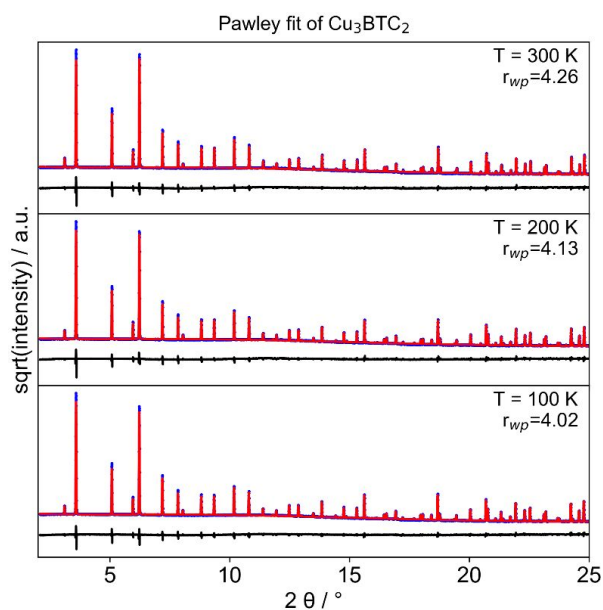


Figure S 8: Representative Pawley fits of the VTPXRD data of Cu_3BTC_2 at 100 K, 200 K and 300 K. The experimental data (blue) was fitted (red) using the cubic space group Fm-3m. The difference curve is given in black and the r_{wp} values are shown in the top right corner.

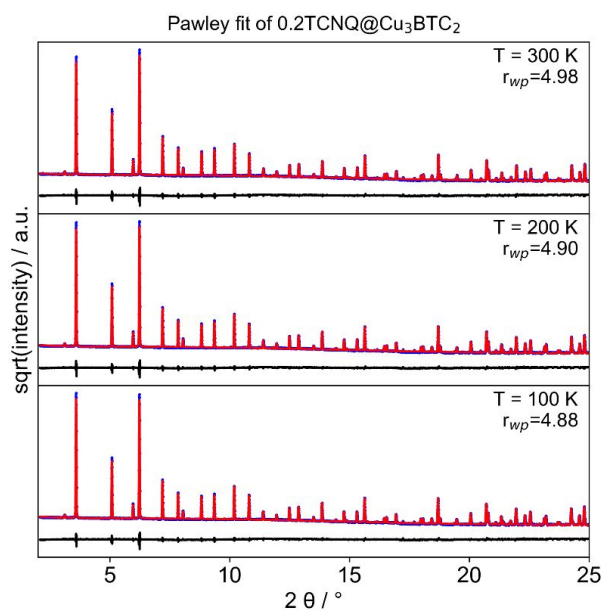


Figure S 9: Representative Pawley fits of the VTPXRD data of $0.2\text{TCNQ}@\text{Cu}_3\text{BTC}_2$ at 100 K, 200 K and 300 K. The experimental data (blue) was fitted (red) using the cubic space group Fm-3m. The difference curve is given in black and the r_{wp} values are shown in the top right corner.

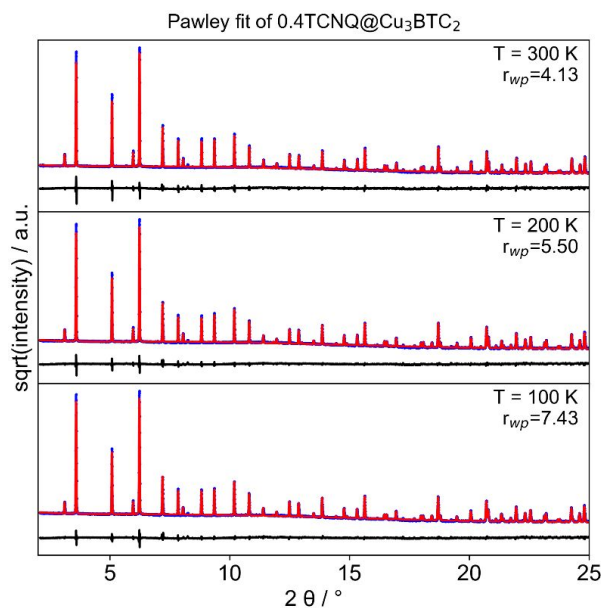


Figure S 10: Representative Pawley fits of the VTPXRD data of 0.4TCNQCu₃BTC₂ at 100 K, 200 K and 300 K. The experimental data (blue) was fitted (red) using the cubic space group Fm-3m. The difference curve is given in black and the r_{wp} values are shown in the top right corner.

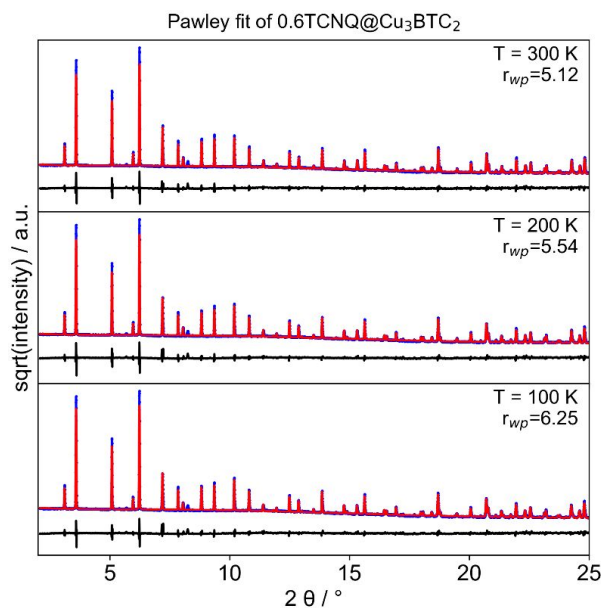


Figure S 11: Representative Pawley fits of the VTPXRD data of 0.6TCNQCu₃BTC₂ at 100 K, 200 K and 300 K. The experimental data (blue) was fitted (red) using the cubic space group Fm-3m. The difference curve is given in black and the r_{wp} values are shown in the top right corner.

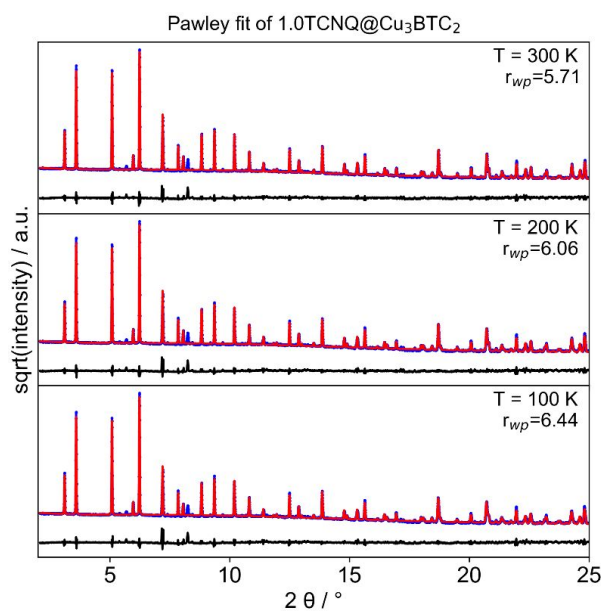


Figure S 12: Representative Pawley fits of the VTPXRD data of 1.0TCNQCu₃BTC₂ at 100 K, 200 K and 300 K. The experimental data (blue) was fitted (red) using the cubic space group Fm-3m. The difference curve is given in black and the r_{wp} values are shown in the top right corner.

With increasing TCNQ amount, new reflections occur (e.g. 5.68°, 8.25°). The potential origin of these reflections was discussed in reference [1].

Pawley profile fit outputs

Crystallographic information from VTPXRD data was extracted by Pawley profile fitting using TOPAS V5 software. Refinement parameters, *i.e.* weighted-profile *R*-factor (*r_{wp}*), expected *R*-factor (*r_{exp}*), and the goodness of fit (*gof*), as well as the lattice parameter (*a*) and the unit cell volume (*V*) are listed for every sample and every temperature step.

Table S 1: Fitting parameters and crystallographic information for Cu₃BTC₂.

T / K	r _{wp}	r _{exp}	gof	a / Å	V / Å ³
100	4.01847	1.19147	3.37270	26.28112	18152.29263
110	3.95095	1.19767	3.29887	26.28008	18150.13993
120	3.90582	1.19993	3.25505	26.27877	18147.43275
130	3.92407	1.19401	3.28645	26.27734	18144.45916
140	3.97991	1.20281	3.30885	26.27561	18140.87765
150	3.91441	1.20263	3.25488	26.27422	18138.00167
160	4.09133	1.19580	3.42141	26.27238	18134.19296
170	3.92237	1.20049	3.26729	26.27119	18131.73110
180	4.09960	1.20075	3.41420	26.26972	18128.68884
190	3.96166	1.20693	3.28244	26.26848	18126.11187
200	4.13273	1.21801	3.39302	26.26695	18122.94632
210	3.97864	1.20456	3.30298	26.26598	18120.94969
220	4.16768	1.20168	3.46822	26.26440	18117.68250
230	4.03433	1.20167	3.35726	26.26346	18115.73628
240	4.17906	1.20794	3.45965	26.26189	18112.48502
250	4.11588	1.20734	3.40904	26.26102	18110.69007
260	4.17829	1.20170	3.47697	26.25936	18107.24780
270	4.15955	1.20504	3.45180	26.25841	18105.27910
280	4.19485	1.20775	3.47327	26.25674	18101.83689
290	4.14436	1.21144	3.42103	26.25584	18099.95693
300	4.26453	1.20387	3.54235	26.25421	18096.60112
310	4.17133	1.20887	3.45060	26.25333	18094.77528

Table S 2: Fitting parameters and crystallographic information for 0.2TCNQ@Cu₃BTC₂.

T / K	r _{wp}	r _{exp}	gof	a / Å	V / Å ³
100	4.87734	1.09889	4.43844	26.26128	18111.22811
110	4.89946	1.10296	4.44211	26.26045	18109.49289
120	4.88384	1.10638	4.41426	26.25947	18107.47705
130	4.85966	1.10094	4.41412	26.25833	18105.11275
140	4.85313	1.11000	4.37218	26.25757	18103.54831
150	4.86900	1.10751	4.39634	26.25624	18100.78375
160	4.89884	1.10629	4.42816	26.25573	18099.74842
170	4.92835	1.10579	4.45684	26.25411	18096.38354

180	4.87309	1.11077	4.38714	26.25354	18095.21003
190	4.94521	1.11190	4.44751	26.25187	18091.76046
200	4.89938	1.10661	4.42737	26.25133	18090.64192
210	5.10172	1.10752	4.60644	26.24961	18087.09050
220	4.92745	1.11136	4.43369	26.24910	18086.02562
230	4.68917	1.10688	4.23637	26.24764	18083.01221
240	4.94849	1.11541	4.43647	26.24680	18081.28523
250	4.69420	1.11136	4.22385	26.24548	18078.54848
260	4.93898	1.11122	4.44464	26.24462	18076.77537
270	4.64689	1.10947	4.18840	26.24393	18075.34262
280	4.97898	1.11505	4.46525	26.24260	18072.59723
290	4.65229	1.11427	4.17519	26.24175	18070.83416
300	4.97957	1.11082	4.48280	26.24054	18068.33319
310	4.62253	1.11159	4.15849	26.23934	18065.85596

Table S 3: Fitting parameters and crystallographic information for 0.4TCNQ@Cu₃BTC₂.

T / K	r _{wp}	r _{exp}	gof	a / Å	V / Å ³
100	7.43016	1.14140	6.50967	26.26171	18112.10791
110	7.43145	1.14811	6.47275	26.26128	18111.20940
120	7.34352	1.14770	6.39847	26.26019	18108.95930
130	7.27044	1.14457	6.35212	26.25929	18107.09869
140	6.93027	1.15007	6.02597	26.25870	18105.88367
150	7.00743	1.14751	6.10665	26.25721	18102.80335
160	6.52056	1.14471	5.69623	26.25682	18101.98965
170	6.61092	1.14503	5.77356	26.25565	18099.57294
180	6.01001	1.14638	5.24261	26.25506	18098.34513
190	6.15131	1.14801	5.35823	26.25379	18095.71930
200	5.50259	1.15450	4.76622	26.25339	18094.90606
210	5.61129	1.14308	4.90894	26.25202	18092.05799
220	5.06162	1.14060	4.43770	26.25177	18091.55853
230	5.22847	1.13741	4.59683	26.25042	18088.75341
240	4.61679	1.14331	4.03810	26.25030	18088.50574
250	4.76640	1.14127	4.17640	26.24901	18085.83488
260	4.37752	1.13586	3.85394	26.24862	18085.03896
270	4.38439	1.13491	3.86320	26.24758	18082.89516
280	4.18416	1.13815	3.67627	26.24716	18082.01373
290	4.23099	1.13894	3.71485	26.24593	18079.48724
300	4.13307	1.13225	3.65031	26.24550	18078.58293
310	4.18476	1.13377	3.69103	26.24418	18075.85385

Table S 4: Fitting parameters and crystallographic information for 0.6TCNQ@Cu₃BTC₂.

T / K	r_wp	r_exp	gof	a / Å	V / Å ³
100	6.25348	1.19815	5.21929	26.25344	18095.00877
110	6.20968	1.19352	5.20282	26.25278	18093.63214
120	6.14994	1.19628	5.14091	26.25223	18092.50462
130	6.13466	1.20328	5.09829	26.25150	18090.98652
140	6.00330	1.20151	4.99648	26.25100	18089.95031
150	6.03844	1.20154	5.02557	26.24995	18087.77945
160	5.86117	1.20438	4.86656	26.24949	18086.83129
170	5.94174	1.20716	4.92210	26.24819	18084.14351
180	5.72339	1.19992	4.76979	26.24762	18082.96373
190	5.81739	1.20710	4.81932	26.24578	18079.17779
200	5.54496	1.20444	4.60376	26.24599	18079.60436
210	5.57388	1.20223	4.63629	26.24454	18076.60954
220	5.41066	1.20125	4.50418	26.24457	18076.67359
230	5.45372	1.20887	4.51143	26.24297	18073.36154
240	5.33874	1.20585	4.42735	26.24302	18073.45578
250	5.32715	1.20465	4.42217	26.24165	18070.64044
260	5.25026	1.20848	4.34450	26.24126	18069.83479
270	5.24029	1.20984	4.33141	26.24014	18067.51872
280	5.23341	1.20078	4.35833	26.23960	18066.40209
290	5.16923	1.20615	4.28574	26.23859	18064.30839
300	5.12461	1.20610	4.24890	26.23794	18062.97261
310	5.12665	1.21269	4.22749	26.23679	18060.59814

Table S 5: Fitting parameters and crystallographic information for 1.0TCNQ@Cu₃BTC₂.

T / K	r_wp	r_exp	gof	a / Å	V / Å ³
100	6.43607	1.13478	5.67166	26.22317	18032.48600
110	6.40052	1.13858	5.62149	26.22268	18031.46926
120	6.31327	1.13165	5.57883	26.22251	18031.12064
130	6.28485	1.13745	5.52540	26.22200	18030.07106
140	6.27911	1.13690	5.52299	26.22199	18030.05361
150	6.17579	1.13658	5.43368	26.22087	18027.73368
160	6.18750	1.14144	5.42080	26.22005	18026.04120
170	6.09975	1.14389	5.33244	26.21876	18023.38070
180	6.13075	1.14648	5.34747	26.21831	18022.46031
190	6.02280	1.14321	5.26832	26.21720	18020.17471
200	6.06062	1.14453	5.29527	26.21651	18018.75112
210	5.95205	1.15133	5.16971	26.21567	18017.01070
220	5.99292	1.15146	5.20462	26.21546	18016.58741
230	5.91437	1.15121	5.13752	26.21416	18013.89347

240	5.92182	1.14724	5.16178	26.21365	18012.84214
250	5.78037	1.16010	4.98265	26.21257	18010.63288
260	5.82500	1.15398	5.04776	26.21206	18009.57327
270	5.73384	1.16111	4.93823	26.21098	18007.34223
280	5.73480	1.16181	4.93610	26.21084	18007.06317
290	5.72695	1.16819	4.90240	26.20994	18005.21033
300	5.70618	1.16037	4.91754	26.20966	18004.63780
310	5.71323	1.16644	4.89799	26.20876	18002.78368

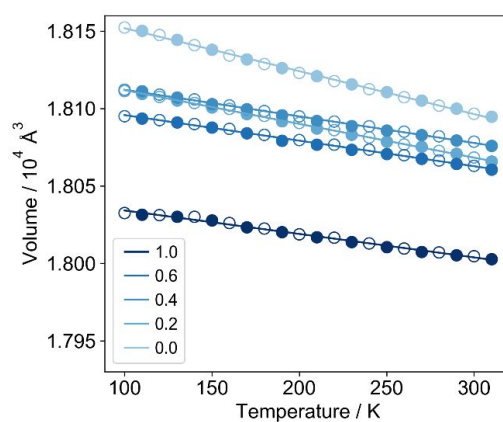


Figure S 13: Absolute unit cell volume of $x\text{TCNQ}@Cu_3\text{BTC}_2$ (x given in the legend) plotted against the temperature. Data from cooling (empty circles) and heating (filled circles) cycle recorded in 20 K steps. Please note that the volume of $0.2\text{TCNQ}@Cu_3\text{BTC}_2$ at 300 K is smaller when compared to $0.4\text{TCNQ}@Cu_3\text{BTC}_2$. This finding might point at a complex ordering mechanism of TCNQ within the pores, which is expected to be closely related to diffusion limitations and in turn plays a larger role for $0.4\text{TCNQ}@Cu_3\text{BTC}_2$.

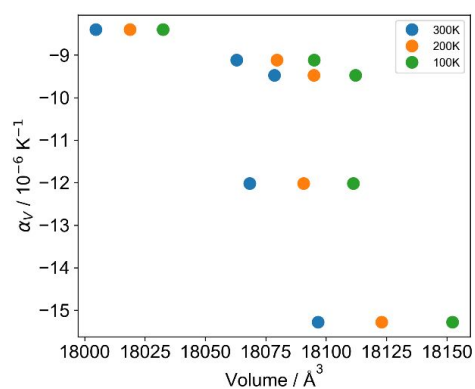


Figure S 14: Thermal expansion coefficient in dependence of the unit cell volume at a 100 K, 200 K and 300 K.

Raman spectroscopy

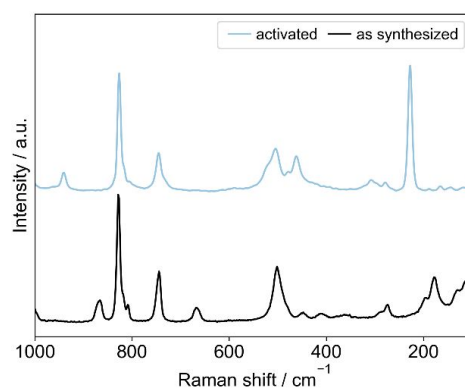


Figure S 15: Raman spectra of Cu_3BTC_2 after synthesis and washing with DMF (black) and after activation (light blue). The spectra are in good agreement with reference data from ³, and ⁴ (as synthesized).

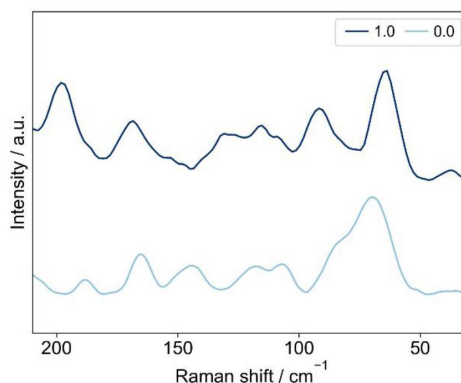


Figure S 16: Raman spectra of pristine Cu₃BTC₂ (light blue) and 1.0TCNQ@Cu₃BTC₂ (dark blue).

Far infrared spectroscopy

FIR spectra were recorded on three different instruments. The details for each instrument are provided below.

† High quality spectra were recorded on a Bruker VERTEX 70V vacuum spectrometer in the range of 600 – 30 cm⁻¹. The instrument is equipped with a Si-supported beamsplitter, a ceramic source and a DTGS detector using a GladiATR accessory (Pike, USA).

‡ Further spectra were recorded with a dynamically aligned Bio-Rad FTS-60A spectrometer using a GladiATR accessory with a diamond ATR element. A thermostated DTGS detector with polyethylene windows and a 6 μm Mylar beamsplitter were used. The optical bench was purged with dry N₂. Data was recorded between 600 – 35 cm⁻¹.

§ The third spectrometer was a Bruker VERTEX 70V FTIR operated under a flow of dry N₂. The spectrometer was equipped with a Si-supported beamsplitter and a RT-DTGS detector. The detection limit was 48 – 600 cm⁻¹.

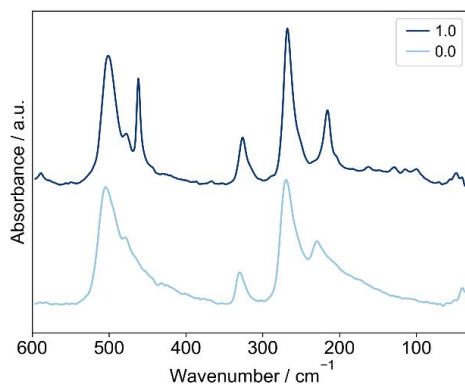


Figure S 17: Far infrared ATR spectra of pristine Cu₃BTC₂ and 1.0TCNQ@Cu₃BTC₂ recorded on a Bruker VERTEX 70V vacuum spectrometer[†]. All ATR spectra have been ATR corrected.

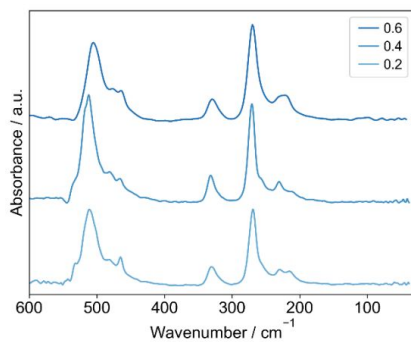


Figure S 18: Far infrared ATR spectra of *x*TCNQ@Cu₃BTC₂ (*x* given in the legend) recorded on a Bio-Rad FTS-60A spectrometer[‡]. All ATR spectra have been ATR corrected.

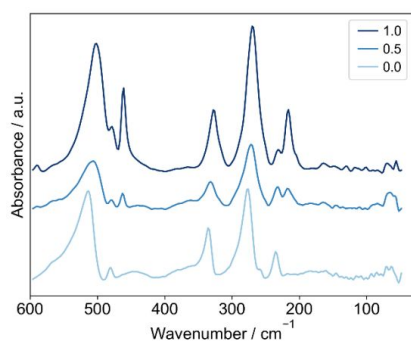


Figure S 19: Far infrared absorbance spectra of *x*TCNQ@Cu₃BTC₂ (*x* given in the legend) recorded on a Bruker VERTEX 70V FTIR spectrometer[§] in polyethylene pellets.

Table S 6: Low frequency FIR bands[&] of $x\text{TCNQ}@Cu_3\text{BTC}_2$. Values are given in cm^{-1} and band intensities are abbreviated as medium (m), weak (w), and very weak (vw) and assignments according to reference [4].

x = 0.0[†]	x = 0.2[‡]	x = 0.4[‡]	x = 0.5[§]	x = 0.6[‡]	x = 1.0[†]	Assignment⁴
(~28) [*]	-	-	-	-	32.2 w	Paddlewheel deformation and translational motion
35.0 w	-	-	-	-	40.8 w	
40.0 m	44.1 m	46.8 m	-	42.8 m	47.9 m	Organic linker trampoline-like motion
50.7 vw	51.4 vw	51.6 vw	54.0 vw	53.6 vw	55.7 vw	
60.4 vw	61.0 vw	-	61.8 w	62.5 w	63.3 vw	Paddlewheel deformation and translational motion involving linker rotation
68.9 vw	-	-	69.1 w	-	70.9 vw	Paddlewheel deformation and cluster rocking mode w/ organic linker rotation

[†] recorded on a Bruker VERTEX 70V vacuum spectrometer

[‡] recorded on a Bio-Rad FTS-60A spectrometer

[§] recorded on a Bruker VERTEX 70V FTIR spectrometer under a flow of N_2

[&] none of the listed bands coincide with the pure rotational lines of water vapor

^{*} predicted

References

1. Schneider, C.; Ukaj, D.; Koerver, R.; Talin, A. A.; Kieslich, G.; Pujari, S. P.; Zuilhof, H.; Janek, J.; Allendorf, M. D.; Fischer, R. A., High Electrical Conductivity and High Porosity in a Guest@MOF Material: Evidence of TCNQ Ordering within Cu₃BTC₂ Micropores. *Chem. Sci.* **2018**, *9*, 7405-7412.
2. Bhunia, M. K.; Hughes, J. T.; Fettinger, J. C.; Navrotsky, A., Thermochemistry of Paddle Wheel MOFs: Cu-HKUST-1 and Zn-HKUST-1. *Langmuir* **2013**, *29*, 8140-8145.
3. Prestipino, C.; Regli, L.; Vitillo, J. G.; Bonino, F.; Damin, A.; Lamberti, C.; Zecchina, A.; Solari, P.; Kongshaug, K.; Bordiga, S., Local Structure of Framework Cu (II) in HKUST-1 Metallorganic Framework: Spectroscopic Characterization upon Activation and Interaction with Adsorbates. *Chem. Mater.* **2006**, *18*, 1337-1346.
4. Ryder, M. R.; Civalleri, B.; Cinque, G.; Tan, J.-C., Discovering Connections between Terahertz Vibrations and Elasticity Underpinning the Collective Dynamics of the HKUST-1 Metal–Organic Framework. *CrystEngComm* **2016**, *18*, 4303-4312.

6.5 Supporting Information Study V

Supplementary Information

Retrofitting Metal-Organic Frameworks

Schneider et al.

Table of content:

Supplementary Note 1: Definition of the host-guest system.....	3
Structure of the MOF system	3
Structure of the cross linker	3
Geometric relation between MOF and CL	4
Supplementary Note 2: Input Parameters for RetroFit	7
Structural parameters of the MOF system	7
Structural parameters of the cross linker	7
Single point DFT calculations	7
Supplementary Note 3: Algorithm of the RetroFit program	10
Supplementary Note 4: Restrictions and limitations of RetroFit	13
Supplementary Note 5: Results of the DFT single point calculations.....	14
Supplementary Note 6: Interpolation error	16
Supplementary Note 7: Results of the RetroFit algorithm	18
Supplementary Note 8: Results from RetroFit for NOTT-100 and NOTT-101.....	21
Supplementary Note 9: Powder X-ray diffraction	23
Supplementary Note 10: Fourier transform infrared spectroscopy.....	26
Supplementary Note 11: Scanning electron microscopy.....	28
Supplementary Note 12: Electrical conductivity measurements.....	30
Supplementary References	32

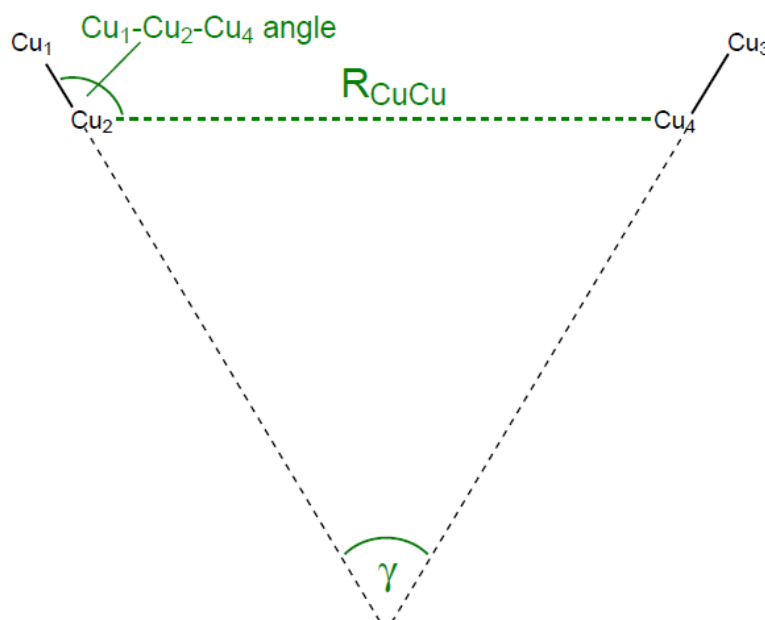
Supplementary Note 1: Definition of the host-guest system

The user of RetroFit has to identify the metal-OMS vector of the MOF as well as the vector of the donor groups of the cross linker (CL) to determine the angles γ and α as described in the manuscript. In the following, this is described for the example of a Cu paddlewheel MOF and a nitrile CL. However, this approach can universally be applied to other MOFs and CLs.

Structure of the MOF system

The relative position of two open metal sites in a Cu paddlewheel MOF can be described by the distance between the two Cu atoms (Cu_2 and Cu_4) R_{CuCu} that are available for coordination and the angle of the CuCu vectors of the two paddle wheels γ or by the $\text{Cu}_1\text{-Cu}_2\text{-Cu}_4$ angle (see Supplementary Figure 1), which are dependent via

$$\gamma = 180^\circ - 2 \cdot (180^\circ - \alpha(\text{Cu}_1 - \text{Cu}_2 - \text{Cu}_4)) \quad (\text{eq. 1})$$



Supplementary Figure 1: Geometric description of the MOF.

Structure of the cross linker

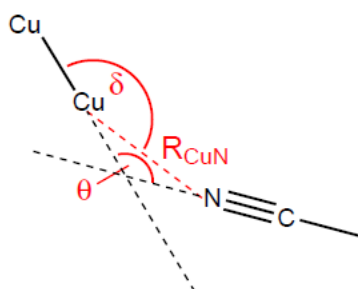
The CL can be described by the distance of the N atoms of the two coordinating nitrile groups R_{NN} and the angle of the two CN vectors α (see Supplementary Figure 2).



Supplementary Figure 2: Geometric description of the cross linker.

Geometric relation between MOF and CL

The orientation of a CL symmetrically bridging two paddlewheels can be described by the distance between a coordinating nitrile group and the Cu site R_{CuN} and the two angles δ and θ (see Supplementary Figure 3).



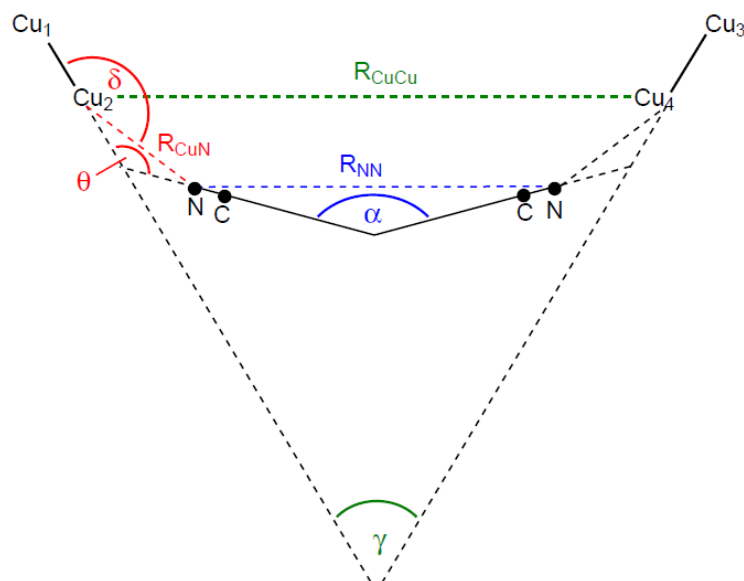
Supplementary Figure 3: Geometric description of the relative orientation of the MOF and the cross linker.

The parameters defining the three subsystems are summarized in Supplementary Table 1.

Supplementary Table 1: Summary of the subsystems that describe the host-guest complex and their respective geometric parameters.

System	Parameters
Cu paddlewheel MOF	R_{CuCu} and γ or R_{CuCu} , and $\angle(\text{Cu}_1 - \text{Cu}_2 - \text{Cu}_4)$
Cross linker	R_{NN} and α
Host-Guest	R_{CuN} , δ and θ

Combining the geometric relations from Supplementary Figure 1 - Supplementary Figure 3 defines the entire host-guest complex with seven parameters (see Supplementary Table 1), as illustrated in Supplementary Figure 4.



Supplementary Figure 4: 2D representation of the geometric relations defining the host-guest system.

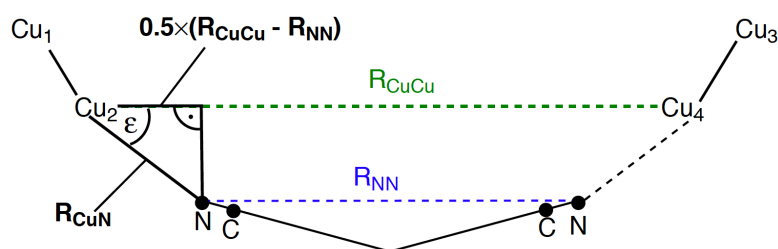
In the following, it is shown that α , θ and γ are interdependent. Therefore, the auxiliary angle κ , which is the angle in the $\text{Cu}_2\text{-Cu}_4\text{-}\gamma$ triangle, is defined:

$$\kappa = 90^\circ - \frac{\gamma}{2} \quad (\text{eq. 2})$$

The angle between $\text{N-Cu}_2\text{-Cu}_4$, which is the auxiliary angle ε , is therefore:

$$\varepsilon = \kappa - (180^\circ - \delta) = \delta - \frac{\gamma}{2} - 90^\circ \quad (\text{eq. 3})$$

Now, a right-angled triangle, spanned by the distances R_{CuN} and $\frac{1}{2}(R_{\text{CuCu}} - R_{\text{NN}})$ (including angle ε), can be defined (see Supplementary Figure 5).



Supplementary Figure 5: Right-angled triangle defined by R_{CuN} , $\frac{1}{2}(R_{\text{CuCu}} - R_{\text{NN}})$ and ε .

Now, the following cosine relation can be expressed:

$$\cos(\varepsilon) = \cos\left(\delta - \frac{\gamma}{2} - 90^\circ\right) = \sin\left(\delta - \frac{\gamma}{2}\right) = \frac{1 R_{CuCu} - R_{NN}}{2 R_{CuN}} \quad (\text{eq. 4})$$

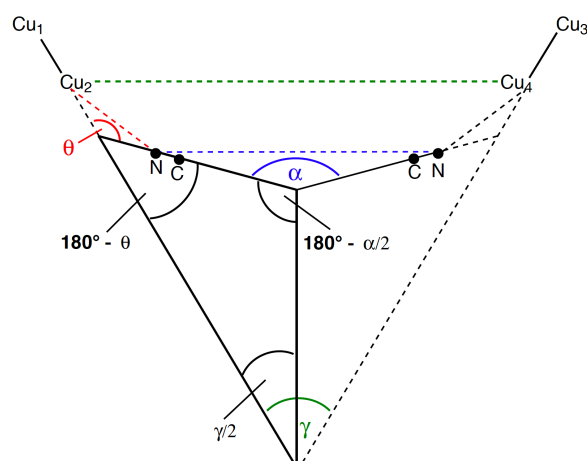
In addition, a second triangle can be defined (see Supplementary Figure 6). In this triangle, $\frac{\gamma}{2}$, $180^\circ - \theta$ and $180^\circ - \frac{\alpha}{2}$ have an angle sum of 180° :

$$180^\circ = 180^\circ - \theta + \frac{\gamma}{2} + 180^\circ - \frac{\alpha}{2} \quad (\text{eq. 5})$$

This equation can be rearranged to:

$$\alpha = 360^\circ + \gamma - 2\theta \quad (\text{eq. 6})$$

Consequently, the entire host-guest system can be described by six variables, i.e. R_{CuCu} , R_{NN} , R_{CuN} , α , γ , and δ , or R_{CuCu} , R_{NN} , R_{CuN} , α , θ , and δ , or R_{CuCu} , R_{NN} , R_{CuN} , α , γ , and θ .



Supplementary Figure 6: Right-angled triangle defined by $\frac{\gamma}{2}$, $180^\circ - \theta$ and $180^\circ - \frac{\alpha}{2}$.

In the retrofitting tool, the input parameters of a molecule (α and R_{NN}) and of the MOF-system (R_{CuCu} and γ) are used. As the description of the whole system requires 6 variables, a screening of the 2 missing variables (R_{CuN} and δ) is required in order to find the optimal position on a MIP (see below).

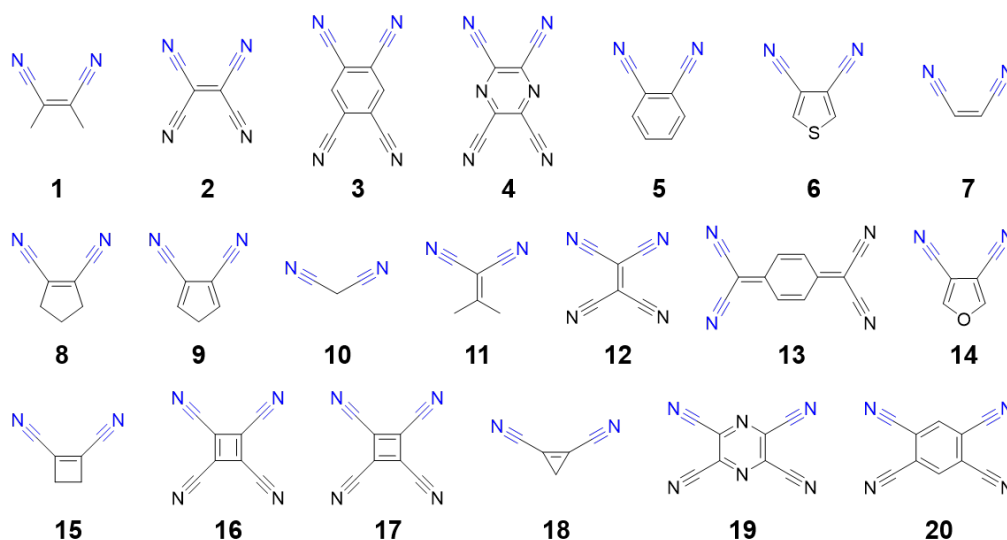
Supplementary Note 2: Input Parameters for RetroFit

Structural parameters of the MOF system

The geometric information of the MOF system (R_{CuCu} and γ) is extracted from the crystal structure (cif-file) of the MOF and is a manual input. Please refer to the How-To for further information.

Structural parameters of the cross linker

All molecule geometries were optimized with the Gaussian09 program package.¹ Optimization was performed with DFT with a B3LYP hybrid functional and a 6-31G basis set.^{2, 3} For the optimization the *tight* convergence criterion was used and the Hessian was recalculated after each optimization step (keyword 'calcall'). All molecules were symmetry restricted during the optimization process (see Supplementary Figure 7). The resulting Gaussian output file was converted to the xyz-format using Open Babel (version 2.3.2) and then imported into the retrofit tool using the Atomic Simulation Environment (ASE) (version 3.16.0) to compute R_{NN} and α .



Supplementary Figure 7: Library of dicyano-CLs used in this work. CLs 2, 3, 4, 12, 13, 16, 17, 19, and 29 were restricted to D_{2h} symmetry while CLs 1, 5-11, 14, 15, and 18 were restricted to C_{2v} symmetry during the optimization with Gaussian.

Single point DFT calculations

To access energies in the host-guest system, a simple model was chosen and transferred to the real system. Precisely, we optimized a Cu(II) formate paddlewheel and an acetonitrile molecule, respectively, and then arranged the two entities that the nitrile group points towards the OMS of the paddlewheel. By varying R_{CuN} , δ and θ according to the parameters given in Supplementary Table 2, we obtained an energy of the system for every combination of the three parameters, which allows the generation of a model interaction potential (MIP). Two screenings were performed: one with the acetonitrile in the Cu-O plane and another one with the acetonitrile in the plane of the O-Cu-O angle bisector. Both screenings yielded similar energy values and therefore

we proceeded with the values for the in-plane scan. The configuration with the lowest energy is defined as 0 kcal/mol and all energies are given as energy differences ΔE .

The single point calculations were done on a DFT level of theory using the TURBOMOLE (V7.1) software package.⁴ The hybrid functional B3LYP^{3,5} was used with a TZVPP basis set⁶ and a fine 'm5' grid⁷ for all elements. The multipole-accelerated⁸ resolution of the identity approximation^{9,10} was used for performance reasons. Grimmes D3¹¹ was employed to properly account for dispersive interactions. The SCF convergence criterion was set to 10^{-6} Hartree.

The spin-state of the Cu^{2+} dimer with a total of 18 d-electrons was assigned to be the ferromagnetically coupled triplet state (eight occupied d orbitals and two singly occupied d orbitals with alpha spin). Even though the spin state in a Copper paddlewheel MOF is the open-shell singlet state (eight occupied d orbitals and two singly occupied d-orbitals, one with alpha and one with beta spin), the excited state we chose is experimentally only 292.2 cm^{-1} ,¹² and in a comparable hybrid (B3LYP/cc-pVDZ-PP/UDFT) calculation 372 cm^{-1} above the ground state energy,¹³ which at room temperature makes it notably populated. Computing the antiferromagnetically coupled ground state or applying e.g. a multireference treatment however, requires a more involved theoretical description, which is why we chose here to focus on the low lying excited state. This was justified in the aforementioned computational study, where the two states were compared with respect to their energies, geometries and vibrational frequencies/modes and were found to be "nearly indistinguishable".¹³

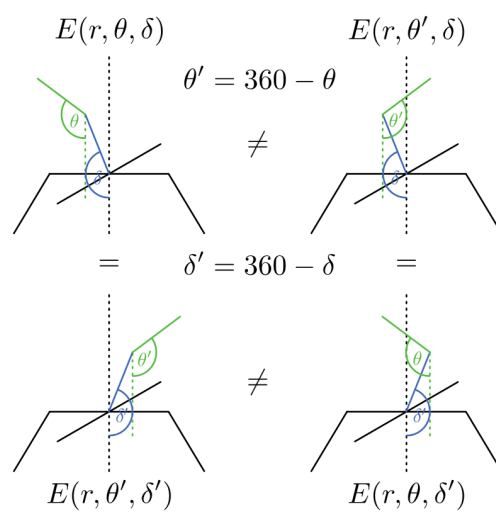
Due to the electronic configuration, the calculations were carried out spin-unrestricted.

Supplementary Table 2: Details about the scanning grid for the MIP of the paddlewheel – acetonitrile system.

System	Start	End	Step size
R_{CuN}	1.8 Å	5.0 Å	0.2 Å
δ	90°	180°	5°
θ	90°	270°	5°

Due to symmetry reasons, we can mirror the resulting three-dimensional MIP for displacements of δ and $\theta > 180^\circ$ according to eq. 7 and Supplementary Figure 8. This way we obtained a MIP in the intervals $R_{\text{CuN}} = [1.8 \text{ \AA}, 5.0 \text{ \AA}]$, $\delta = [90^\circ, 270^\circ]$, $\theta = [90^\circ, 270^\circ]$.

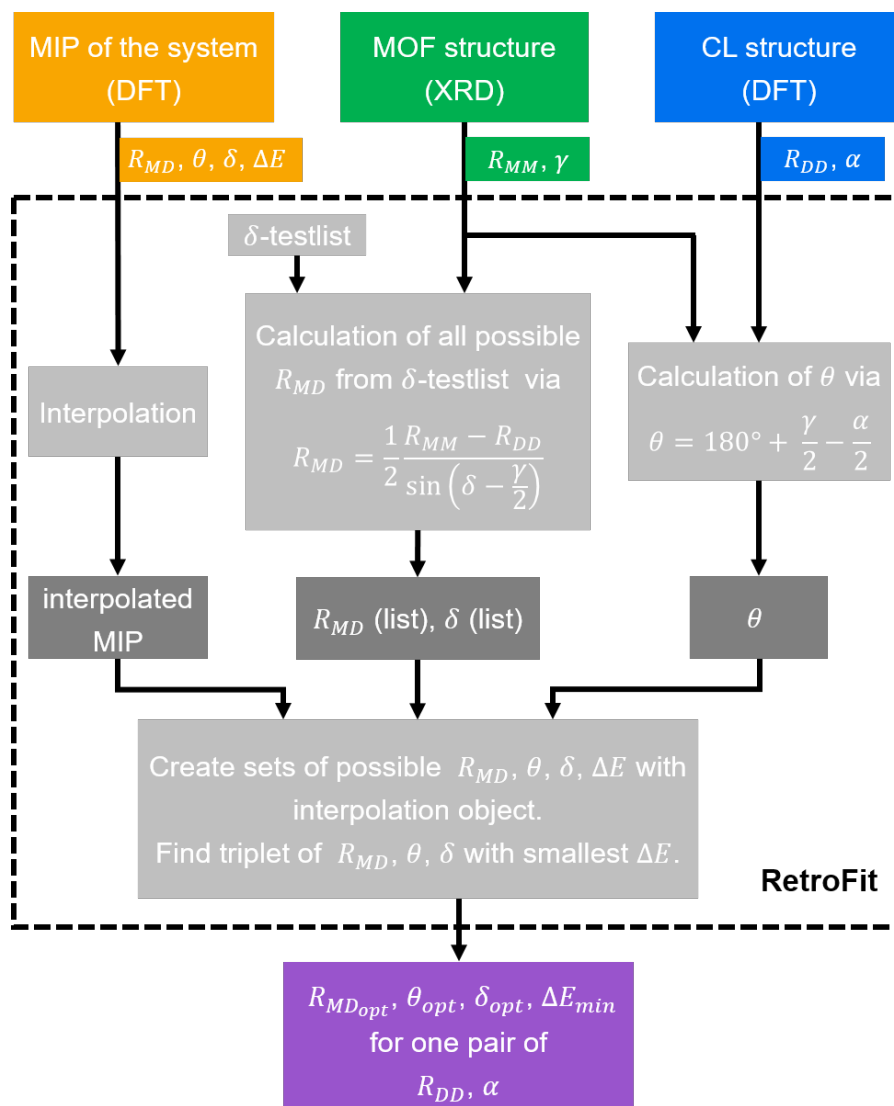
$$E(R_{\text{CuN}}, \delta, \theta) = E(R_{\text{CuN}}, 360 - \delta, 360 - \theta) \quad (\text{eq. 7})$$



Supplementary Figure 8: Symmetry relations used to mirror the energies obtained from DFT calculations.

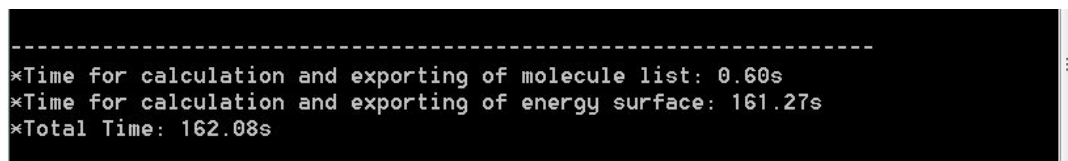
Supplementary Note 3: Algorithm of the RetroFit program

The program code is written in the open source programming language Python™ (available at <http://www.python.org>). First, the data of the paddlewheel MIP (R_{MD} , δ , θ and energy ΔE) is imported and interpolated. As interpolation method, a regular grid interpolator from the Scipy package was used (the class `scipy.interpolate.RegularGridInterpolator`). This interpolation method uses trilinear interpolation. As method-tag, 'linear' was chosen. The interpolation results in an object, which has as input R_{MD} , δ and θ and returns the respective energy value E (i.e. ΔE) and works within the boundaries of the MIP as defined in Supplementary Table 2, including the mirroring of δ and θ for angles $>180^\circ$. Second, the geometric information of the MOF system (R_{MM} and $\varphi(M_1 - M_2 - M_4)$, although γ is used as describing angle in rest of the program) and guest molecules (α , R_{DD}) are imported. Note, for the ease of use the $\varphi(M_1 - M_2 - M_4)$ is used as input value as it can be easily obtained from the MOF crystal structure. For non-paddlewheel MOFs this angle is defined by the vector M-M and a virtual vector between one metal center and the direction of its OMS. This data is used to calculate via (eq. 4) and (eq. 6) an energetically optimal triple of R_{MD} , δ and θ . Hereby, θ can be easily calculated from α and γ with (eq. 6). In order to obtain R_{MD} and δ , (eq. 6) is used. As this equation has two unknown variables, it is not straight forward to calculate both quantities simultaneously. Therefore, a set of δ values (δ -testlist) is used to calculate a respective set of R_{MD} values. Subsequently, the δ -testlist, the set of R_{MD} values and θ is used to calculate with the interpolation object a set of energies. The lowest energy value of the set is identified. By doing this, the energetically most favorable coordinates R_{MD} , δ and θ of a given guest molecule with the geometry defined by α and R_{DD} in a MOF system defined by R_{MM} and γ are obtained for the respective input MIP data. A flowchart of the described algorithm is shown in Supplementary Figure 9.



Supplementary Figure 9: General workflow of the RetroFit program with emphasis on the various steps that are performed within the Python-based code. The result of one cycle is a ΔE_{min} value (purple) for a given CL@MOF system. When performed for various CLs for one parent MOF with OMS, CLs can be ranked with respect to their applicability in a retrofit experiment based on their ΔE_{min} values. A how-to guideline is provided as a separate part of the supplementary information.

The execution time of the code depends on the selected step size of the δ -testlist and the step size of the parameters α and R_{NN} used to generate the energy map. Using a step size of 100 for the three parameters, which we found reasonable, the execution time is in the order of a few minutes using a typical personal computer (Supplementary Figure 10).



```
-----  
*Time for calculation and exporting of molecule list: 0.60s  
*Time for calculation and exporting of energy surface: 161.27s  
*Total Time: 162.08s
```

Supplementary Figure 10: Screenshot of the reported runtime of RetroFit. The code was executed on a personal computer (Windows 10) using a step size of 100 for δ , α and R_{NN} .

Supplementary Note 4: Restrictions and limitations of RetroFit**Open metal-site of MOF**

In this model, all four Cu atoms are located in one plane and consequently the Cu-OMS vector is also located in that plane. Therefore, this model works for 2-dimensional systems that have a mirror plane, meaning at least a C_{2v} symmetry. For systems in which the Cu-OMS vectors are not in one plane additional assumptions are necessary (see results for the NOTT systems below).

Guest Molecule

All guest molecules are defined by their functional groups, which are in this case nitrile groups. The two nitrile groups (i.e. the C-N vectors) have to be in one plane for the system to be mirror symmetric to each other. Hence, a C_{2v} symmetry of this four-atom system is required, or further assumptions are necessary.

Interaction potential of model system

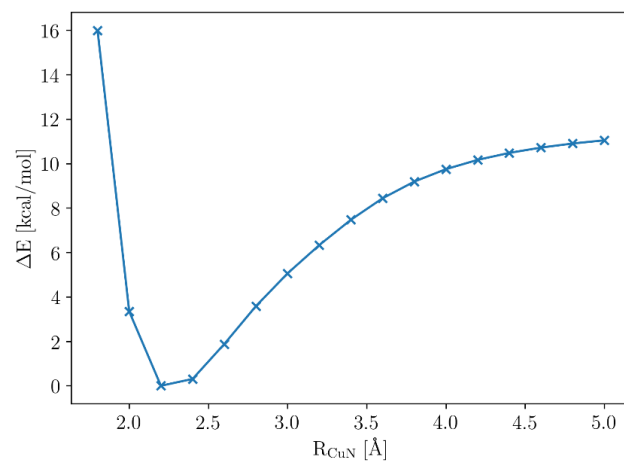
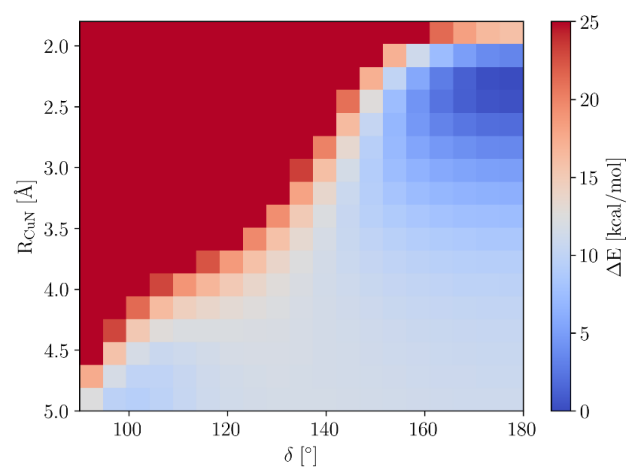
For every new metal – functional group pair a new MIP has to be calculated, which requires some DFT calculations.

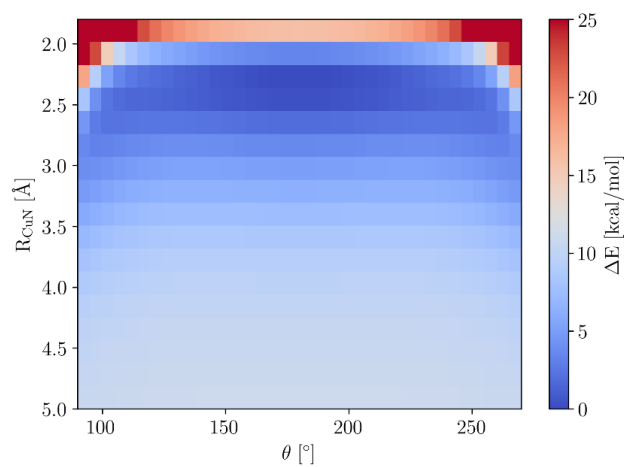
Interpolation

In the retrofit program an interpolation of the MIP data is performed. Hence, interpolated data are only available in the limits of the calculated MIP data (see Supplementary Table 2).

General

As no geometrical optimization is performed by the RetroFit program, all components are considered rigid. Therefore, the framework and the molecule do not change their geometry and bond lengths and angles are always constant in each subsystem. In addition, no dispersion interactions or interactions between two guest molecules are taken into consideration. For a more accurate simulation, the entire system had to be calculated by DFT at significantly higher computational costs.

Supplementary Note 5: Results of the DFT single point calculations**Supplementary Figure 11:** Slice of the acetonitrile – Cu paddlewheel MIP with $\delta = 180^\circ$ and $\theta = 180^\circ$.**Supplementary Figure 12:** Slice of the acetonitrile – Cu paddlewheel MIP with $\theta = 180^\circ$.



Supplementary Figure 13: Slice of the acetonitrile – Cu paddlewheel MIP with $\delta = 180^\circ$.

Supplementary Note 6: Interpolation error

In order to verify the interpolation of the the MIP, we have checked for error values originating from the interpolation itself. The set of Energies $E(\{\alpha, \theta, \delta\})$ was linearly interpolated to obtain a hypothesis $\hat{E}(\{\alpha, \theta, \delta\})$ for any point inside the set of linearly spaced points $\alpha_i, \theta_i, \delta_i$.

The Error of interpolation at any of these points is given by

$$ERR(\{\alpha, \theta, \delta\}) = E(\{\alpha, \theta, \delta\}) - \hat{E}(\{\alpha, \theta, \delta\}) \quad (\text{eq. 8})$$

We divide the space into cubelets with dimensions $0.2 \text{ \AA} \times 5^\circ \times 5^\circ$. For each cubelet, a maximum error is estimated.

In order to find an upper limit for the error in each cubelet, the diagonal of the cubelet is considered (from $\alpha_i, \theta_i, \delta_i$ to $\alpha_{i+1}, \theta_{i+1}, \delta_{i+1}$).

According to the mean value theorem, we can estimate the interpolation error for a linear interpolation of a point x between two adjacent linearly spaced points x_i and x_{i+1} (e.g $x \in [x_i, x_{i+1}]$) in the following way:

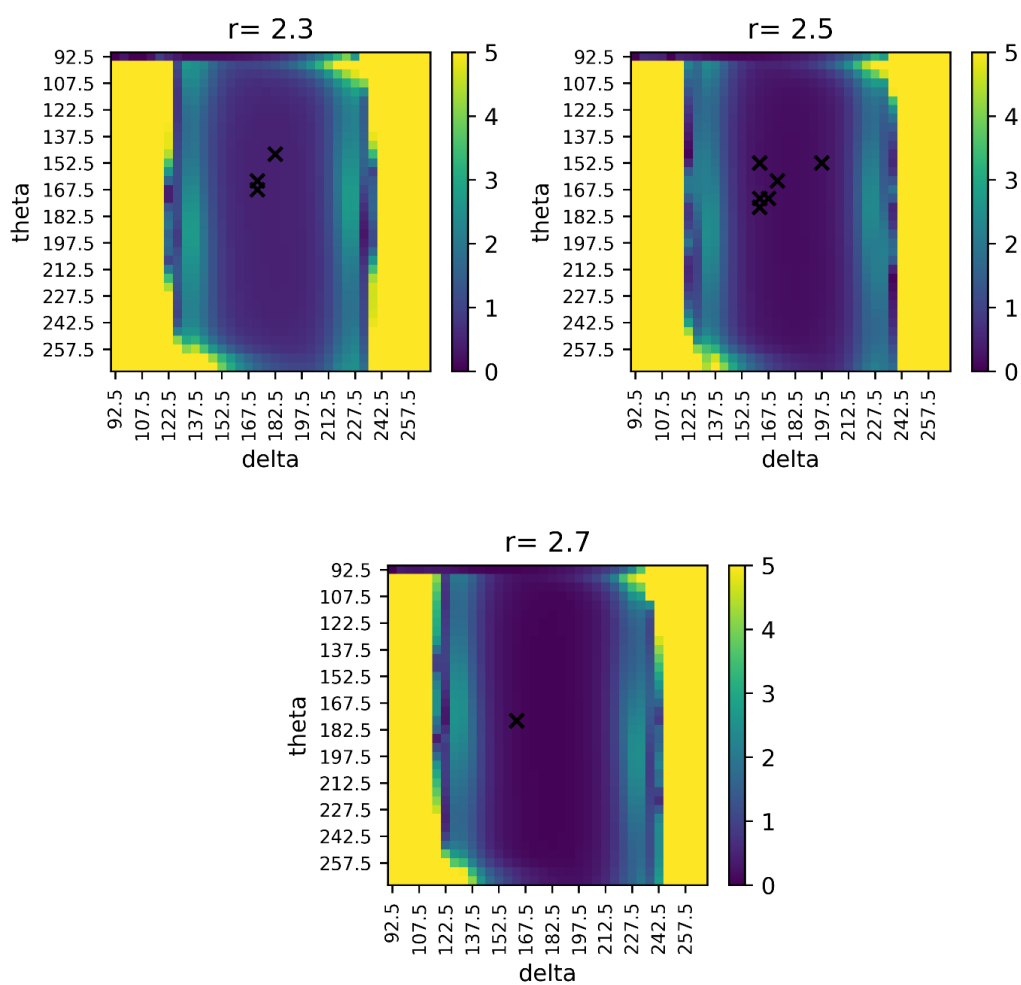
$$ERR(x) \leq \max_{x \in [x_i, x_{i+1}]} \left(\frac{(x - x_i)(x - x_{i+1})}{2} \right) \cdot \max_{x' \in [x_i, x_{i+1}]} (f^{(2)}(x')) \quad (\text{eq. 9})$$

$f^{(2)}(x')$ is the second derivative for $x \in [x_i, x_{i+1}]$. Since the maximum value of the derivative is not known, we estimate it from the numerically calculated second derivatives at the nearest evaluation points x_i and x_{i+1} and choose the largest value of these two.

As we have a multi-dimensional problem, we estimate the error in each direction along the sides of the cubelet (from $\alpha_i, \theta_i, \delta_i$ to $\alpha_{i+1}, \theta_i, \delta_i$, from $\alpha_i, \theta_i, \delta_i$ to $\alpha_{i+1}, \theta_i, \delta_i$ and from $\alpha_i, \theta_{i+1}, \delta_i$ to $\alpha_i, \theta_i, \delta_{i+1}$) and then estimate the total error in a cubelet as:

$$ERR(\{\alpha, \theta, \delta\}) = \sqrt{ERR_r^2 + ERR_\theta^2 + ERR_\delta^2} \quad (\text{eq. 10})$$

Supplementary Figure 14 depicts the interpolation errors for the slices $R_{\text{CuN}} = 2.3, 2.5$ and 2.7 \AA with insets of all of the evaluated CL molecules. All molecules are in a low-error area and hence our results are inside a reasonable margin of error. The output of RetroFit provides energy penalties with full precision. Based on these considerations, we suggest to give the energy penalties as within the accuracy of three decimal places, as done for our retrofitted test-systems, see Supplementary Note 7.



Supplementary Figure 14: Interpolation errors of the interpolated acetonitrile – Cu paddlewheel MIP. For visualization purposes, slices of the four-dimensional MIP are shown at $R_{\text{CuN}} = 2.3, 2.5,$ and 2.7 Å. The error increases from dark blue to yellow and the scale is given in kcal / mol. The CLs tested in this study are indicated by a black “x” and are all located in the low-error area.

Supplementary Note 7: Results of the RetroFit algorithm

RetroFit calculates the optimal position of a CL (R_{CuN} , δ , θ) within a given MOF and provides energy deviation ΔE from the ideal configuration. This allows to rank the tested CLs according to their fit, i.e. lowest ΔE values, and represents a guideline for experimentalists. The energies for all tested CLs and MOFs studied in this work are provided in Supplementary Table 3.

Supplementary Table 3: Energy penalties ΔE calculated for the fit of different dicyano-CLs in Cu_3BTC_2 , NOTT-100 and NOTT-101 using the RetroFit algorithm.

CL	Guest	$R_{\text{NN}} / \text{\AA}$	$\Delta E / \text{kcal mol}^{-1}$				
			Cu_3BTC_2	NOTT-100 3,5-pos.	NOTT-100 3,3'-pos.	NOTT-101 3,5-pos.	NOTT-101 3,3''-pos.
1	1,2-dimethyl-1,2-dicyanoethylene	4.077	4.203	3.835	0.311	4.281	9.881
2	TCNE (cis)	4.095	4.175	3.826	0.349	4.252	9.864
3	TCNB (ortho)	4.114	4.107	3.746	0.339	4.182	9.842
4	tetracyanopyrazine (ortho)	4.127	4.077	3.705	0.339	4.151	9.828
5	1,2-dicyanobenzene	4.134	4.014	3.642	0.318	4.089	9.817
6	3,4-dicyanothiophen	4.333	3.175	2.864	0.606	3.238	9.541
7	cis-dicyanoethylene	4.370	2.965	2.646	0.723	3.030	9.469
8	1,2-dicyanocyclopentene	4.424	2.847	2.522	0.793	2.908	9.366
9	dicyanocyclopentadiene	4.424	2.847	2.522	0.793	2.908	9.366
10	malononitrile	4.431	2.317	1.964	1.266	2.395	9.211
11	dicyano-2-methylpropene	4.433	2.305	1.952	1.291	2.383	9.203
12	TCNE (geminal)	4.436	2.292	1.940	1.289	2.371	9.197
13	TCNQ (geminal)	4.447	2.241	1.889	1.328	2.319	9.170
14	3,4-dicyanofuran	4.551	2.330	1.949	1.286	2.405	9.176
15	1,2-dicyanocyclobutene	5.016	0.789	0.664	5.299	0.837	8.157
16	tetracyanoclobutene (single bond)	5.082	0.702	0.535	5.482	0.708	8.043

17	tetracyanoclobutene (double bond)	5.132	0.650	0.494	6.794	0.658	7.847
18	1,2-dicyanocyclopropene	5.772	0.797	0.870	11.682	0.744	5.919
19	tetracyanopyrazine (meta)	6.761	4.049	4.596	12.097	3.976	2.333
20	TCNB (meta)	6.893	4.815	5.472	15.884	4.689	1.882

Categorization of the energy penalties:

In order to evaluate and categorize the output values of RetroFit, i.e. the energy penalty ΔE , it is worth looking at the binding energy of the entire retrofitted system (CL@MOF). Considering the two coordination bonds formed between a CL and the MOF, the energy gain E_{Retrofit} can be approximated by (eq. 11).

$$E_{\text{Retrofit}} = 2 (E_{\text{Binding}} - \Delta E) \quad (\text{eq. 11})$$

From the acetonitrile – Cu paddlewheel MIP at $\delta = 180^\circ$ and $\theta = 180^\circ$ (Supplementary Figure 11) we can calculate the binding energy E_{Binding} of the ideal configuration as

$$E_{\text{Binding}} = E(R_{\text{CuN}} = 5.0) - E(R_{\text{CuN}} = 2.2) = 11.05 \text{ kcal/mol}. \quad (\text{eq. 12})$$

A ditopic binding situation, i.e. retrofitting, is favored over a monotopic coordination of only one donor group to the OMS, if

$$E_{\text{Retrofit}} > E_{\text{Binding}}. \quad (\text{eq. 13})$$

From (eq. 11) and (eq. 13) follows that retrofitting of nitrile-CLs in Cu-paddlewheel MOFs is favored over a monotopic coordination if

$$\Delta E < \frac{1}{2} E_{\text{Binding}} \approx 5.5 \text{ kcal/mol}. \quad (\text{eq. 14})$$

For the results in this study (see Supplementary Table 3) we suggest the general categorization shown in Supplementary Table 4.

Supplementary Table 4: Proposed categorization of the RetroFit results.

$\Delta E / \text{kcal mol}^{-1}$	Category
0 – 2.5	good fit
2.5 – 5.0	medium fit
> 5.0	bad / no fit

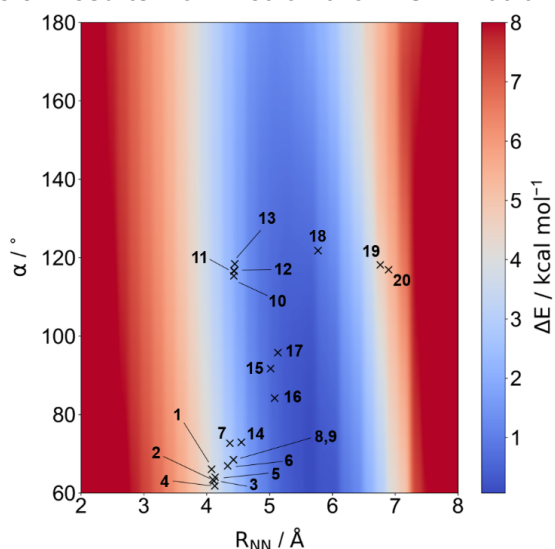
Supplementary Table 5: Comparison of the input parameters and results of the retrofit program and the DFT calculation of TCNQ@Cu₃BTC₂ of reference [14].

Parameter	DFT ¹⁴	RetroFit [§]	RetroFit with perturbation [§]
R _{CuCu} / Å	7.99969	7.9997	7.9997
$\gamma / ^\circ$	60.0	60.0	60.0
R _{NN} / Å	4.614	4.447	4.614
$\alpha / ^\circ$	132.34	118.42	123.34
R _{CuN} / Å	2.324	2.492	2.397
$\delta / ^\circ$	163.08	164.54	165.08
$\theta / ^\circ$	143.75	150.79	143.8
$\Delta E / \text{kcal mol}^{-1}$	-	2.24	1.59

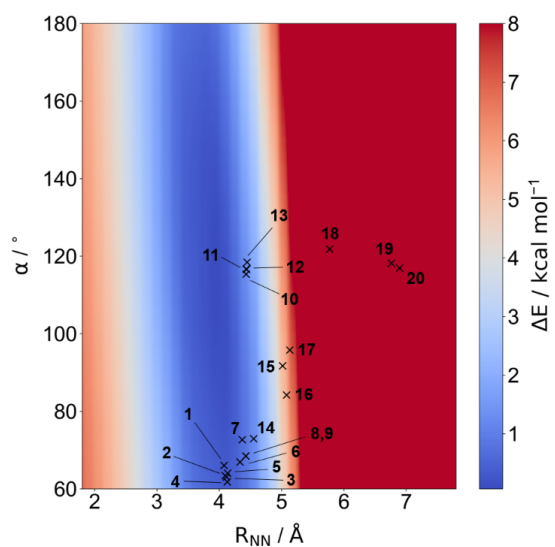
[§] Values obtained following the regular RetroFit routine. R_{NN} and α for TCNQ were optimized as described above.

[§] Using R_{NN} and α for TCNQ from the DFT optimized structure,¹⁴ i.e. taking into account the distortion of the CL, results in a lower ΔE , showing that RetroFit slightly overestimates ΔE (see Supplementary Note 4: Restrictions and limitations of RetroFit).

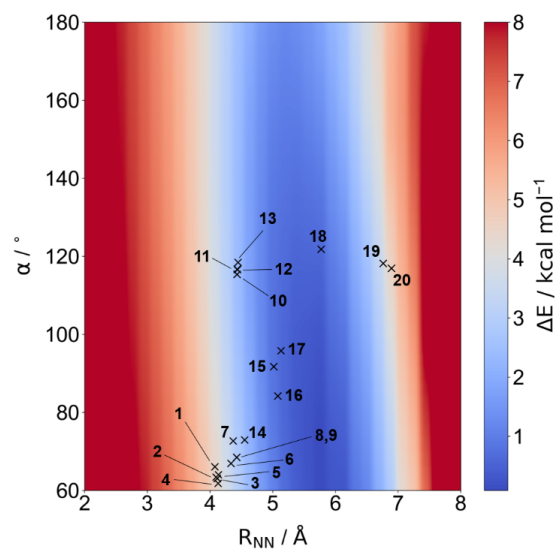
Supplementary Note 8: Results from RetroFit for NOTT-100 and NOTT-101



Supplementary Figure 15: RetroFit map for the 3,5-position of NOTT-100 and dinitrile-CLs. The energy penalty ΔE for the CL parameters R_{NN} and α is given as a color code increasing from blue to red. The tested molecules are marked on the map and listed on the right side with increasing ΔE . Energies exceeding the color scale bar are set to 8 kcal/mol for better visualization.

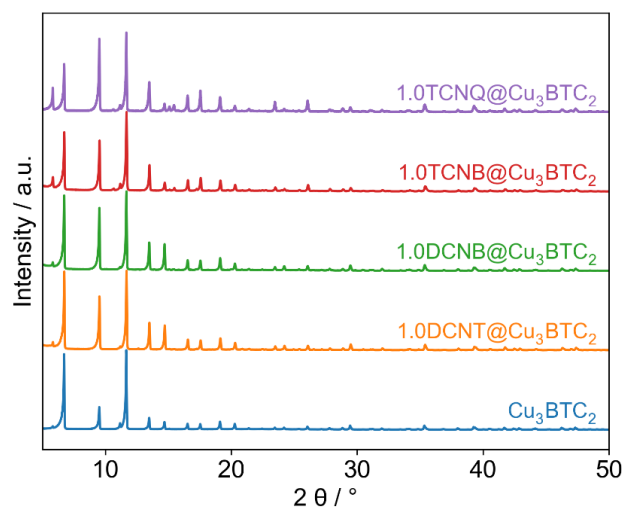


Supplementary Figure 16: RetroFit map for the 3,3'-position of NOTT-100 and dinitrile-CLs. The energy penalty ΔE for the CL parameters R_{NN} and α is given as a color code increasing from blue to red. The tested molecules are marked on the map and listed on the right side with increasing ΔE . Energies exceeding the color scale bar are set to 8 kcal/mol for better visualization.

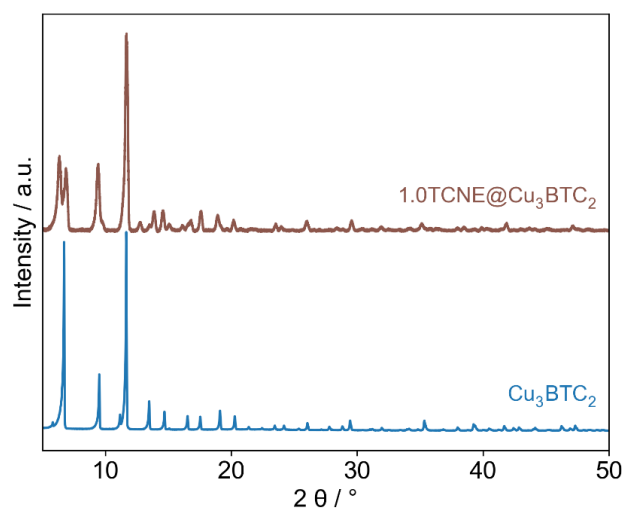


Supplementary Figure 17: RetroFit map for the 3,5-position of NOTT-101 and dinitrile-CLs. The energy penalty ΔE for the CL parameters R_{NN} and α is given as a color code increasing from blue to red. The tested molecules are marked on the map and listed on the right side with increasing ΔE . Energies exceeding the color scale bar are set to 8 kcal/mol for better visualization.

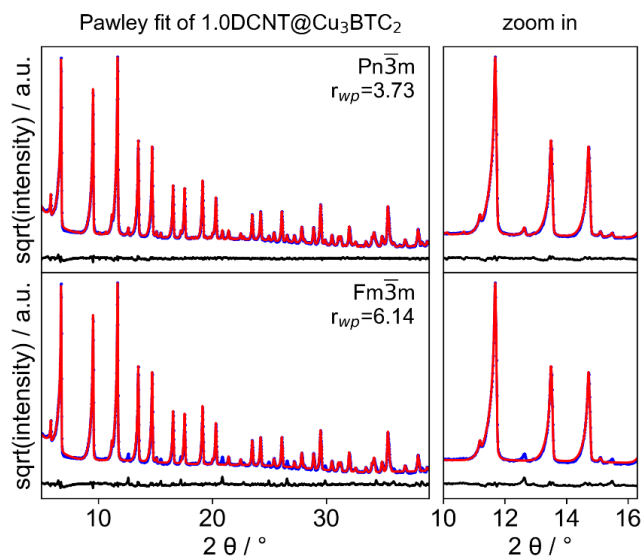
Supplementary Note 9: Powder X-ray diffraction



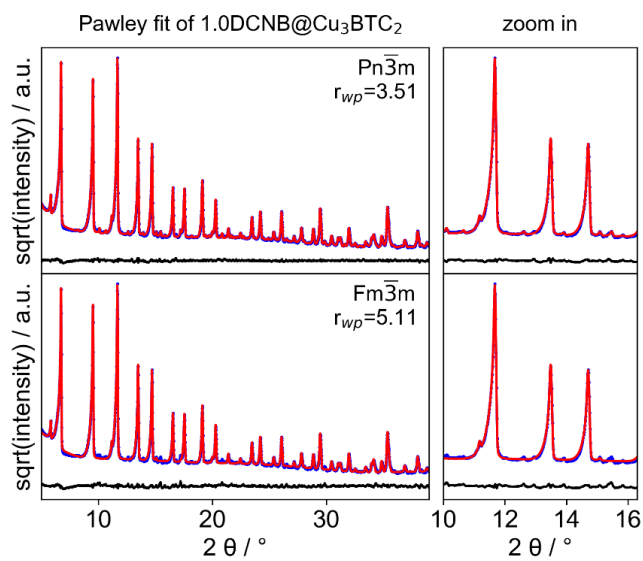
Supplementary Figure 18: Powder X-ray diffractograms of Cu₃BTC₂ (blue) and CL@Cu₃BTC₂ with CL = DCNT (orange), DCNB (green), TCNB (red), TCNQ (purple).



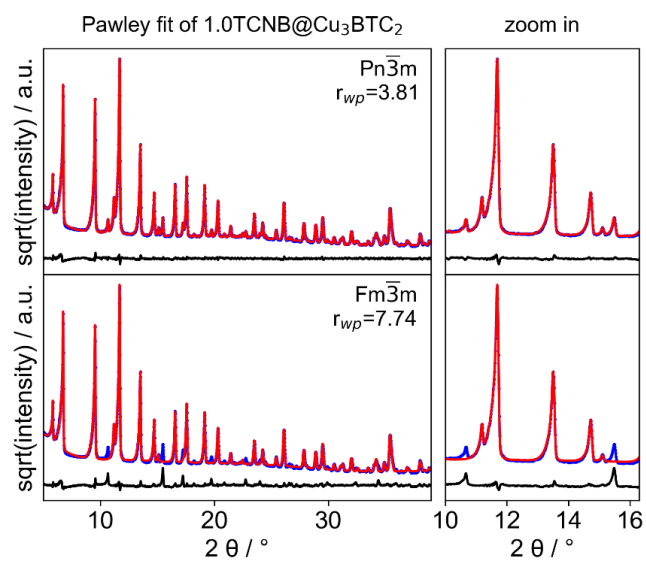
Supplementary Figure 19: Powder X-ray diffractograms of TCNE@Cu₃BTC₂ (brown) and Cu₃BTC₂ (blue).



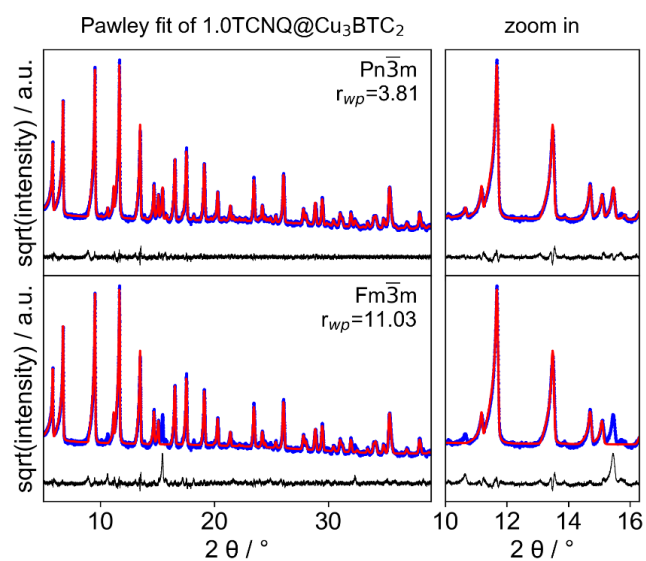
Supplementary Figure 20: Comparison of the Pawley profile fits for PXRD data of DCNT@Cu₃BTC₂ using the crystallographic space groups Fm-3m and Pn-3m.



Supplementary Figure 21: Comparison of the Pawley profile fits for PXRD data of DCNB@Cu₃BTC₂ using the crystallographic space groups Fm-3m and Pn-3m.



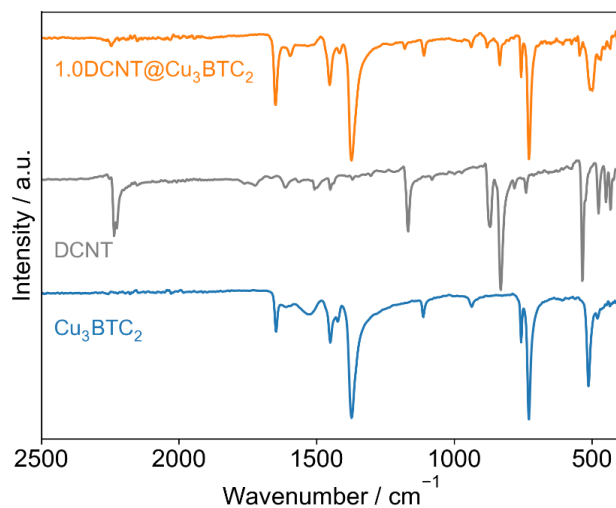
Supplementary Figure 22: Comparison of the Pawley profile fits for PXRD data of TCNB@Cu₃BTC₂ using the crystallographic space groups Fm-3m and Pn-3m.



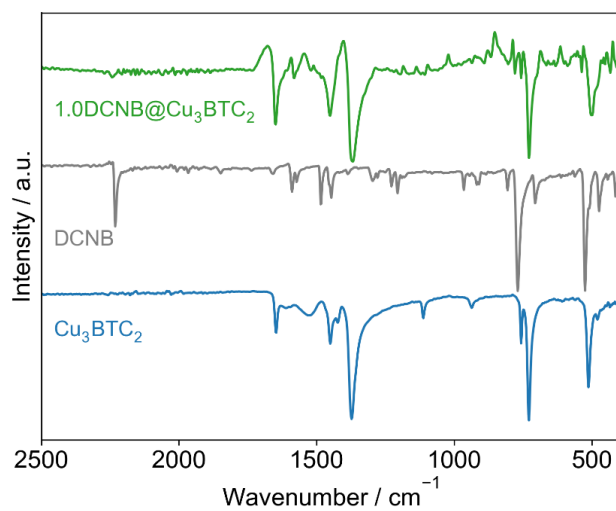
Supplementary Figure 23: Comparison of the Pawley profile fits for PXRD data of TCNQ@Cu₃BTC₂ using the crystallographic space groups Fm-3m and Pn-3m.

Supplementary Note 10: Fourier transform infrared spectroscopy

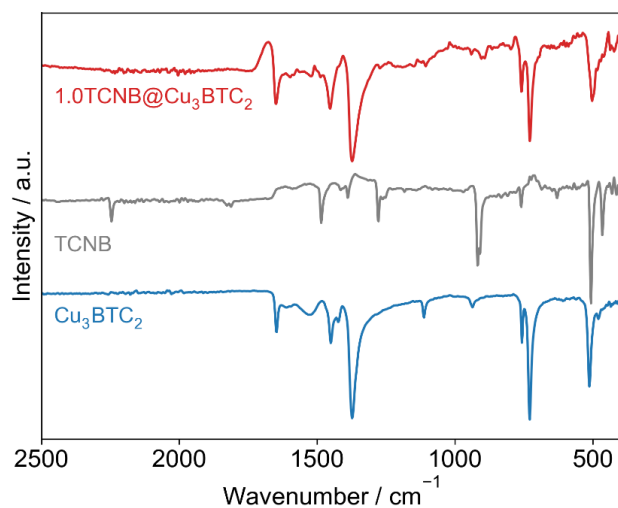
Fourier transform infrared spectroscopy (FTIR) measurements of powder samples were performed inside an Ar-filled glovebox on an ALPHA FTIR spectrometer (Bruker). The instrument was equipped with a Pt attenuated total reflectance (ATR) unit. 64 scans per measurement were recorded at room temperature in the range of 400–4000 cm^{-1} with a resolution of 2 cm^{-1} .



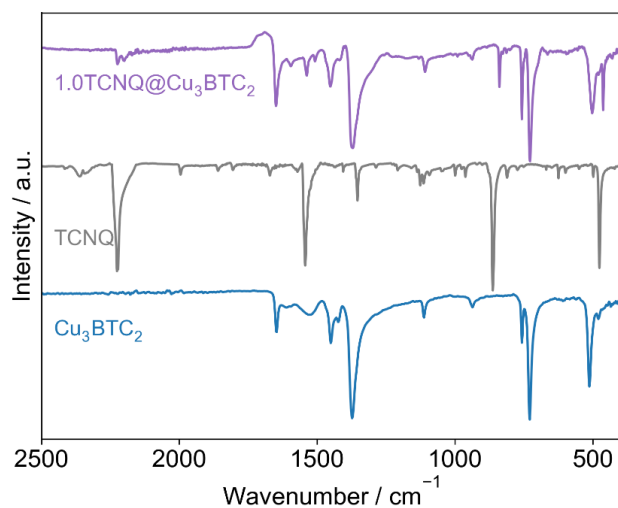
Supplementary Figure 24: IR transmission spectrum of pristine Cu₃BTC₂, DCNB and DCNB@Cu₃BTC₂. The spectra are background corrected and normalized. A vertical offset is applied for visualization.



Supplementary Figure 25: IR transmission spectrum of pristine Cu_3BTC_2 , DCNB and DCNB@ Cu_3BTC_2 . The spectra are background corrected and normalized. A vertical offset is applied for visualization.



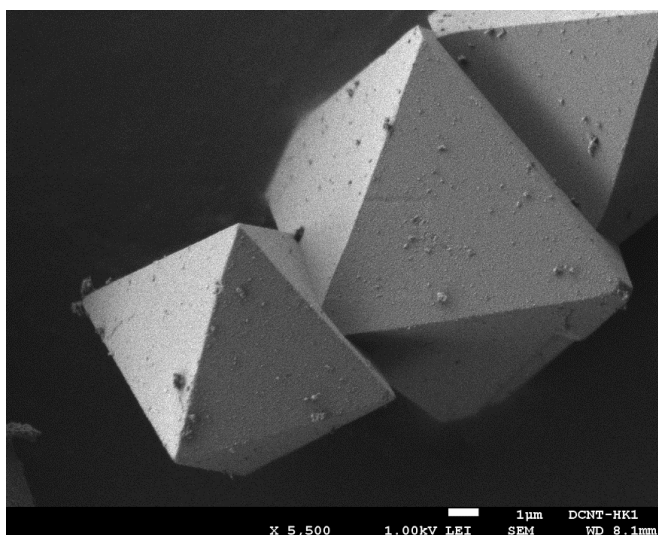
Supplementary Figure 26: FTIR transmission spectrum of pristine Cu_3BTC_2 , TCNQ and TCNQ@ Cu_3BTC_2 . The spectra are background corrected and normalized. A vertical offset is applied for visualization.



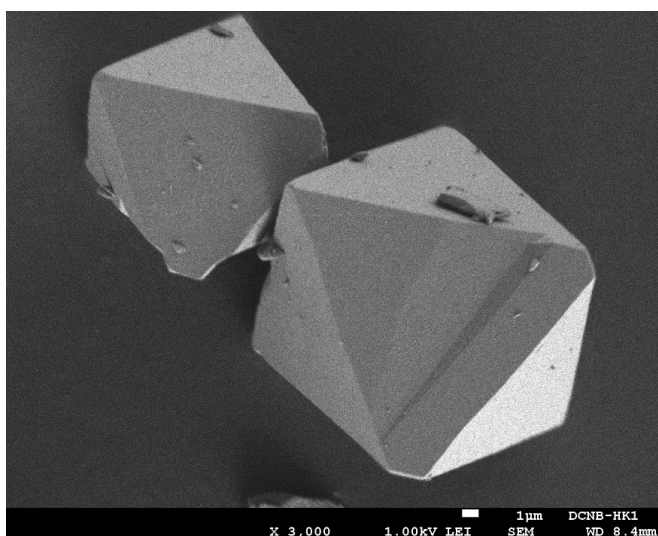
Supplementary Figure 27: FTR transmission spectrum of pristine Cu_3BTC_2 , TCNQ and TCNQ@ Cu_3BTC_2 . The spectra are background corrected and normalized. A vertical offset is applied for visualization.

Supplementary Note 11: Scanning electron microscopy

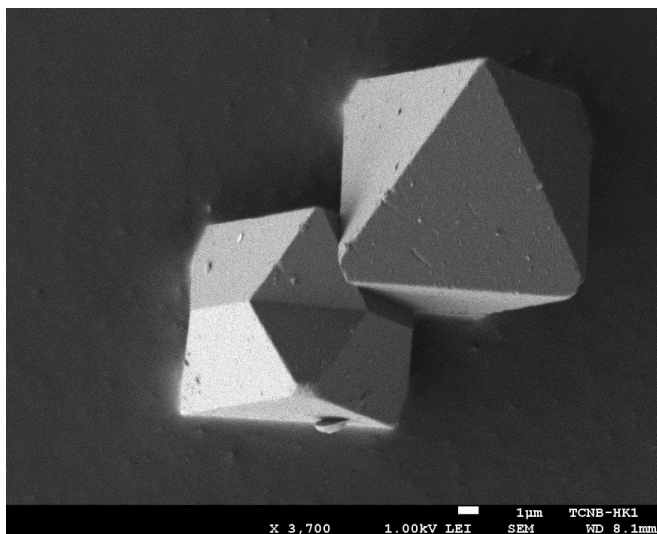
SEM images were recorded using a JEOL JSM-7500F field emission scanning electron microscope operated in gentle beam mode.



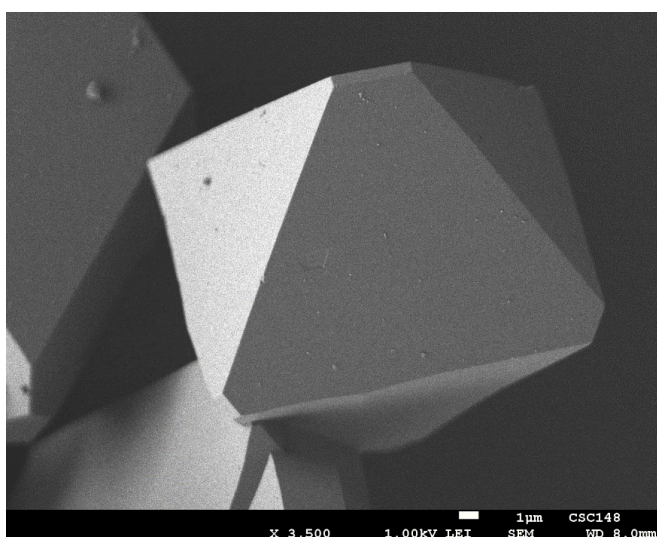
Supplementary Figure 28: SEM image of 1.0DCNT@Cu₃BTC₂.



Supplementary Figure 29: SEM image of 1.0DCNB@Cu₃BTC₂.



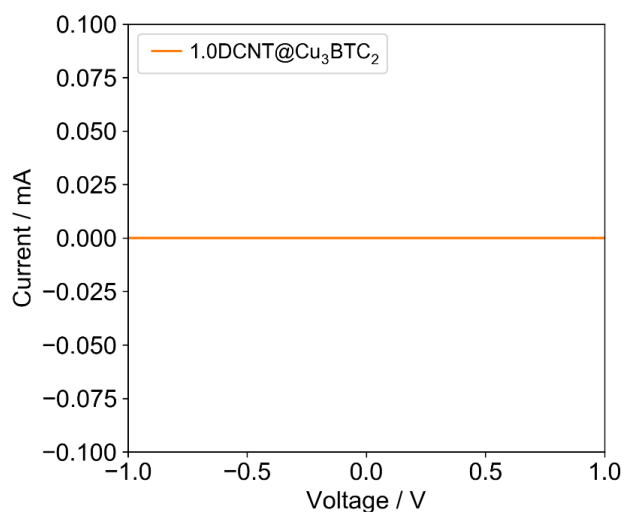
Supplementary Figure 30: SEM image of 1.0TCNB@Cu₃BTC₂.



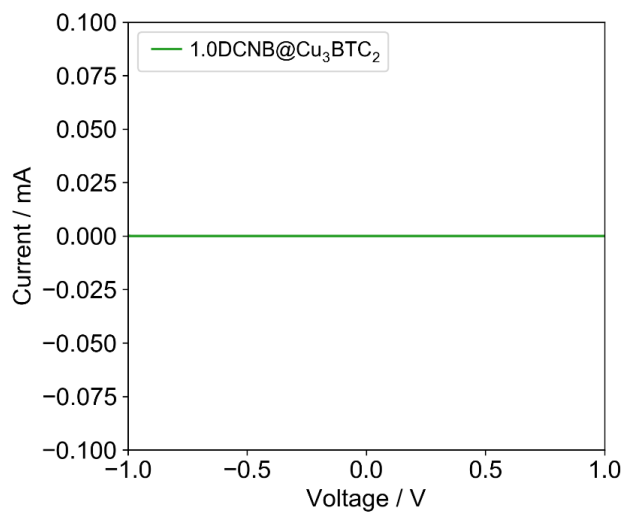
Supplementary Figure 31: SEM image of 1.75TCNE@Cu₃BTC₂.

Supplementary Note 12: Electrical conductivity measurements

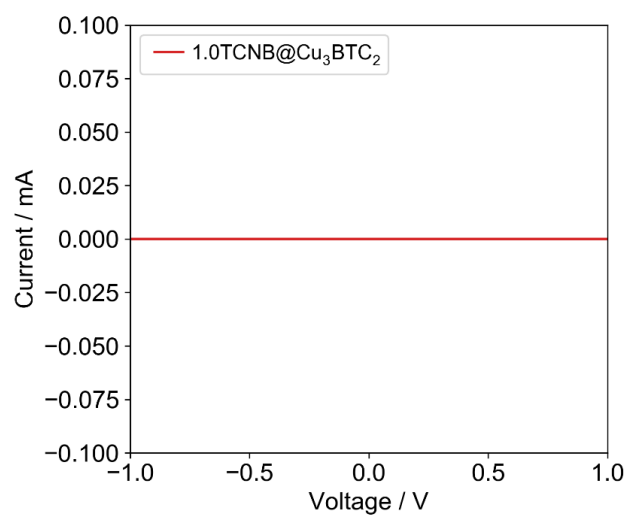
The electrical conductivity of the materials was determined by *IV* measurements in a 2-point probe press cell. Inside the glovebox, powders were filled into the cell and compressed between stainless steel cylinders (1 cm diameter) at 3 t. A detailed description of the cell can be found elsewhere.¹⁵ The *IV*-curves were recorded using a Gamry Reference 3000 potentiostat.



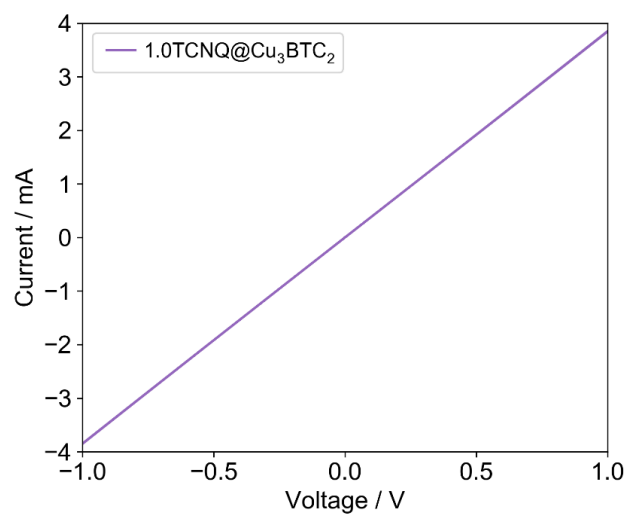
Supplementary Figure 32: *IV* curve of DCNT@Cu₃BTC₂.



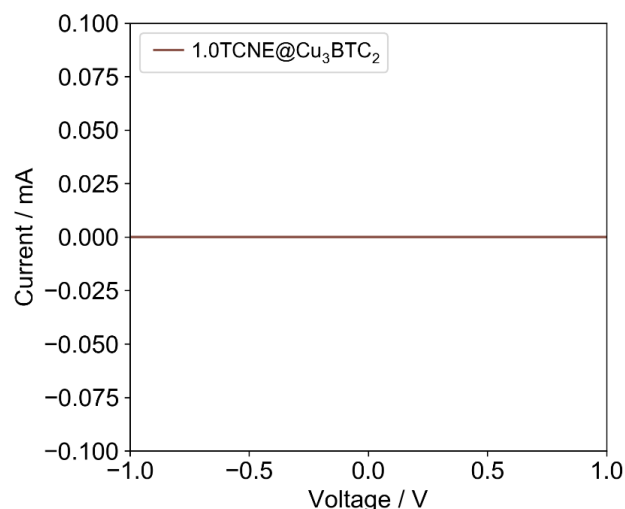
Supplementary Figure 33: *IV* curve of DCNB@Cu₃BTC₂.



Supplementary Figure 34: I/V curve of TCNB@Cu₃BTC₂.



Supplementary Figure 35: I/V curve of TCNQ@Cu₃BTC₂. The conductivity is in the order of 10^{-4} S/cm.



Supplementary Figure 36: *IV* curve of TCNE@Cu₃BTC₂.

We observed no current for any of the host-guest materials with DCNT, DCNB, TCNB, or TCNE as the guest. The insulating character of these materials can be the result of different redox potentials of the guests. For instance, the one electron reduction potential for TCNB is -0.71 V vs. S.C.E. and 0.19 V vs. S.C.E. for TCNQ.¹⁶ However, the reduction potential of TCNE (0.24 V vs. S.C.E.¹⁶) is very close to the one of TCNQ, but we did not observe any conductivity for TCNE@Cu₃BTC₂ either. As we observe significant structural changes from the PXRD data of TCNE@Cu₃BTC₂ the interpretation of the properties is rather speculative. Under consideration of the SEM images, indicating no by-phase for any of the new host guest materials, it is possible that the CuTCNQ by-phase is the main contributor to the electrical conductivity of TCNQ@Cu₃BTC₂ prepared via vapor phase infiltration.

Supplementary References

1. Frisch M. J., et al. Gaussian 16 Rev. B.01. (ed[^](eds) (2016).
2. Ditchfield R., Hehre W. J., Pople J. A. Self-Consistent Molecular-Orbital Methods. IX. An Extended Gaussian-Type Basis for Molecular-Orbital Studies of Organic Molecules. *J. Chem. Phys.* **54**, 724-728 (1971).
3. Lee C., Yang W., Parr R. G. Development of the Colle-Salvetti Correlation-Energy Formula into a Functional of the Electron Density. *Phys. Rev. B* **37**, 785-789 (1988).
4. Ahlrichs R., Bär M., Häser M., Horn H., Kölmel C. Electronic structure calculations on workstation computers: The program system turbomole. *Chem. Phys. Lett.* **162**, 165-169 (1989).
5. Becke A. D. A new Mixing of Hartree-Fock and Local Density-Functional Theories. *J. Chem. Phys.* **98**, 1372-1377 (1993).
6. Weigend F., Häser M., Patzelt H., Ahlrichs R. RI-MP2: Optimized Auxiliary Basis Sets and Demonstration of Efficiency. *Chem. Phys. Lett.* **294**, 143-152 (1998).
7. Treutler O., Ahlrichs R. Efficient molecular numerical integration schemes. *J. Chem. Phys.* **102**, 346-354 (1995).

8. Sierka M., Hogekamp A., Ahlrichs R. Fast evaluation of the Coulomb potential for electron densities using multipole accelerated resolution of identity approximation. *J. Chem. Phys.* **118**, 9136-9148 (2003).
9. Eichkorn K., Treutler O., Öhm H., Häser M., Ahlrichs R. Auxiliary basis sets to approximate Coulomb potentials. *Chem. Phys. Lett.* **240**, 283-290 (1995).
10. Eichkorn K., Weigend F., Treutler O., Ahlrichs R. Auxiliary basis sets for main row atoms and transition metals and their use to approximate Coulomb potentials. *Theor. Chem. Acc.* **97**, 119-124 (1997).
11. Grimme S., Antony J., Ehrlich S., Krieg H. A consistent and accurate ab initio parametrization of density functional dispersion correction (DFT-D) for the 94 elements H-Pu. *J. Chem. Phys.* **132**, 154104 (2010).
12. Elmali A. The Magnetic Super-Exchange Coupling in Copper(II) Acetate Monohydrate and a Redetermination of the Crystal Structure. *Turk. J. Phys.* **24**, 667-672 (2000).
13. Tafipolsky M., Amirjalayer S., Schmid R. First-Principles-Derived Force Field for Copper Paddle-Wheel-Based Metal–Organic Frameworks. *J. Phys. Chem. C* **114**, 14402-14409 (2010).
14. Talin A. A., et al. Tunable Electrical Conductivity in Metal–Organic Framework Thin-Film Devices. *Science* **343**, 66-69 (2014).
15. Schneider C., et al. High Electrical Conductivity and High Porosity in a Guest@MOF Material: Evidence of TCNQ Ordering within Cu3BTC2 Micropores. *Chem. Sci.* **9**, 7405-7412 (2018).
16. Peover M. E. Reduction potentials and intermolecular charge-transfer spectra of organic acceptor molecules. Part 4.-Nitrobenzenes. *J. Chem. Soc. Faraday Trans.* **60**, 479-483 (1964).

7 Appendix

7.1 Complete List of Publications

7.1.1 Publications on which this Thesis is Based

A) Journal contributions

- [6] **C. Schneider**, M. Mendt, A. Pöpl, V. Crocellà, R. A. Fischer, Scrutinizing the Pore Chemistry and the Importance of Cu(I) Defects in TCNQ-loaded Cu_3BTC_2 by a Multi-Technique Spectroscopic Approach. *ACS Appl. Mater. Interfaces*, **2020**, *12*, 1024-1035.
- [5] M. Rivera-Torrente, M. Filez, **C. Schneider**, E. C. van der Feltz, K. Wolkersdörfer, M. Wark, R. A. Fischer, and B. M. Weckhuysen, In-Situ Micro-Spectroscopic Imaging of Guests@MOF Crystals: The Case of TCNQ-Loaded HKUST-1. *Phys. Chem. Chem. Phys.*, **2019**, *21*, 25678-25689.
- [4] **C. Schneider**[‡], D. Bodesheim[‡], J. Keupp, R. Schmid, G. Kieslich, Retrofitting Metal-Organic Frameworks. *Nat. Commun.* **2019**, *10*, 4921.
- [3] **C. Schneider**, D. Bodesheim, M. G. Ehrenreich, V. Crocellà, J. Mink, R. A. Fischer, K. T. Butler, G. Kieslich, Tuning the Negative Thermal Expansion Behavior of the Metal-Organic Framework Cu_3BTC_2 by Retrofitting. *J. Am. Chem. Soc.* **2019**, *141*, 10504-10509.
- [2] K. Thürmer[‡], **C. Schneider**[‡], V. Stavila, R. W. Friddle, F. Léonard, R. A. Fischer, M. D. Allendorf, A. A. Talin, Surface Morphology and Electrical Properties of Cu_3BTC_2 Thin Films Before and After Reaction with TCNQ. *ACS Appl. Mater. Interfaces*, **2018**, *10*, 39400-39410.
- [1] **C. Schneider**, D. Ukaj, R. Koerver, A. A. Talin, G. Kieslich, S. P. Pujari, H. Zuilhof, J. Janek, M. D. Allendorf, R. A. Fischer, High Electrical Conductivity and High Porosity in a Guest@MOF Material: Evidence of TCNQ Ordering within Cu_3BTC_2 Micropores. *Chem. Sci.* **2018**, *9*, 7405-7412.

B) Conference Contributions

- [5] *6th International Conference on Metal-Organic Frameworks and Open Framework Compounds*, Auckland, New Zealand, December 2018, oral presentation: *Unraveling the structure-property relationship in electrically conductive TCNQ@Cu₃BTC₂*
- [4] *Workshop Electrochemical and Electrical Characterization of Films of Coordination Network Compounds*, Oldenburg, Germany, June 2018, poster presentation: *Electrical conductivity in vapor-phase loaded TCNQ@Cu₃BTC₂*
- [3] *2nd European Conference on Metal-Organic Frameworks and Porous Polymers*, Delft, Netherlands, November 2017, poster presentation: *Electrical conductivity in vapor-phase loaded Guest@HKUST-1 materials*
- [2] *19. JCF Frühjahrssymposium*, Mainz, Germany, March 2017, poster presentation: *Guest-Induced Electrical Conductivity in Metal-Organic Frameworks*
- [1] *5th International Conference on Metal-Organic Frameworks and Open Framework Compounds*, Long Beach (CA), USA, September 2016, poster presentation: *Electrical Conductivity and Morphology Changes of HKUST-1 single crystals and thin films upon exposure to TCNQ*

7.1.2 Other Publications

A) Journal Contributions

- [4] D. C. Mayer, A. Manzi, R. Medishetty, B. Winkler, **C. Schneider**, G. Kieslich, A. Pöthig, J. Feldmann, R. A. Fischer, Controlling Multiphoton Absorption Efficiency by Chromophore Packing in Metal–Organic Frameworks. *J. Am. Chem. Soc.* **2019**, *141*, 11594-11602.
- [3] A. Schneemann, R. Rudolf, S. Henke, Y. Takahashi, H. Banh, I. Hante, **C. Schneider**, S.-i. Noro, R. A. Fischer, Linker Functionalisation Triggers an Alternative 3D-Topology for Zn-Isophthalate-4,4'-Bipyridine Frameworks. *Dalton Trans.* **2017**, *46*, 8198-8203.
- [2] W. Zhang, K. Freitag, S. Wannapaiboon, **C. Schneider**, K. Epp, G. Kieslich, R. A. Fischer, Elaboration of a Highly Porous Ru^{II,III} Analogue of HKUST-1. *Inorg. Chem.* **2016**, *55*, 12492-12495.
- [1] V. Stavila, **C. Schneider**, C. Mowry, T. R. Zeitler, J. A. Greathouse, A. L. Robinson, J. M. Denning, J. Volponi, K. Leong, W. Quan, M. Tu, R. A. Fischer, M. D. Allendorf, Thin Film Growth of nbo MOFs and their Integration with Electroacoustic Devices. *Adv. Funct. Mater.* **2016**, *26*, 1699-1707.

B) Conference Contributions

- [1] *1st European Conference on Metal-Organic Frameworks and Porous Polymers*, Potsdam, Germany, October 2015, oral presentation: *Electrically Conducting Copper Paddlewheel Metal-Organic Frameworks*

7.2 Reprint Permissions

Study I:

Rightslink® by Copyright Clearance Center

https://s100.copyright.com/AppDispatchServlet#formTop



The screenshot shows the RightsLink interface. At the top left is the Copyright Clearance Center logo. To its right is the RightsLink logo. Further right are navigation buttons for Home, Create Account, and Help, along with a LIVE CHAT button. Below the Copyright Clearance Center logo is the ACS Publications logo with the tagline "Most Trusted. Most Cited. Most Read." The main content area displays the following information:

Title: Surface Morphology and Electrical Properties of Cu₃BTC₂ Thin Films Before and After Reaction with TCNQ

Author: Konrad Thürmer, Christian Schneider, Vitalie Stavila, et al

Publication: Applied Materials

Publisher: American Chemical Society

Date: Nov 1, 2018

Copyright © 2018, American Chemical Society

On the right side, there is a LOGIN box with the text: "If you're a copyright.com user, you can login to RightsLink using your copyright.com credentials. Already a RightsLink user or want to learn more?"

PERMISSION/LICENSE IS GRANTED FOR YOUR ORDER AT NO CHARGE

This type of permission/license, instead of the standard Terms & Conditions, is sent to you because no fee is being charged for your order. Please note the following:

- Permission is granted for your request in both print and electronic formats, and translations.
- If figures and/or tables were requested, they may be adapted or used in part.
- Please print this page for your records and send a copy of it to your publisher/graduate school.
- Appropriate credit for the requested material should be given as follows: "Reprinted (adapted) with permission from (COMPLETE REFERENCE CITATION). Copyright (YEAR) American Chemical Society." Insert appropriate information in place of the capitalized words.
- One-time permission is granted only for the use specified in your request. No additional uses are granted (such as derivative works or other editions). For any other uses, please submit a new request.

[BACK](#)
[CLOSE WINDOW](#)

Copyright © 2019 Copyright Clearance Center, Inc. All Rights Reserved. [Privacy statement](#). [Terms and Conditions](#).
Comments? We would like to hear from you. E-mail us at customercare@copyright.com

Study II:

High electrical conductivity and high porosity in a Guest@MOF material: evidence of TCNQ ordering within Cu_3BTC_2 micropores

C. Schneider, D. Ukaj, R. Koerver, A. A. Talin, G. Kieslich, S. P. Pujari, H. Zuilhof, J. Janek, M. D. Allendorf and R. A. Fischer, *Chem. Sci.*, 2018, **9**, 7405

DOI: 10.1039/C8SC02471E

This article is licensed under a [Creative Commons Attribution-NonCommercial 3.0 Unported Licence](#). Material from this article can be used in other publications provided that the correct acknowledgement is given with the reproduced material and it is not used for commercial purposes.

Reproduced material should be attributed as follows:

- For reproduction of material from NJC:
[Original citation] - Published by The Royal Society of Chemistry (RSC) on behalf of the Centre National de la Recherche Scientifique (CNRS) and the RSC.
- For reproduction of material from PCCP:
[Original citation] - Published by the PCCP Owner Societies.
- For reproduction of material from PPS:
[Original citation] - Published by The Royal Society of Chemistry (RSC) on behalf of the European Society for Photobiology, the European Photochemistry Association, and RSC.
- For reproduction of material from all other RSC journals:
[Original citation] - Published by The Royal Society of Chemistry.

Information about reproducing material from RSC articles with different licences is available on our [Permission Requests page](#).

Study III:

Rightslink® by Copyright Clearance Center

10.01.20, 00:04



RightsLink®



Home



Help



Email Support



Sign in



Create Account

ACS Publications
Most Trusted. Most Cited. Most Read.**Scrutinizing the Pore Chemistry and the Importance of Cu(I) Defects in TCNQ-Loaded Cu₃(BTC)₂ by a Multitechnique Spectroscopic Approach**

Author: Christian Schneider, Matthias Mendt, Andreas Pöppel, et al

Publication: Applied Materials

Publisher: American Chemical Society

Date: Jan 1, 2020

Copyright © 2020, American Chemical Society

PERMISSION/LICENSE IS GRANTED FOR YOUR ORDER AT NO CHARGE

This type of permission/license, instead of the standard Terms & Conditions, is sent to you because no fee is being charged for your order. Please note the following:

- Permission is granted for your request in both print and electronic formats, and translations.
- If figures and/or tables were requested, they may be adapted or used in part.
- Please print this page for your records and send a copy of it to your publisher/graduate school.
- Appropriate credit for the requested material should be given as follows: "Reprinted (adapted) with permission from (COMPLETE REFERENCE CITATION). Copyright (YEAR) American Chemical Society." Insert appropriate information in place of the capitalized words.
- One-time permission is granted only for the use specified in your request. No additional uses are granted (such as derivative works or other editions). For any other uses, please submit a new request.

BACK

CLOSE WINDOW

© 2020 Copyright - All Rights Reserved | [Copyright Clearance Center, Inc.](#) | [Privacy statement](#) | [Terms and Conditions](#)
Comments? We would like to hear from you. E-mail us at customer care@copyright.com

Study IV:

Rightslink® by Copyright Clearance Center

<https://s100.copyright.com/AppDispatchServlet#formTop>

RightsLink®

Home

Create Account

Help

ACS Publications
Most Trusted. Most Cited. Most Read.**Title:** Tuning the Negative Thermal Expansion Behavior of the Metal–Organic Framework Cu3BTC2 by Retrofitting**Author:** Christian Schneider, David Bodesheim, Michael G. Ehrenreich, et al**Publication:** Journal of the American Chemical Society**Publisher:** American Chemical Society**Date:** Jul 1, 2019

Copyright © 2019, American Chemical Society

LOGIN

If you're a **copyright.com user**, you can login to RightsLink using your copyright.com credentials. Already a **RightsLink user** or want to [learn more?](#)

PERMISSION/LICENSE IS GRANTED FOR YOUR ORDER AT NO CHARGE

This type of permission/license, instead of the standard Terms & Conditions, is sent to you because no fee is being charged for your order. Please note the following:

- Permission is granted for your request in both print and electronic formats, and translations.
- If figures and/or tables were requested, they may be adapted or used in part.
- Please print this page for your records and send a copy of it to your publisher/graduate school.
- Appropriate credit for the requested material should be given as follows: "Reprinted (adapted) with permission from (COMPLETE REFERENCE CITATION). Copyright (YEAR) American Chemical Society." Insert appropriate information in place of the capitalized words.
- One-time permission is granted only for the use specified in your request. No additional uses are granted (such as derivative works or other editions). For any other uses, please submit a new request.

BACK

CLOSE WINDOW

Copyright © 2019 [Copyright Clearance Center, Inc.](#) All Rights Reserved. [Privacy statement.](#) [Terms and Conditions.](#) Comments? We would like to hear from you. E-mail us at customercare@copyright.com

Study V:

Rightslink® by Copyright Clearance Center

<https://s100.copyright.com/AppDispatchServlet?imprint=Nature&oa=C...>

RightsLink®



Home



Help



Email Support



Sign In



Create Account

Retrofitting metal-organic frameworks

Author: Christian Schneider et al

Publication: Nature Communications

Publisher: Springer Nature

Date: Oct 29, 2019

*Copyright © 2019, Springer Nature***SPRINGER NATURE**

Creative Commons

This is an open access article distributed under the terms of the [Creative Commons CC BY](#) license, which permits unrestricted use, distribution, and reproduction in any medium, provided the original work is properly cited.

You are not required to obtain permission to reuse this article.

To request permission for a type of use not listed, please contact [Springer Nature](#)

© 2019 Copyright - All Rights Reserved | [Copyright Clearance Center, Inc.](#) | [Privacy statement](#) | [Terms and Conditions](#)
Comments? We would like to hear from you. E-mail us at customercare@copyright.com